Universitat Autònoma de Barcelona

# Diseño de Filtros de Microondas basados en líneas de transmisión de onda lenta mediante técnicas de Space Mapping

**Marco Antonio Orellana Gutiérrez**

**ADVERTIMENT.** L'accés als continguts d'aquesta tesi queda condicionat a l'acceptació de les condicions d'ús establertes per la següent llicència Creative Commons: http://cat.creativecommons.org/?page_id=184

**ADVERTENCIA.** El acceso a los contenidos de esta tesis queda condicionado a la aceptación de las condiciones de uso establecidas por la siguiente licencia Creative Commons: http://es.creativecommons.org/blog/licencias/

**WARNING.** The access to the contents of this doctoral thesis it is limited to the acceptance of the use conditions set by the following Creative Commons license: https://creativecommons.org/licenses/?lang=en

# Diseño de Filtros de Microondas basados en líneas de transmisión de onda lenta mediante técnicas de Space Mapping

**Tesis Doctoral realizada por**

**Marco Antonio Orellana Gutiérrez**

**Bajo la dirección de**

**Ferran Martín Antolín**

Bellaterra (Cerdanyola del Vallès), Septiembre 2016

**Universitat Autònoma de Barcelona**

**Doctorado en Ingeniería Electrónica y de Telecomunicación**

**Departamento de Ingeniería Electrónica, UAB**

**Centro de Investigación en Metamateriales para la Innovación en Tecnologías Electrónica y de Comunicaciones, CIMITEC – UAB**

# Diseño de Filtros de Microondas basados en líneas de transmisión de onda lenta mediante técnicas de Space Mapping

**Tesis Doctoral realizada por**

**Marco Antonio Orellana Gutiérrez**

**Bajo la dirección de**

**Ferran Martín Antolín**

**Firma:** Ferran Martín Antolín **Firma:** Marco Orellana Gutiérrez

Bellaterra (Cerdanyola del Vallès), Septiembre 2016

**Dr. Ferran Martín Antolín**

Profesor del Departamento de Ingeniería Electrónica de la Universitat Autònoma de Barcelona,

**CERTIFICA:**

Que la tesis titulada: "**Diseño de Filtros de Microondas basados en líneas de transmisión de onda lenta mediante técnicas de Space Mapping**" ha sido escrita por **Marco Antonio Orellana Gutiérrez** bajo su supervisión.

Y para certificarlo, firma la presente.

**Firma:** Ferran Martín Antolín

Bellaterra, 20 de Septiembre del 2016

# Contenido

# Agradecimientos

Deseo agradecer a mi director, Ferran Martín Antolín, por su apoyo en todo momento, sus ideas innovadoras, por introducirme a la ingeniería de microondas y por permitirme trabajar en su grupo de investigación. Agradezco al investigador Jordi Selga Ruiz por su apoyo y por introducirme a los métodos de optimización de circuitos de microondas. A ambos les agradezco muchísimo sus enseñanzas, su paciencia y su confianza en mí. Estoy sumamente agradecido, esta etapa ha sido muy valiosa en mi formación.

Deseo agradecer por su compañerismo a los miembros del grupo CIMITEC, Jordi Bonache, Gerard Sisó, Anna Cedenilla, Lijuan Su, Pau Aguilà, Ferran Paredes, Paris Vélez, Simone Zuffanelli, Gerard Zamora y Cristian Herrojo. Doy las gracias a mis compañeros del Departamento, Enrique Colomés y Zhen Zhan.

Agradezco a todos los profesores del Departamento de Ingeniería Electrónica y al personal administrativo por sus enseñanzas y ayuda.

Deseo agradecer a los profesores de la Escuela de Ingeniería Eléctrica de la Universidad de Costa Rica por su buena formación. Agradezco el apoyo de los profesores Jorge Arturo Romero, Randolph Steinvorth y Luis Diego Marín.

Agradezco muchísimo el apoyo de la Universidad de Costa Rica en la etapa de Máster y de Doctorado en la UAB. Doy las gracias al proyecto E2nhance de Erasmus Mundus por apoyarme en la etapa de Máster en la UAB.

Deseo dedicar este trabajo a mis padres, Silvano, María de los Angeles y José Antonio.

# Resumen

Este trabajo (presentado como compendio de publicaciones) representa una contribución a las líneas de transmisión artificiales. Específicamente se pudo diseñar de forma automática estructuras (líneas de transmisión) de onda lenta basadas en parches capacitivos de EBGs (del inglés, *Electromagnetic Band Gaps*) a frecuencias de microondas. Estas estructuras presentan una razón de onda lenta que produce una reducción del tamaño del circuito de microondas, puesto que la longitud de onda en la estructura es menor que en una línea de transmisión ordinaria. Además, si se concatenan varias estructuras de onda lenta es posible obtener bandas de rechazo y así suprimir bandas espurias. Se dedica un capítulo a la síntesis de estas estructuras.

Estas estructuras optimizadas podrán encontrar varias aplicaciones, donde se sustituye una línea de transmisión ordinaria por una línea de transmisión artificial. Se tomará en cuenta la impedancia característica de la línea ordinaria y su longitud eléctrica a una frecuencia de operación para la síntesis de estas líneas de transmisión de onda lenta.

En la tesis se pudo aplicar éste método de diseño de estructuras de onda lenta a la síntesis automática de filtros pasabanda de banda ancha, en concreto, se realizó una mejora a los filtros de Levy. Se incorporaron estructuras EBG para reducir la longitud del filtro y además suprimir el primer espurio, se logró obtener una amplia banda de rechazo debido a la concatenación de varias estructuras de onda lenta. Para los filtros mejorados se obtuvo respuestas electromagnéticas que coinciden muy bien con el filtro canónico de Levy.

Por último se pudo sintetizar filtros pasabanda basados en pares de líneas acopladas con carga capacitiva a frecuencias de microondas. Se presentaron dos ejemplos de filtros Chebyshev, se obtuvo una gran coincidencia (ajuste en los ceros de reflexión, ancho de banda y frecuencia central) en la respuesta electromagnética y el esquemático ideal al sintetizar cada sección de los filtros por separado y luego concatenar las secciones optimizadas. Estos filtros muestran el efecto de onda lenta y se reduce su longitud, además es posible suprimir las bandas espurias hasta varios armónicos. Debido a las propiedades de los EBG son filtros muy eficientes suprimiendo espurios.

Ambas aplicaciones se implementan completamente en tecnología planar y su síntesis se debe gracias al funcionamiento en conjunto del programa *Matlab* y de un simulador electromagnético. A la vez estos resultados son posibles gracias a un algoritmo ASM (*Aggressive Space Mapping*) que permite obtener soluciones óptimas.

# 1

# Motivación y Objetivos

Esta tesis es un desarrollo a los metamateriales planares o líneas de transmisión basadas en metamateriales. En concreto, se ha logrado optimizar estructuras de onda lenta basadas en EBG con carga capacitiva y también aplicar éstas estructuras al desarrollo de distintos tipos de filtros de microondas.

Estas líneas de transmisión artificiales exhiben una longitud eléctrica e impedancia Bloch a una determinada frecuencia de operación que es posible controlar. Debido a la carga capacitiva también es posible controlar el efecto de onda lenta y consecuentemente miniaturizar los circuitos de microondas. Con estas estructuras periódicas es también posible suprimir bandas espurias para circuitos de elementos distribuidos por el conocido efecto Bragg.

El primer objetivo es describir una metodología fundamental para sintetizar una celda unitaria con efecto de onda lenta, basado en una línea de transmisión con un parche capacitivo. El segundo objetivo es el de encontrar una primera aplicación de estas estructuras EBG optimizadas, en particular se pudo sintetizar filtros de Levy de banda ancha, esto de una forma sistemática. El tercer objetivo es el de sintetizar filtros pasabanda tipo Chebyshev, estos basados en pares de líneas acopladas con carga capacitiva.

Si bien en el pasado se ha realizado un esfuerzo por obtener filtros de microondas usando metamateriales en tecnología planar, es hasta hace poco que es posible obtenerlos de forma óptima dado que existen las herramientas matemáticas necesarias. En esta tesis se ha trabajado con optimización por Mapeo Espacial, en particular con "*Aggressive Space Mapping*" (ASM). Para obtener los circuitos óptimos es necesario trabajar en conjunto con un programa de programación (*Matlab*) y otro de simulación electromagnética *(Agilent Momentum*).

De forma detallada el esquema de la tesis es:

El Capítulo 2 presenta una introducción al estado del arte en líneas de transmisión de onda lenta y de otras estructuras EBG, se presenta además el método de la matriz de transferencia para el cálculo de la relación de dispersión e impedancia Bloch, los cuales fueron usados extensamente en la tesis. También se brinda una introducción a los Algoritmos de Mapeo Espacial y se presenta el Mapeo Espacial Agresivo (ASM) que es una mejora del método.

El Capítulo 3 presenta un trabajo muy fundamental sobre la síntesis de líneas de transmisión de onda lenta basadas en parches capacitivos. Este trabajo proporciona la topología exacta para una estructura de onda lenta con sus respectivas especificaciones de impedancia Bloch, longitud eléctrica y razón de onda lenta a una determinada frecuencia de operación. Se presenta varios ejemplos de síntesis y la elaboración teórica de este trabajo.

El Capítulo 4 presenta las primeras aplicaciones que se han encontrado para estas líneas de transmisión con parches capacitivos. Se presenta la síntesis automática de filtros pasabanda de banda ancha basados en estructuras EBG y también la síntesis de filtros pasabanda basados en líneas acopladas con carga capacitiva. Estos resultados han sido obtenidos por un proceso de optimización automática. Estos filtros que se han encontrado presentan una supresión de bandas espurias y además tienen dimensiones reducidas por el efecto de onda lenta.

En el Capítulo 5 se resumen las conclusiones destacadas de los resultados obtenidos en este trabajo.

Los resultados presentados en esta tesis han sido posibles gracias al grupo CIMITEC (*Centre d'Investigació en Metamaterials per a la Innovació en Tecnologíes Electrónica i de Comunicacions*), el cual forma parte del Departamento de Ingeniería Electrónica de la UAB. El grupo CIMITEC es un centro de investigación y transferencia tecnológica dedicado a obtener soluciones innovadoras y a medida para sistemas de comunicaciones. Este grupo está formado por doctores, ingenieros y técnicos con un alto grado de especialización. CIMITEC aplica su tecnología basada en los llamados Metamateriales en los siguientes campos: Antenas y tags para sistemas de Identificación por Radiofrecuencia (RFID), Comunicaciones de alta velocidad, Filtros y otros

componentes de RF/microondas de altas prestaciones, Electrónica impresa, Sensores y Síntesis automatizada de componentes entre otros.

Este trabajo ha sido apoyado por los gobiernos Español y Catalán por medio de varios proyectos y contratos, algunos de ellos son:

- Proyectos TEC2013-40600-R y TEC2013-49221-EXP de MINECO-España.
- Proyectos TEC2010-17512 METATRANSFER, CONSOLIDER EMET CSD2008-00066 de MINECO-España.
- Proyecto 2014SGR-157 de AGAUR-*Generalitat de Catalunya.*
- El autor agradece el apoyo de la Universidad de Costa Rica, MICITT y CONICIT para estudiar en la Universidad Autónoma de Barcelona.

# 2

# Introducción y Estado del Arte

En este capítulo se introducen las líneas de transmisión de onda lenta y se estudia el método de la matriz de transferencia, el cual es muy útil para el análisis de estructuras periódicas. Estas estructuras se pueden usar para la construcción de líneas de transmisión artificiales. Se presenta la deducción de las fórmulas para la relación de dispersión y para la impedancia Bloch, ambas variables definen la ingeniería de dispersión y su control es importante para problemas de ingeniería de microondas.

Se presenta además una introducción a los algoritmos de Mapeo Espacial. Estos encontraron aplicaciones inicialmente para resolver problemas de electromagnetismo, donde se requiere una alta capacidad de procesamiento de información. El Mapeo Espacial se ha extendido a otras disciplinas. El "*Aggressive Space Mapping* (ASM)" es una mejora del método y ha sido útil para la resolución de problemas de circuitos de microondas en tecnología planar. El ASM es el método usado en esta tesis.

Quisiéramos destacar que en los artículos para presentar la tesis por compendio de publicaciones (fundamentales y no fundamentales), se comparan nuestros resultados con otros de la literatura, especialmente en el artículo C.

# 2.1 Líneas de transmisión de onda lenta

Los cristales electromagnéticos o *Electromagnetic Band Gaps* (EBGs), conocidos como PBGs (*Photonic Band Gaps*) o cristales fotónicos a frecuencias ópticas, son estructuras periódicas capaces de inhibir la propagación de onda a ciertas frecuencias debido al conocido efecto Bragg, derivado de la periodicidad [1, 2].

En tecnología planar, las estructuras basadas en EBGs han sido propuestas en aplicaciones tales como reflectores de microondas [3-7], resonadores de alta calidad [8, 9], supresión de espurios en filtros [10-14] y supresión de armónicos en circuitos activos [15-19], entre otros.

En las aplicaciones previas, las estructuras EBG consisten típicamente de líneas de transmisión con un grabado en el plano de masa, por ejemplo mediante perforaciones en posiciones periódicas, ó de una modulación en la anchura de la línea (una línea de transmisión no uniforme). En ambos casos, las bandas de rechazo aparecen en la frecuencia Bragg [20], dada por

$$f = \frac{v_p}{2l} \tag{2.1}$$

y sus armónicos, donde $v_p$ es la velocidad de fase y $l$ es el período de la estructura EBG.

Otras líneas de transmisión periódicas son implementadas cargando una línea *host* con capacidades en derivación. Tales elementos reactivos incrementan la capacitancia efectiva de la línea, proveyendo un efecto de onda lenta que reduce la velocidad de fase [21-28]. Así las estructuras cargadas con parches capacitivos, se comportan como líneas de transmisión de onda lenta con bandas de rechazo, relacionadas con su periodicidad. De acuerdo a esto, tales líneas artificiales pueden ser usadas para reducir el tamaño de los dispositivos en circuitos planares y para suprimir bandas espurias, inherentes a circuitos distribuidos [13]. Para evitar la presencia de elementos discretos se prefiere las líneas cargadas con parches capacitivos, pues es menos costoso y de menor complejidad [29].

Las líneas de transmisión de onda lenta son estructuras que exhiben una velocidad de fase menor que su correspondiente convencional implementado en el mismo substrato. Debido al comportamiento de onda lenta, la longitud de onda es también menor (comparada a la línea convencional) y consecuentemente el tamaño del circuito de microondas puede ser reducido significativamente [30].

Típicamente las líneas de transmisión de onda lenta son implementadas cargando periódicamente una línea *host* con parches capacitivos conectados en derivación. Gracias a esta carga capacitiva, la capacidad efectiva de la línea es incrementada y la velocidad de fase es reducida. Estas líneas con carga capacitiva tienen aplicaciones para la miniaturización de circuitos [23,31]. Además, debido a la periodicidad, estas líneas de transmisión con carga exhiben bandas de rechazo, que son de interés para la supresión de espurios. Así las estructuras de onda lenta encuentran aplicaciones en diseños de circuitos de microondas con tamaño reducido y supresión de espurios [32].

Para satisfacer las especificaciones usuales de diseño, impedancia característica, longitud eléctrica y razón de onda lenta (razón de la velocidad de fase de la línea con carga y sin carga), un proceso de optimización es necesario.

En la tesis se propone una síntesis automática para líneas cargadas con parches capacitivos, basada en mapeo espacial [33-35]. Esta herramienta de síntesis ha sido aplicada para el diseño de muchos circuitos planares de microondas [36-44]. En este trabajo específicamente una variante denominada *Aggressive Space Mapping* (ASM) es usada [34].

Recientemente, se ha propuesto una técnica ASM de dos pasos, la cual es muy útil para circuitos de microondas que pueden ser descritos por un esquemático circuital, donde el esquemático óptimo (aquel que satisface las especificaciones) es determinado (en el primer paso) y luego es generado el layout del circuito automáticamente, en el segundo paso [45, 46].

Similarmente en este trabajo se ha implementado un algoritmo de dos pasos para la síntesis de líneas de transmisión de onda lenta. Mediante el primer paso se determina el esquemático óptimo, que consiste en una línea de transmisión (línea *host*) y una capacidad en derivación. Luego, a través de la capacitancia óptima, la impedancia característica y longitud eléctrica de la línea host se genera automáticamente el layout.

Habiendo realizado el aporte fundamental de cómo sintetizar de forma óptima líneas de transmisión de onda lenta con parches capacitivos, el paso natural es encontrar aplicaciones. Las primeras aplicaciones que se han reportado en la tesis son aplicaciones a diferentes tipos de filtros de microondas.

### 2.1.1 Método de la matriz de transferencia y relación de dispersión

Para obtener la relación de dispersión, el método de la matriz de transferencia es muy útil en casos donde los campos en dos posiciones separadas físicamente por un periodo pueden ser expresados como mutuamente dependientes a través de una matriz de transferencia, ésta propia de una celda unitaria [20]. Esto se observa en la figura 2.1

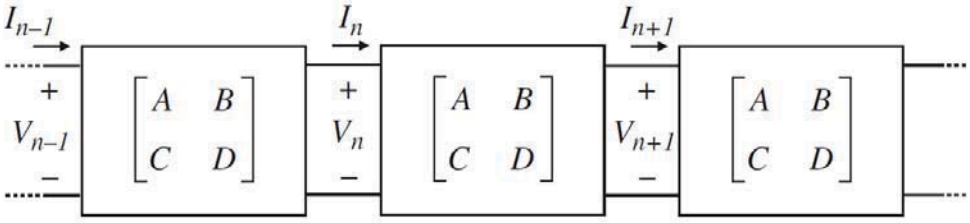


**Figura 2.1**. Estructura periódica donde cada celda unidad está descrita por una matriz ABCD

Los voltajes y corrientes al lado de cada celda unitaria están relacionadas por la matriz ABCD, de acuerdo a:

$$\begin{pmatrix} V_n \\ I_n \end{pmatrix} = \begin{pmatrix} A & B \\ C & D \end{pmatrix} \begin{pmatrix} V_{n+1} \\ I_{n+1} \end{pmatrix} \tag{2.2}$$

Además, de acuerdo al teorema de Floquet, los voltajes y corrientes en los planos *n* y *n+1* solo difieren en el factor de propagación, siendo así,

$$V_{n+1} = e^{-\gamma l} V_n \tag{2.3a}$$

$$I_{n+1} = e^{-\gamma l} I_n \tag{2.3b}$$

De las ecuaciones anteriores se sigue:

$$\begin{pmatrix} V_n \\ I_n \end{pmatrix} = \begin{pmatrix} A & B \\ C & D \end{pmatrix} \begin{pmatrix} V_{n+1} \\ I_{n+1} \end{pmatrix} = \begin{pmatrix} e^{\gamma l} V_{n+1} \\ e^{\gamma l} I_{n+1} \end{pmatrix} \tag{2.4}$$

o

$$\begin{pmatrix} A - e^{\gamma l} & B \\ C & D - e^{\gamma l} \end{pmatrix} \begin{pmatrix} V_{n+1} \\ I_{n+1} \end{pmatrix} = 0 \tag{2.5}$$

Obsérvese que de acuerdo a (2.4) y (2.5), los voltajes y corrientes propagándose por la línea son los vectores propios. Para una solución no trivial, el determinante de la matriz debe ser cero:

$$AD + e^{2\gamma l} - (A + D)e^{\gamma l} - BC = 0 \tag{2.6}$$

Dado que para un sistema recíproco se cumple que $AD$ - $BC$ = 1, (2.6) puede ser expresada como:

$$e^{\gamma l} + e^{-\gamma l} = A + D \tag{2.7}$$

y la relación de dispersión puede ser escrita como

$$\cosh(\gamma l) = \frac{A + D}{2} \tag{2.8}$$

En un medio sin pérdidas y recíproco, el lado derecho de (2.8) es puramente real. Esto indica que la constante de propagación es totalmente real ($\gamma = \alpha$, $\beta = 0$) o puramente imaginaria ($\gamma = j\beta$, $\alpha = 0$). En el primer caso, la onda Bloch es atenuada a través de la línea.

Para el caso $\gamma = j\beta$ y $\alpha = 0$, $\cosh(\gamma l) = \cos(\beta l)$, así (2.8) se escribe como:

$$\cos(\beta l) = \frac{A + D}{2} \tag{2.9}$$

La expresión (2.9) es válida para las regiones de propagación, donde el módulo del lado derecho de la expresión es menor que 1. Si la celda unitaria de la estructura periódica es simétrica con respecto a un plano equidistante de los puertos de entrada y salida, se cumple que $A = D$, y luego (2.9) puede ser simplificada a:

$$\cos(\beta l) = A \tag{2.10}$$

### 2.1.2 Impedancia Bloch

Otro parámetro importante es la relación entre el voltaje y la corriente en cualquier posición (plano) de la estructura periódica [20]. A partir de (2.5) se obtiene:

$$(A - e^{\gamma l})V_{n+1} + BI_{n+1} = 0 \tag{2.11}$$

Se sigue que:

$$\frac{V_{n+1}}{I_{n+1}} = \frac{-B}{A - e^{\gamma l}} \ , \forall n \tag{2.12}$$

La expresión (2.12) no depende del plano donde la relación entre el voltaje y la corriente es calculada. Esto indica la impedancia característica de una línea de transmisión, definida como la relación entre el voltaje y la corriente para una onda propagándose en cualquier posición de la línea. Sin embargo, como las ondas propagándose en una estructura periódica son ondas Bloch, es más conveniente identificar la impedancia dada en (2.12) como la impedancia Bloch, $Z_B$. Aislando la expresión para $e^{\gamma l}$ de (2.7) y sustituyéndola en (2.12), se sigue que la impedancia Bloch tiene dos soluciones:

$$Z_B^{\pm} = -\frac{2B}{A - D \mp \sqrt{(A+D)^2 - 4}} \tag{2.13}$$

una corresponde a ondas progresivas y la otra para ondas regresivas. En las regiones de propagación, $(A+D)^2 < 4$ y las dos soluciones tienen la misma magnitud, idéntica parte real e imaginaria, de signo opuesto. En las regiones prohibidas (band gap), las dos soluciones son puramente imaginarias y exhiben diferente magnitud, a menos que la celda unitaria sea simétrica.

Para el caso de la celda unitaria simétrica, $A = D$, lo cual simplifica la impedancia Bloch a:

$$Z_B^{\pm} = \pm\frac{B}{\sqrt{A^2 - 1}} \tag{2.14}$$

Si se considera una celda simétrica ya sea en T o en π, como en la figura 2.2, es posible expresar la relación de dispersión como:

$$\cos(\beta l) = 1 + \frac{Z_s(\omega)}{Z_p(\omega)} \tag{2.15}$$

Donde $Z_s$ y $Z_p$ son las impedancias en serie y en derivación, respectivamente.

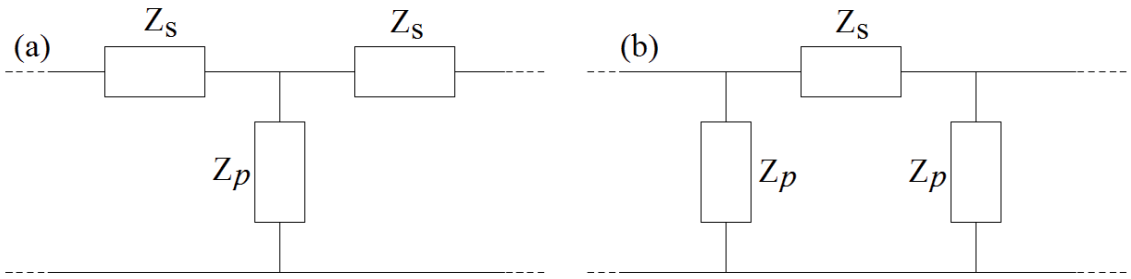


**Figura 2.2**: Modelo de circuito en T (a) y en π (b)

La impedancia Bloch para un circuito en T se puede escribir como:

$$Z_{B_T}(\omega) = \sqrt{Z_s(\omega)[Z_s(\omega) + 2Z_p(\omega)]} \tag{2.16}$$

Y si la estructura es modelada como un circuito en π la impedancia Bloch es:

$$Z_{B_\pi}(\omega) = \sqrt{\frac{Z_s(\omega)Z_p(\omega)/2}{1 + \frac{Z_s(\omega)}{2Z_p(\omega)}}} \tag{2.17}$$

Para esta tesis se ha trabajado con las expresiones (2.9) y (2.14).

## 2.2 Introducción a algoritmos de mapeo espacial

El Mapeo Espacial (*Space Mapping*, SM) es una técnica usada extensivamente para la síntesis y optimización de componentes de microondas. Está técnica usa dos espacios de simulación [33, 35]: (i) el espacio de Optimización, $\mathbf{X}_c$, donde las variables están relacionadas con el modelo grueso, que es simple y computacionalmente eficiente, pero no es exacto, y ii) el espacio de validación, $\mathbf{X}_f$, donde las variables están ligadas al modelo fino, típicamente más complejo y computacionalmente intensivo, pero significativamente más preciso.

En cada espacio, un vector columna define a los parámetros del modelo. Cada uno de estos vectores se denomina $\mathbf{x_f}$ y $\mathbf{x_c}$ para los espacios fino y grueso, respectivamente y las correspondientes respuestas se denominan $\mathbf{R_f(x_f)}$ y $\mathbf{R_c(x_c)}$. Para aplicaciones de microondas, las respuestas están relacionadas con los parámetros de dispersión.

La idea clave detrás de cualquier optimización con Mapeo Espacial es de generar una apropiada transformación de parámetros tal que

$$\mathbf{x_c} = \mathbf{P}(\mathbf{x_f}) \tag{2.18}$$

Mapeando los parámetros del modelo fino hacia los parámetros del modelo grueso, se cumple en una determinada región:

$$\begin{aligned} &\left\|\mathbf{R_f}(\mathbf{x_f}) - \mathbf{R_c}(\mathbf{x_c})\right\| \le \eta \\ &\mathbf{R_c}(\mathbf{P}(\mathbf{x_f})) \approx \mathbf{R_f}(\mathbf{x_f}) \end{aligned} \tag{2.19}$$

donde η es un pequeño número positivo cercano a cero. Este proceso se puede ilustrar en la figura 2.3.

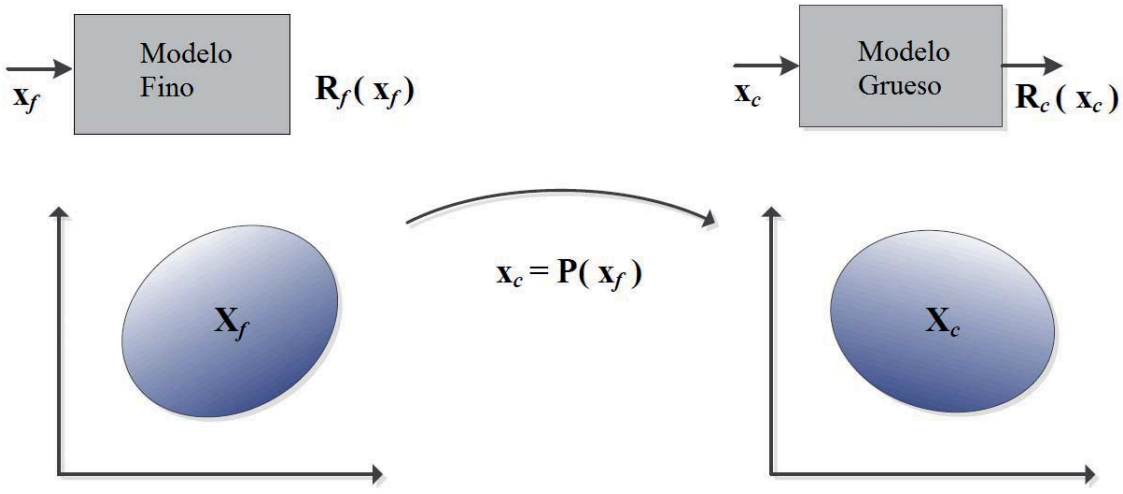


**Figura 2.3**. Ilustración de Mapeo Espacial

Si la función **P** es invertible, se cumple la siguiente transformación inversa:

$$\mathbf{x_f} = \mathbf{P}^{-1}(\mathbf{x_c^*}) \tag{2.20}$$

La función **P** es usada para encontrar la solución del modelo fino, ésta es la imagen de la solución objetivo del modelo grueso $\mathbf{x_c}^*$, que brinda la respuesta objetivo $\mathbf{R_c}(\mathbf{x_c}^*)$. Sin embargo la determinación de **P** de acuerdo al procedimiento en [33] sigue un proceso iterativo que es un poco ineficiente.

### 2.2.1 Mapeo Espacial Agresivo (ASM)

La eficiencia del método fue mejorada introduciendo iteraciones de tipo quasi-Newton, provocando una convergencia más rápida, usando la fórmula clásica de Broyden y dando lugar al denominado *Aggressive Space Mapping* (ASM) [34]. El objetivo en un algoritmo ASM es de minimizar la función error y resolver el siguiente sistema de ecuaciones no lineales:

$$\mathbf{f}(\mathbf{x_f}) = \mathbf{P}(\mathbf{x_f}) - \mathbf{x_c^*} = 0 \tag{2.21}$$

Asúmase que $\mathbf{x_f}^{(j)}$ es la aproximación en la iteración *j* del vector del espacio de validación y $\mathbf{f}^{(j)}$ la función error correspondiente a $\mathbf{f}(\mathbf{x_f}^{(j)})$.

El próximo vector en el proceso iterativo $\mathbf{x_f}^{(j+1)}$ es obtenido por una iteración de tipo quasi-Newton de acuerdo a:

$$\mathbf{x_f}^{(j+1)} = \mathbf{x_f}^{(j)} + \mathbf{h}^{(j)} \tag{2.22}$$

donde $\mathbf{h}^{(j)}$ está dado por:

$$\mathbf{h}^{(j)} = -\left(\mathbf{B}^{(j)}\right)^{-1}\mathbf{f}^{(j)} \tag{2.23}$$

y $\mathbf{B}^{(j)}$ es un aproximado de la matriz Jacobiana $\mathbf{J}_m$ de **f** respecto $\mathbf{x}_f$ en $\mathbf{x_f}^{(j)}$

$$\mathrm{J}_m(\mathrm{x}_f^{(j)}) = \left(\frac{\partial \mathrm{f}^T(\mathrm{x}_f)}{\partial \mathrm{x}_f}\right)^T\Bigg|_{\mathrm{x}_f = \mathrm{x}_f^{(j)}} \tag{2.24}$$

En el caso de esta tesis, el vector inicial del modelo fino $\mathbf{x_f}^{(1)}$, relacionado con el vector objetivo del modelo grueso es determinado a través de expresiones analíticas y la primera matriz de Broyden $\mathbf{B}^{(1)}$ es inicializada como sigue:

$$\mathbf{B}^{(1)} = \begin{pmatrix} \frac{\partial x_{c1}}{\partial x_{f1}} & \frac{\partial x_{c1}}{\partial x_{f2}} & \cdots & \frac{\partial x_{c1}}{\partial x_{fm}} \\ \frac{\partial x_{c2}}{\partial x_{f1}} & \frac{\partial x_{c2}}{\partial x_{f2}} & \cdots & \frac{\partial x_{c2}}{\partial x_{fm}} \\ \vdots & \vdots & \cdots & \vdots \\ \frac{\partial x_{cm}}{\partial x_{f1}} & \frac{\partial x_{cm}}{\partial x_{f2}} & \cdots & \frac{\partial x_{cm}}{\partial x_{fm}} \end{pmatrix} \tag{2.25}$$

Donde las derivadas son obtenidas a través de la siguiente aproximación:

$$\frac{\partial x_{ci}}{\partial x_{fi}} \approx \frac{\Delta x_{ci}}{\Delta x_{fi}} \tag{2.26}$$

Los diferenciales $\Delta x_{fi}$ son una pequeña perturbación en los parámetros del modelo fino y a través de una aplicación de extracción de parámetros directa es posible obtener $\Delta x_{ci}$, la variación que implica en el modelo grueso. Para inicializar la matriz de Broyden, ésta operación se debe repetir *m* veces (una vez por cada columna), lo que implica que se debe realizar *m* simulaciones electromagnéticas.

Para los siguientes pasos ( $j > 1$ ) la matriz de Broyden es actualizada por la fórmula clásica de Broyden:

$$\mathbf{B}^{(j+1)} = \mathbf{B}^{(j)} + \frac{\mathbf{f}(\mathbf{x}_f^{(j)} + \mathbf{h}^{(j)}) - \mathbf{f}(\mathbf{x}_f^{(j)}) - \mathbf{B}^{(j)}\mathbf{h}^{(j)}}{\mathbf{h}^{(j)T}\mathbf{h}^{(j)}} \mathbf{h}^{(j)T} \tag{2.27}$$

Se obtiene así la simplificación (combinando 2.23 y 2.27) de la fórmula clásica de Broyden [34, 47], para cada iteración ésta es:

$$\mathbf{B}^{(j+1)} = \mathbf{B}^{(j)} + \frac{\mathbf{f}^{(j+1)}\mathbf{h}^{(j)T}}{\mathbf{h}^{(j)T}\mathbf{h}^{(j)}} \tag{2.28}$$

En (2.28), $\mathbf{f}^{(j+1)}$ es obtenida evaluando (2.21) usando algún método de extracción de parámetros, proveyendo los parámetros del modelo grueso a partir de la respuesta de los parámetros del modelo fino.

En el caso de esta tesis se ha usado el método de extracción directo de parámetros. En éste método, los parámetros del modelo grueso son inferidos de los parámetros S obtenidos por simulación, a través de ecuaciones para alguna frecuencia de interés.

El procedimiento difiere en cado caso, porque depende de la topología y de las variables del modelo grueso. El método de extracción se explica con detalle en cada sección correspondiente.

La implementación del algoritmo ASM es descrito a través de un diagrama de flujo como en la figura 2.4. El proceso itera hasta que la norma de la función error es más pequeña que un valor $\eta$, usualmente se usa una norma de error menor a 0.5 % o 1.0 %.

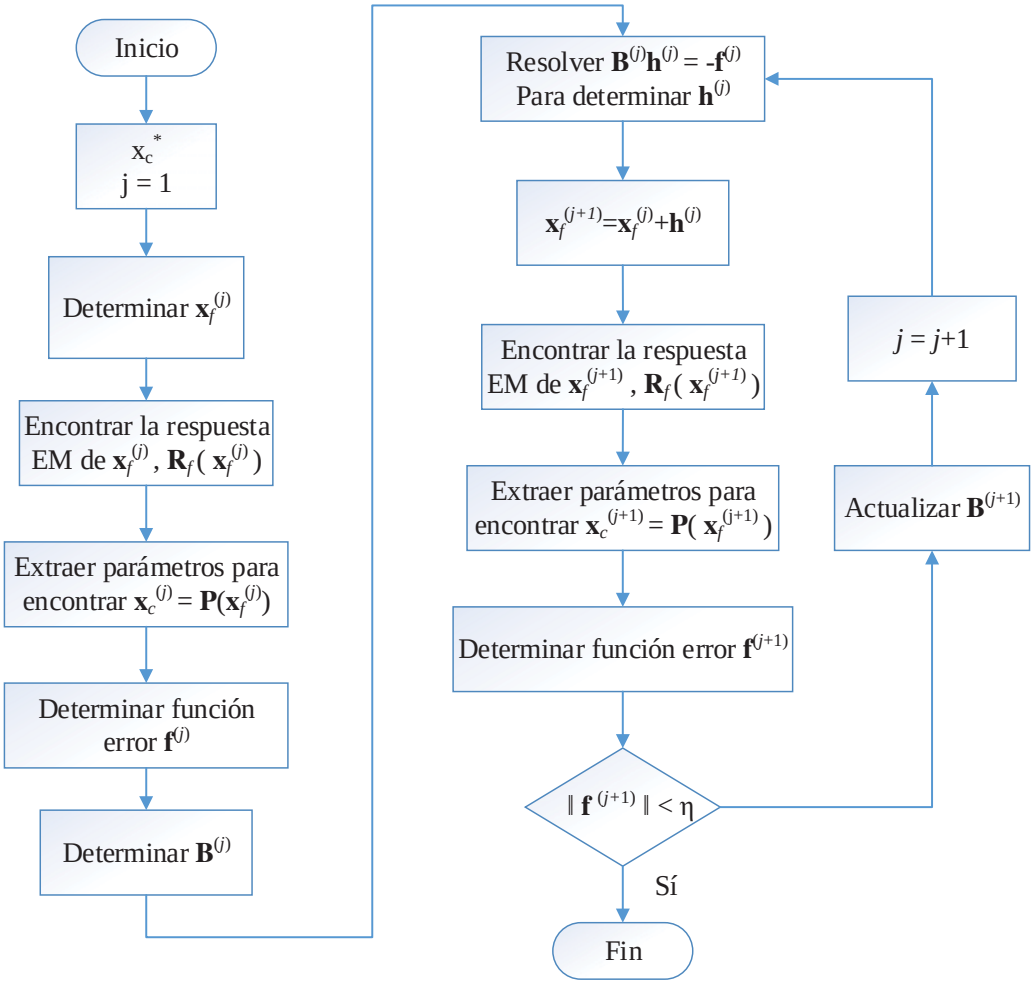


**Figura 2.4.** Diagrama de flujo de un algoritmo ASM

# 3

# Síntesis de líneas de transmisión de onda lenta basadas en parches capacitivos

En este capítulo se estudia la síntesis automática de estructuras de onda lenta en líneas microstrip cargadas con capacidades en derivación. Debido a las capacidades en derivación, la capacitancia efectiva de la línea es incrementada y la velocidad de fase en la estructura es disminuida. El objetivo es obtener el layout óptimo de la estructura de onda lenta de forma totalmente desatendida, esto a partir de las especificaciones (impedancia Bloch, longitud eléctrica y razón de onda lenta). Se ha obtenido una solución a través de un algoritmo ASM de dos pasos. Se presentan cuatro ejemplos para ilustrar el método propuesto.

Este trabajo fue publicado en la revista *International Journal of RF and Microwave Computer-Aided Engineering* en Septiembre 2015, la publicación es: "*Synthesis of slow-wave structures based on capacitive-loaded lines through aggressive space mapping (ASM)*", el trabajo constituye el **Artículo A** de la relación de artículos fundamentales de esta tesis. Los tres ejemplos de síntesis mostrados en el **Artículo A** se muestran con más detalle en este capítulo.

# 3.1 Estructuras de onda lenta

El esquemático de la estructura de onda lenta considerada en este trabajo es el de la figura 3.1. La línea *host* con constante de fase *k* (longitud eléctrica de la celda unitaria *kl*) e impedancia característica $Z_0$, es periódicamente cargada con capacidades en derivación $C_{ls}$. Nos referiremos a *k* y $Z_0$ como la constante de fase e impedancia característica de la línea sin carga, respectivamente; Esto para distinguirlo de $Z_B$ (impedancia Bloch) y la constante de fase $\beta$ de la línea cargada con capacidades.

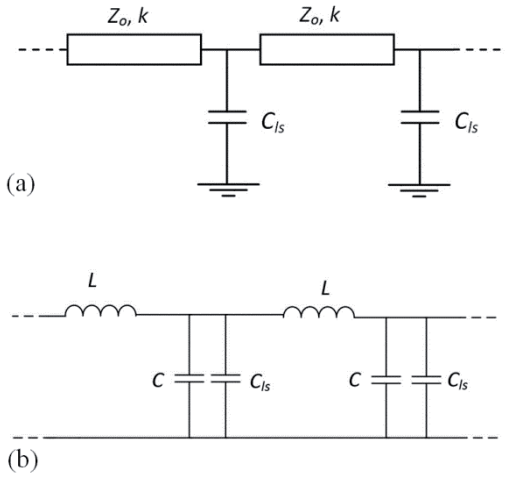


**Figura 3.1.** Esquemático de la estructura de onda lenta basada en una línea de transmisión con capacidad en derivación (a) y modelo equivalente basada en elementos discretos (b).

Para obtener la relación de dispersión y la impedancia Bloch del esquemático en la Fig. 3.1(a) se realiza a partir de la celda unitaria simétrica (ambos lados de longitud eléctricas *kl/2* para la línea sin carga) y aplicando el análisis de estructuras periódicas de [48]. En particular los elementos de la matriz ABCD se obtienen de esta forma:

$$\begin{bmatrix} A & B \\ C & D \end{bmatrix} = \begin{bmatrix} \cos(kl/2) & jZ_0 \sin(kl/2) \\ j\frac{1}{Z_0}\sin(kl/2) & \cos(kl/2) \end{bmatrix} \cdot \begin{bmatrix} 1 & 0 \\ j\omega C_{ls} & 1 \end{bmatrix} \cdot \begin{bmatrix} \cos(kl/2) & jZ_0 \sin(kl/2) \\ j\frac{1}{Z_0}\sin(kl/2) & \cos(kl/2) \end{bmatrix} \quad (3.1)$$

A partir de (3.1) y de las ecuaciones (2.9) y (2.14), se obtienen las expresiones

$$\cos\ \beta l = \cos\ kl - \frac{\omega C_{ls} Z_0}{2} \sin\ kl \quad (3.2)$$

$$Z_B = \frac{Z_0[\sin kl - Z_0 \omega C_{ls} \sin^2(kl/2)]}{\sqrt{1-(\cos kl - \frac{1}{2} Z_0 \omega C_{ls} \sin kl)^2}} \quad (3.3)$$

Además de la relación de dispersión (3.2) y de la impedancia Bloch (3.3) ha de haber otra ecuación. Esta viene de la razón de onda lenta:

$$swr = \frac{v_p}{v_{po}} = \frac{\omega/\beta}{\omega/k} = \frac{kl}{\beta l} \tag{3.4}$$

Las ecuaciones (3.2), (3.3) y (3.4) definen un sistema de tres ecuaciones no lineales con tres incógnitas. Se observa que son ecuaciones de difícil manipulación, y típicamente para propósitos de diseño se usa el modelo basado en elementos discretos. Éste se muestra en la Fig. 3.1(b), donde *C* y *L* son la capacitancia e inductancia por sección.

De acuerdo al modelo basado en elementos discretos la impedancia Bloch, la longitud eléctrica (de la línea con carga) de la celda unitaria y la razón de onda lenta están dadas por:

$$Z_B = \sqrt{\frac{L}{C + C_{ls}}} \tag{3.5}$$

$$\phi_{cell} = \beta l = \omega\sqrt{L(C + C_{ls})} \tag{3.6}$$

$$swr \equiv \alpha = \frac{v_p}{v_{po}} = \frac{l/\sqrt{L(C + C_{ls})}}{l/\sqrt{LC}} = \frac{1}{\sqrt{1 + \frac{C_{ls}}{C}}} \tag{3.7}$$

Para propósitos de diseño también es útil la inversión de las tres ecuaciones anteriores:

$$L = \frac{\phi_{cell} \cdot Z_B}{\omega} \tag{3.8}$$

$$C = \frac{\alpha^2 \cdot \phi_{cell}}{\omega \cdot Z_B} \tag{3.9}$$

$$C_{ls} = \frac{\phi_{cell}(1 - \alpha^2)}{\omega \cdot Z_B} \tag{3.10}$$

Sin embargo, la validez del modelo de la Figura 3.1(b) es restringido para valores grandes de $C_{ls}$ comparados con *C*. Si se cumple la condición $C_{ls} >> C$, la concordancia entre el modelo con elementos discretos y el esquemático (semi-discreto) es buena hasta la frecuencia de corte. Sin embargo la condición ($C_{ls} >> C$ ) no siempre se cumple, por eso se justifica la determinación de las ecuaciones (3.2), (3.3) y (3.4).

En este trabajo se realizó un algoritmo ASM para solucionar (3.2), (3.3) y (3.4). Pudo haberse usado otro método numérico, pero se optó por uno ASM que es simple, rápido y exacto. Como se ha comentado en la Introducción, se ha desarrollado un algoritmo de dos pasos para la síntesis de estructuras de onda lenta, el primer paso provee el esquemático óptimo que cumple las especificaciones y el segundo paso genera el layout de forma automática.

## 3.2 Primer ASM: Determinación del esquemático óptimo

Este paso es completamente matemático. A partir de las especificaciones, impedancia Bloch $Z_B$, longitud eléctrica de la celda unitaria con carga $\beta l$ y razón de onda lenta *swr*, se ha de determinar el conjunto de valores de $Z_0$, $kl$ y $C_{ls}$ en las ecuaciones (3.2), (3.3) y (3.4) que brinda la solución a las especificaciones. En este problema se define al modelo fino como $\mathbf{x_f} = [Z_0; kl; C_{ls}]$; y al modelo grueso como la solución $\mathbf{x_c} = [Z_B; \beta l; swr]$, estas cada uno con su objetivo.

Para inicializar el algoritmo necesitamos un primer vector del modelo fino a partir de expresiones analíticas que relacionen el modelo grueso con el modelo fino. Se ha de tomar en cuenta que la impedancia de la línea sin carga es:

$$Z_0 = \sqrt{\frac{L}{C}} \tag{3.11}$$

y la longitud eléctrica de la línea sin carga es:

$$kl = \omega\sqrt{LC} \tag{3.12}$$

Teniendo en cuenta las ecuaciones (3.11) y (3.12) y las ecuaciones a partir del modelo discreto (3.8), (3.9) y (3.10), se puede obtener el primer vector del modelo fino $\mathbf{x_f}^{(1)}$. Las variables con (*) indican target/valores objetivos. Se sigue que este primer vector es:

$$\mathrm{x}_f^{(1)} = \begin{bmatrix} Z_0^{(1)} \\ kl^{(1)} \\ C_{ls}^{(1)} \end{bmatrix} = \begin{bmatrix} \dfrac{Z_B^*}{\alpha^*} \\ \phi^* \cdot \alpha^* \\ \dfrac{\phi^* \cdot (1-(\alpha^*)^2)}{\omega \cdot Z_B^*} \end{bmatrix} \tag{3.13}$$

De este primer vector del espacio fino, se extrae el primer vector $\mathbf{x_c}^{(1)}$ del modelo grueso por simulación circuital, en este caso se evalúa las ecuaciones (3.2), (3.3) y (3.4).

Este conjunto de tres ecuaciones sirve para extraer parámetros y no hay necesidad de simulación electromagnética. Este vector $\mathbf{x_c}^{(1)}$ se compara con las variables objetivo del modelo grueso $\mathbf{x_c}^{*}$ y eso brinda la primer función error, ecuación (2.21).

El error y la magnitud relativa son:

$$\begin{aligned} \mathrm{f}^{(j+1)} &= \mathrm{x}_c^{j+1} - \mathrm{x}_c^{*} = \mathrm{P}(\mathrm{x}_f^{j+1}) - \mathrm{x}_c^{*} \\ \mathrm{f}^{(j+1)} &= [Z_{\mathrm{B}} - Z_{\mathrm{B}}^{*}; \phi - \phi^{*}; \alpha - \alpha^{*}] \end{aligned} \tag{3.14}$$

$$\left|\mathrm{f}^{(j+1)}\right| = \sqrt{\left(\frac{Z_{\mathrm{B}}}{Z_{\mathrm{B}}^{*}} - 1\right)^2 + \left(\frac{\phi}{\phi^{*}} - 1\right)^2 + \left(\frac{\alpha}{\alpha^{*}} - 1\right)^2} \tag{3.15}$$

Si esta función error no es menor que un cierto valor, se ha de calcular la matriz de Broyden **B**.

Para obtener una primera aproximación de esta matriz, se ha de perturbar sutilmente cada variable del modelo fino, luego se obtiene la respuesta circuital/matemática, extrayendo parámetros y así obtener los valores del modelo grueso correspondiente a cada perturbación. Los cambios relativos pueden ser expresados en la matriz:

$$\mathrm{B}^{(1)} = \begin{pmatrix} \frac{\delta Z_{\mathrm{B}}}{\delta Z_0} & \frac{\delta Z_{\mathrm{B}}}{\delta kl} & \frac{\delta Z_{\mathrm{B}}}{\delta C_{ls}} \\ \frac{\delta \beta l}{\delta Z_0} & \frac{\delta \beta l}{\delta kl} & \frac{\delta \beta l}{\delta C_{ls}} \\ \frac{\delta swr}{\delta Z_0} & \frac{\delta swr}{\delta kl} & \frac{\delta swr}{\delta C_{ls}} \end{pmatrix} \tag{3.16}$$

Una vez que la matriz $\mathbf{B}^{(1)}$ es conocida, los parámetros del modelo fino de la siguiente iteración pueden ser obtenidos por (2.22) y el proceso es iterado hasta que se obtiene la convergencia.

Este primer ASM se visualiza mejor con el diagrama de Flujo en la Figura 3.2, a esta primera etapa se la ha denominado el Módulo Analizador.

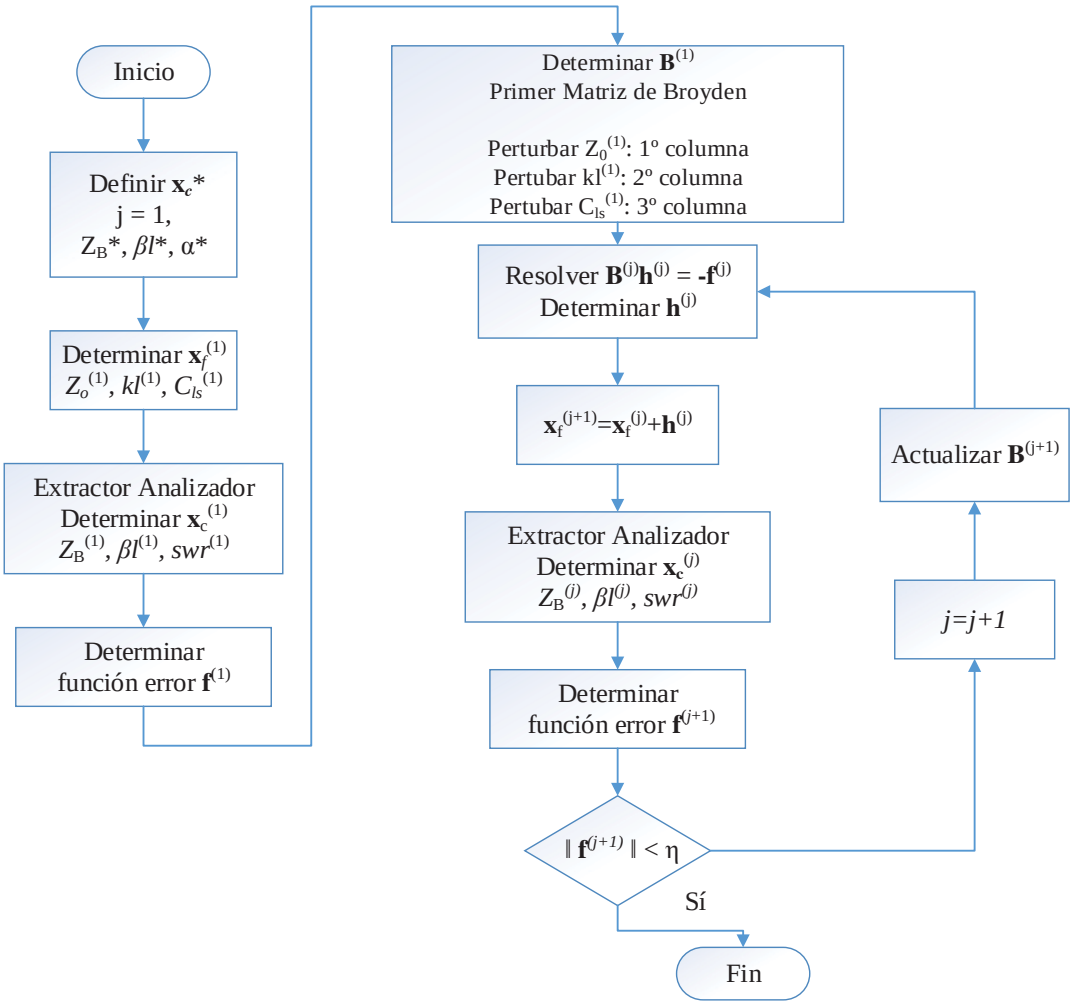


**Figura 3.2**. Diagrama de flujo para el Módulo Analizador (Primer ASM)

## 3.3 Segundo ASM: Determinación del layout

Una vez que el esquemático óptimo ha sido obtenido, el layout es determinado a través de un segundo ASM. El primer paso es la determinación de la longitud $l_p$ del parche capacitivo, éste es un parche cuadrado. La capacidad en derivación es $C_{ls}$, que vino determinada previamente por el módulo analizador. La geometría del parche capacitivo es la de la Figura 3.3(a), donde un parche cuadrado es conectado a una línea *host* a través de un acceso corto y ancho, con el fin de evitar algún efecto inductivo. En todo este trabajo, la distancia entre la línea *host* y el parche capacitivo se ha fijado a $l_{acc}$ = 0.583 mm; y el ancho del acceso $W_{acc}$ se fija a una fracción de la dimensión de la longitud del parche $l_p$. Se ha demostrado que 50% de $l_p$ es una buena opción.

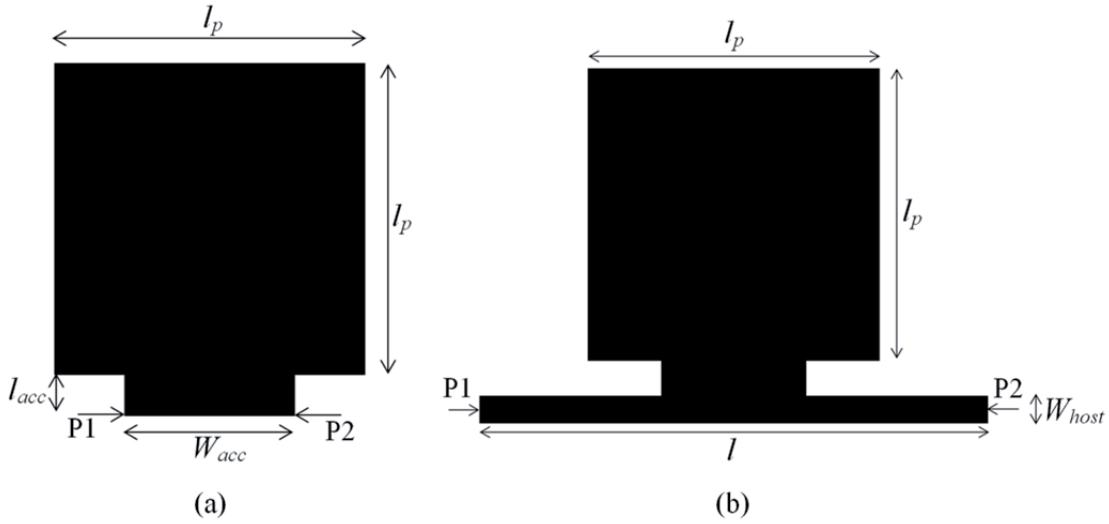


**Figura 3.3**. Topología y dimensiones relevantes, del parche capacitivo (a) y toda la celda unitaria de onda lenta (b)

A partir de la Figura 3.3(a) un algoritmo ASM de una variable es necesario para determinar $l_p$. La variable del modelo grueso es la capacitancia $C_{ls}$ y la variable del modelo fino es $l_p$. El primer valor de $l_p$ es calculado del valor objetivo de $C_{ls}$ (determinado en el primer ASM), a través de la fórmula del condensador de placas paralelas. Luego la capacitancia del parche es inferida de la simulación electromagnética considerando los puertos indicados en la Figura 3.3(a), específicamente determinando la admitancia de una carga en derivación [48].

A partir de la simulación electromagnética se puede inferir la capacidad del parche, en este caso se tiene una carga en derivación pura, siendo el elemento $C$ de la matriz ABCD igual a la admitancia. Para determinar la capacidad del parche $C_{ls}$ a la frecuencia de operación, el extractor sigue la siguiente ecuación:

$$C = \frac{1}{Z_0}\frac{(1-S_{11})^2-(S_{21})^2}{2S_{21}} \qquad (3.17)$$
$$C = Y = j\omega C_{ls}$$

La capacitancia extraída es comparada con su objetivo. La matriz de Broyden consta de un solo elemento cuyas unidades son pF/mm, **B** es inicializada variando la dimensión del parche $l_p^{(1)}$ y observando la variación de $C_{ls}^{(1)}$, finalmente se itera el proceso hasta encontrar la solución. Este sub-proceso se puede visualizar mejor con un diagrama de flujo en la Figura 3.4.

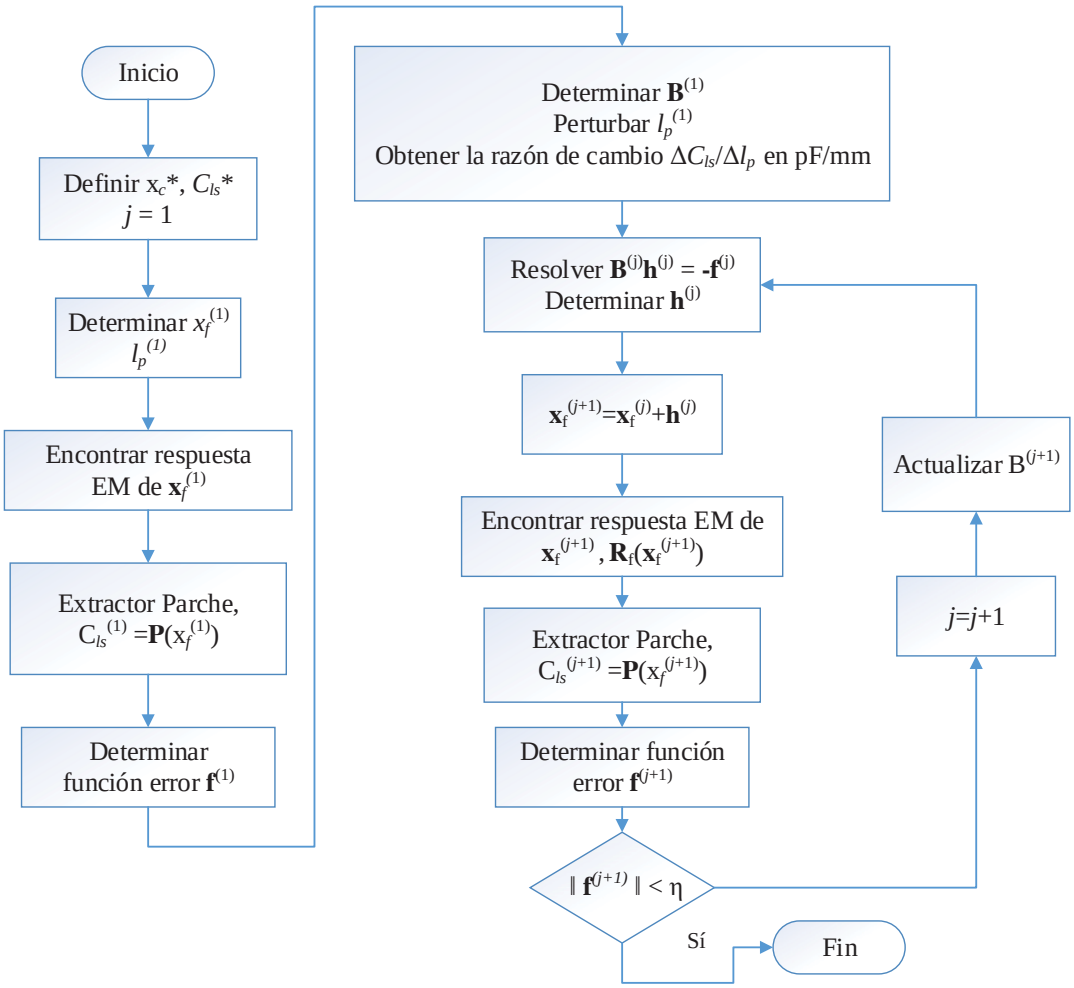


**Figura 3.4**. Diagrama de flujo para 2º ASM (Primer Sub-Proceso, determinación de $l_p$)

El ancho de la línea *host* ($W_{host}$) no es considerado una variable de optimización, dado que éste viene determinado por ecuaciones para líneas microstrip, que brindan el ancho de la línea host como una función de la impedancia característica $Z_0$ y los parámetros del substrato.

Con el valor final obtenido en el analizador para $Z_0^{\,f}$ y los parámetros del substrato, $h$ (altura del substrato) y $\varepsilon_r$ (permitividad relativa del substrato)), es posible calcular $W_{host}$, esto con las ecuaciones en [48]:

$$\frac{W}{h}=\begin{cases}\dfrac{8e^{A}}{e^{2A}-2}, \text{si } \dfrac{W}{h}<2\\ \dfrac{2}{\pi}\left[B-1-\ln(2B-1)+\dfrac{\varepsilon_r-1}{2\varepsilon_r}\left[\ln(B-1)+0.39-\dfrac{0.61}{\varepsilon_r}\right]\right], \text{si } \dfrac{W}{h}>2\end{cases} \tag{3.18}$$

donde

$$A=\frac{Z_0}{60}\sqrt{\frac{\varepsilon_r+1}{2}}+\frac{\varepsilon_r-1}{\varepsilon_r+1}\left(0.23+\frac{0.11}{\varepsilon_r}\right) \tag{3.19}$$

$$B=\frac{377\pi}{2Z_0\sqrt{\varepsilon_r}} \tag{3.20}$$

La dimensión que queda por determinar de la Figura 3.3(b) es la longitud $l$ de la línea host. Ésta es determinada a través de otro sub-proceso ASM, donde la variable del modelo grueso es la longitud eléctrica de la línea cargada, ésta es $\beta l$, en vez de $kl$ (longitud eléctrica de la línea sin carga). Con este sub-proceso se corrige cualquier desplazamiento de fase introducido por el parche capacitivo.

El primer valor de $l^{(1)}$ es obtenido a partir de la longitud eléctrica final $kl^{f}$ obtenida en el módulo analizador. Ésta es determinada inicialmente por estas ecuaciones:

$$\varepsilon_{eff}=\frac{\varepsilon_r+1}{2}+\frac{\varepsilon_r-1}{2}\cdot\frac{1}{\sqrt{1+12\cdot h/W}} \tag{3.21}$$

$$v_p=\frac{c}{\sqrt{\varepsilon_{eff}}} \tag{3.22}$$

$$l^{(1)}=kl^{f}\cdot\frac{v_p}{\omega_o} \tag{3.23}$$

Luego, la longitud eléctrica de toda la estructura con carga es inferida a partir de la simulación electromagnética y es comparada con el valor objetivo de $\beta l^*$, para así determinar la función error. En este caso el módulo extractor calcula la longitud eléctrica de toda la celda a partir de la simulación electromagnética, se lee a la frecuencia de operación los parámetros S y se usa la siguiente ecuación para el extractor:

$$\beta l = \cos^{-1}\left(\frac{\cos(\phi_{S_{21}})}{|S_{21}|}\right) \tag{3.24}$$

La matriz de Broyden es un solo elemento en °/mm, es inicializada variando la dimensión $l^{(1)}$ de la estructura y obteniendo la variación en $\beta l$. Luego el proceso itera de acuerdo a (2.22) hasta encontrar la solución. Este segundo sub-proceso se puede visualizar mejor con un diagrama de flujo en la Figura 3.5.

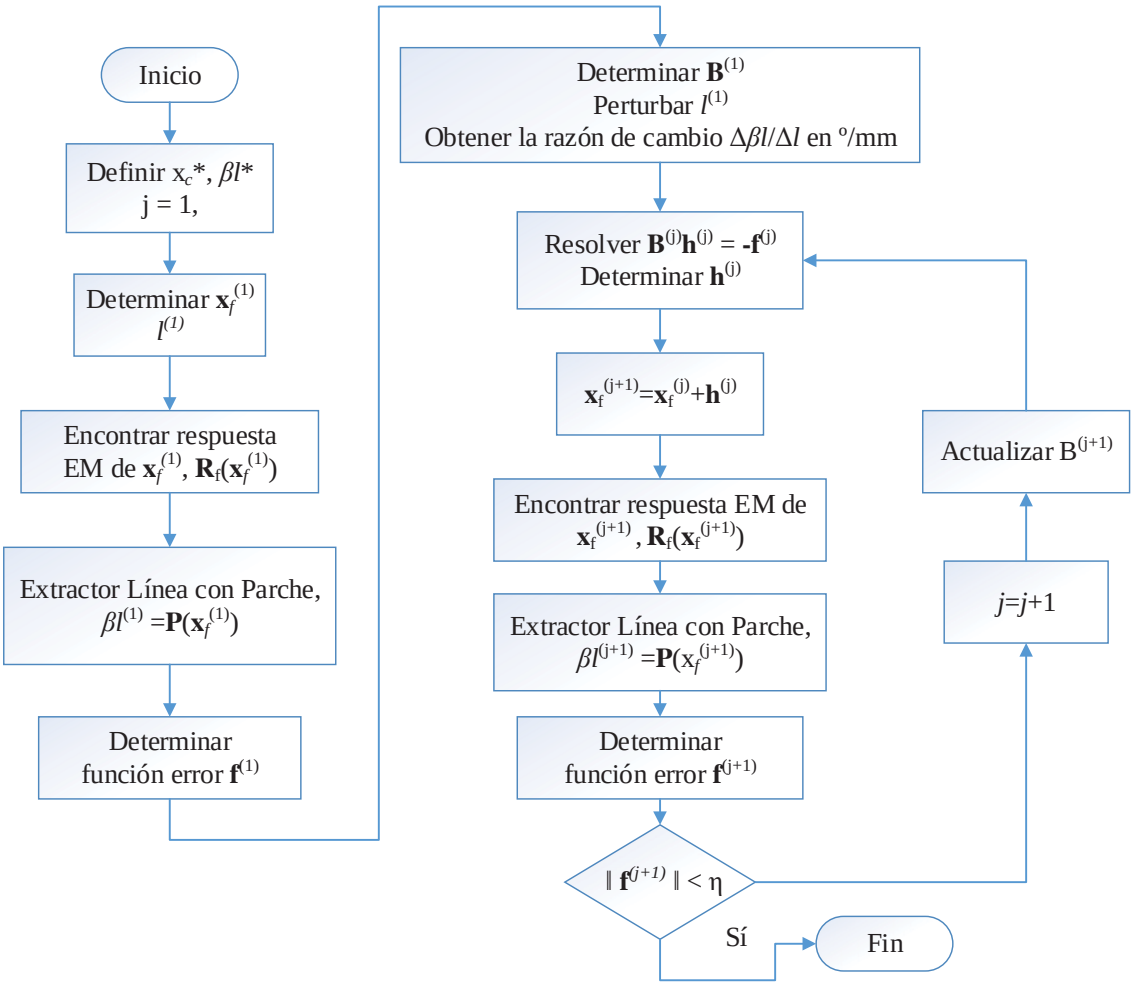


**Figura 3.5**. Diagrama de flujo para 2º ASM ( Segundo Sub-Proceso, determinación de $l$ )

La geometría de la celda unitaria de onda lenta se muestra en la Figura 3.3(b). Se ha propuesto dos sub-procesos ASM independientes con sólo una variable debido a la escasa interacción entre $C_{ls}$ y $\beta l$. En el segundo ASM, las variables de optimización $C_{ls}$ y $\beta l$ dependen fuertemente de la dimensión del parche $l_p$ y de la longitud de la línea *host* $l$, respectivamente. Este método provee resultados exactos y de forma rápida.

Todo el proceso, que consta de dos pasos ASM es visualizado en la Figura 3.6. Usando esta estrategia, la síntesis de estructuras de onda lenta puede ser llevada a cabo de forma automática y desatendida por el diseñador.

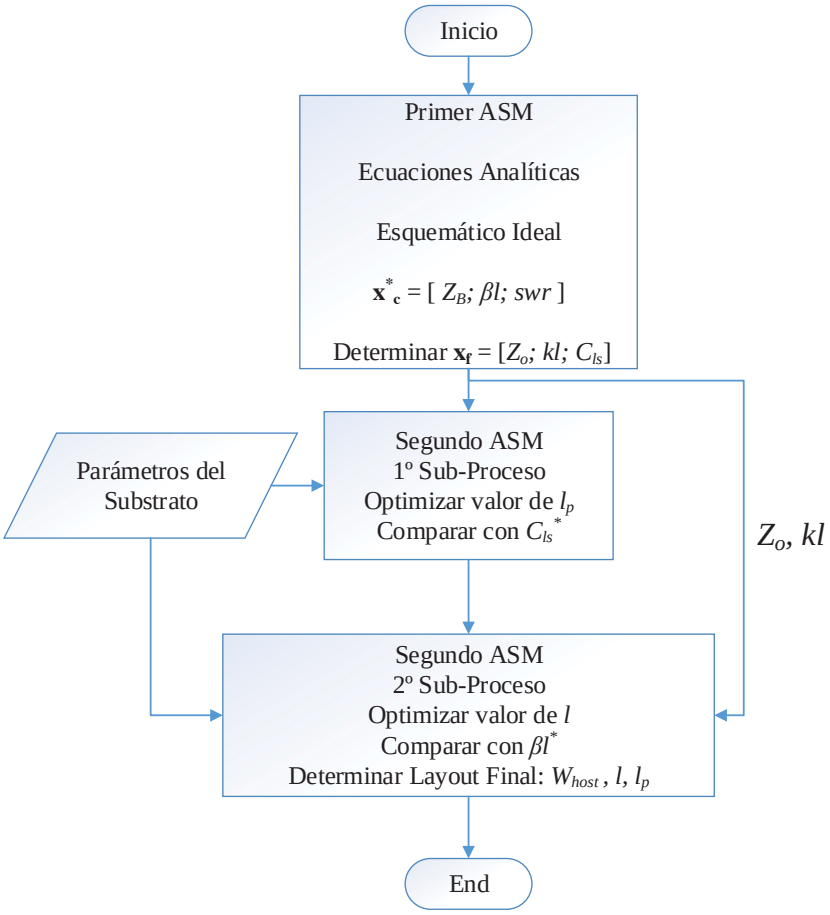


**Figura 3.6**. Diagrama de flujo para el algoritmo de dos pasos para la síntesis de estructuras de onda lenta.

## 3.4 Ejemplos de síntesis

Para ilustrar el potencial del método propuesto, hemos considerado cuatro ejemplos:

1) Celda de longitud eléctrica $\beta l$ = 90º, Impedancia Bloch = 50 Ω, *swr* = 0.5.

2) Celda de longitud eléctrica $\beta l$ = 45º, Impedancia Bloch = 50 Ω, *swr* = 0.5.

3) Estructura de longitud eléctrica igual a 90º, Impedancia Bloch = 50 Ω, *swr* = 0.5, compuesta por tres celdas en cascada de 30º.

4) Estructura de longitud eléctrica igual a 180º, Impedancia Bloch = 50 Ω, *swr* = 0.5, compuesta por cuatro celdas en cascada de 45º.

La frecuencia de operación en todos los casos es $f_0$ = 1 GHz.

### 3.4.1 Ejemplo 1: $\beta l$ = 90º, $Z_B$ = 50 Ω, *swr* = 0.5

Para las especificaciones dadas, se sigue con las ecuaciones (3.8)-(3.10) que los elementos discretos para la Figura 3.1(b) son $C$ = 1.25 pF, $C_{ls}$ = 3.75 pF y $L$ = 12.5 nH. A partir de la ecuación 3.13 los valores del primer vector del modelo fino $\mathbf{x}_f^{(1)}$ son: $Z_0$ = 100.0 Ω, $kl$ = 45.0º y $C_{ls}$ = 3.75 pF. Usando el primer algoritmo ASM, es posible determinar el esquemático óptimo. La convergencia con un error de 0.033% ha sido obtenida luego de 5 iteraciones. Los valores finales del modelo fino son $Z_0$ = 120.7 Ω, $kl$ = 45.0º y $C_{ls}$ = 2.63 pF

La magnitud del error para este 1º ASM se observa en la siguiente gráfica en la Figura 3.7

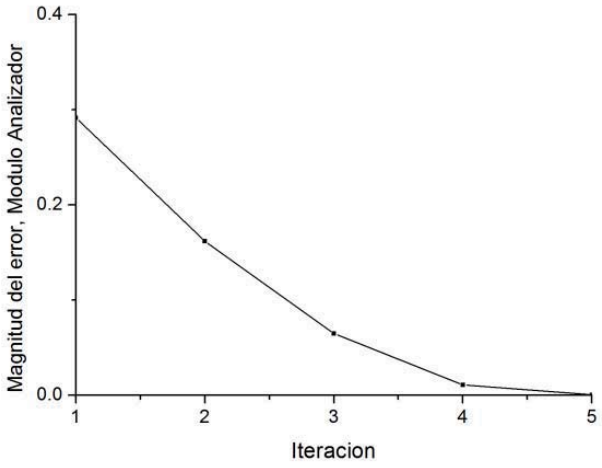


**Figura 3.7**. Evolución de la magnitud del error, módulo analizador, celda de 90º

En la siguiente tabla 3.1 se observa como varían las variables en este caso:

**Tabla 3.1**: Evolución de variables para Ejemplo 1, Módulo Analizador celda de 90º

| | **Modelo Fino** | | | | **Modelo Grueso** | | |
|---|---|---|---|---|---|---|---|
| It. | $Z_0$ | $kl$ | $C_{ls}$ | | $Z_B$ | $\beta l$ | $swr$ |
| 1 | 100.00 Ω | 45.00º | 3.75 pF | | 36.50 Ω | 97.23º | 0.463 |
| 2 | 124.16 Ω | 45.66º | 2.21 pF | | 56.77 Ω | 85.26º | 0.535 |
| 3 | 118.54 Ω | 44.52º | 2.84 pF | | 47.20 Ω | 91.59º | 0.486 |
| 4 | 120.34 Ω | 44.89º | 2.67 pF | | 49.53 Ω | 90.21º | 0.498 |
| 5 | 120.72 Ω | 45.00º | 2.63 pF | | 50.01 Ω | 89.99º | 0.500 |

La respuesta del esquemático (usando los valores previos para el modelo fino) se puede observar en la figura 3.8, donde se observa el coeficiente de transmisión y de reflexión, la impedancia característica y la longitud eléctrica.

A nivel de esquemático se cumple las especificaciones para el modelo grueso $Z_B$ = 50.01 Ω, $\beta l$ = 89.99º y $swr$ = 0.50.

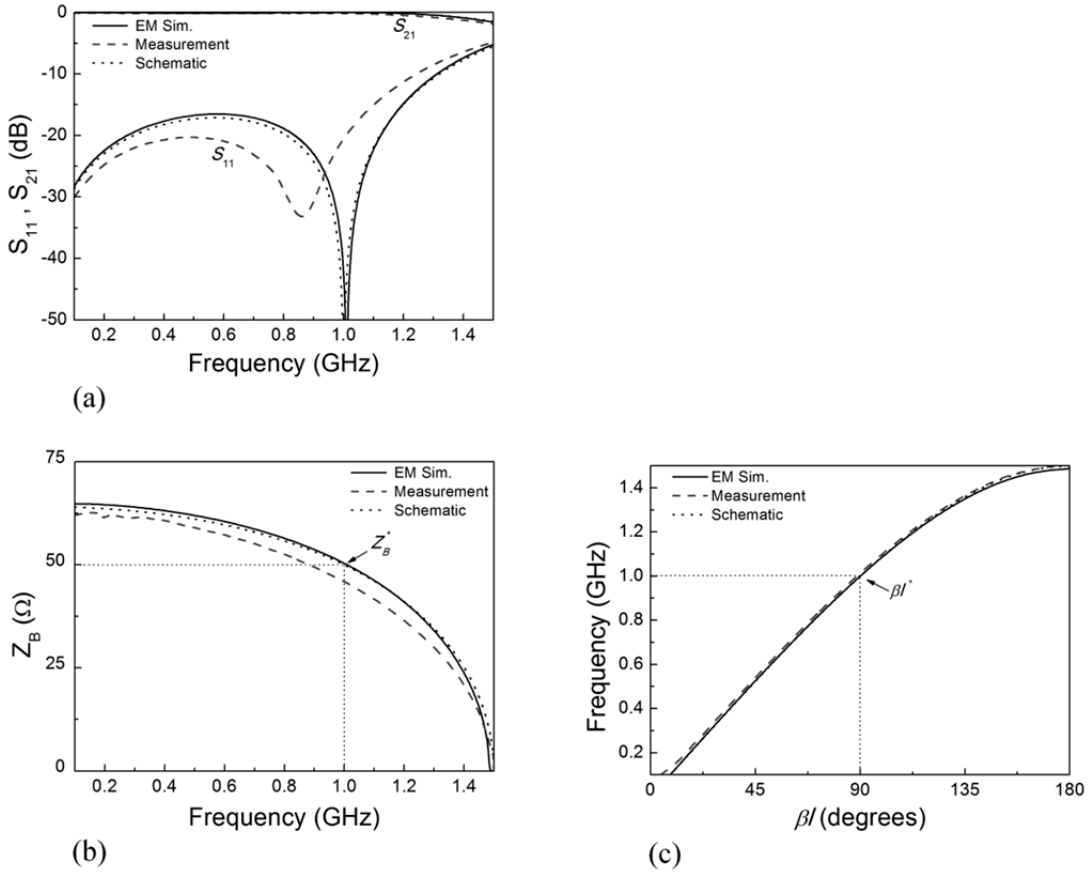


**Figura 3.8**. Respuesta de la celda considerada en ejemplo 1. (a) Coeficiente de transmisión y de reflexión. (b) Impedancia característica y (c) Longitud eléctrica.

Las simulaciones electromagnéticas se han obtenido con el *Keysight Momentum* y la respuesta del esquemático con el simulador circuital *Keysight ADS*.

Una vez el esquemático óptimo ha sido obtenido, la aplicación del segundo ASM nos lleva al layout de la Figura 3.9. Se ha implementado en un substrato *RO4003C* con constante dieléctrica $\varepsilon_r$ = 3.55 y grosor $h$ = 0.813 mm. La respuesta de ésta estructura inferida de la simulación electromagnética, es también mostrada en la Figura 3.8, se observa que a nivel de layout se cumple las especificaciones en la frecuencia de operación.

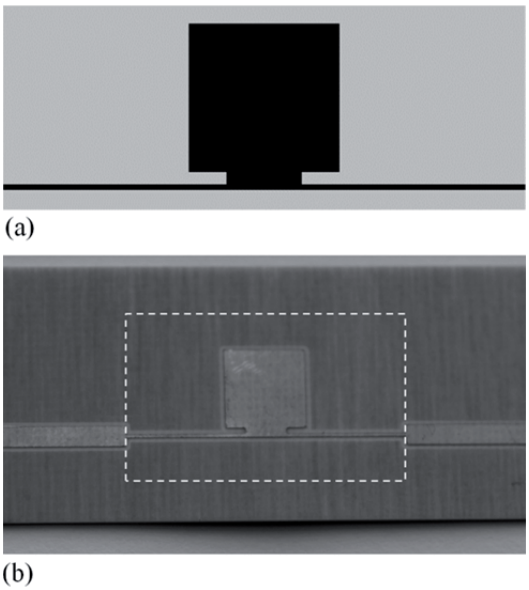


**Figura 3.9**. Layout (a) y fotografía (b) de la celda sintetizada para el Ejemplo 1, celda de 90º. Dimensiones son $l$ = 25.19 mm, $l_p$ = 7.23 mm, $W_{acc}$ = 3.61 mm (0.5$l_p$), $W_{host}$ = 0.27 mm

Para el segundo paso ASM, para el 1º sub-proceso para la determinación de $l_p$ se presentan los resultados en la tabla 3.2 y para el 2º sub-proceso para la determinación de $l$ se presenta la Tabla 3.3

**Tabla 3.2**: Evolución de variables para Ejemplo 1, 2º ASM – 1º Sub-proceso, celda de 90º

| It. | **Modelo Fino**, $l_p$ | | **Modelo Grueso**, $C_{ls}$ | Error |
|---|---|---|---|---|
| 1 | 8.257 mm | | 3.394 pF | 28.77 % |
| 2 | 7.296 mm | | 2.685 pF | 1.85 % |
| 3 | 7.230 mm | | 2.640 pF | 0.13 % |

**Tabla 3.3**: Evolución de variables para Ejemplo 1, 2º ASM – 2º Sub-proceso, celda de 90º

| It. | **Modelo Fino**, $l$ | | **Modelo Grueso**, $\beta l$ | Error |
|---|---|---|---|---|
| 1 | 23.792 mm | | 86.234º | 4.184% |
| 2 | 25.186 mm | | 90.050º | 0.055% |

El segundo ASM no optimiza la dimensión del parche $l_p$, la longitud de la estructura $l$ y $W_{host}$ todas las variables a la vez. En vez de eso, simplemente se ha optimizado la dimensión del parche y la longitud de la celda, por dos sub-procesos ASM independientes con sólo una variable de optimización cada uno. Consecuentemente el segundo paso ASM es rápido y capaz de proveer resultados exactos. Es importante mencionar que la optimización se ha realizado a una frecuencia de operación. A frecuencias suficientemente altas (cerca de la frecuencia de corte), las discrepancias se deben a efectos distribuidos del parche capacitivo, dado que no pueden ser despreciados. Así, estas discrepancias son atribuidas a una limitación del modelo por esquemático, donde la capacitancia es descrita por un elemento discreto. Se debe destacar que el algoritmo de síntesis es muy eficiente, en pocas iteraciones se puede obtener la celda a nivel de layout. El proceso es totalmente desatendido y puede durar menos de tres minutos. Para cada simulación se ha usado una alta densidad de mallado (para la celda de 90º se ha mallado hasta 1.5 GHz y la densidad de mallado es de 300 celdas/longitud de onda).

La celda de la Figura 3.9(b) ha sido fabricada por la microfresadora *LPKF HF100* y ha sido caracterizada por medio del analizador de red *E8364B* de *Agilent* y por el accesorio de prueba modelo *3680-20* de *Anritsu*.

La medición para la celda unitaria prototipo de los parámetros S, de la impedancia Bloch y la longitud eléctrica también se observa en la Figura 3.8. Para obtener una medición de la celda unidad se ha aplicado un proceso *de-embedding* para sustraer el efecto de las líneas de acceso y poder medir en los planos extremos de la celda unitaria. Se pudo demostrar con este ejemplo que el método de dos pasos ASM es eficiente y rápido para la síntesis de estructuras de onda lenta.

### 3.4.2 Ejemplo 2: $\beta l$ = 45º, $Z_B$ = 50 Ω, *swr* = 0.5

Para las especificaciones dadas, se sigue con las ecuaciones (3.8)-(3.10) que los elementos discretos para la Fig. 3.1(b) son $C$ = 0.625 pF, $C_{ls}$ = 1.875 pF y $L$ = 6.25 nH. A partir de la ecuación 3.13 los valores del primer vector del modelo fino $\mathbf{x}_f^{(1)}$ son: $Z_0$ = 100.0 Ω, $kl$ = 22.5º y $C_{ls}$ = 1.875 pF. Usando el primer algoritmo ASM, es posible determinar el esquemático óptimo. La convergencia con un error de 0.074 % ha sido obtenida luego de 3 iteraciones. Los valores finales del modelo fino son $Z_0$ = 104.10 Ω, $kl$ = 22.50º y $C_{ls}$ = 1.73 pF. La magnitud del error para este 1º ASM se observa en la siguiente gráfica en la Figura 3.10

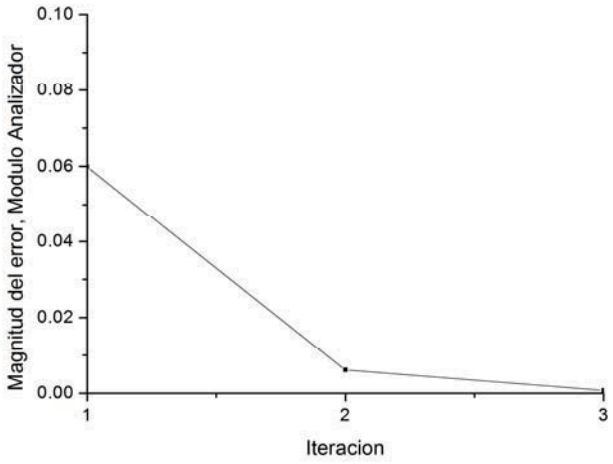


**Figura 3.10**. Evolución de la magnitud del error, módulo analizador, celda de 45º

En la siguiente tabla 3.4 se observa como varían las variables en este caso:

**Tabla 3.4**: Evolución de variables para Ejemplo 2, Módulo Analizador celda de 45º

| | **Modelo Fino** | | | | **Modelo Grueso** | | |
|---|---|---|---|---|---|---|---|
| It. | $Z_0$ | $kl$ | $C_{ls}$ | | $Z_B$ | $\beta l$ | *swr* |
| 1 | 100.00 Ω | 22.50º | 1.875 pF | | 47.21 Ω | 45.696º | 0.492 |
| 2 | 104.23 Ω | 22.53º | 1.717 pF | | 50.23 Ω | 44.909º | 0.502 |
| 3 | 104.10 Ω | 22.50º | 1.734 pF | | 49.97 Ω | 45.010º | 0.500 |

La respuesta del esquemático se muestra en la Figura 3.11, se cumple las especificaciones en la frecuencia de operación. A nivel de esquemático las especificaciones luego de la convergencia son $Z_B$ = 49.97 Ω, $\beta l$ = 45.01º y *swr* = 0.50.

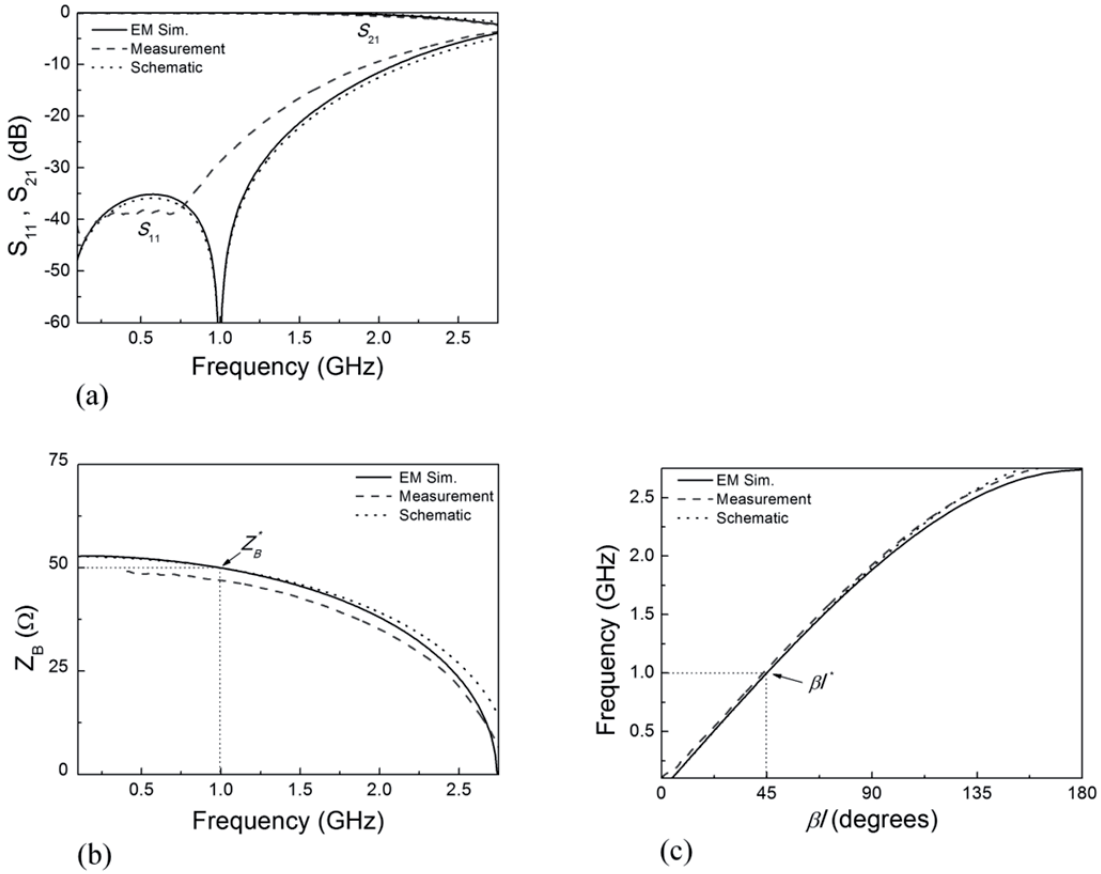


**Figura 3.11**. Respuesta de la celda considerada en ejemplo 2. (a) Coeficiente de transmisión y de reflexión. (b) Impedancia característica y (c) Longitud eléctrica

La aplicación del segundo paso ASM provee el layout de la figura 3.12, el mismo substrato *RO4003C* ha sido usado. Se presenta la simulación electromagnética también en la Figura 3.11 y se observa que a nivel de layout las especificaciones se cumplen en una buena aproximación. Se observa adaptación a 1 GHz. En la Figura 3.11 también se observa la medición de los parámetros S para el prototipo de la Figura 3.12(b). La impedancia Bloch y la longitud eléctrica se infieren de los parámetros S, también se muestran para el prototipo.

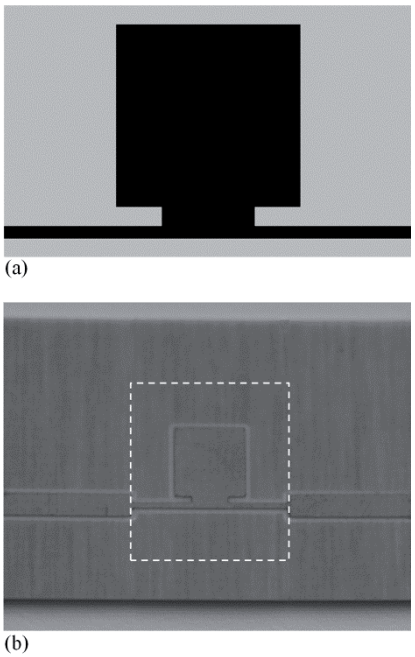


**Figura 3.12**. Layout (a) y fotografía (b) de la celda sintetizada para el Ejemplo 2, celda de 45º. Dimensiones son $l$ = 12.73 mm, $l_p$ = 5.75 mm, $W_{acc}$ = 2.87 mm (0.5$l_p$), $W_{host}$ = 0.41 mm.

Para el segundo paso ASM, para el 1º sub-proceso para la determinación de $l_p$ se presentan los resultados en la Tabla 3.5 y para el 2º sub-proceso para la determinación de $l$ se presenta la Tabla 3.6

**Tabla 3.5**: Evolución de variables para Ejemplo 2, 2º ASM – 1º Sub-proceso, celda de 45º

| It. | **Modelo Fino**, $l_p$ | | **Modelo Grueso**, $C_{ls}$ | Error |
|---|---|---|---|---|
| 1 | 6.696 mm | | 2.297 pF | 32.50 % |
| 2 | 5.823 mm | | 1.778 pF | 2.54 % |
| 3 | 5.748 mm | | 1.737 pF | 0.18 % |

**Tabla 3.6**: Evolución de variables para Ejemplo 2, 2º ASM – 2º Sub-proceso, celda de 45º

| It. | **Modelo Fino**, $l$ | | **Modelo Grueso**, $\beta l$ | Error |
|---|---|---|---|---|
| 1 | 11.78 mm | | 42.586º | 5.365 % |
| 2 | 12.73 mm | | 44.980º | 0.044 % |

### 3.4.3 Ejemplo 3: $\phi_{cell}$ = 30º, $Z_B$ = 50 Ω, *swr* = 0.5, Estructura de 90º (Concatenación de 3 celdas)

Para la celda unitaria de 30º, para las especificaciones dadas, de las ecuaciones (3.8)-(3.10), los elementos discretos para la Figura 3.1(b) son $C$ = 0.417 pF, $C_{ls}$ = 1.25 pF y $L$ = 4.167 nH. A partir de la ecuación 3.13 los valores del primer vector del modelo fino $\mathbf{x}_f^{(1)}$ son: $Z_0$ = 100 Ω, $kl$ = 15.0º y $C_{ls}$ = 1.25 pF. Usando el primer algoritmo ASM, es posible determinar el esquemático óptimo. La convergencia con un error de 0.168 % ha sido obtenida luego de 2 iteraciones. Los valores finales del modelo fino son $Z_0$ = 101.79 Ω, $kl$ = 15.01º y $C_{ls}$ = 1.20 pF. La magnitud del error para este 1º ASM se observa en la siguiente gráfica en la Figura 3.13

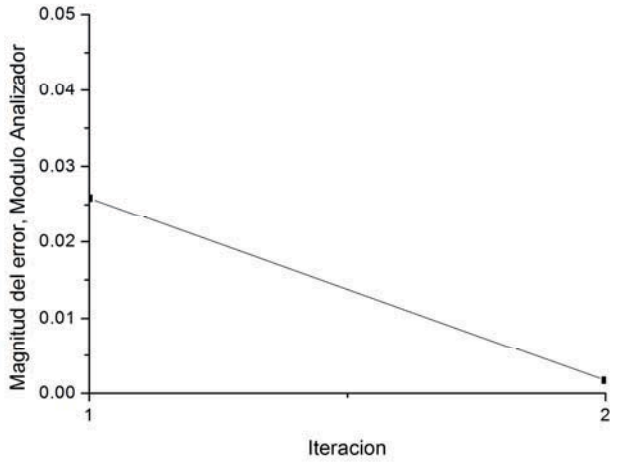


**Figura 3.13**. Evolución de la magnitud del error, módulo analizador, celda de 30º

En la siguiente tabla 3.7 se observa como varían las variables para el módulo analizador en este caso:

**Tabla 3.7**: Evolución de variables para Ejemplo 3, Módulo Analizador celda unitaria de 30º

| | **Modelo Fino** | | | | **Modelo Grueso** | | |
|---|---|---|---|---|---|---|---|
| It. | $Z_0$ | $kl$ | $C_{ls}$ | | $Z_B$ | $\beta l$ | *swr* |
| 1 | 100.00 Ω | 15.00º | 1.250 pF | | 48.80 Ω | 30.20º | 0.497 |
| 2 | 101.79 Ω | 15.01º | 1.204 pF | | 50.06 Ω | 29.99º | 0.500 |

A nivel de esquemático para la celda unitaria las especificaciones luego de la convergencia son $Z_B$ = 50.06 Ω, $\phi_{cell}$ = 29.99º y *swr* = 0.50. La respuesta a nivel circuital y a nivel de layout son mostradas en la figura 3.14

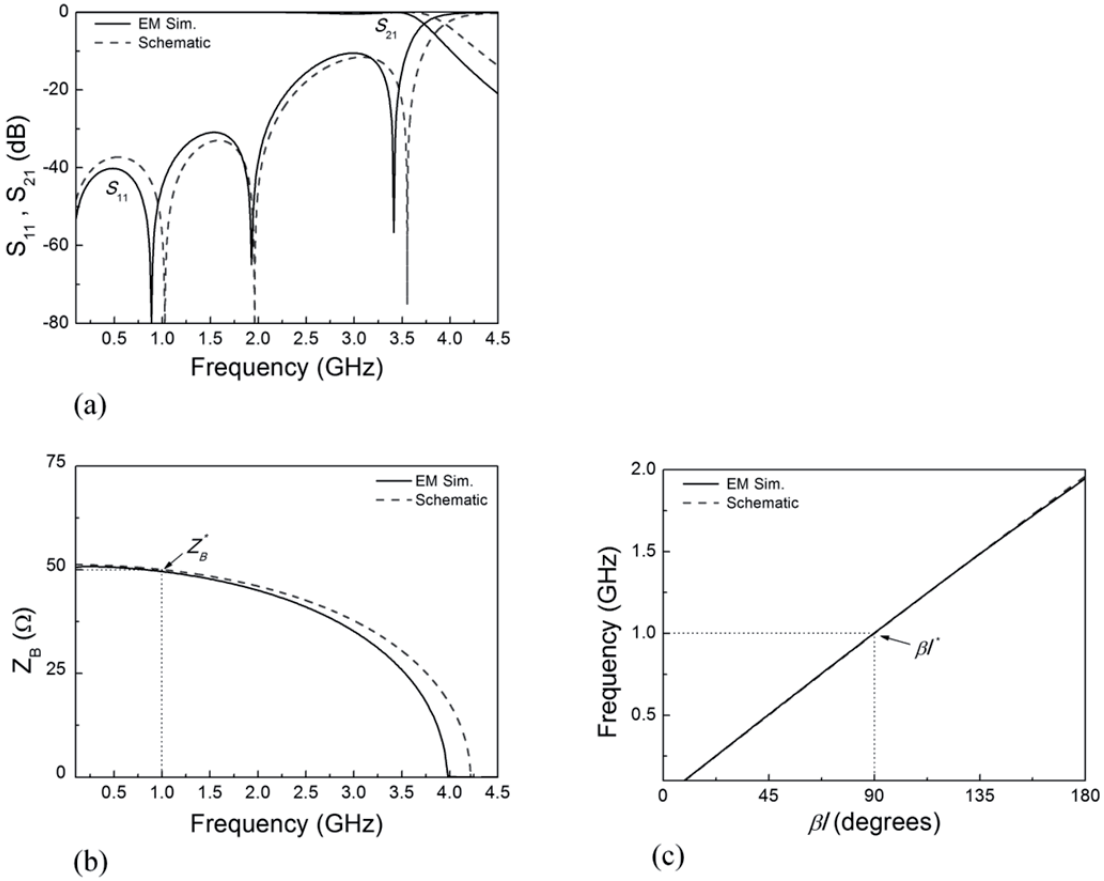


**Figura 3.14**. Respuesta de la Estructura considerada en ejemplo 3. (a) Coeficiente de transmisión y de reflexión para las tres celdas concatenadas. (b) Impedancia característica de la celda unidad y (c) Longitud eléctrica de la concatenación de tres celdas.

La aplicación del Segundo paso ASM provee el layout mostrado en la Figura 3.15, se considera el mismo substrato *RO4003C*

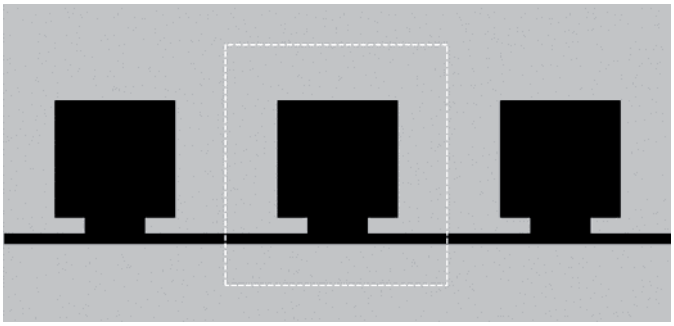

**Figura 3.15**. Layout de la estructura sintetizada en el Ejemplo 3. Para la celda unitaria de 30º las dimensiones son $l$ = 8.62 mm, $l_p$ = 4.69 mm, $W_{acc}$ = 2.35 mm (0.5$l_p$), $W_{host}$ = 0.44 mm.

Para el segundo paso ASM, para el 1º sub-proceso para la determinación de $l_p$ se presentan los resultados en la tabla 3.8 y para el 2º sub-proceso para la determinación de $l$ se presenta la Tabla 3.9

**Tabla 3.8**: Evolución de variables para Ejemplo 3, 2º ASM – 1º Sub-proceso, celda de 30º

| It. | **Modelo Fino**, $l_p$ | | **Modelo Grueso**, $C_{ls}$ | Error |
|---|---|---|---|---|
| 1 | 5.582 mm | | 1.649 pF | 36.92 % |
| 2 | 4.764 mm | | 1.241 pF | 3.06 % |
| 3 | 4.690 mm | | 1.207 pF | 0.24 % |

**Tabla 3.9**: Evolución de variables para Ejemplo 3, 2º ASM – 2º Sub-proceso, celda de 30º

| It. | **Modelo Fino**, $l$ | | **Modelo Grueso**, $\beta l$ | Error |
|---|---|---|---|---|
| 1 | 7.85 mm | | 28.08º | 6.40 % |
| 2 | 8.62 mm | | 29.94º | 0.20 % |

La diferencia principal en éste caso es que se observan dos ceros de reflexión adicionales (acople por fase). Este acople ocurre a aquellas frecuencias donde la longitud eléctrica de la estructura es un múltiplo de $\pi$ [49].

### 3.4.4 Ejemplo 4: $\phi_{cell}$ = 45º, $Z_B$ = 50 Ω, *swr* = 0.5, Estructura de 180º (Concatenación de 4 celdas)

En referencia al Ejemplo 2 de este capítulo, para la celda unitaria de 45º, los valores finales del modelo fino son $Z_0$ = 104.10 Ω, $kl$ = 22.50º y $C_{ls}$ = 1.73 pF y a nivel de esquemático las especificaciones luego de la convergencia para la celda unitaria: $Z_B$ = 49.97 Ω, $\beta l$ = 45.01º y *swr* = 0.50. La respuesta electromagnética y circuital, y el layout de toda la estructura (compuesta de cuatro celdas) se muestran en las figuras 3.16 y 3.17, respectivamente. Nótese en este caso que tres ceros de reflexión adicionales son esperados (acople por fase) [49]. Sin embargo, a la frecuencia de operación (1 GHz) ocurre el acople por fase y acople de impedancia al mismo tiempo, por lo que sólo dos ceros de reflexión adicionales pueden ser observados.

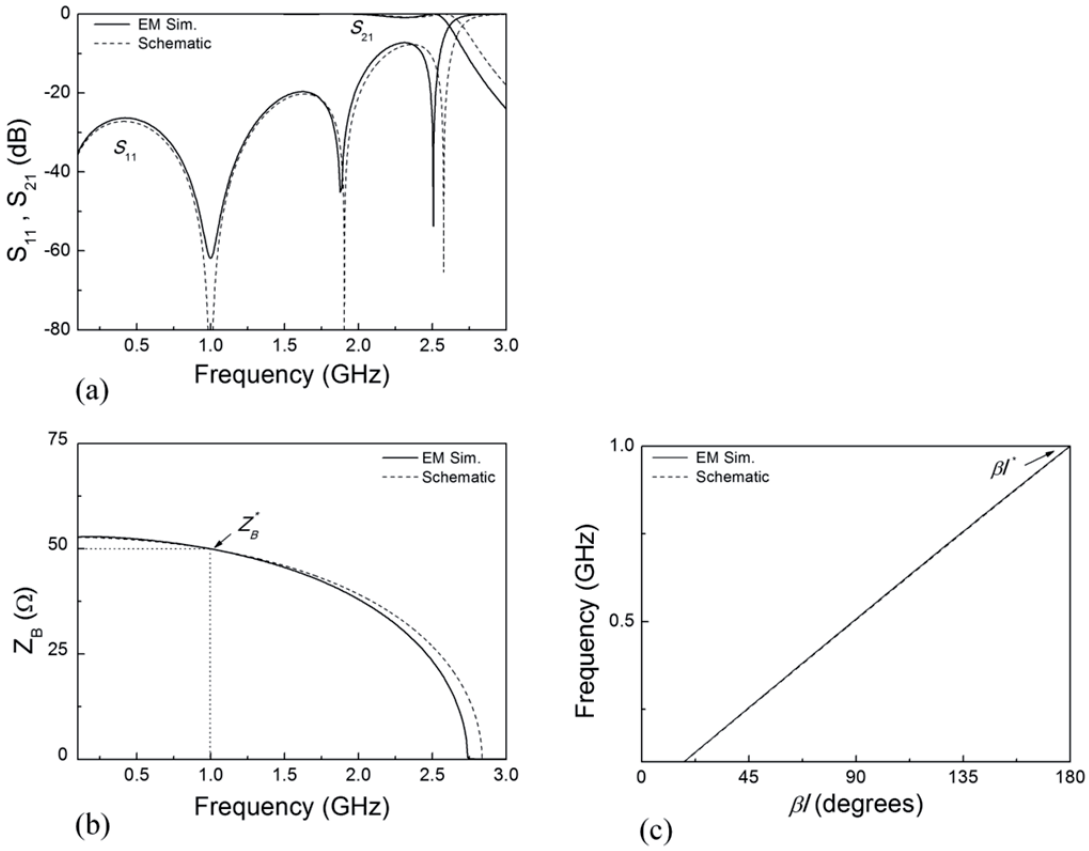


**Figura 3.16**. Respuesta de la estructura considerada en ejemplo 4. (a) Coeficiente de transmisión y de reflexión. (b) Impedancia característica de la celda unitaria y (c) Longitud eléctrica del conjunto de cuatro celdas

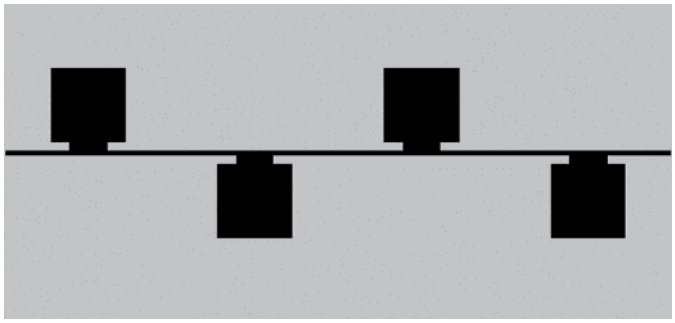

**Figura 3.17**. Layout de la estructura sintetizada para el Ejemplo 4. Para la celda unitaria, las dimensiones son $l$ = 12.73 mm, $l_p$ = 5.75 mm, $W_{acc}$ = 2.87 mm (0.5$l_p$), $W_{host}$ = 0.41 mm.

## 3.5 Conclusiones

En resumen, se ha desarrollado un algoritmo de dos pasos para la síntesis de líneas de transmisión de onda lenta basadas en parches capacitivos. El primer paso ASM determina el esquemático óptimo a partir de las especificaciones de impedancia Bloch, longitud eléctrica y razón de onda lenta. El segundo paso ASM provee el layout final de la estructura de onda lenta. Es relevante que el layout de la estructura es determinado a partir de las especificaciones de una forma desatendida y automática.

# 4

# Aplicaciones

Este capítulo considera dos aplicaciones. En primer lugar estudia la síntesis automática de filtros pasabanda de banda ancha operando en frecuencias de microondas y basados en estructuras EBG con carga capacitiva. El objetivo primordial es sustituir líneas de transmisión ordinarias por líneas de transmisión artificiales que exhiban la misma longitud eléctrica e impedancia característica a la frecuencia de corte inferior del filtro. Estos filtros son implementados totalmente en tecnología planar. Debido a las cargas capacitivas se produce un efecto de onda lenta que reduce el tamaño de los filtros. Se estudia un método de síntesis de forma sistemática, donde las estructuras EBG son obtenidas de forma desatendida. Se presentan tres ejemplos.

La segunda aplicación trata sobre la síntesis de filtros pasabanda, basados en pares de líneas acopladas con carga capacitiva. Éstos presentan una reducción en su longitud y además una supresión de espurios. El diseño de estos filtros se ha logrado por un proceso ASM que optimiza las cargas capacitivas y otro segundo proceso ASM de tres variables que optimiza la estructura del par de líneas acopladas con carga capacitiva. El layout inicial se encuentra a través de la determinación del esquemático ideal, éste se determina con un análisis para los modos par e impar de la estructura. Se presentan dos ejemplos para ilustrar el potencial del método de diseño: un filtro Chebyshev de tercer orden y otro de quinto orden. Ambas aplicaciones muestran el efecto de onda lenta con la consiguiente disminución de dimensiones. Además, debido a la periodicidad se consigue una buena eliminación de espurios.

# 4.1 Síntesis automática de filtros pasabanda de banda ancha basados en estructuras EBG

La publicación "*Automated synthesis of wideband bandpass filters based on slow-wave EBG structures*" aceptada por la revista CMC (*Computers, Materials & Continua*), trató sobre líneas de transmisión artificiales incorporando estructuras EBG, aplicadas al diseño de filtros de banda ancha que son capaces de proveer bandas de paso muy anchas pero también con eliminación de bandas espurias. Este trabajo es el **artículo B** de la relación de artículos que constituyen la parte fundamental de esta tesis.

Remplazando parte de los elementos distribuidos (secciones de líneas de transmisión ordinarias) con líneas con parches capacitivos (estudiados en el Capítulo 3), las bandas espurias pueden ser sustancialmente rechazadas. Además, la longitud del filtro puede ser reducida debido al efecto de onda lenta.

## 4.1.1 Filtros pasabanda de banda ancha basados en stubs en derivación: topología y diseño

Se revisa brevemente la topología y el diseño de estos filtros de banda ancha (sin EBG) en los cuales los filtros con EBG de esta tesis fueron inspirados. Tales filtros consisten de una cascada de stubs en derivación de igual longitud eléctrica, alternándose con líneas de transmisión del doble de longitud eléctrica. El análisis de este tipo de filtros fue realizado por Levy [50]. Usando *n* stubs, una función de grado *2n-1* es implementada en estos filtros, que son útiles para generar filtros de banda ancha. Sin embargo las bandas espurias están también presentes en su respuesta en frecuencia.

El esquemático de este tipo de filtros se muestra en la Figura 1 de la **publicación B**. La red mostrada en la Figura 1 de tal publicación implementa la función de transferencia en la expresión (4.1) como una función de la variable de frecuencia normalizada $\theta = \theta_c f/f_c$ [51].

$$\left|S_{21}(\theta)\right|^2 = \frac{1}{1+\kappa^2 F_n^2(\theta)} \tag{4.1}$$

con

$$F_n(\theta) = \frac{\left(1+\sqrt{1-x_c^2}\right)\cdot T_{2n-1}\left(\frac{x}{x_c}\right) - \left(1-\sqrt{1-x_c^2}\right)\cdot T_{2n-3}\left(\frac{x}{x_c}\right)}{2\cdot\cos\left(\frac{\pi}{2}-\theta\right)} \tag{4.2}$$

$$x = \sin\left(\frac{\pi}{2}-\theta\right) \tag{4.3}$$

$$x_c = \sin\left(\frac{\pi}{2}-\theta_c\right) \tag{4.4}$$

Donde $T_n = \cos\left(n\cdot\cos^{-1}(x)\right)$ y $\kappa$ es la constante de rizado del filtro pasabanda. El ancho de banda del filtro es delimitado por las frecuencias $f_c$ y $(\pi/\theta_c - 1)f_c$, por lo que el ancho de banda puede ser controlado por el valor de la longitud eléctrica $\theta_c$. Los valores de impedancia de los stubs en cortocircuito y de los elementos de línea pueden ser escogidos para el filtro pasaaltos óptimo [51].

### 4.1.2 Estructuras de onda lenta basadas en líneas cargadas capacitivamente

Los filtros considerados en la sección previa exhiben bandas espurias igual de anchas, y la primera banda espuria es muy cercana a la banda de interés. Estas bandas espurias pueden ser eliminadas cargando las secciones de líneas con parches capacitivos [32]. El efecto de las capacitancias en las secciones de línea es doble: (i) Bandas de rechazo aparecen en el espectro de transmisión de estas secciones de línea como consecuencia de la periodicidad; (ii) La velocidad de fase es reducida dado que la capacitancia efectiva por sección de línea es incrementada. Así cargando las secciones de línea con parches capacitivos, no solo los espurios del filtro pueden ser suprimidos, además también la longitud del filtro puede ser reducida.

Además de lo estudiado en el Capítulo 3 de la tesis, para resolver el problema de filtros pasabanda miniaturizados son necesarias otras ecuaciones. Basado en el modelo discreto de la Fig. 3.1 (b), que es un equivalente de una línea cargada periódicamente, la primera banda de paso de la estructura es delimitada por la siguiente frecuencia de corte (frecuencia Bragg) [20].

$$f_B = \frac{1}{\pi\sqrt{L(C+C_{ls})}} \tag{4.5}$$

y la frecuencia superior de la primera banda espuria es:

$$f_s = \frac{1}{2\sqrt{LC}} \tag{4.6}$$

Un aspecto muy importante de ser considerado en la presente aplicación de estas líneas cargadas capacitivamente concierne a la posición de la frecuencia Bragg, dada en (4.5). Esta frecuencia debe ser forzada a estar entre la primera banda de paso (banda de interés) y la primera banda espuria; de otra forma la primera banda espuria no es eficientemente suprimida o la banda de interés se vería afectada. Es posible a través de la ecuación para la frecuencia Bragg (4.5) y de la ecuación para la longitud eléctrica de la celda unitaria (3.6), obtener la siguiente expresión:

$$\phi_{cell} = \frac{2 f_c}{f_B} \tag{4.7}$$

Asumamos que el número de celdas unitarias de onda lenta para cada línea de transmisión (de longitud eléctrica $2\theta_c$) es $N$, así para ésta aplicación la longitud eléctrica de la celda unitaria es $\phi_{cell} = 2\theta_c / N$ a la frecuencia $f_c$ del filtro pasabanda. De acuerdo a (4.7) se sigue para ésta aplicación que la frecuencia Bragg es $f_B = Nf_c / \theta_c$.

Un aspecto importante en ésta aplicación es la determinación del número $N$ de estructuras EBG que se han de incorporar en cada línea de transmisión de longitud eléctrica $2\theta_c$. Para esto se ha de fijar la frecuencia Bragg de la estructura EBG entre dos frecuencias clave. La frecuencia superior de la banda de paso y la frecuencia inferior de la primer banda espuria están dados por $(\pi/\theta_c - 1)f_c$ y $(\pi/\theta_c + 1)f_c$, respectivamente, se sigue que la frecuencia Bragg está entre:

$$\begin{aligned} \left(\frac{\pi}{\theta_c} - 1\right) f_c < f_B < \left(\frac{\pi}{\theta_c} + 1\right) f_c \\ \left(\frac{\pi}{\theta_c} - 1\right) f_c < \frac{N f_c}{\theta_c} < \left(\frac{\pi}{\theta_c} + 1\right) f_c \\ \pi - \theta_c < N < \pi + \theta_c \end{aligned} \tag{4.8}$$

De acuerdo al análisis anterior, $N$ no puede ser arbitrario, y los valores posibles son dependientes de $\theta_c$. Para las tabulaciones en [51], los valores de $\theta_c$ pueden ir de los 25º - 35º, esto indica que $N = 3$ para estos posibles casos.

### 4.1.3 Ejemplo 1: $f_c$ = 1.0 GHz, $BW$ = 3.0 GHz, $n$ = 3, $L_{Ar}$ = 0.1 dB

Con estos parámetros de filtros, la longitud eléctrica de los stubs es de $\theta_c$ = 36º, y así las secciones de líneas de transmisión donde se sustituirá por estructuras EBG es entonces $2\theta_c$ = 72º. Las impedancias características y longitudes eléctricas de las secciones de línea y de los stubs en cortocircuito, así como sus longitudes y anchuras se muestran en la Fig. 3(a) de la **publicación B**. Se ha implementado en un substrato *RO4003C* con grosor $h$ = 0.813 mm y constante dieléctrica $\varepsilon_r$ = 3.55. La Fig. 3(b) de la publicación B muestra la respuesta a nivel circuital y electromagnético del filtro convencional. Se observa la banda espuria muy cerca de la banda de interés.

Se remplaza las secciones de líneas de transmisión cuya impedancia característica es de 48.59 Ω con líneas de transmisión de onda lenta con carga capacitiva. Se considera $swr$ = 0.5. De acuerdo al valor de $\theta_c$ el número de celdas para la sección es de $N$ = 3. A la vez $\phi_{cell} = \beta l = 24^\circ$. A partir de la ecuación 3.13 los valores del primer vector del modelo fino $\mathbf{x}_f^{(1)}$ son: $Z_0$ = 97.18 Ω, $kl$ = 12.0º y $C_{ls}$ = 1.03 pF. Usando el primer algoritmo ASM es posible determinar el esquemático óptimo, la convergencia con un error relativo de 0.09% ha sido obtenida luego de 2 iteraciones. Los valores finales para el modelo fino son $Z_0$ = 98.28 Ω, $kl$ = 12.0º y $C_{ls}$ = 1.01 pF.

La longitud eléctrica y la impedancia característica a nivel de esquemático y electromagnético usando los valores previos se muestra en la Figura 4 de la **publicación B**. La respuesta en frecuencia que resulta de concatenar tres celdas se muestra en la Figura 5 de la publicación B. En vista de la figura 4 se obtiene a nivel de esquemático los siguientes resultados para el modelo grueso $Z_B$ = 48.62 Ω, $\beta l$ = 23.99º y $swr$ = 0.50, a la frecuencia $f_c$ = 1.0 GHz.

Una vez que el esquemático óptimo ha sido obtenido, la aplicación del segundo ASM lleva al layout de la estructura de onda lenta unitaria con dimensiones óptimas de la Figura 6 de la publicación B. Las dimensiones son $l$ = 6.767 mm, $l_p$ = 4.282 mm, $W_{acc}$ = 2.141 mm ($0.5l_p$), $l_{acc}$ = 0.583 mm, $W_{host}$ = 0.475 mm

La simulación electromagnética considerando tres celdas también se muestra en la Figura 5 de la **publicación B** y se observa que la frecuencia Bragg se encuentra entre la frecuencia superior de la banda de paso y la frecuencia inferior de la banda espuria. La frecuencia Bragg obtenida por simulación electromagnética tiene el valor correcto, y se obtiene una amplia banda de rechazo, la cual es útil para la supresión de la banda espuria del filtro.

Concatenando tres celdas unitarias a nivel de layout, es posible construir el filtro mejorado con carga capacitiva para las secciones de línea de longitud $2\theta_c$. El filtro final a nivel de layout se observa en la Fig. 7(b) de la **publicación B**, donde se compara con el filtro convencional en la Fig. 7(a) de la publicación B. La respuesta electromagnética de los dos filtros se comprara en la Fig. 7(c) de tal publicación, éstas sin pérdidas. Se observa una reducción significativa de tamaño debido al efecto de onda lenta. La fotografía del prototipo se muestra en la Fig. 8(a) de la **publicación B** y la Fig. 8(b) de la publicación muestra la respuesta del prototipo comparada con la simulación electromagnética del filtro mejorado incluyendo pérdidas. Gracias a la presencia de las líneas con carga capacitiva, una atenuación muy significativa de la banda espuria es lograda (mejor a 36 dB hasta 10 GHz).

### 4.1.4 Ejemplo 2: $f_c$ = 1.4 GHz, $BW$ = 4.8 GHz, $n$ = 3, $L_{Ar}$ = 0.1 dB

Con estos parámetros del filtro y del substrato, la longitud eléctrica de los stubs es de $\theta_c$ = 33.16º, así las secciones de líneas de transmisión donde se sustituirá por estructuras EBG es entonces $2\theta_c$ = 66.32º. Las impedancias características y longitudes eléctricas de las secciones de línea y de los stubs en cortocircuito, así como sus longitudes y anchuras se muestran en la Fig. 4.1(a). Se ha implementado en un substrato *RO4003C* con grosor $h$ = 0.813 mm y constante dieléctrica $\varepsilon_r$ = 3.55. La Fig. 4.1 (b) muestra la respuesta a nivel circuital y electromagnético del filtro convencional, se observa la banda espuria, muy cerca de la banda de interés.

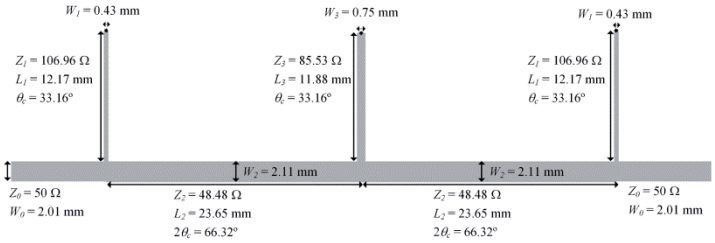


(a)

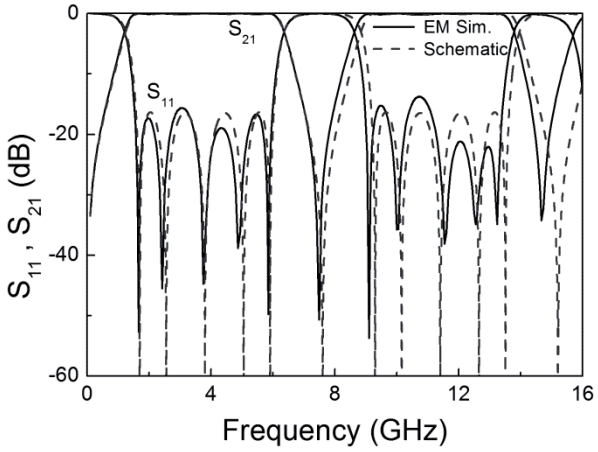


(b)

**Figura 4.1**. (a) Layout del filtro convencional considerado en el Ejemplo 2. (b) Respuesta electromagnética y circuital

Se procede a remplazar las secciones de líneas de transmisión cuya impedancia característica es de 48.48 Ω con líneas de transmisión de onda lenta con carga capacitiva. Se considera *swr* = 0.5. De acuerdo al valor de $\theta_c$ el número de celdas para la sección es de $N = 3$. A la vez $\phi_{cell} = \beta l = 22.11^{\circ}$. A partir de la ecuación 3.13 los valores del primer vector del modelo fino $\mathbf{x}_f^{(1)}$ son: $Z_0$ = 96.96 Ω, $kl$ = 11.05º, $C_{ls}$ = 0.68 pF. Usando el primer algoritmo ASM es posible determinar el esquemático óptimo, la convergencia con un error relativo de 0.07% ha sido obtenida luego de 2 iteraciones. Los valores finales para el modelo fino son $Z_0$ = 97.89 Ω, $kl$ = 11.05º y $C_{ls}$ = 0.66 pF.

La longitud eléctrica y la impedancia característica a nivel de esquemático y electromagnético usando los valores previos se muestra en la Figura 4.2. La respuesta en frecuencia que resulta de concatenar tres celdas se muestra en la Figura 4.3.

En vista de la figura 4.2 se obtiene a nivel de esquemático los siguientes resultados para el modelo grueso $Z_B$ = 48.51 Ω, $\beta l$ = 22.10º y *swr* = 0.50, esto a $f_c$ = 1.4 GHz

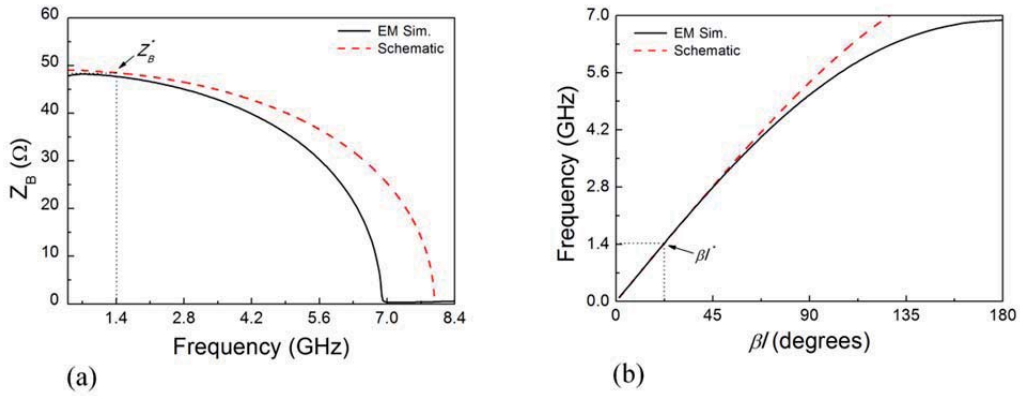


**Figura 4.2**. Impedancia característica (a) y longitud eléctrica de la celda unitaria sintetizada (b)

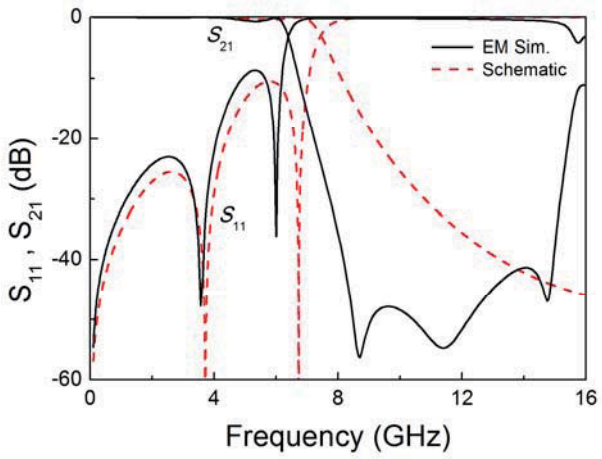


**Figura 4.3**. Respuesta en frecuencia de la línea artificial sintetizada constituida por tres celdas.

Una vez que el esquemático óptimo ha sido obtenido, la aplicación del segundo ASM lleva al layout de la estructura de onda lenta unitaria con dimensiones óptimas, en referencia a la figura 3.3, las dimensiones del layout para este ejemplo son $l$ = 4.488 mm, $l_p$ = 3.345 mm, $W_{acc}$ = 1.672 mm (0.5$l_p$), $W_{host}$ = 0.48 mm, $l_{acc}$ = 0.583 mm

La simulación electromagnética considerando tres celdas también se muestra en la Figura 4.3 y se observa que la frecuencia Bragg se encuentra entre la frecuencia superior de la banda de paso y la frecuencia inferior de la banda espuria. La frecuencia Bragg obtenida por simulación electromagnética es correcta, y se obtiene una amplia banda de rechazo, la cual es útil para la supresión de la banda espuria del filtro.

Concatenando tres celdas unitarias a nivel de layout, es posible construir el filtro mejorado con carga capacitiva para las secciones de línea de longitud $2\theta_c$. El filtro final a nivel de layout se observa en la Fig. 4.4(a), donde se compara con el filtro convencional. La respuesta electromagnética de los dos filtros son comparadas en la Fig. 4.4(b), éstas simulaciones son sin pérdidas. Se observa una reducción significativa de tamaño debido al efecto de onda lenta.

Debido a la presencia de las líneas con carga capacitiva, una atenuación muy significativa de la banda espuria es lograda (mejor a 30 dB hasta 16 GHz a nivel de simulación electromagnética).

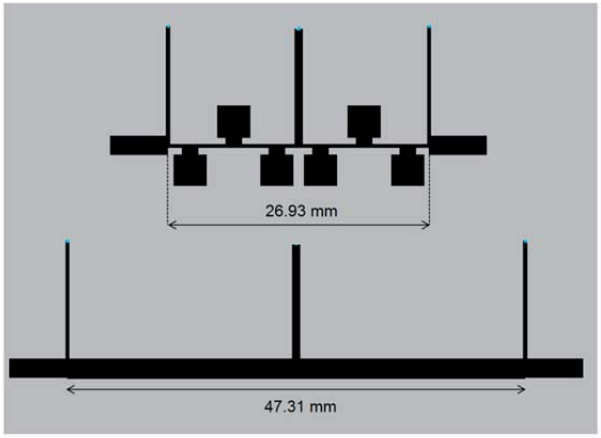


(a)

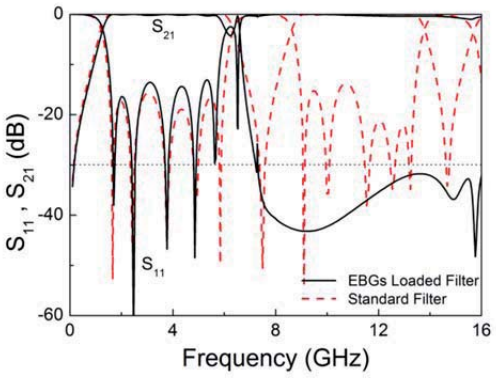


(b)

**Figura 4.4**. Layout de ambos filtros (con carga capacitiva y convencional) comparados (a) y simulación electromagnética de ambos filtros (b). Las dimensiones se indican

Este ejemplo fue presentado en el trabajo "*Application of Aggressive Space Mapping (ASM) Optimization to the Design of Electromagnetic Bandgap (EBG) based Wideband Microwave Bandpass Filters*", en el congreso Internacional "*First International Workshop on Metamaterials by Design, Theory, Methods, and Applications to Communications and Sensing"*, en París en Diciembre 2015. Este trabajo es el **artículo D** de la relación de artículos no fundamentales de esta tesis.

### 4.1.5 Ejemplo 3: $f_c$ = 1.4 GHz, $BW$ = 4.8 GHz, $n$ = 3, $L_{Ar}$ = 0.1 dB, substrato Arlon

Con las especificaciones del filtro y del substrato, la longitud eléctrica de los stubs es de $\theta_c$ = 33.16º, así las secciones de líneas de transmisión donde se sustituirá por estructuras EBG es entonces $2\theta_c$ = 66.32º. Las impedancias características y longitudes eléctricas de las secciones de línea y de los stubs en cortocircuito, así como sus longitudes y anchuras se muestran en la Fig. 4.5(a). Se ha diseñado en un substrato *Arlon* con grosor $h$ = 0.675 mm y constante dieléctrica $\varepsilon_r$ = 2.4. La Fig. 4.5 (b) muestra la respuesta a nivel circuital y electromagnético del filtro convencional, se observa la banda espuria, muy cerca de la banda de interés. En la Fig. 4.5(a) se muestra el layout del filtro convencional optimizado previamente con ASM. Este ejemplo se basa en [32].

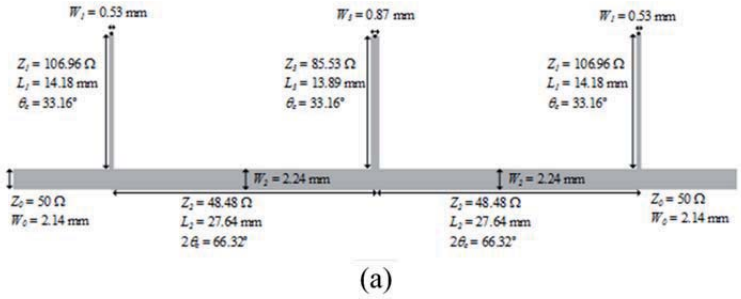


(a)

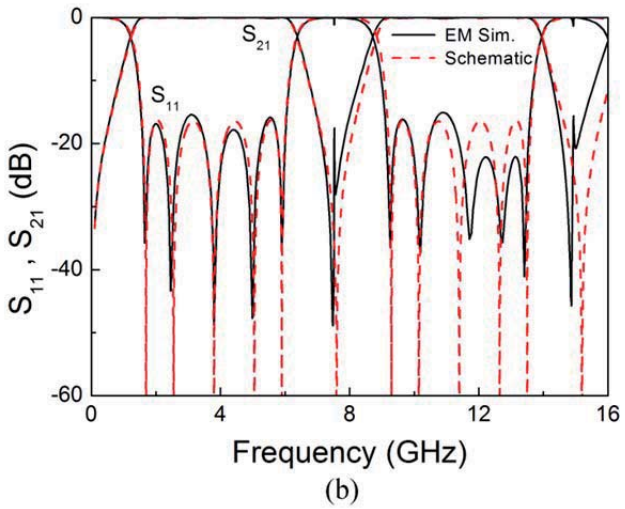


(b)

**Figura 4.5**. (a) Layout del filtro convencional considerado en el Ejemplo 3. (b) Respuesta electromagnética y circuital

Se reemplaza las secciones de líneas de transmisión cuya impedancia característica es de 48.48 Ω con líneas de transmisión de onda lenta con carga capacitiva. Se considera *swr* = 0.5. De acuerdo al valor de $\theta_c$ el número de celdas para la sección es de *N* = 3. A la vez $\phi_{cell} = \beta l = 22.11^{o}$. A partir de la ecuación 3.13 los valores del primer vector del modelo fino $\mathbf{x}_f^{(1)}$ son: $Z_0$ = 96.96 Ω, *kl* = 11.05º y $C_{ls}$ = 0.68 pF. Usando el primer algoritmo ASM es posible determinar el esquemático óptimo, la convergencia con un error relativo de 0.07% ha sido obtenida luego de 2 iteraciones. Los valores finales para el modelo fino son $Z_0$ = 97.89 Ω, *kl* = 11.05º y $C_{ls}$ = 0.66 pF.

La longitud eléctrica, la impedancia característica a nivel de esquemático y por simulación electromagnética y la respuesta en frecuencia que resulta de concatenar tres celdas unitarias tienen forma similar a las presentadas en ejemplo #2, puesto que son las mismas especificaciones del filtro, difiere el substrato. Se obtiene a nivel de esquemático los siguientes resultados para el modelo grueso $Z_B$ = 48.51 Ω, $\beta l$ = 22.10º y *swr* = 0.50, esto a $f_c$ = 1.4 GHz

Habiendo obtenido el esquemático óptimo, la aplicación del segundo ASM lleva al layout de la estructura de onda lenta unitaria con dimensiones óptimas. En referencia a la figura 3.3, las dimensiones del layout de la estructura para este ejemplo son *l* = 5.132 mm, $l_p$ = 3.794 mm, $W_{acc}$ = 1.897 mm ($0.5l_p$), $W_{host}$ = 0.574 mm, $l_{acc}$ = 0.583 mm. Estas dimensiones son mayores que las del Ejemplo #2, es el filtro con las mismas especificaciones, pero con un substrato con menor permitividad.

Concatenando tres celdas unitarias a nivel de layout, es posible construir el filtro mejorado con carga capacitiva para las secciones de línea de longitud $2\theta_c$. El filtro final a nivel de layout se observa en la Fig. 4.6(a), donde se compara con el filtro convencional. La respuesta electromagnética de los dos filtros son comparadas en la Fig. 4.6(b), éstas simulaciones son sin pérdidas. Se observa una reducción significativa de tamaño debido al efecto de onda lenta. Debido a la presencia de las líneas con carga capacitiva, una atenuación muy significativa de la banda espuria es lograda (mejor a 35 dB hasta 16 GHz a nivel de simulación electromagnética).

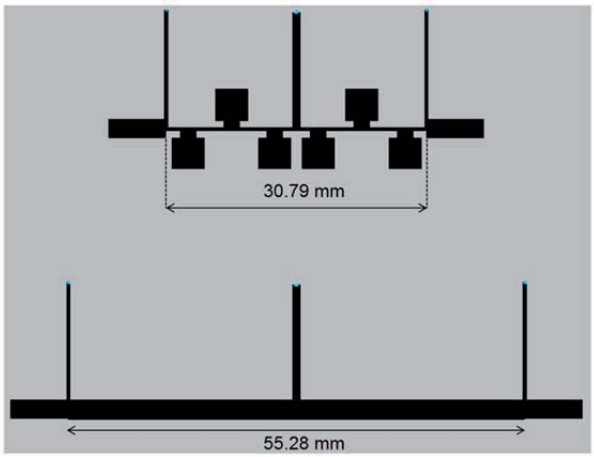


(a)

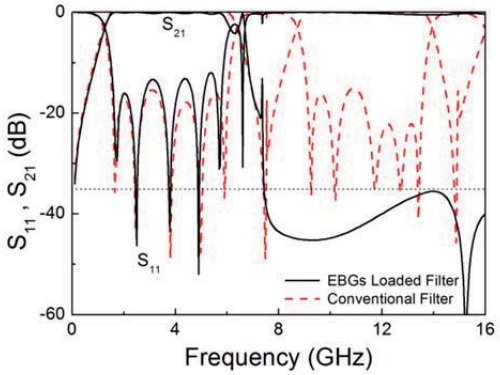


(b)

**Figura 4.6**. Layout de ambos filtros (con carga capacitiva y convencional) comparados (a) y simulación electromagnética de ambos filtros (b), para Ejemplo 3. Las dimensiones se indican.

## 4.2 Filtros pasabanda basados en pares de líneas acopladas con carga capacitiva

La publicación "*Design of Capacitively-Loaded Coupled Line Bandpass Filters with Compact Size and Spurious Suppression*" enviada a la revista IEEE-MTT (*IEEE Transactions on Microwave Theory and Techniques*), trató sobre filtros pasabanda implementados como una cascada de pares de líneas acopladas cargados periódicamente con parches capacitivos. Este trabajo es el **artículo C** de la relación de artículos no fundamentales.

Las líneas de transmisión de onda lenta periódicamente cargadas con capacitancias son elementos prometedores para el diseño de filtros compactos y libres de espurios basados en pares de líneas acopladas. El concepto de estructura de onda lenta basado en carga capacitiva también ha sido usado para la reducción de dimensiones en circuitos CMOS y en dispositivos activos operando en ondas milimétricas [26-28]-[52,53].

En ésta publicación se obtuvo pares de líneas acopladas con parches capacitivos, mostrando efecto de onda lenta. Estas estructuras fueron aplicadas a la implementación de filtros pasa banda con una amplia banda de rechazo. La estrategia de diseño es basada en optimización por ASM, donde los layouts de los pares de líneas acopladas con carga capacitiva son automáticamente generados a partir de parámetros de diseño: impedancias par e impar y longitud eléctrica, a la vez que la razón de onda lenta (que determina el nivel de miniaturización del filtro final comparado con el filtro convencional).

### 4.2.1 Topología y diseño del par de líneas acopladas con carga capacitiva.

La topología y el esquemático de la celda unitaria se muestran en la Figura 1 de la **publicación C** (Fig.1 (a) y (b) respectivamente). Los parches cuadrados son descritos por dos capacitancias $C_{ls}$. Las impedancias $Z_{oe}$ y $Z_{oo}$ son las impedancias características para los modos par e impar respectivamente, del par de líneas acopladas sin carga. Los circuitos equivalentes para los modos par e impar, inferidos al remover una de las mitades y considerando el plano de simetría como una pared magnética (modo par) o una pared eléctrica (modo impar) se muestran en la Fig.1 (c) y Fig.1 (d) respectivamente, de la publicación C.

La relación de dispersión para el modo par está dada por [20]:

$$\cos(\beta_e l) = \cos(k_e l) - \frac{\omega C_{ls} Z_{oe}}{2} \sin(k_e l) \tag{4.9}$$

además la impedancia característica (Bloch) para el modo par es:

$$Z_{Be} = \frac{Z_{oe}\left\{\sin(k_e l) - Z_{oe}\omega C_{ls} \sin^2(k_e l/2)\right\}}{\sin(\beta_e l)} \tag{4.10}$$

Expresiones idénticas son obtenidas para la dispersión e impedancia Bloch para el modo impar simplemente al cambiar los subíndices:

$$\cos(\beta_o l) = \cos(k_o l) - \frac{\omega C_{ls} Z_{oo}}{2} \sin(k_o l) \tag{4.11}$$

$$Z_{Bo} = \frac{Z_{oo}\left\{\sin(k_o l) - Z_{oo}\omega C_{ls} \sin^2(k_o l/2)\right\}}{\sin(\beta_o l)} \tag{4.12}$$

Otro parámetro importante en estas líneas artificiales con carga capacitiva es la razón de onda lenta, definida como la razón de velocidades de fase, o equivalentemente como la razón de constantes de fase, de la línea sin carga entre la de la línea con carga. La razón de onda lenta es definida para cada modo, puesto que en general no son iguales.

$$swr_e = \frac{k_e l}{\beta_e l} \tag{4.13}$$

$$swr_o = \frac{k_o l}{\beta_o l} \tag{4.14}$$

#### 4.2.1.1 Diseño del par de líneas acopladas con carga capacitiva: Determinación del esquemático

Se ha de proveer los parámetros eléctricos del circuito de la Fig. 1(b) de la **publicación C**: $C_{ls}$, $Z_{oe}$, $Z_{oo}$ y también $k_e l$ y $k_o l$. Dado que el propósito de este trabajo es el diseño de filtros pasabanda basados en pares de líneas acopladas, las impedancias Bloch para los modos par e impar de la estructura CLCL (*Capacitively – Loaded Coupled Line*) son dictadas por las especificaciones del filtro (orden, ancho de banda fraccional y nivel de rizado) de acuerdo a fórmulas conocidas [48, 51]. Sin embargo, debido a la dispersión, las impedancias Bloch son dependientes de la frecuencia y por tanto los valores requeridos de $Z_{Be}$ y $Z_{Bo}$ son forzados a la frecuencia central $f_0$. Cada sección CLCL (compuesta al menos por una celda unitaria) debe exhibir una longitud eléctrica a $f_0$ de $\pi/2$ para cada modo; dado que ésto no es posible en la práctica, el

procedimiento usual es el de forzar el promedio de la longitud eléctrica de la estructura CLCL en función de las longitudes eléctricas de ambos modos,

$$N\frac{(\varphi_e|_{f_0}+\varphi_o|_{f_0})}{2}=\frac{\pi}{2} \tag{4.15}$$

donde $N$ es el número de celdas unitarias de la estructura CLCL. Para la solución del problema se ha fijado la razón de onda lenta correspondiente al modo par $swr_e$. Esta variable $swr_e$ no está relacionada con el rendimiento del filtro, sólo con el tamaño del filtro.

La inspección de las siete ecuaciones (4.9)-(4.15) revela que hay ocho incógnitas en el modelo, estas son: $C_{ls}$, $Z_{oe}$, $Z_{oo}$, $k_el$, $k_ol$, $swr_o$, $\beta_ol$ y $\beta_el$ ($Z_{Be}$, $Z_{Bo}$ y $swr_e$ son fijadas). Sin embargo, $k_el$ y $k_ol$ están relacionadas a través de $Z_{oe}$ y $Z_{oo}$, lo que indica que los parámetros del modelo pueden ser unívocamente determinados. El procedimiento detallado sobre cómo resolver el conjunto de ecuaciones se presenta en la **publicación C**, este procedimiento toma en cuenta el substrato sobre el cual se diseña.

Consideremos el siguiente ejemplo de diseño: Filtro pasabanda Chebyshev de orden 3, con frecuencia central $f_0$ = 2.4 GHz, ancho de banda fraccional $FBW$ = 8% y nivel de rizado $L_{Ar}$ = 0.15 dB. Con estas especificaciones, las impedancias de las secciones primera y cuarta (secciones extremas) son $Z_{Be}$ = 72.12 Ω y $Z_{Bo}$ = 38.91 Ω. Fijamos $swr_e$ = 0.5, se trabaja con $N$ = 2 celdas para estas secciones, así $(\varphi_e + \varphi_o)/2 = \pi/4$ a 2.4 GHz. La aplicación del algoritmo considerando los parámetros del substrato Rogers *RO3010* con constante dieléctrica $\varepsilon_r$ = 10.2 y grosor $h$ = 1.27 mm, brinda los siguientes resultados, $C_{ls}$ = 0.57 pF, $Z_{oe}$ = 152.76 Ω, $Z_{oo}$ = 58.65 Ω, $k_el$ = 26.6º, $k_ol$ = 24.9º, $swr_o$ = 0.68, $\beta_ol$ = 36.9°, y $\beta_el$ = 53.2°. A partir de estos valores, se ha obtenido los parámetros S para el esquemático de cuatro puertos, y a partir de transformaciones conocidas [54], se ha inferido los parámetros S para los modos par e impar. Transformando a parámetros *ABCD*, se ha obtenido la impedancia Bloch y la longitud eléctrica para cada modo. Los resultados se muestran en la Figura 2 de la **publicación C** y demuestra que los valores objetivos se cumplen en buena aproximación.

#### 4.2.1.2 Optimización de la supresión de espurios

El número de celdas $N$ por sección de cada par de líneas acopladas no puede ser arbitrariamente seleccionado. $N$ debe ser determinado a través de un procedimiento sistemático, para garantizar que el primer y un cierto número de bandas espurias del

filtro pasabanda sean eficientemente suprimidas. Consideremos la Figura 3 de la **publicación C**, correspondiente al modelo con elementos discretos. Se asume que la interacción entre ambas líneas es dominado por acoplamiento eléctrico y que la longitud eléctrica de la celda unitaria es pequeña. $L$ y $C$ son la inductancia y capacitancias de la línea, $C_{ls}$ es la capacitancia de los parches cuadrados y $C_c$ es el acoplamiento capacitivo entre las líneas. El modelo para excitación tanto en modo par e impar se muestran también en la Figura 3 de tal artículo.

La longitud eléctrica e impedancias Bloch de los modelos en esquemático en la Figs. 1(c) y (d) y los modelos en elementos discretos en las Figs. 3(b) y (c) convergen a bajas frecuencias (longitudes eléctricas pequeñas) y tienden a divergir a medida que la frecuencia se aproxima a las frecuencias de corte de los modos fundamentales (modos par e impar). Tales frecuencias de corte determinan el inicio de la banda de rechazo para cada modo.

Aunque los pares de líneas acopladas con carga capacitiva (CLCLs) son estructuras dispersivas, si se trabaja suficientemente lejos de la frecuencia de corte, se puede asumir que las impedancias Bloch para los modos par e impar son independientes de la frecuencia, estas son:

$$Z_{Be} = \sqrt{\frac{L}{C + C_{ls}}} \tag{4.16}$$

$$Z_{Bo} = \sqrt{\frac{L}{C + C_{ls} + 2C_c}} \tag{4.17}$$

Similarmente, las longitudes eléctricas (para la celda unitaria) para los modos par e impar pueden ser expresadas como funciones lineales de la frecuencia, dadas por:

$$\varphi_{e,cell} = \beta_e l = \omega\sqrt{L(C + C_{ls})} \tag{4.18}$$

$$\varphi_{o,cell} = \beta_o l = \omega\sqrt{L(C + C_{ls} + 2C_c)} \tag{4.19}$$

En el marco del modelo discreto, para los modos par e impar, la razón de onda lenta para cada modo fundamental están dadas por:

$$swr_e = \frac{k_e l}{\beta_e l} = \frac{\omega\sqrt{LC}}{\omega\sqrt{L(C + C_{ls})}} = \frac{1}{\sqrt{1 + \frac{C_{ls}}{C}}} \tag{4.20}$$

$$swr_o = \frac{k_o l}{\beta_o l} = \frac{\omega\sqrt{L(C+2C_c)}}{\omega\sqrt{L(C+C_{ls}+2C_c)}} = \frac{1}{\sqrt{1+\dfrac{C_{ls}}{C+2C_c}}} \tag{4.21}$$

Para un nivel de acoplamiento bajo ($C >> 2C_c$), las constantes de fase y la razón de onda lenta para ambos modos puede ser considerada como la misma. Consideremos esta aproximación. La expresión (4.15) puede ser escrita como:

$$\varphi\Big|_{f_0} = \frac{\pi}{2N} \tag{4.22}$$

donde $\varphi = \varphi_e = \varphi_o$. Para determinar $N$, se ha de encontrar una relación entre la frecuencia de corte $f_C$ de la estructura CLCL y la frecuencia central del filtro $f_0$. La frecuencia de corte es la frecuencia Bragg dada en (4.5), es decir $f_B = f_C$. Combinando (4.5) y (4.18) se obtiene

$$\varphi\Big|_{f_0} = 2\pi f_0\sqrt{L(C+C_{ls})} = 2\frac{f_0}{f_C} \tag{4.23}$$

Introduciendo (4.22) en (4.23), la razón entre la frecuencia de corte y la frecuencia central del filtro puede ser expresada como:

$$\frac{f_C}{f_0} = \frac{4N}{\pi} \tag{4.24}$$

En filtros pasabanda, la primera banda espuria aparece en $2f_0$. Para la supresión de esa banda es necesario que $f_C < 2f_0$. De acuerdo a la condición anterior y a (4.24) se sigue que el número de celdas unitarias en el par de líneas acopladas, debe satisfacer:

$$N < \frac{\pi}{2} \tag{4.25}$$

El resultado implica que $N = 1$, si el número de celdas unitarias $N \geq 2$ implica que la primer banda espuria no puede ser suficientemente suprimida. Sin embargo no es necesario que el número de celdas unitarias para cada par de líneas acopladas sea el mismo. La expresión (4.25) indica que al menos un par de líneas acopladas debe ser diseñado con una sola celda unitaria. En la práctica, en los filtros presentados en la tesis, se diseña combinando secciones con una y con dos celdas para cada par de líneas acopladas.

Para estimar la capacidad de una sección CLCL para rechazar espurios, se ha de estimar la frecuencia superior de la banda de rechazo, $f_s$, dada en la expresión (4.6). Dividiendo (4.6) entre (4.5) se obtiene:

$$\frac{f_S}{f_C} = \frac{\pi}{2}\sqrt{1+\frac{C_{ls}}{C}} = \frac{\pi}{2}\frac{1}{swr} \tag{4.26}$$

con $swr = swr_e = swr_o$. Introduciendo (4.24) en (4.26) se obtiene:

$$\frac{f_S}{f_0} = \frac{2N}{swr} \tag{4.27}$$

En (4.27) se estima el número de bandas espurias que pueden ser rechazadas. Con $N = 1$ (valor necesario para suprimir el primer espurio) y $swr = 0.5$ (correspondiente a una reducción del 50 %). Con estos valores en la expresión (4.27) se obtiene $f_S = 4f_0$, y así se espera que desde el primer ($2f_0$) hasta el segundo ($3f_0$) espurio sean eficientemente suprimidos. En términos generales con las ecuaciones (4.24) y (4.27) se puede determinar el rango para el cual la estructura CLCL puede suprimir eficientemente los espurios.

### 4.2.2 Optimización de la estructura CLCL mediante ASM

Los filtros pasabanda considerados son implementados como una cascada de secciones CLCL, y se asume que el acoplamiento entre secciones no es significativo, así cada par de líneas acopladas con carga capacitiva es sintetizada independientemente. Además, las dimensiones de los parches capacitivos son optimizadas independientemente usando un sub-proceso ASM de una variable para cada espacio del algoritmo. Éste sub-proceso se explica con detalle en la sección 3.3 y el layout del parche capacitivo se observa en la Fig. 3.3(a). El sub-proceso se visualiza en el diagrama de flujo de la Fig. 3.4. Así, primero se determina las dimensiones del parche y éstas dimensiones no son variables de optimización en el algoritmo ASM de tres variables específicamente desarrollado para obtener el layout del par de líneas acopladas con carga capacitiva. Por conveniencia, designamos al primer algoritmo de una variable como Parche-ASM, y al segundo algoritmo para toda la estructura del par de líneas acopladas con carga capacitiva como CLCL-ASM.

Para el algoritmo CLCL-ASM, las variables en el espacio de validación son el ancho $W$, la separación $S$ y la longitud $d$, del par de líneas acopladas sin carga, como en la

Figura 5 de la **publicación C**. Observe que la longitud $d$ debe satisfacer $d = N \cdot l$. En principio las variables en el espacio grueso deberían ser la impedancia Bloch para los modos par e impar ($Z_{Be}$ y $Z_{Bo}$) y el promedio de la longitud eléctrica de los dos modos a la frecuencia de operación $f_0$. La razón es que los valores objetivos de estas impedancias ($Z_{Be}^*$ y $Z_{Bo}^*$) para cada estructura CLCL están dados por las especificaciones del filtro y también la longitud eléctrica promedio de la estructura CLCL ha de cumplir $\varphi_{av}^* = \pi/2$. Esto es lo típico para filtros pasabanda implementados con pares de líneas acopladas (sin carga capacitiva). Sin embargo para el algoritmo se han considerado diferentes variables de optimización, como se detalla en breve.

Para la figura 5 del **artículo C**, un par de líneas acopladas con carga capacitiva, consideremos el circuito de dos puertos (resultado de dejar dos puertos cruzados en circuito abierto). Se asume que la longitud eléctrica de ambos modos son idénticas ($\varphi = N\varphi_e = N\varphi_o$). Así la impedancia imagen de este circuito está relacionada con $Z_{Be}$, $Z_{Bo}$ y $\varphi$ por [48]:

$$Z_I = \frac{1}{2}\sqrt{(Z_{Be} - Z_{Bo})^2 \csc^2\varphi - (Z_{Be} + Z_{Bo})^2 \cot^2\varphi} \tag{4.28}$$

lo anterior toma su valor máximo cuando $\varphi = \pi/2$

$$Z_{I,\max} = \frac{Z_{Be} - Z_{Bo}}{2} \tag{4.29}$$

Además, la parte real de la impedancia imagen alrededor $\varphi = \pi/2$ está delimitada por una banda con frecuencias de corte, con fases $\varphi_1$ y $\varphi_2$, dadas por

$$\cos\varphi_1 = -\cos\varphi_2 = \frac{Z_{Be} - Z_{Bo}}{Z_{Be} + Z_{Bo}} \tag{4.30}$$

Nótese que a partir de los valores objetivos de $Z_{Be}^*$ y $Z_{Bo}^*$, es posible definir valores objetivos para la impedancia imagen máxima, $Z_{I,max}^*$ y para la fase de la frecuencia de corte inferior $\varphi_1^*$. La impedancia imagen puede ser inferida a partir de la simulación de parámetros S de la estructura de dos puertos y convirtiendo a parámetros ABCD

$$Z_I = \frac{B}{\sqrt{A^2 - 1}} \tag{4.31}$$

A partir de la impedancia imagen, es posible identificar $Z_{I,max}$ y $\varphi_1$. Usando (4.29) y (4.30), $Z_{Be}$ y $Z_{Bo}$ pueden ser extraídas. Sin embargo $Z_{I,max}$ y $\varphi_1$ son las variables de optimización en el espacio grueso.

La fase $\varphi$ del par de líneas acopladas con carga capacitiva está relacionada con la fase de la estructura de dos puertos, $\psi$, por [48].

$$\cos\psi = \frac{Z_{Be} + Z_{Bo}}{Z_{Be} - Z_{Bo}} \cos\varphi \tag{4.32}$$

además

$$\cos\psi = \frac{A + D}{2} = A \tag{4.33}$$

dado que $A = D$ en este caso. A partir de los parámetros S y transformando a parámetros *ABCD*, la fase de la estructura de dos puertos, $\psi$, puede ser inferida. Observe que de acuerdo a (4.32) $\psi = \pi/2$ brinda $\varphi = \pi/2$ y viceversa. Por lo que es posible usar directamente $\psi$ para propósitos de optimización y considerar la frecuencia a la cual $\psi = \pi/2$ ($f_{\pi/2}$) como la tercer variable del espacio grueso. Evidentemente el objetivo será $f_{\pi/2}{}^{*} = f_0$.

Nótese que, forzando $\psi = \pi/2$ no significa que el promedio de las longitudes eléctricas sea estrictamente $\pi/2$ (pero será muy cercano a ese valor). Sin embargo, se ha demostrado que con este procedimiento, el filtro final que consta de la concatenación de varios pares de líneas acopladas con carga capacitiva, provee una respuesta muy cercana a la ideal u objetivo.

Una vez que las tres variables del espacio fino y grueso han sido determinadas, el algoritmo CLCL-ASM es implementado. El primer layout es generado a partir de los valores de $Z_{oe}$, $Z_{oo}$, $Nk_el$, $Nk_ol$ derivados del procedimiento en la sección 4.2.1 y el calculador de línea (*LineCal* de ADS). Las dimensiones de los parches capacitivos son inferidas de un sub-proceso ASM independiente (Parche-ASM). Estas dimensiones para el parche son las consideradas durante todo el algoritmo CLCL-ASM y estas no cambian. A partir del layout inicial, los parámetros del modelo grueso ($Z_{I,max}$, $\varphi_1$, $f_{\pi/2}$) son extraídos y comparados con sus valores objetivos para determinar la primer función error. Luego el nuevo layout del proceso iterativo es inferido a partir de (2.22), con **h** dado por (2.23) y la matriz de Broyden inicial dada por:

$$\mathrm{B}^{(1)} = \begin{pmatrix} \dfrac{\partial Z_{I,\max}}{\partial W} & \dfrac{\partial Z_{I,\max}}{\partial S} & \dfrac{\partial Z_{I,\max}}{\partial d} \\ \dfrac{\partial \varphi_1}{\partial W} & \dfrac{\partial \varphi_1}{\partial S} & \dfrac{\partial \varphi_1}{\partial d} \\ \dfrac{\partial f_{\pi/2}}{\partial W} & \dfrac{\partial f_{\pi/2}}{\partial S} & \dfrac{\partial f_{\pi/2}}{\partial d} \end{pmatrix} \tag{4.34}$$

El proceso es iterado hasta que la convergencia es obtenida. Para los siguientes dos ejemplos el algoritmo termina cuando la siguiente norma del error es menor que el 0.5 %.

$$\left\|\mathrm{f}_{norm}\right\| = \sqrt{\left(\frac{f_{\pi/2}}{f^{*}_{\pi/2}} - 1\right)^2 + \left(\frac{\varphi_1}{\varphi^{*}_1} - 1\right)^2 + \left(\frac{Z_{I,\max}}{Z^{*}_{I,\max}} - 1\right)^2} \tag{4.35}$$

### 4.2.3 Ejemplo 1, Filtro de tercer orden

Hemos generado el layout de un filtro de orden tres constituido por cuatro secciones CLCL, como un primer ejemplo. Se ha considerado una respuesta Chebyshev con frecuencia central $f_0$ = 1.0 GHz, ancho de banda fraccional FBW = 8% y nivel de rizado de $L_{Ar}$ = 0.1 dB. Con estas especificaciones, las impedancias para los pares de líneas acopladas son $Z_{Be}$ = 73.54 Ω y $Z_{Bo}$ = 38.64 Ω para las secciones extremas (pares 1 y 4), y $Z_{Be}$ = 56.44Ω y $Z_{Bo}$ = 44.89 Ω para las secciones 2 y 3. El layout del filtro convencional optimizado, inferido a partir de una versión simplificada del ASM propuesto (éste no tiene parches capacitivos en su estructura) se observa en la Fig. 6(a) de la **publicación C**. Se ha diseñado en un substrato Rogers *RO3010,* con grosor $h$ = 1.27 mm y constante dieléctrica $\varepsilon_r$ = 10.2. Para el filtro convencional la respuesta en frecuencia es mostrada en la Fig. 7 de la publicación C, donde se observa la presencia de las bandas espurias (a $2f_0$ y frecuencias armónicas más altas). Del filtro convencional se observa que cumple las especificaciones de frecuencia central, ancho de banda y nivel de rizado.

Para el diseño del filtro pasabanda, basado en pares de líneas acopladas con carga capacitiva, se ha considerado diseñar con una sola celda para las secciones 2 y 3, en tanto que para las secciones 1 y 4 se ha diseñado con dos pares de parches capacitivos. Con lo anterior, diseñando con una sola celda y con dos celdas es posible asegurar una amplia banda de rechazo. Esto fue mostrado en la sección 4.2.1.2. La razón de onda lenta para el modo par ha sido $swr_e$ = 0.5. Usando las ecuaciones (4.9)-(4.15), es posible determinar los valores para los parches capacitivos y los parámetros eléctricos de los pares de líneas sin carga. Todos estos valores se muestran en la Tabla I de la **publicación C**. Estos valores son los elementos del esquemático de la Fig. 1 de la publicación C usados para determinar el layout inicial para el algoritmo ASM.

Con los valores en la Tabla I, es posible determinar los valores iniciales del espacio fino a través del *LineCal*, (excepto el primer $l_p$ que es obtenido a través de la fórmula del condensador de placas paralelas). Los valores del modelo fino para el layout inicial se muestran en la Tabla II de la **publicación C**.

Una vez que se ha podido determinar el layout inicial, la aplicación del algoritmo Parche-ASM permite determinar las longitudes $l_p$ deseadas para las secciones 1 y 4 y para las secciones 2 y 3. Luego, la aplicación del algoritmo CLCL-ASM provee los pares de líneas acopladas con carga capacitiva optimizados. Para las secciones 1 y 4 diseñadas con dos pares de parches se obtiene la convergencia luego de 5 iteraciones. Para las secciones 2 y 3 diseñadas con solo una celda se obtiene la convergencia luego de 12 iteraciones. Las variables del espacio fino luego de la convergencia se muestran en la Tabla III de la **publicación C**. Las variables del modelo grueso luego de la convergencia se muestran en la Tabla IV de la publicación C.

La Fig. 8 de la publicación C muestra la impedancia imagen y la longitud eléctrica $\psi$ para varias iteraciones de ambas secciones, aquellas diseñadas con una sola celda (secciones 2 y 3) y las diseñadas con dos celdas (secciones 1 y 4). Se puede apreciar como las curvas evolucionan progresivamente hasta que las variables del modelo grueso alcanzan a los valores objetivo. El layout final del filtro diseñado, generado al concatenar los pares óptimos de líneas acopladas con carga capacitiva se muestra en la Fig. 6(b) de la publicación C. Se observa una reducción substancial en comparación al filtro convencional, esto debido al efecto de onda lenta. La simulación electromagnética de este filtro con cargas capacitivas se muestra también en la Fig. 7 de la publicación C. Se puede ver como la respuesta en la región de interés es muy similar a la del filtro convencional, además como las bandas espurias son eficientemente suprimidas hasta frecuencias muy altas. Luego de concatenar las estructuras CLCL optimizadas no es necesario un proceso de post-optimización.

El filtro diseñado ha sido fabricado por la microfresadora *LPKF HF100* y ha sido caracterizado por medio del analizador de red *PNA N5221A* de *Agilent.* La respuesta en frecuencia de la medición se muestra en la Fig. 9(b) de la **publicación C**, donde se compara con la simulación electromagnética con pérdidas. Se puede ver que hay una coincidencia razonable entre ambas respuestas. Para el prototipo fabricado se obtiene un rechazo de las bandas espurias mejor a 30 dB hasta $5f_0$.

#### 4.2.3.1 Método Opcional en base al modelo de elementos discretos para el Ejemplo 1, Filtro de tercer orden

En base al modelo de elementos discretos de la Figura 3 de la **publicación C** es posible determinar las impedancias $Z_{oe}$ y $Z_{oo}$ para el par de líneas sin carga. A partir de las ecuaciones (4.16) y (4.17) y asumiendo que $C >> 2C_c$, se sigue,

$$Z_{Be} = \sqrt{\frac{L}{C}} \cdot \frac{1}{\sqrt{1+\frac{C_{ls}}{C}}} = Z_{oe} \cdot swr \tag{4.36}$$

$$Z_{Bo} = \sqrt{\frac{L}{C+2C_c}} \cdot \frac{1}{\sqrt{1+\frac{C_{ls}}{C+2C_c}}} = Z_{oo} \cdot swr \tag{4.37}$$

así las impedancias para el par de líneas sin carga son $Z_{oe} = Z_{Be}/swr$ y $Z_{oo} = Z_{Bo}/swr$, lo anterior asume que $swr = swr_e = swr_o$. Con las ecuaciones (4.16), (4.18), (4.20) es posible determinar $C_{ls}$ a partir del modelo discreto, dada por

$$C_{ls} = \frac{\varphi_{e,cell}\left(1-swr^2\right)}{\omega \cdot Z_{Be}} \tag{4.38}$$

Para el Ejemplo 1, en las secciones 1 y 4 se determina $Z_{Be}$ = 73.54 Ω y $Z_{Bo}$ = 38.64 Ω, para las secciones 2 y 3 se encuentra $Z_{Be}$ = 56.44 Ω y $Z_{Bo}$ = 44.89 Ω. Si la razón de onda lenta es $swr$ = 0.5, se sigue con el planteamiento anterior que las impedancias de los pares de líneas sin carga han de ser el doble de los valores anteriores. En la Tabla 4.1 se observa los valores de los parámetros eléctricos usados para determinar el layout inicial, de acuerdo a la Fig. 3 de la publicación.

**Tabla 4.1**: Elementos del Esquemático de la Figura 3 del **artículo C** usados para determinar el layout inicial

| Sección | $Z_{oe}$ (Ω) | $Z_{oo}$ (Ω) | $C_{ls}$ (pF) | Longitud Eléctrica sin carga |
|---|---|---|---|---|
| 1,4 | 147.08 | 77.27 | 1.275 | 45° |
| 2,3 | 112.88 | 89.78 | 3.322 | 45° |

Con los valores anteriores y con los parámetros del substrato, es posible inferir las variables iniciales para el modelo fino a través del *LineCal*, excepto $l_p$ que viene determinada a través de la fórmula del condensador de placas paralelas, estos valores se observan en la Tabla 4.2.

**Tabla 4.2**: Elementos del espacio fino para el layout inicial, método elementos discretos

| Sección | $W$(mm) | $S$(mm) | $d$(mm) | $l_p$ (mm) |
|---|---|---|---|---|
| 1,4 | 0.0981 | 0.4406 | 15.238 | 4.234 |
| 2,3 | 0.1469 | 1.4826 | 15.055 | 6.835 |

Con el layout inicial determinado, la aplicación del algoritmo Parche-ASM provee una longitud $l_p$ = 3.394 mm para la secciones 1 y 4, y $l_p$ = 5.730 mm para las secciones 2 y 3. La aplicación del algoritmo CLCL-ASM provee el layout final del filtro luego de 24 iteraciones para las secciones 2 y 3, y luego de 29 iteraciones para las secciones 1 y 4.

En comparación con el método basado en elementos semi-discretos, la convergencia es más lenta con el método de elementos discretos y las curvas del error mejoran significativamente con el método del modelo semi-discreto. Para las secciones 2 y 3, el método de elementos discretos inicia con un error del 66.3%, en tanto que con el método de elementos semi-discretos el error inicia en 16.2%. Para las secciones 1 y 4, con el método de elementos discretos el error inicia en 33.5%, con el método semi-discreto el error inicia en 5.6 %. Ciertamente la convergencia es mejor con el método de elementos semi-discretos.

Las variables de cada espacio (fino y grueso) luego de la convergencia se muestran en las tablas 4.3 y 4.4 respectivamente.

**Tabla 4.3**: Elementos del espacio fino, luego de la convergencia, método elementos discretos

| Sección | $W$(mm) | $S$(mm) | $d$(mm) | $l_p$ (mm) |
|---|---|---|---|---|
| 1,4 | 0.1872 | 0.2014 | 18.499 | 3.394 |
| 2,3 | 0.1462 | 0.3091 | 15.457 | 5.730 |

**Tabla 4.4**: Elementos espacio grueso, luego de la convergencia, método elementos discretos

| Sección | $Z_{I,max}(\Omega)$ | $\varphi_1$ | $f_{\pi/2}$ (GHz) | $C_{ls}$ (pF) |
|---|---|---|---|---|
| 1,4 | 17.429 | 1.260 | 1.000 | 1.298 |
| 2,3 | 5.789 | 1.453 | 1.000 | 3.335 |

El layout final del filtro diseñado con el método de elementos discretos se observa en la figura 4.7, simplemente al concatenar las secciones sintetizadas de forma automática. Se compara con el filtro convencional optimizado con el algoritmo CLCL-ASM (sin el parche).

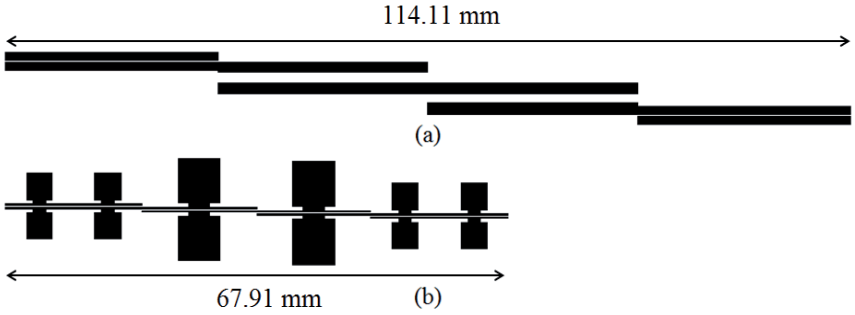


**Figura 4.7**. Layout de ambos filtros, convencional (a) y con carga capacitiva diseñado con el método de elementos discretos (b), para Ejemplo 1. Las dimensiones se indican.

Se observa en la Fig. 4.7 una reducción significativa (del 59%) en la longitud del filtro con estructuras CLCL, debido al efecto de onda lenta. También el método de elementos discretos provee un filtro aún más reducido que el que se obtiene con el método de elementos semi-discretos en la Figura 6 de la **publicación C**. Esto se debe a que el método de elementos discretos estima capacitancias mayores para los parches capacitivos de las secciones 2 y 3, resultando en un filtro de longitud menor.

La simulación electromagnética del filtro pasabanda con estructuras CLCL a partir del modelo discreto se observa en la Figura 4.8(b), donde se compara con el filtro convencional optimizado y el esquemático ideal. Se observa como las bandas espurias son eficientemente suprimidas, el rechazo de las bandas es mejor a 40 dB hasta 5 GHz. Se muestra además el detalle en la banda de interés en la Fig. 4.8(a), en ésta se compara el filtro-CLCL con el esquemático ideal y se observa la gran similitud en la región de interés.

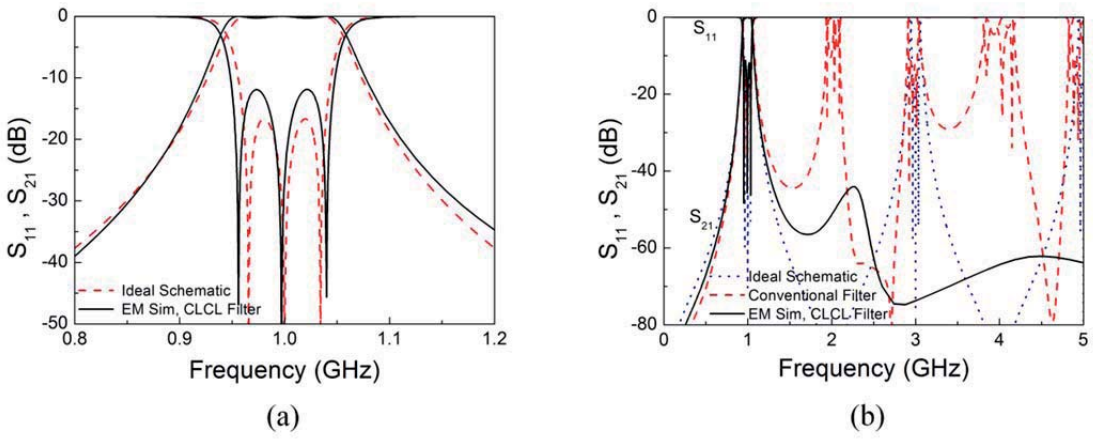


**Figura 4.8**. Respuesta electromagnética del filtro-CLCL a partir de modelo discreto. (a) Detalle de la banda (b) Respuesta electromagnética hasta frecuencias altas.

### 4.2.4 Ejemplo 2, Filtro de quinto orden

Para demostrar el potencial del método propuesto basado en optimización por ASM, un segundo ejemplo es considerado. Específicamente, un filtro pasabanda Chebyshev de orden 5, constituido por seis secciones CLCL optimizadas. El filtro tiene las siguientes especificaciones: $f_0$ = 1.8 GHz, $FBW$ = 8% y nivel de rizado $L_{Ar}$ = 0.1 dB. De acuerdo a las especificaciones las impedancias son $Z_{Be}$ = 72.03 Ω y $Z_{Bo}$ = 38.93 Ω para los pares de líneas de las secciones 1 y 6, $Z_{Be}$ = 55.51 Ω y $Z_{Bo}$ = 45.49 Ω para las secciones 2 y 5, y $Z_{Be}$ = 54.11 Ω y $Z_{Bo}$ = 46.47 Ω para los pares de líneas de las secciones 3 y 4. El layout del filtro final es generado en un substrato *RO3010* con grosor $h$ = 1.27 mm y constante dieléctrica $\varepsilon_r$ = 10.2. Se realiza una comparación entre el filtro final con pares de líneas acopladas con carga capacitiva y el filtro convencional en la Figura 11 de la **publicación C**, las simulaciones son sin pérdidas. Se puede observar que hay una muy buena coincidencia en las respuestas en la región de interés ya sea de frecuencia central, ancho de banda y nivel de rizado, pero además de esto se muestra la capacidad del filtro-CLCL para suprimir espurios.

Para diseñar el filtro-CLCL pasabanda de orden 5, se ha considerado una celda para las secciones 2, 3, 4 y 5, y para las secciones 1 y 6 se ha considerado dos pares de parches capacitivos. Además diseñar con una y dos celdas cada sección posibilita el suprimir los espurios eficientemente como fue demostrado en la sección 4.2.1.2. Este ejemplo toma $swr_e$ = 0.5 para cada sección. Con este valor y resolviendo (4.9)-(4.15) es posible determinar las capacitancias de los parches y los parámetros eléctricos de los pares de líneas acopladas sin carga. Estos valores se muestran en la Tabla V de la **publicación C**. Con estos valores es posible determinar los elementos del modelo fino para el layout inicial, estos se muestran en la Tabla VI de la publicación C.

Las variables del modelo fino ($W$, $S$, $d$, $l_p$) luego de la convergencia se muestran en la Tabla VII de la **publicación C**. Las variables del modelo grueso ($Z_{Imax}$, $\varphi_1$, $f_{\pi/2}$ y $C_{ls}$) luego de la convergencia se muestran en la Tabla VIII de la publicación. Se muestra el prototipo diseñado en la Fig. 12(a) de la publicación. En la Fig. 12(b) del artículo C se puede observar una coincidencia razonable entre la medición del prototipo y la simulación electromagnética del filtro-CLCL con pérdidas. El rechazo de bandas espurias es mejor a 45 dB hasta $4f_0$.

La figura 4.9 muestra el detalle en la banda de interés, para las simulaciones electromagnéticas del filtro convencional optimizado y para el filtro-CLCL. El filtro convencional tiene una longitud total de 93.64 mm y el filtro-CLCL tiene una longitud total de 65.71 mm. El filtro-CLCL se miniaturiza en un factor del 70% comparado con el filtro convencional.

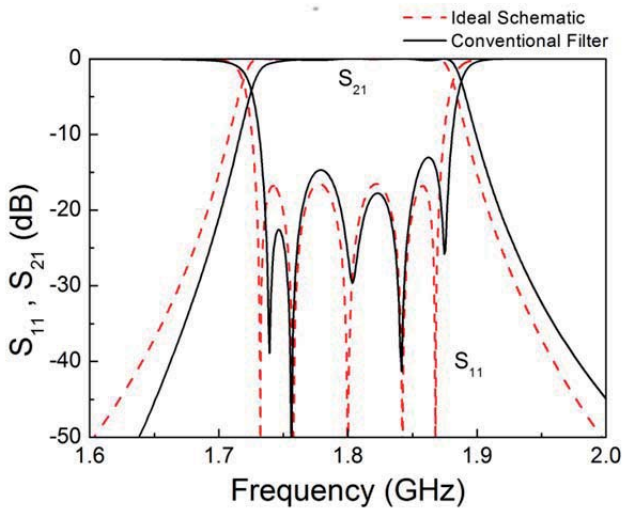


(a)

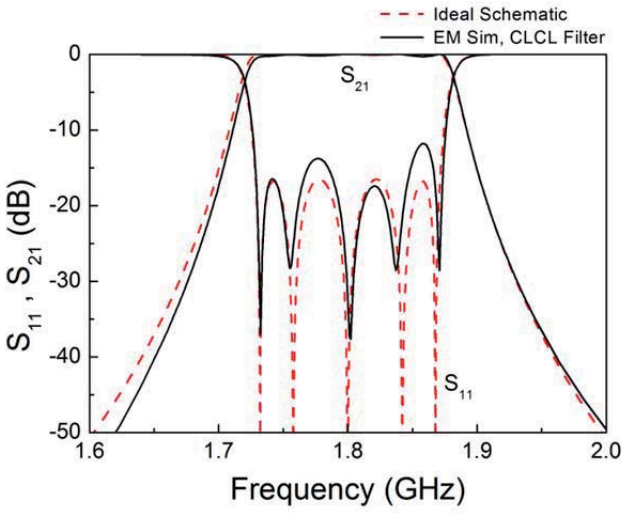


(b)

**Figura 4.9**. Respuesta del filtro convencional en la región de interés (a) respuesta del filtro-CLCL en la región de interés (b). Ambas respuestas electromagnéticas se comparan con el esquemático ideal.

## 4.3 Conclusiones

En resumen, en la sección 4.1 se pudo demostrar que la optimización por ASM de estructuras de onda lenta estudiadas en el capítulo 3 puede ser aplicada a la síntesis de filtros pasabanda de banda ancha basados en estructuras EBG con carga capacitiva. Gracias al efecto de onda lenta de estas líneas artificiales con carga capacitiva el filtro puede ser miniaturizado significativamente. Además el filtro es libre del primer espurio debido a las propiedades de reflexión de las líneas cargadas con EBG.

A la vez en la sección 4.2 se pudo demostrar que secciones de pares de líneas acopladas con carga capacitiva (estructuras CLCL) son elementos prometedores para la reducción del tamaño de filtros pasabanda y para la supresión de espurios hasta frecuencias altas. Se demostró una metodología basada en el análisis de los modos par e impar para estas estructuras. Luego un proceso ASM de tres variables fue desarrollado para obtener el layout final que cumple las especificaciones del filtro. Los dos ejemplos que se presentaron tienen una reducción de aproximadamente el 30% de la longitud total y además tienen una amplia banda de rechazo hasta varios armónicos.

# 5

# Conclusiones

La tesis es una contribución a las líneas de transmisión de onda lenta basadas en EBGs con carga capacitiva. El **Capítulo 2** presentó una introducción al estado del arte de las líneas de transmisión de onda lenta, y además se presentó el método de la matriz de transferencia para estructuras periódicas y una introducción a los algoritmos de Mapeo Espacial, con los que hemos sintetizado de forma automatizada las estructuras de esta tesis, en particular usamos el método ASM (*Aggressive Space Mapping*).

Del **Capítulo 3** se concluye que fue posible desarrollar un algoritmo de optimización para la síntesis de líneas de transmisión de onda lenta constituidas por una línea microstrip cargada con parches capacitivos. Se desarrolló un algoritmo de dos pasos, donde el primer paso determina el esquemático óptimo a partir de las especificaciones. El segundo paso, con dos sub-procesos ASM independientes, provee el layout de la estructura de onda lenta a partir de la celda esquemática óptima. Se presentaron cuatro ejemplos para demostrar el potencial del método de síntesis propuesto. El layout de la estructura es determinado a partir de las especificaciones de una forma desatendida. El primer ASM determina el esquemático ideal a partir de las especificaciones, impedancia Bloch, longitud eléctrica y razón de onda lenta. Luego el segundo ASM determina el layout de la estructura de onda lenta a partir del esquemático ideal.

Este trabajo es muy fundamental y abre posibilidades de formas de aplicarlo, donde se sustituye a líneas de transmisión ordinarias con una impedancia característica y longitud eléctrica determinada por su equivalente en estructura de onda lenta (línea de transmisión artificial), pero siendo ésta de dimensiones menores.

Del **Capítulo 4** en la **sección 4.1** se pudo demostrar que la optimización por ASM de estructuras de onda lenta estudiadas en el capítulo 3 puede ser aplicada a la síntesis de filtros pasabanda de banda ancha basados en estructuras EBG con carga capacitiva. Para

ésta aplicación fue importante determinar la frecuencia Bragg en función de la cantidad de celdas unitarias de onda lenta concatenadas. El incorporar estas líneas artificiales con estructuras EBG con carga capacitiva produce que el filtro pasabanda pueda ser miniaturizado significativamente. Además el filtro es libre de espurios puesto que la concatenación de tres celdas de onda lenta exhibe una amplia banda de rechazo. En los tres ejemplos presentados se logró una gran coincidencia en los ceros de reflexión debido a que las secciones de línea para el filtro con EBG tiene las mismas características de banda para la frecuencia de corte inferior que el filtro canónico, y el ancho de banda se conserva al sustituir la línea de transmisión ordinaria con líneas de transmisión con EBG.

En la **sección 4.2**, se pudo demostrar un proceso de síntesis mediante ASM para filtros pasabanda basados en pares de líneas acopladas con carga capacitiva (CLCL). Comparados con sus filtros convencionales, los filtros propuestos son más pequeños y libres de espurios hasta frecuencias altas (hasta el cuarto o quinto armónico), debido al efecto de onda lenta y a las bandas de rechazo que aparecen debido a la periodicidad. Se propuso un método de diseño a partir del análisis para los modos par e impar de la estructura CLCL a nivel de esquemático que permite obtener el layout inicial. Específicamente a partir de las especificaciones del filtro se determina las impedancias características par e impar y longitudes eléctricas para los pares de líneas sin carga que permite obtener el layout inicial, el cual es inferido a través del *LineCal* (calculador de líneas de transmisión de *Keysight ADS*). Para suprimir eficientemente los espurios el número de celdas para cada par de líneas acopladas no puede ser arbitrario. En los ejemplos reportados se trabaja con una y con dos celdas para cada estructura CLCL lo cual permite suprimir a partir del primer espurio. Se pudo desarrollar un algoritmo ASM de tres variables para determinar el layout óptimo de la estructura CLCL. Se pudo sintetizar dos filtros pasabanda, uno de tercer orden y otro de quinto orden que demuestran la eficacia del algoritmo, totalmente desatendido. Se optimizó cada estructura CLCL por separado y luego se concatenaron las estructuras CLCL, no siendo necesario un proceso de post-optimización. El filtro final satisface las especificaciones.

Como conclusión general se ha iniciado una línea de investigación sobre líneas de transmisión de onda lenta basadas en EBGs con carga capacitiva. Se pudo encontrar aplicaciones a estas estructuras, al desarrollo de diferentes tipos de filtros de microondas, y se ha demostrado que es posible aplicar estas estructuras a la miniaturización de circuitos de microondas y al diseño de circuitos de microondas libres de bandas espurias por el conocido efecto Bragg de estructuras periódicas.

# Referencias


[1] E. Yablonovitch, “Photonic band gap structures”, *J. Opt. Soc. Amer. B* 10, pp. 283-295, 1993.

[2] J. D. Joannopoulos, R. D. Meade, and J. N. Winn, *Photonic Crystals: Molding the Flow of Light*, Princeton, NJ, Princeton University Press, 1995.

[3] Y. Qian, V. Radistic and T. Itoh, “Simulation and experiment of photonic band-gap structures for microstrip circuits”, *Proc. Asia-Pacific Microwave Conf.*, Hong Kong, Dec. 1997, pp. 585-588.

[4] M. J. Erro, M. A. G. Laso, T. Lopetegi, D. Benito, M. J. Garde, and M. Sorolla, “Optimization of tapered bragg reflectors in microstrip technology,” *Int. J. Infrared Millimeter Waves*, vol. 21, pp. 231- 245, 2000.

[5] M. A. G. Laso, T. Lopetegi, M. J. Erro, D. Benito, M. J. Garde and Mario Sorolla, “Novel wideband photonic bandgap microstrip structures”, *Microw. Opt. Techn. Lett.*, vol. 24, pp. 357-360, 2000.

[6] F. Falcone, T. Lopetegi, M. Irisarri, M. A. G. Laso, M. J. Erro, and M. Sorolla, "Compact photonic bandgap microstrip structures", *Microw. Opt. Techn. Lett.*, vol 23, pp. 233-236, 1999.

[7] M. A. G. Laso, T. Lopetegi, M. J. Erro, D. Benito, M. J. Garde, and M. Sorolla, “Multiple-frequency-tuned photonic bandgap microstrip structures”, *IEEE Microw. Guided Wave Lett.*, vol. 10, pp. 220-222, 2000.

[8] T. Lopetegi, F. Falcone, and M. Sorolla, “Bragg reflectors and resonators in microstrip technology based on electromagnetic crystal structures”, *Int. J. Infrared Millimeter Waves*, vol. 20, pp. 1091-1102, 1999.

[9] T-Y. Yun, K. Chang, “Uniplanar one-dimensional photonic-bandgap structures and resonators”, *IEEE Trans. Microw. Theory Tech.*, vol. 49, pp. 549-553, 2001.

[10] T. Lopetegi, M.A.G. Laso, J. Hernández, M. Bacaicoa, D. Benito, M.J. Garde, M. Sorolla and M. Guglielmi, “New microstrip wiggly-line filters with spurious passband suppression”, *IEEE Trans. Microw. Theory Tech*., vol. 49, pp 1593-1598, 2001.

[11] T. Lopetegi, M.A.G. Laso, F. Falcone, F. Martín, J. Bonache, L. Pérez-Cuevas, M. Sorolla, "Microstrip wiggly line band pass filters with multispurious rejection", *IEEE Microw. Wireless Compon. Lett.*, vol. 14, pp. 531-533, 2004.

[12] F. Martín, F. Falcone, J. Bonache, T. Lopetegi, M.A.G. Laso, M. Sorolla, "New periodic-loaded electromagnetic bandgap coplanar waveguide with complete spurious passband suppression", *IEEE Microw. Wireless Compon. Lett*., vol. 12, pp. 435-437, 2002.

[13] F. Martín, J. Bonache, I. Gil, F. Falcone, T. Lopetegi, M.A.G,. Laso and M. Sorolla, "Compact spurious free CPW band pass filters based on electromagnetic bandgap structures", *Microw. Opt. Techn. Lett*, vol. 40, pp. 146-148, 2004.

[14] F. Martín, F. Falcone, J. Bonache, M.A.G. Laso, T. Lopetegi, M. Sorolla, "Dual electromagnetic bandgap CPW structures for filter applications", *IEEE Microw. Wireless Compon. Lett.*, vol. 13, pp. 393-395, 2003.

[15] V. Radisic, Y. Qian, and T. Itoh, "Broad-band power amplifier using dielectric photonic bandgap structure", *IEEE Microw. Guided Wave Lett.*, vol. 8, pp. 13-14, 1998.

[16] C. Y. Hang, V. Radisic, Y. Qian, and T. Itoh, "High efficiency power amplifier with novel PBG ground plane for harmonic tuning", *IEEE MTT-S Int. Microw. Symp. Dig*., Anaheim, CA, June 1999, pp. 807-810.

[17] F. R. Yang, Y. Qian, and T. Itoh, "A novel uniplanar compact PBG structure for filter and mixer applications", *IEEE MTT-S Int. Microw. Symp. Dig*., Anaheim, CA, June 1999, pp. 919-922.

[18] Q. Xue, K. M. Shum, and C. H. Chan, "Novel oscillator incorporating a compact microstrip resonant cell", *IEEE Microw. Wireless Compon. Lett.*, vol. 11, pp. 202-204, 2001.

[19] Y. T. Lee, J. S. Lim, J. S. Park, D. Ahn, and S. Nam, "A novel phase noise reduction technique in oscillators using defected ground structure", *IEEE Microw. Wireless Compon. Lett.*, vol. 12, pp. 39-41, 2002.

[20] F. Martín, *Artificial Transmission Lines for RF and Microwave Applications*, John Wiley, Hoboken, NJ, 2015.

[21] A. Görür, "A novel coplanar slow-wave structure," *IEEE Microw. Guided Wave Lett*., vol. 4, pp. 86–88, 1994.

[22] A. Görür, C. Karpuz and M. Alkan, "Characteristics of periodically loaded CPW structures", *IEEE Microw. Guided Wave Lett.*, vol. 8, pp. 278-280, 1998.

[23] J. Sor, Y. Qian, and T. Itoh, "Miniature low-loss CPW periodic structures for filter applications", *IEEE Trans. Microw. Theory Tech.*, vol. 49, pp. 2336-2341, 2001.

[24] D. Nesic, "A new type of slow-wave 1-D PBG microstrip structure without etching in the ground plane for filter and other applications", *Microw. Opt. Techn. Lett.*, vol. 33, pp. 440-443, 2002.

[25] F. Martín, F. Falcone, J. Bonache, M.A.G. Laso, T. Lopetegi, M. Sorolla, “New CPW low pass filter based on a slow wave structure”, *Microw. Opt. Techn. Lett*., vol. 38, pp. 190-193, 2003.

[26] D. Kaddour, H. Issa, A.-L. Franc, N. Corrao, E. Pistono, F. Podevin, J.-M. Fournier, J.-M. Duchamp, and P. Ferrari, "High-Q slow-wave coplanar transmission lines on 0.35-µm CMOS process*", IEEE Microw. Wireless Compon. Lett*., vol. 19, pp. 542-544, 2009.

[27] A.-L. Franc, D. Kaddour, H. Issa, E. Pistono, N. Corrao, J.-M. Fournier and P. Ferrari, "Impact of technology dispersion on slow-wave high performance shielded CPW transmission lines characteristics", *Microw. Opt. Techn. Lett.*, vol. 52, pp. 2786, 2789, 2010.

[28] M. Abdel Aziz, H. Issa, D. Kaddour, F. Podevin, A.M.E. Safwat, E. Pistono, J.-M. Duchamp, A. Vilcot, J.-M. Fournier, and P. Ferrari, "Slow-wave high-Q coplanar striplines in CMOS technology and their RLCG model", *Microw. Opt. Techn. Lett.*, vol. 54, pp. 650-654, 2012.

[29] M. Orellana, J. Selga, M. Sans, A. Rodríguez, V. Boria, F.Martín, "Synthesis of slow-wave structures based on capacitive-loaded lines through aggressive space mapping (ASM)", *International Journal of RF and Microwave Computer-Aided Engineering*, vol. 25, pp. 629-638, September 2015.

[30] F. Martín, J. Bonache, M. Durán-Sindreu, J. Naqui, F. Paredes, G. Zamora, “Artificial transmission lines”, in Wiley Encyclopedia of Electrical and Electronic Engineering, July 2012.

[31] S.G. Mao and M.Y. Chen, “A novel periodic electromagnetic bandgap structure for finite-width conductor-backed coplanar waveguides”, *IEEE Microwave and Wireless Components Lett.*, vol 11, pp. 261–263, 2001.

[32] J. García-García, J. Bonache and F. Martín, “Application of electromagnetic bandgaps (EBGs) to the design of ultra wide band pass filters (UWBPFs) with good out-of-band performance”, *IEEE Transactions on Microwave Theory and Techniques*, vol. 54, pp. 4136 - 4140, Dec. 2006.

[33] J.W. Bandler, R.M. Biernacki, S.H. Chen, P.A. Grobelny and R.H. Hemmers, “Space mapping technique for electromagnetic optimization”, *IEEE Transactions on Microwave Theory and Techniques*, vol. 42, pp. 2536-2544, Dec. 1994.

[34] J.W. Bandler, R.M. Biernacki, S.H. Chen, R.H. Hemmers, and K. Madsen, “Electromagnetic optimization exploiting aggressive space mapping”, *IEEE Transactions on Microwave Theory and Techniques*, vol. 43, pp. 2874-2882, Dec. 1995.

[35] S. Koziel, Q.S. Cheng, J.W. Bandler, “Space mapping”, *IEEE Microwave Magazine*, vol. 9, pp. 105-122, Dec. 2008.

[36] S. Koziel and J.W. Bandler, “Space-mapping optimization with adaptive surrogate model”, *IEEE Transactions on Microwave Theory and Techniques*, vol. 55, pp. 541-546, March 2007.

[37] S. Koziel, Q.S. Cheng and J.W. Bandler, “Improving efficiency of space mapping optimization of microwave structures and devices”, *IEEE MTT-S International Microwave Symposium Digest*, pp. 1995-1998, 3-8 June 2007, Honolulu, HI, (USA).

[38] S. Koziel, J.W. Bandler and Q.S. Cheng, “Robust trust-region space-mapping algorithms for microwave design optimization”, *IEEE Transactions on Microwave Theory and Techniques*, vol. 58, pp. 2166-2174, Aug. 2010.

[39] Q.S Cheng, J.W. Bandler, N. K. Nikolova and S. Koziel, “Fast space mapping modeling with adjoint sensitivity”, *IEEE MTT-S International Microwave Symposium Digest*, pp. 1-4, 5-10 June 2011, Baltimore, MD, (USA).

[40] L. J. Rogla, J. E. Rayas-Sanchez, V. E. Boria, and J. Carbonell, "EM-Based Space Mapping Optimization of Left-handed Coplanar Waveguide Filters with Split Ring Resonators", *IEEE MTT-S International Microwave Symposium Digest*, pp. 111-114, 3-8 June 2007.

[41] P. J. Bradley, "Robust surrogate-based optimization of planar metamaterial structures", *IEEE International Conference on Wireless Information Technology and Systems*, pp. 1-4, 11-16 Nov. 2012.

[42] P. J. Bradley, "Quasi-newton model-trust region approach to surrogate-based optimisation of planar metamaterial structures", *Progress In Electromagnetics Research B*, vol. 47, pp. 1-17, 2013.

[43] J. Selga, A. Rodríguez, V.E. Boria, and F. Martín, “Synthesis of split rings based artificial transmission lines through a new two-step, fast converging, and robust aggressive space mapping (ASM) algorithm”, *IEEE Transactions on Microwave Theory and Techniques*, vol. 61(6), pp. 2295-2308, June 2013.

[44] J. Selga, A. Rodríguez, J. Naqui, M. Durán-Sindreu, V.E. Boria and F. Martín, “Application of aggressive space mapping (ASM) to the efficient synthesis of stepped impedance resonators (SIRs)”, *European Microwave Conference*, Nuremberg (Germany), 2013.

[45] J. Selga, M. Sans, A. Rodríguez, J. Bonache, V. Boria, F. Martín, “Automated synthesis of planar wideband bandpass filters based on stepped impedance resonators (SIRs) and shunt stubs through aggressive space mapping (ASM)”, *IEEE MTT-S International Microwave Symposium Digest*, pp. 1-4, 1-6 June 2014, Tampa, FL (USA).

[46] M. Sans, J. Selga, A. Rodríguez, J. Bonache, V.E. Boria, and F. Martín, “Design of planar wideband bandpass filters from specifications using a two-step aggressive space mapping (ASM) optimization algorithm”, *IEEE Transactions on Microwave Theory and Techniques*, vol. 62, pp. 3341-3350, Dec. 2014.

[47] C. G. Broyden, "A Class of Methods for Solving Nonlinear Simultaneous Equations", *Mathematics of Computation*, vol. 19, no. 92, pp. 577-593, Oct. 1965.

[48] D.M. Pozar, *Microwave engineering*, Addison Wesley, 1990.

[49] R. Marqués, F. Martín, and M. Sorolla. *Metamaterials with negative parameters: Theory, design and microwave applications*, Wiley, 2008.

[50] R. Levy, "A new class of distributed prototype filters with applications to mixed lumped/distributed component design", *IEEE Trans. Microw. Theory Tech*., vol. 18, pp. 1064-1071, 1970.

[51] J.S Hong, M.L Lancaster, *Microstrip Filters for RF/Microwave Applications*, New York, John Wiley, 2001

[52] T. LaRocca, J.Y.C Liu, and M.C.F. Chang, "60 GHz CMOS amplifiers using transformer-coupling and artificial dielectric differential transmission lines for compact design", *IEEE J. Solid-State Circuits*, vol. 44, pp. 1425-1435, 2009.

[53] J.J. Lee and C. S. Park, "A slow-wave microstrip line with a high-Q and a high dielectric constant for millimeter-wave CMOS applications", *IEEE Microw. Wireless Compon. Lett.*, vol. 20, pp.381-383, 2010.

[54] W.R. Eisenstadt, *Microwave Differential Circuit Design Using Mixed-Mode S-parameters*, Artech House, Norwood, MA, 2006.

[55] J. Selga, *"Synthesis of Microwave Circuits Based on Metamaterials using Aggressive Space Mapping Algorithms"*. Tesis Doctoral, Universitat Autònoma de Barcelona, Departamento de Ingeniería Electrónica, 2013.

# Anexo A

## Matlab y Agilent Momentum

El objetivo de éste Anexo es describir de forma general cómo el programa *Matlab* interacciona con el simulador electromagnético *Agilent Momentum* para resolver los problemas de optimización de circuitos de microondas [55].

El *Agilent Momentum* utiliza un conjunto de archivos donde se encuentra toda la información del layout y de la simulación electromagnética. El objetivo general de los programas realizados es que *Matlab* pueda controlar un simulador electromagnético y transferir la información de los resultados de las simulaciones al algoritmo ASM. *Matlab* ejecuta un algoritmo ASM y necesita llamar constantemente al simulador electromagnético. Para ejecutar una simulación electromagnética el *Agilent Momentum* necesita ciertos archivos de datos con la información de coordenadas del layout, parámetros de substrato, opciones de la simulación y características de mallado. *Matlab* crea archivos de datos desde un programa principal, entre los principales:

- El archivo de estímulo *.sti* determina el tipo de simulación que se ejecutará (lineal, adaptativa, puntos singulares), también determina el rango de frecuencia.
- El archivo de tecnología *.tch* proporciona al simulador los parámetros del substrato como la constante dieléctrica y el grosor del substrato.
- El archivo de opciones de simulación *.opt* proporciona los parámetros de mallado. También indica la ruta donde se almacenarán los resultados de la simulación en archivos *ds.txt*.
- El archivo *.proj* donde se encuentran las coordenadas del layout generado u optimizado.

Durante todo el algoritmo es importante definir un layout con las coordenadas a través de las variables geométricas del vector del espacio fino $\mathbf{x_f}$. Una vez se crea el layout *Matlab* llama al simulador electromagnético y crea un archivo de datos con los resultados de la simulación. Una vez la simulación ha sido realizada *Matlab* debe leer los resultados de la simulación en el archivo "*ds.txt*". Esta tarea es realizada por la función *READ_DS* la cual lee el archivo de datos y obtiene la matriz de parámetros S y también la magnitud y la fase, para un sistema de dos puertos obtiene $mag(S_{11})$, $mag(S_{21})$, $ph(S_{11})$ y $ph(S_{21})$.

Finalmente, los programas en *Matlab* infieren los parámetros del modelo grueso, a través de un método de extracción de parámetros directo, que es particular para cada topología. Se calculan los parámetros del modelo grueso $\mathbf{x_c}$, a través de la respuesta en parámetros S y mediante ecuaciones en frecuencias singulares. Cada programa principal consta de una función para extraer parámetros.

# Publicaciones del Autor

## Revistas Internacionales

**M. Orellana**, J. Selga, P. Vélez, M. Sans, A. Rodríguez, J. Bonache, V. Boria, F. Martín,"*Design of Capacitively-Loaded Coupled Line Bandpass Filters with Compact Size and Spurious Suppression"*, **IEEE Transactions on Microwave Theory and Techniques**, (*Enviado*)

**M. Orellana**, J. Selga, P. Vélez, M. Sans, A. Rodríguez, V. Boria, F. Martín, *"Automated synthesis of wideband bandpass filters based on slow-wave EBG structures"*, **Computers, Materials & Continua**, (*Aceptado*)

**M. Orellana**, J. Selga, M. Sans, A. Rodríguez, V. Boria, F.Martín, "*Synthesis of slow-wave structures based on capacitive-loaded lines through aggressive space mapping (ASM)*", **International Journal of RF and Microwave Computer-Aided Engineering**, vol. 25, pp. 629-638, September 2015.

J. Selga, A. Rodríguez, **M. Orellana**, V. Boria, F. Martín, "*Automated synthesis of transmission lines loaded with complementary split ring resonators (CSRRs) and open complementary split ring resonators (OCSRRs) through aggressive space mapping (ASM)*", **Applied Physics A**, Volume 117, Issue 2, pp 557-565, November 2014.

## Congresos Internacionales

Jordi Selga, Paris Vélez, **Marco Orellana**, Jordi Bonache, Ferran Martín, "*Recent Advances in the Design of Compact Microwave Components Based on Reactively-Loaded Transmission Lines"*, IEEE MTT-S **Latin America Microwave Conference,** Puerto Vallarta, México, 12-14 December, 2016 (*Enviado*)

Jordi Selga, Paris Vélez, **Marco Orellana**, Marc Sans, Ana Rodriguez, Vicente Boria, Ferran Martín, *"Size Reduction and Spurious Suppression in Microstrip Coupled Line Bandpass Filters by means of Capacitive Electromagnetic Bandgaps"*, 2016 IEEE MTT-S **International Microwave Symposium (IMS),** San Francisco, 22-27 May, 2016.

**Marco Orellana**, Jordi Selga, Paris Vélez, Marc Sans, Ana Rodríguez, Vicente Boria, Ferran Martín, "*Application of Aggressive Space Mapping (ASM) Optimization to the Design of Electromagnetic Bandgap (EBG) based Wideband Microwave Bandpass Filters*", **First International Workshop on Metamaterials by Design, Theory, Methods, and Applications to Communications and Sensing**, Paris Saclay, 2-3 December, 2015.

Jordi Selga, Ana Rodríguez, **Marco Orellana**, Vicente Boria, Ferran Martín, *"Automated Synthesis of Transmission Lines Loaded with Complementary Split Ring Resonators (CSRRs) through Aggressive Space Mapping "*, **Meta '14, 5th International Conference on Metamaterials, Photonic Crystals and Plasmonics**, Singapore, 20-23 May, 2014.

# Relación de artículos

## Relación de artículos para presentar la tesis por compendio de publicaciones

### Fundamentales

#### Artículo A:

**M. Orellana**, J. Selga, M. Sans, A. Rodríguez, V. Boria, F.Martín, "*Synthesis of slow-wave structures based on capacitive-loaded lines through aggressive space mapping (ASM)*", **International Journal of RF and Microwave Computer-Aided Engineering**, vol. 25, pp. 629-638, September 2015

#### Artículo B:

**M. Orellana**, J. Selga, P. Vélez, M. Sans, A. Rodríguez, V. Boria, F. Martín, *"Automated synthesis of wideband bandpass filters based on slow-wave EBG structures"*, **Computers, Materials & Continua**, *(Aceptado)*

### No Fundamentales

#### Artículo C:

**M. Orellana**, J. Selga, P. Vélez, M. Sans, A. Rodríguez, J. Bonache, V. Boria, F. Martín,"*Design of Capacitively-Loaded Coupled Line Bandpass Filters with Compact Size and Spurious Suppression"*, **IEEE Transactions on Microwave Theory and Techniques**, (*Enviado*)

#### Artículo D:

**Marco Orellana**, Jordi Selga, Paris Vélez, Marc Sans, Ana Rodríguez, Vicente Boria, Ferran Martín, "*Application of Aggressive Space Mapping (ASM) Optimization to the Design of Electromagnetic Bandgap (EBG) based Wideband Microwave Bandpass Filters*", **First International Workshop on Metamaterials by Design, Theory, Methods, and Applications to Communications and Sensing**, Paris Saclay, 2-3 December, 2015.

#### Artículo E:

Jordi Selga, Paris Vélez, **Marco Orellana**, Marc Sans, Ana Rodriguez, Vicente Boria, Ferran Martín, *"Size Reduction and Spurious Suppression in Microstrip Coupled Line Bandpass Filters by means of Capacitive Electromagnetic Bandgaps"*, 2016 IEEE MTT-S **International Microwave Symposium (IMS),** San Francisco, 22-27 May, 2016.

# Publicaciones Fundamentales de la Tesis

# Synthesis of Slow-Wave Structures Based on Capacitive-Loaded Lines Through Aggressive Space Mapping (ASM)

**Marco Orellana,[1] Jordi Selga,[1] Marc Sans,[1] Ana Rodríguez,[2] Vicente Boria,[2] Ferran Martín[1]**

[1]GEMMA/CIMITEC, Departament d'Enginyeria Electrònica, Universitat Autònoma de Barcelona, 08193 Bellaterra, Spain
[2]Departamento de Comunicaciones-iTEAM, Universidad Politécnica de Valencia, 46022 Valencia, Spain

ABSTRACT: **This article is focused on the automated synthesis of slow-wave structures based on microstrip lines loaded with patch capacitors. Thanks to the presence of the shunt capacitors, the effective capacitance of the line is enhanced, and the phase velocity of the structure can be made significantly smaller than the one of the unloaded line. The target is to achieve the layout of the slow-wave structure able to provide the required slow-wave ratio, characteristic (Bloch) impedance and electrical length (i.e., the usual specifications in the design of slow-wave transmission lines). To this end, a two-step synthesis method, based on the aggressive space mapping (ASM) algorithm, is proposed for the first time. Through the first ASM algorithm, the circuit schematic providing the target specifications is determined. Then, the second ASM optimizer is used to generate the layout of the structure. To illustrate the potential of the proposed synthesis method, three application examples are successfully reported. The two-step ASM algorithm is able to provide the layout of the considered structures from the required specifications, without the need of an external aid in the process.** © 2015 Wiley Periodicals, Inc. Int J RF and Microwave CAE 25:629–638, 2015.

**Keywords:** space mapping; slow-wave transmission lines; microwave circuits optimization; planar components miniaturization

## I. INTRODUCTION

Slow-wave transmission lines are wave guiding structures exhibiting a phase velocity smaller than the one corresponding to ordinary lines implemented in the same substrate. Owing to the slow-wave behavior of these lines, the wavelength is also small, as compared to ordinary lines, and hence the circuit size can be significantly reduced (see the recent review on artificial transmission lines [1], that includes slow-wave transmission lines). Typically, slow-wave transmission lines are implemented by periodically loading a host line with shunt connected capacitors, either lumped or semilumped (e.g., patch capacitors). By means of this capacitive loading, the effective capacitance of the line is enhanced and the phase velocity is reduced. Slow-wave transmission lines have found applications in microwave circuit miniaturization [2–4]. However, due to periodicity, these structures exhibit stop bands, which are of interest for spurious suppression. Thus, slow-wave structures have been applied to the design of microwave circuits with reduced size and spurious suppression [5, 6].

Slow-wave transmission lines implemented by means of capacitively loaded lines are relatively simple structures. However, to satisfy the usual specifications for circuit design, namely, characteristic impedance, electrical length, and slow-wave ratio (i.e., the ratio between the phase velocity of the loaded and unloaded line), optimization is typically necessary. In this article, we propose an

Correspondence to: M. Orellana; e-mail: marcoantonio.orellana@e-campus.uab.cat

DOI: 10.1002/mmce.20901
Published online 27 March 2015 in Wiley Online Library (wileyonlinelibrary.com).

© 2015 Wiley Periodicals, Inc.

automated synthesis process for capacitively loaded slow-wave transmission lines based on space mapping (SM) [7–9]. This synthesis technique has been applied to the design of many planar microwave circuits [10–18]. Specifically, in this work a variant called aggressive space mapping (ASM) [8] is used. Recently, we have proposed a two-step ASM technique useful for microwave circuits described by a circuit schematic, where the optimum schematic (i.e., the one that satisfies specifications) is first determined (first step), and then the circuit layout is automatically generated (second step) [19, 20]. This two-step ASM technique has been successfully applied to the design of bandpass filters based on stepped impedance resonators and shunt stubs coupled through admittance inverters [19, 20]. Similarly, we have implemented a two-step ASM algorithm for the synthesis of slow-wave transmission lines. Through the first algorithm, the optimum schematic, consisting on a cascade of transmission line sections (host line) and shunt capacitors, is determined. Then, from the optimum capacitance value and host line characteristics (impedance and electrical length), the layout is automatically generated.

The work is organized as follows. In the second section, the lumped element equivalent circuit model of the considered slow-wave structures, and the main design formulas, are provided. Section III is focused on the general formulation of ASM. Section IV is devoted to the description of the new proposed two-step ASM synthesis algorithm. Finally, three illustrative synthesis examples of slow wave transmission lines are reported in Section V. The conclusions are highlighted in Section VI.

## II. SLOW-WAVE STRUCTURES BASED ON CAPACITIVELY LOADED LINES

The schematic of the slow-wave structures considered in this work is depicted in Figure 1a. The host line, with phase constant $k$ (electrical length of the unit cell $kl$), and characteristic impedance $Z_0$, is periodically loaded with shunt connected capacitances, $C_{ls}$. From now on, we will refer to $k$ and $Z_0$ as the phase constant and characteristic impedance of the unloaded line, respectively, to distinguish such variables from the corresponding characteristic impedance (actually Bloch impedance), $Z_B$, and phase constant, $\beta$, of the capacitively loaded lines. The dispersion relation and Bloch impedance of the structure of Figure 1 can be obtained from the ABCD matrix of the unit cell, following standard Bloch wave analysis of periodic structures [21]. In particular, the dispersion relation is given by:

$$\cos \beta l = \cos kl - \frac{\omega C_{ls} Z_0}{2} \sin kl \tag{1}$$

The Bloch impedance is given by:

$$Z_B = \frac{Z_0 [\sin kl - Z_0 \omega C_{ls} \sin^2 (kl/2)]}{\sqrt{1 - \left(\cos kl - \frac{1}{2} Z_0 \omega C_{ls} \sin kl\right)^2}} \tag{2}$$

and the slow-wave ratio is given by:

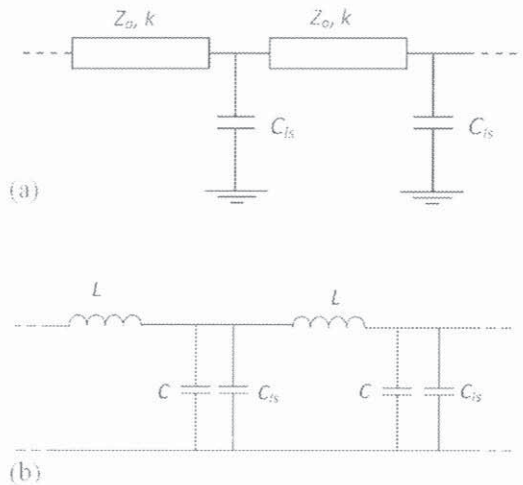


**Figure 1** Schematic of the slow-wave structure based on a capacitively loaded line (a), and lumped element equivalent circuit model (b).

$$swr = \frac{v_p}{v_{po}} = \frac{\omega/\beta}{\omega/k} = \frac{kl}{\beta l} \tag{3}$$

The previous expressions are cumbersome and, typically, the lumped element equivalent circuit model is invoked for design purposes. It is depicted in Figure 1b, where $C$ and $L$ are the per-section capacitance and inductance of the line. According to this model, the Bloch impedance, the electrical length (unit cell) and the slow wave ratio are given by:

$$Z_B = \sqrt{\frac{L}{C + C_{ls}}} \tag{4}$$

$$\phi_{Cell} = \beta l = \omega \sqrt{L(C + C_{ls})} \tag{5}$$

$$swr = \frac{v_p}{v_{po}} = \frac{l/\sqrt{L(C + C_{ls})}}{l/\sqrt{LC}} = \frac{1}{\sqrt{1 + \frac{C_{ls}}{C}}} \tag{6}$$

respectively. From the previous expressions, the elements of the circuit of Figure 1b can be easily isolated. However, the validity of the model of Figure 1b is restricted to large values of $C_{ls}$ as compared to $C$. Indeed, if the condition $C_{ls} >> C$ is satisfied, the agreement between the lumped element model and the schematic is good up to the cutoff frequency (at low frequencies, the model is valid regardless of the relative values between $C$ and $C_{ls}$). However, this condition ($C_{ls} >> C$) is not always satisfied. This justifies the first ASM proposed in this work, where, from the element values provided by isolation of expressions (4)–(6), we determine the optimum schematic of Figure 1a, namely, the one that satisfies the target specifications. An alternative to this ASM process would be the numerical solution of expressions (1)–(3), but we have

opted for implementing an ASM algorithm, which is simple, fast and accurate. Indeed, the first ASM provides a technique for the numerical solution of expressions (1)–(3).

## III. GENERAL FORMULATION OF ASM

Space mapping (SM) is a technique extensively used for the synthesis and optimization of microwave components. It uses two simulation spaces [7–9]: (i) the optimization space, $\mathbf{X_c}$, where the variables are linked to a coarse model, which is simple and computationally efficient, although not accurate and (ii) the validation space, $\mathbf{X_f}$, where the variables are linked to a fine model, typically more complex and CPU intensive, but significantly more precise. In each space, a vector containing the different model parameters can be defined. Let us call such vectors $\mathbf{x_f}$ and $\mathbf{x_c}$ in the fine and coarse model spaces, respectively, and let us designate by $\mathbf{R_f}(\mathbf{x_f})$ and $\mathbf{R_c}(\mathbf{x_c})$ their corresponding responses. The key idea behind any SM optimization process is to generate an appropriate parameter transformation

$$\mathbf{x_c}=\mathbf{P}(\mathbf{x_f}) \tag{7}$$

mapping the fine model parameter space to the coarse model parameter space such that

$$\|\mathbf{R_f}(\mathbf{x_f})-\mathbf{R_c}(\mathbf{x_c})\| \leq \eta \tag{8}$$

in some predefined region, $\|\cdot\|$ being a certain suitable norm and $\eta$ a small positive number close to zero. If $\mathbf{P}$ is invertible, then the inverse transformation:

$$\mathbf{x_f}=\mathbf{P}^{-1}(\mathbf{x_c^*}) \tag{9}$$

is used to find the fine model solution, which is the image of the coarse model solution, $\mathbf{x_c^*}$, that gives the target response, $\mathbf{R_c}(\mathbf{x_c^*})$.

The determination of $\mathbf{P}$ according to the procedure reported in [7] follows an iterative process that is rather inefficient. The efficiency of the method was improved by introducing a quasi-Newton type iteration [8], resulting in a faster convergence, and giving rise to the so-called ASM [8]. The goal in ASM is to minimize the following error function:

$$\mathbf{f}(\mathbf{x_f})=\mathbf{P}(\mathbf{x_f})-\mathbf{x_c^*} \tag{10}$$

Let us assume that $\mathbf{x_f^{(j)}}$ is the $j$th approximation to the solution in the validation space, and $\mathbf{f^{(j)}}$ the error function corresponding to $\mathbf{f}(\mathbf{x_f^{(j)}})$. The next vector of the iterative process $\mathbf{x_f^{(j+1)}}$ is obtained by a quasi-Newton iteration according to

$$\mathbf{x_f^{(j+1)}}=\mathbf{x_f^{(j)}}+\mathbf{h^{(j)}} \tag{11}$$

where $\mathbf{h^{(j)}}$ is given by:

$$\mathbf{h^{(j)}}=-\left(\mathbf{B^{(j)}}\right)^{-1}\mathbf{f^{(j)}} \tag{12}$$

and $\mathbf{B^{(j)}}$ is an approximate to the Jacobian matrix which is also updated by a simplification of the classical Broyden formula [8, 22] at each iterative step.

$$\mathbf{B^{(j+1)}}=\mathbf{B^{(j)}}+\frac{\mathbf{f^{(j+1)}}\mathbf{h^{(j)T}}}{\mathbf{h^{(j)T}}\mathbf{h^{(j)}}} \tag{13}$$

In (13), $\mathbf{f^{(j+1)}}$ is obtained by evaluating (10) using a certain parameter extraction method providing the coarse model parameters from the fine model parameters, and the super-index $T$ stands for transpose.

The implementation of the ASM algorithm is well reported in [8]. In the next section, the new proposed two-step ASM synthesis algorithm is explained in detail.

## IV. THE PROPOSED TWO-STEP ASM SYNTHESIS METHOD

The developed ASM algorithm for the unattended synthesis of slow-wave structures based on capacitively loaded lines is divided in two steps: (i) the determination of the optimum schematic, providing the required specifications and (ii) the generation of the layout. Let us now describe in detail both ASM stages.

### *A. First ASM: Determination of the Optimum Schematic*

For the determination of the schematic [given by the circuit of Fig. 1a, in coherence with the rest of the text] providing the target specifications, we have developed a specific ASM algorithm. The variables of the coarse space are the three specifications: Bloch impedance, $Z_B$, electrical length per unit cell, $\beta l$, and slow-wave ratio, *swr*. The response of these variables in the coarse space is simply given by the electrical simulation of the circuit of Figure 1b with the element values inferred from expressions (4)–(6). The variables of the fine model are $Z_0$, $kl$, and $C_{ls}$, and the response of this model is given by the circuit simulation of the schematic of Figure 1a.

To initiate this first ASM, we must provide the values of the variables of the fine model according to some criterion. The most straightforward one is to identify $C_{ls}$ with the value of this variable inferred by isolation of (4)–(6). The values of $C$ and $L$ also provide $Z_0$, that is,

$$Z_o=\sqrt{\frac{L}{C}} \tag{14}$$

and $kl$, given by:

$$kl=\omega\sqrt{LC} \tag{15}$$

Once the variables of the fine model are determined, the response is obtained by circuit simulation of the schematic (Fig. 1a, in coherence with the rest of the text). From this response (or by means of expressions 1–3), we extract the variables of the coarse model corresponding to the first iteration $\mathbf{x_c^{(1)}}$. Then, we compare such values with the target $(\mathbf{x_c^*})$ and this gives the first error function (10). Unless this error function is smaller than a certain

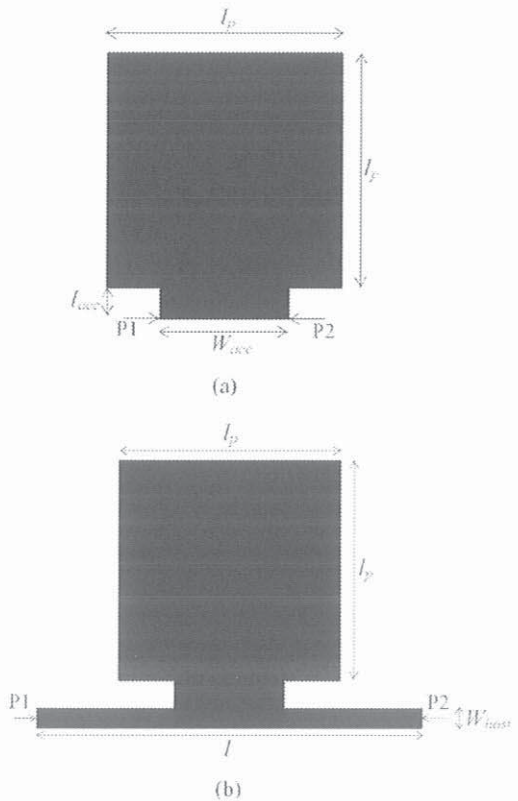


**Figure 2** Topology and relevant dimensions of the capacitive patch (a) and whole unit cell (b).

predetermined value, the matrix **B** must be calculated. To obtain the first approximation to this matrix, we slightly perturb each variable of the fine model from the first value inferred as indicated above. Then we obtain the circuit response, and from it we obtain the resulting variables of the coarse model corresponding to each perturbation. The relative changes can be expressed in a matrix form as follows:

$$\mathbf{B}^{(1)} = \begin{pmatrix} \frac{\delta Z_B}{\delta Z_0} & \frac{\delta Z_B}{\delta kl} & \frac{\delta Z_B}{\delta C_{ls}} \\ \frac{\delta \beta l}{\delta Z_0} & \frac{\delta \beta l}{\delta kl} & \frac{\delta \beta l}{\delta C_{\mathrm{ls}}} \\ \frac{\delta swr}{\delta Z_0} & \frac{\delta swr}{\delta kl} & \frac{\delta swr}{\delta C_{ls}} \end{pmatrix} \tag{16}$$

which corresponds to the initial matrix **B**. Once the matrix $\mathbf{B}^{(1)}$ is known, the fine model parameters of the following iteration can be derived from (11), and the process is iterated until convergence is obtained.

*B. Second ASM: Determination of the Layout*

Once the optimum schematic has been obtained, the layout is determined through a second iterative ASM process.

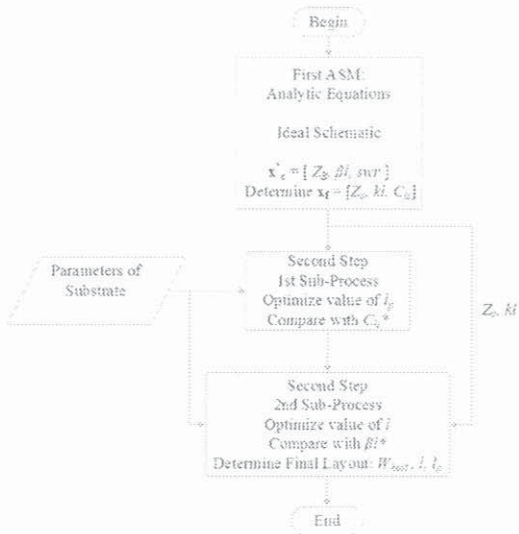


**Figure 3** Flow diagram of the proposed two-step ASM.

The first step is the determination of the side length ($l_p$) of the capacitive patch corresponding to the shunt capacitor, $C_{ls}$. The geometry is depicted in Figure 2a, where a square shaped patch connected to the host line through a wide and short access strip (to avoid any inductive effect) is considered. In this work, the distance between the host line and the patch (length of the access strip, $l_{\mathrm{acc}}$) is set to a fixed value (0.583 mm), whereas its width ($W_{acc}$) is set to a fraction of the patch dimension $l_p$ (specifically, it has been found that 50% of the patch dimension is a good choice).

To determine $l_p$ an independent one variable ASM iterative algorithm has been developed. The variable of the coarse model is the capacitance $C_{ls}$, whereas $l_p$ is the variable of the fine model. The first value of $l_p$ is inferred from the target value of $C_{ls}$ determined from the first ASM, through the parallel plate capacitor formula. Then the capacitance of this patch is inferred from the electromagnetic simulation by considering the ports indicated in Figure 2a, specifically by inferring the admittance of the shunt load [21], and it is compared to the target value. The matrix **B**, actually composed of a single element, is initiated by varying the patch dimension $l_p$ and recording the effects of this variation on the capacitance of the patch. Finally, the process is iterated through (11).

The width of the host line ($W_{host}$) is not considered to be an optimization variable, as the value provided by well-known microstrip formulas [21] (giving the line width as a function of the characteristic impedance $Z_0$ and substrate parameters) are very accurate. The remaining parameter to be determined is the length of the host line, $l$. This is determined through another independent ASM iterative process, where the variable of the coarse model is the electrical length of the loaded line, that is, $\beta l$, rather than $kl$ (the electrical length of the unloaded line). By this

means, we correct any phase shift introduced by the capacitive patch. The first value of $l$ is obtained from the optimum value of $kl$ determined at the first ASM. Then, the phase of the whole loaded structure is inferred from electromagnetic simulation, and it is compared to the target value $\beta l$, to determine the first error function. The iterative process is then initiated by calculating the first approximation to the Broyden matrix, and optimization of $l$ is done through (11), as indicated before in reference to the one-variable ASM algorithm for the determination of $l_p$. Two independent ASM subprocesses with only one variable have been considered due to the lack of interaction between $C_{ls}$ and $\beta l$. On this second ASM, the optimization variables $C_{ls}$ and $\beta l$ strongly depend on the patch dimension $l_p$ and on the length of the host line $l$, respectively. This method provides fast and accurate results. The geometry of the unit cell of the slow-wave structure is depicted in Figure 2b.

For better understanding, the flow diagram of the complete two-step ASM algorithm is depicted in Figure 3. Using this ASM iterative process, the synthesis of slow-wave structures from specifications can be carried out automatically, following a completely unattended scheme.

## V. SYNTHESIS EXAMPLES

To illustrate the potential of the proposed approach, we have considered the synthesis of three different examples: (1) a cell with electrical length $\phi_{\text{cell}} = \beta l = 90°$, Bloch impedance $Z_B = 50\ \Omega$, and slow-wave factor $swr = 0.5$, (2) a cell with electrical length $\phi_{\text{cell}} = \beta l = 45°$, Bloch impedance $Z_B = 50\ \Omega$, and slow-wave factor $swr = 0.5$, and (3) a structure with electrical length $\beta l = 90°$, Bloch impedance $Z_B = 50\ \Omega$, and slow-wave factor $swr = 0.5$, composed by three cascaded unit cells ($\phi_{\text{cell}} = 30°$). The operating frequency in all cases is $f_0 = 1$ GHz.

### *A. Example 1: $\phi_{cell} = 90°$, $Z_B = 50\ \Omega$, $swr = 0.5$*

For the considered target specifications, inversion of expressions (4)–(6) provides the following element values for the circuit of Figure 1b: $C = 1.25$ pF, $C_{ls} = 3.75$ pF and $L = 12.5$ nH. From Eqs. (14 and 15), the values of the first iteration of the fine model, $\mathbf{x}_f^{(1)}$ are: $Z_0 = 100.0\ \Omega$, $kl = 45.0°$, and $C_{ls} = 3.75$ pF. Using the first ASM algorithm, we have determined the optimum schematic. Convergence, with a relative error of 0.033%, has been achieved after five iterations. The resulting values of the fine model are $Z_0 = 120.7\ \Omega$, $kl = 45.0°$, and $C_{ls} = 2.63$ pF. The response of the schematic (using the previous values of the fine model parameters) is depicted in Figure 4 (where the insertion/return loss, characteristic impedance, and electrical length can be observed). In view of this figure, it is clear that the target specification at the schematic level are satisfied to a very good approximation, that is, the resulting electrical length, Bloch impedance and slow-wave factor of the cell after convergence are found to be $Z_B = 50.01\ \Omega$, $\phi_{\text{cell}} = 89.99°$ and $swr = 0.50$, respectively.

Once the optimum schematic has been obtained, the application of the second ASM has led us to the layout

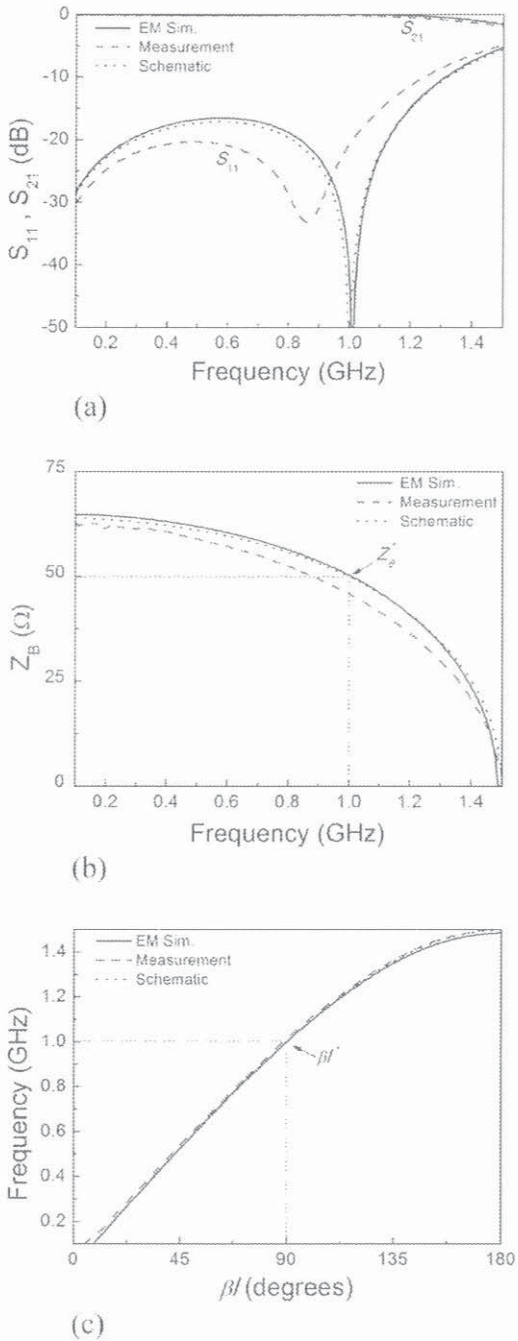


**Figure 4** Response of the cell considered in example 1. (a) Insertion and return loss, (b) characteristic impedance, and (c) electrical length.

depicted in Figure 5 (the *Rogers RO4003C* substrate with dielectric constant $\varepsilon_r = 3.55$ and thickness $h = 0.813$ mm, has been considered). The response of this structure, inferred from electromagnetic simulation using the *Agilent*

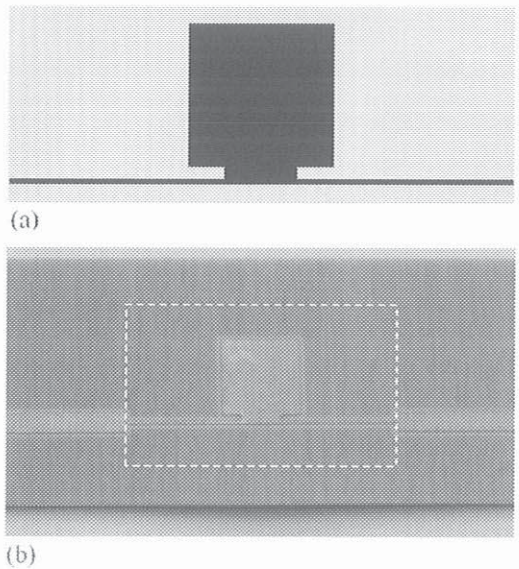


**Figure 5** Layout (a) and photograph (b) of the synthesized cell of example 1. Dimensions are: $l = 25.19$ mm, $l_p = 7.23$ mm, $W_{acc} = 3.61$ mm ($0.5l_p$), $W_{host} = 0.27$ mm

*Momentum* commercial simulator, is also depicted in Figure 4, and reveals that the target specifications are satisfied to a very good approximation at the design frequency, in spite that neither the Bloch impedance nor the slow-wave factor are variables in the optimization process (we have simply optimized patch dimensions and the electrical length of the cell). The second ASM does not involve the optimization of the patch dimensions, length, and width of the line, simultaneously. Rather than this, we have simply optimized the patch dimensions and then the length of the cell, by means of two independent subprocesses with only one optimization variable in each case. Consequently, a very fast second step ASM algorithm has been proven to provide accurate results. It is important to mention that optimization has been done at the considered operating frequency. At sufficiently high frequencies (close to the cutoff frequency), discrepancies arise and are due to the fact that distributed effects in the patch capacitance cannot be neglected. Thus, such discrepancies are attributed to a limitation of the model (schematic), where the patch capacitance is described by a lumped element, but not to the proposed optimization algorithm.

It is remarkable that the synthesis algorithm is very efficient, as revealed by the small number of iterations required to achieve the cell layout. The process is completely unattended and the time spent in a computer with Intel® Core™ i5–3470 Processor is about 3 minutes. It is noteworthy that for each electromagnetic simulation we use a high mesh density to achieve accurate results.

The cell of Figure 5 has been fabricated by means of the *LPKF HF100* drilling machine and has been characterized by means of the *Agilent* E8364B vector network analyzer and the *Anritsu Universal* test fixture Model

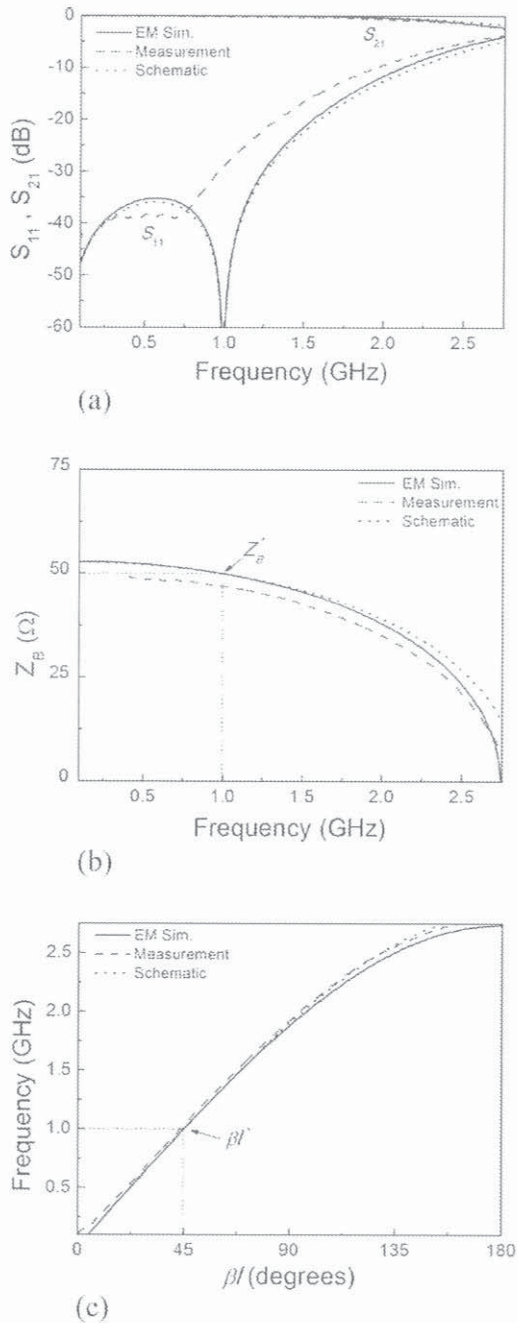


**Figure 6** Response of the cell considered in example 2. (a) Insertion and return loss, (b) characteristic impedance, and (c) electrical length.

3680-20. The measured insertion and return loss, as well as the characteristic impedance and electrical length, are also included in Figure 4. There are some discrepancies attributed to tolerances in cell dimensions and dielectric

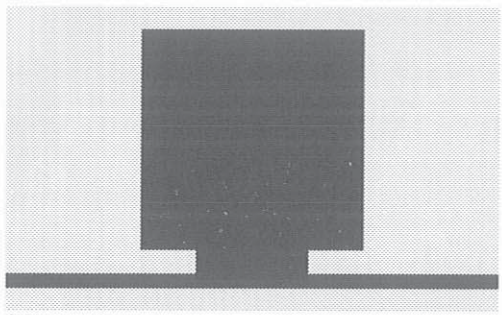

(a)

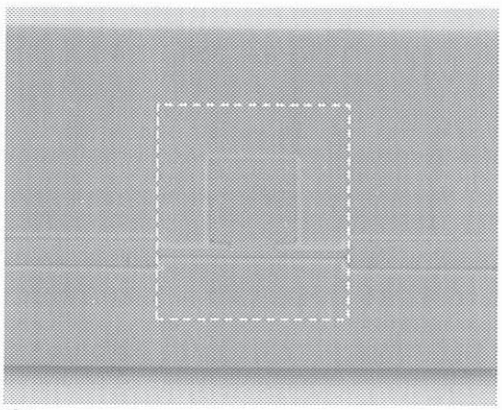

(b)

**Figure 7** Layout (a) and photograph (b) of the synthesized cell of example 2. Dimensions are: $l = 12.73$ mm, $l_p = 5.75$ mm, $W_{acc} = 2.87$ mm ($0.5l_p$), $W_{host} = 0.41$ mm.

constant, and also to the effects of the access lines (despite the fact that a de-embedding process has been applied). For most applications, the experimental results reveal that the fabricated structures can be useful since the required specifications, at the operating frequency, are satisfied to a reasonable approximation. Nevertheless, the experimental results are determined by factors (indicated above) external to the described synthesis process, which provides very accurate results (the idea and implementation of the proposed two-step ASM algorithm has been the main focus of this article and has been demonstrated to be fast and accurate).

*B. Example 2: $\phi_{cell} = 45°$, $Z_B = 50\ \Omega$, $swr = 0.5$*

In this case, expressions (4)–(6) give $C = 0.625$ pF, $C_{ls} = 1.875$ pF and $L = 6.25$ nH, and from Eqs. (14 and 15) the values of the first iteration of the fine model, $\mathbf{x}_\mathbf{f}^{(1)}$ are: $Z_0 = 100.0\ \Omega$, $kl = 22.5°$, and $C_{ls} = 1.875$ pF. The parameters of the optimum schematic (obtained by means of the first ASM algorithm after 3 iterations with a relative error of 0.074 %), are $Z_0 = 104.10\ \Omega$, $kl = 22.50°$, and $C_{ls} = 1.73$ pF. The response of the schematic, depicted in Figure 6, indicates that the target specifications at the schematic level are satisfied to a very good approximation also for this second example. The resulting electrical

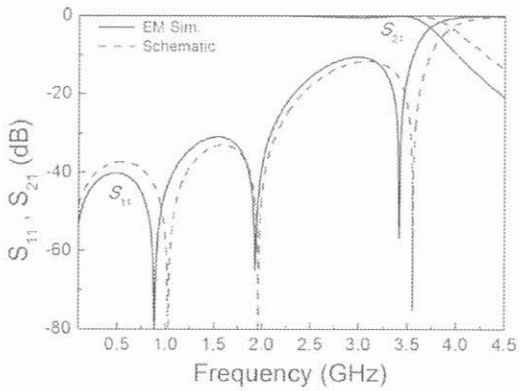


(a)

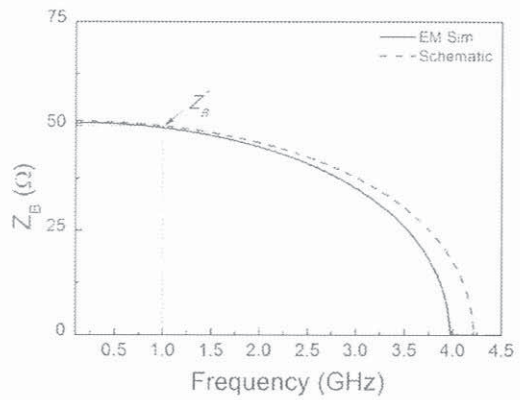


(b)

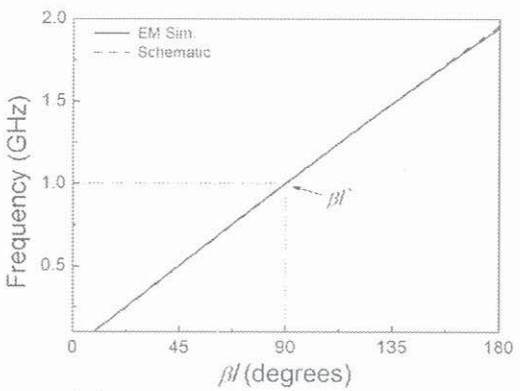


(c)

**Figure 8** Response of the structure considered in example 3. (a) Insertion and return loss, (b) characteristic impedance of the unit cell, and (c) electrical length.

length, Bloch impedance and slow-wave factor of the cell after convergence are found to be $Z_B = 49.97\ \Omega$, $\phi_{cell} = 45.01°$, and $swr = 0.50$, respectively. The application of the second ASM algorithm has provided the layout depicted in Figure 7 (the same substrate has been used).

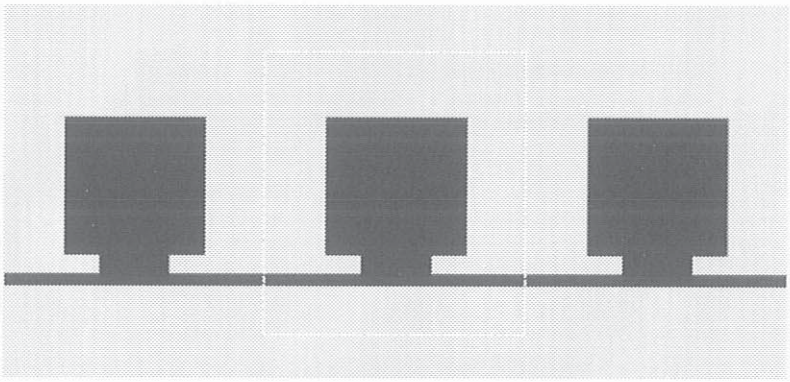

**Figure 9** Layout of the synthesized structure of example 3. For the unit cell, dimensions are: $l = 8.62$ mm, $l_p = 4.69$ mm, $W_{acc} = 2.35$ mm ($0.5l_p$), $W_{host} = 0.44$ mm

The electromagnetic response is also depicted in Figure 6, and reveals that the target specifications are also satisfied to a very good approximation at the design frequency. The measured response is also in good agreement at the design frequency, except for the previously mentioned discrepancies. The characteristic impedance, inferred from the measured *S*-parameters, is noisy below 0.4 GHz and is not shown.

*C. Example 3: Three-cell structure, $\phi_{cell} = 30°$, $Z_B = 50\ \Omega$, $swr = 0.5$*

In this example, three unit cells with $\phi_{cell} = 30°$ are cascaded to obtain a structure with electrical length $\beta l = 90°$ at the operating frequency. In this case, for the unit cell, inversion of expressions (4)–(6) gives $C = 0.417$ pF, $C_{ls} = 1.25$ pF and $L = 4.167$ nH, and from Eqs. (14 and 15) the values of the first iteration of the fine model, $\mathbf{x}_f^{(1)}$ are: $Z_0 = 100.0\ \Omega$, $kl = 15.0°$, and $C_{ls} = 1.25$ pF. On one hand, the parameters of the optimum schematic (obtained by means of the first ASM algorithm after 2 iterations with an error of 0.168%), are $Z_0 = 101.79\ \Omega$, $kl = 15.01°$, and $C_{ls} = 1.20$ pF. On the other hand, the resulting electrical length, Bloch impedance and slow-wave factor of the unit cell after convergence are found to be $Z_B = 50.06\ \Omega$, $\phi_{cell} = 29.99°$, and $swr = 0.50$, respectively. The circuit response of the schematic is depicted in Figure 8. The application of the second ASM algorithm has provided the layout depicted in Figure 9 (the considered substrate is the same as the one of previous examples). The electromagnetic response of whole structure is also depicted in Figure 8, and reveals that the target specifications are also satisfied to a very good approximation at the design frequency. The main difference in this case is that two additional reflexion zeros can be observed (phase matching). This matching occurs at those frequencies where the electrical length of the structure is a multiple of $\pi$ [23].

## VI. CONCLUSIONS

In summary, we have developed an optimization algorithm for the synthesis of slow-wave transmission lines consisting on microstrip lines loaded with patch capacitors. The algorithm, based on the so-called ASM, uses quasi-Newton type iteration, and has been divided in two steps. The first ASM step determines the schematic providing the target specifications (optimum schematic). Specifically, these are the slow-wave ratio, the Bloch impedance and the per-unit-cell electrical length. The second step, with two independent ASM subprocesses, provides the layout of the slow-wave structure from the optimum cell schematic. Three illustrative synthesis examples have been provided to demonstrate the potential of the proposed synthesis approach. The main relevant aspect of the proposed two-step ASM algorithm is that the layout of the structures is determined from the target specifications in a completely unattended scheme.

On one hand, the first ASM determines the schematic providing the target specifications (optimum schematic), that is, the slow-wave ratio, the Bloch impedance and the per-unit-cell electrical length. On the other hand, the second step, with two independent ASM subprocesses, provides the layout of the slow-wave structure from the optimum cell schematic.

## ACKNOWLEDGMENTS

This work has been supported by MINECO-Spain (projects TEC2010-17512 METATRANSFER, TEC2010-21520-C04-01, TEC2013-47037-C5-1-R, CONSOLIDER EMET CSD2008-00066, TEC2013-40600-R and TEC2013-49221-EXP), *Generalitat de Catalunya* (project 2014SGR-157), *Institució Catalana de Recerca i Estudis Avançats* (who has awarded Ferran Martín) and FEDER Funds. Marco Orellana acknowledges the support of the *Universidad de Costa Rica*, MICITT and CONICIT to study at the *Univesitat Autònoma de Barcelona*.

## REFERENCES

1. F. Martín, J. Bonache, M. Durán-Sindreu, J. Naqui, F. Paredes, and G. Zamora, Artificial transmission lines, Wiley Encyclopedia of Electrical and Electronic Engineering, July 2012, pp. 1–25.
2. A. Görür, A novel coplanar slow-wave structure, IEEE Microwave Guided Wave Lett 4 (1994), 86–88.

3. J. Sor, Y. Qian, and T. Itoh, Miniature low loss CPW periodic structures for filter applications, IEEE Trans Microwave Theory Techn 49 (2001), 2336–2341.
4. S.G. Mao and M.Y. Chen, A novel periodic electromagnetic bandgap structure for finite-width conductor-backed coplanar waveguides, IEEE Microwave Wireless Comp Lett 11 (2001), 261–263.
5. F. Martín, F. Falcone, J. Bonache, M.A.G. Laso, T. Lopetegi, and M. Sorolla, New CPW low pass filter based on a slow wave structure, Microwave and Optical Technol Lett 38 (2003), 190–193.
6. J. García-García J. Bonache, and F. Martín, Application of electromagnetic bandgaps (EBGs) to the design of ultra wide band pass filters (UWBPFs) with good out-of-band performance, IEEE Trans Microwave Theory Techn 54 (2006) 4136–4140.
7. J.W. Bandler, R.M. Biernacki, S.H. Chen, P.A. Grobelny, and R.H. Hemmers, Space mapping technique for electromagnetic optimization, IEEE Trans Microwave Theory Techn 42 (1994), 2536–2544.
8. J.W. Bandler, R.M. Biernacki, S.H. Chen, R.H. Hemmers, and K. Madsen, Electromagnetic optimization exploiting aggressive space mapping, IEEE Trans Microwave Theory Techn 43 (1995), 2874–2882.
9. S. Koziel, Q.S. Cheng, and J.W. Bandler, Space mapping, IEEE Microwave Mag 9 (2008), 105–122.
10. S. Koziel and J.W. Bandler, Space-mapping optimization with adaptive surrogate model, IEEE Trans Microwave Theory Techn 55 (2007), 541–546.
11. S. Koziel, Q.S. Cheng, and J.W. Bandler, Improving efficiency of space mapping optimization of microwave structures and devices, In: IEEE MTT-S International Microwave Symposium Digest, Honolulu, HI, 3–8 June 2007, pp. 1995–1998.
12. S. Koziel, J.W. Bandler, and Q.S. Cheng, Robust trust-region space-mapping algorithms for microwave design optimization, IEEE Trans Microwave Theory Techn 58 (2010), 2166–2174.
13. Q.S. Cheng, J.W. Bandler, N.K. Nikolova, and S. Koziel, Fast space mapping modeling with adjoint sensitivity, In: IEEE MTT-S International Microwave Symposium Digest, 5–10 June 2011, Baltimore, MD, pp. 1–4.
14. L.J. Rogla, J.E. Rayas-Sanchez, V.E. Boria, and J. Carbonell, EM-based space mapping optimization of left-handed coplanar waveguide filters with split ring resonators, IEEE MTT-S International Microwave Symposium Digest, Honolulu, Hawai, 3–8 June 2007, pp. 111–114.
15. P.J. Bradley, Robust surrogate-based optimisation of planar metamaterial structures, IEEE International Conference on Wireless Information Technology and Systems, Maui, Hawai, 11–16 Nov. 2012, pp. 1–4.
16. P.J. Bradley, Quasi-newton model-trust region approach to surrogate-based optimisation of planar metamaterial structures, Progress In Electromagnetics Research B, vol. 47, pp. 1–17, 2013.
17. J. Selga, A. Rodríguez, V.E. Boria, and F. Martín, Synthesis of split rings based artificial transmission lines through a new two-step, fast converging, and robust aggressive space mapping (ASM) algorithm, IEEE Transactions on Microwave Theory and Techniques, vol. 61(6), pp. 2295–2308, June 2013.
18. J. Selga, A. Rodríguez, J. Naqui, M. Durán-Sindreu, V.E. Boria and F. Martín, Application of aggressive space mapping (ASM) to the efficient synthesis of stepped impedance resonators (SIRs), European Microwave Conference, Nuremberg (Germany), 2013.
19. J. Selga, M. Sans, A. Rodríguez, J. Bonache, V. Boria, F. Martín, Automated synthesis of planar wideband bandpass filters based on stepped impedance resonators (SIRs) and shunt stubs through aggressive space mapping (ASM), IEEE MTT-S International Microwave Symposium Digest, Tampa, FL, 1–6 June 2014, pp. 1–4.
20. M. Sans, J. Selga, A. Rodríguez, J. Bonache, V.E. Boria, and F. Martín, Design of planar wideband bandpass filters from specifications using a two-step aggressive space mapping (ASM) optimization algorithm, IEEE Trans Microwave Theory Techn 62 (2014), 3341–3350.
21. D.M. Pozar, Microwave engineering, John Wiley & Sons, Hoboken, New Jersey, 2005.
22. C.G. Broyden, A class of methods for solving nonlinear simultaneous equations, Math Comput 19 (1965), 577–593.
23. R. Marqués, F. Martín, and M. Sorolla. Metamaterials with negative parameters: Theory, design and microwave applications, Wiley, Hoboken, New Jersey, 2008.


## BIOGRAPHIES

**Marco Orellana** was born in San José, Costa Rica, in 1985. He earned a Licentiate degree in Electrical Engineering from the Universidad de Costa Rica (UCR) in 2009. In 2011 obtained the Master degree in Micro and Nanoelectronics Engineering at the Universitat Autònoma de Barcelona with the support of the Erasmus Mundus Programme and the UCR. He has been instructor at the School of Electrical Engineering at UCR. He is currently working on his Doctoral Thesis at the Universitat Autònoma de Barcelona focused on the automation of metamaterial-based structures design.

**Jordi Selga** was born in Barcelona, Spain, in 1982. He received the Telecommunications Engineering - Electronic Systems diploma in 2006, the Electronics Engineering degree in 2008 and the PhD degree in Electronics Engineering in 2013 from the Universitat Autònoma de Barcelona (UAB), Barcelona, Spain. Since 2008 is member of CIMITEC-UAB, a research centre on Metamaterials supported by TECNIO (Catalan Government). He was holder of a national research fellowship from the *Formación de Profesorado Universitario* Program of the Education and Science Ministry (Reference AP2008–4707). He is currently working in subjects related to metamaterials, CAD design of microwave devices, EM optimization methods and automated synthesis of planar microwave components at the UAB.

**Marc Sans** was born in Terrassa (Barcelona), Spain, in 1982. He received the B.S. Degree in Telecommunications Engineering - Electronic Systems in 2006, the M.S. Degree in Telecommunications Engineering in 2008 and the M.S. Degree in Electronics Engineering in 2013 from the Universitat Autònoma de Barcelona (UAB). In 2008 he started his professional career as a RF Engineer at Sony-FTVE developing the RF stage of TV receivers. In 2010 he moved to Mier Comunicaciones S.A. to carry out the design of passive and active devices for VHF-UHF broadcasting units. Since 2014 he is working towards the PhD Degree at CIMITEC-UAB in the synthesis of microwave devices based on EM optimization techniques.

**Ana Rodriguez** was born in Lugo, Spain. She received the Telecommunications Engineering degree from the Universidade de Vigo (UV), Spain, in 2008. As a student, she participated in the Erasmus exchange program, developing the Master Thesis at the University of Oulu, Finland. Since the end of 2008, she has joined the Institute of Telecommunications and Multimedia Applications (iTEAM), which is part of the scientific park at the Universitat Politècnica de València (UPV), Spain. She obtained "Master en Tecnología, Sistemas y Redes de Comunicaciones" in 2010 from UPV, and currently is on the way of pursuing Ph.D. degree. Her main research interests include CAD design of microwave devices, EM optimization methods and metamaterials.

**Vicente E. Boria** was born in Valencia, Spain, on May 18, 1970. He received his "Ingeniero de Telecomunicación" degree (with first-class honors) and the "Doctor Ingeniero de Telecomunicación" degree from the Universidad Politécnica de Valencia, Valencia, Spain, in 1993 and 1997, respectively. In 1993 he joined the "Departamento de Comunicaciones", Universidad Politécnica de Valencia, where he has been Full Professor since 2003. In 1995 and 1996, he was holding a Spanish Trainee position with the European Space Research and Technology Centre, European Space Agency (ESTEC-ESA), Noordwijk, The Netherlands, where he was involved in the area of EM analysis and design of passive waveguide devices. He has authored or coauthored 7 chapters in technical textbooks, 75 papers in refereed international technical journals, and over 150 papers in international conference proceedings. His current research interests are focused on the analysis and automated design of passive components, left-handed and periodic structures, as well as on the simulation and measurement of power effects in passive waveguide systems. He has been a member of the IEEE Microwave Theory and Techniques Society (IEEE MTT-S) and the IEEE Antennas and Propagation Society (IEEE AP-S) since 1992. He is reviewer of the IEEE Transactions on Microwave Theory and Techniques, Proceeding of the IET (Microwaves, Antennas and Propagation) and IET Electronics Letters. Since 2013, he serves as Associate Editor of IEEE Microwave and Wireless Components Letters. He is also a member of the Technical Committees of the IEEE-MTT International Microwave Symposium and of the European Microwave Conference.

**Ferran Martín** was born in Barakaldo (Vizcaya), Spain in 1965. He received the B.S. Degree in Physics from the Universitat Autònoma de Barcelona (UAB) in 1988 and the PhD degree in 1992. From 1994 up to 2006 he was Associate Professor in Electronics at the Departament d'Enginyeria Electrònica (Universitat Autònoma de Barcelona), and since 2007 he is Full Professor of Electronics. In recent years, he has been involved in different research activities including modelling and simulation of electron devices for high frequency applications, millimeter wave and THz generation systems, and the application of electromagnetic bandgaps to microwave and millimeter wave circuits. He is now very active in the field of metamaterials and their application to the miniaturization and optimization of microwave circuits and antennas. He is the head of the Microwave Engineering, Metamaterials and Antennas Group (GEMMA Group) at UAB, and director of CIMITEC, a research Center on Metamaterials supported by TECNIO (Generalitat de Catalunya). He has organized several international events related to metamaterials, including Workshops at the IEEE International Microwave Symposium (years 2005 and 2007) and European Microwave Conference (2009), and the Fifth International Congress on Advanced Electromagnetic Materials in Microwaves and Optics (Metamaterials 2011), where he has acted as chair of the Local Organizing Committee. He has acted as Guest Editor for three Special Issues on Metamaterials in three International Journals. He has authored and coauthored over 450 technical conference, letter, journal papers and book chapters, he is coauthor of the book on Metamaterials entitled *Metamaterials with Negative Parameters: Theory, Design and Microwave Applications* (John Wiley & Sons Inc.), and he has generated 14 PhDs. Ferran Martín has filed several patents on metamaterials and has headed several Development Contracts. He is a member of the IEEE Microwave Theory and Techniques Society (IEEE MTT-S). He is reviewer of the IEEE Transactions on Microwave Theory and Techniques and IEEE Microwave and Wireless Components Letters, among many other journals, and he serves as member of the Editorial Board of IET Microwaves, Antennas and Propagation and International Journal of RF and Microwave Computer-Aided Engineering. He is also a member of the Technical Committees of the European Microwave Conference (EuMC) and International Congress on Advanced Electromagnetic Materials in Microwaves and Optics (Metamaterials). Among his distinctions, Ferran Martín has received the 2006 Duran Farell Prize for Technological Research, he holds the *Parc de Recerca UAB – Santander* Technology Transfer Chair, and he has been the recipient of two ICREA ACADEMIA Awards (calls 2008 and 2013).

# Automated synthesis of wideband bandpass filters based on slow-wave EBG structures

Marco Orellana[1], Jordi Selga[1], Paris Vélez[1], Marc Sans[1], Ana Rodríguez[2], Vicente Boria[2] and Ferran Martín[1]

[1] CIMITEC, Departament d'Enginyeria Electrònica, Universitat Autònoma de Barcelona, 08193 Bellaterra, Spain

[2] Departamento de Comunicaciones-iTEAM, Universitat Politècnica de València, 46022 Valencia, Spain.

## Abstract

This paper is focused on the automated synthesis of wideband bandpass filters operating at microwave frequencies and based on electromagnetic bandgap (EBG) structures. The classical counterpart of such filter consists of a combination of transmission line sections and shunt-connected grounded stubs placed at equidistant positions. By replacing the transmission line sections with capacitively-loaded lines (a kind of EBG-based lines) exhibiting the same phase shift at the lower cutoff frequency and the same characteristic (actually Bloch) impedance, filter size is reduced and the spurious pass bands can be efficiently suppressed. In practice, the loading capacitances are implemented by means of patches, in order to achieve a fully planar filter implementation. The presence of the patches reduces the effective phase velocity of the capacitively-loaded lines, thus providing a slow-wave effect useful for filter miniaturization. Moreover, due to periodicity, such EBG-based lines exhibit wide stop bands, which are used for spurious suppression. Even though such EBG-based filters were previously reported by some of the authors, a systematic synthesis method was not applied for filter design. In this paper, the main aim is to demonstrate the potential of aggressive space mapping (ASM) for that purpose, and it will be shown that such filters can be automatically synthesized.

**Keywords:** Electromagnetic bandgaps (EBG), microwave filters, slow-wave transmission lines, space mapping.

## 1. Introduction

Electromagnetic bandgaps (EBGs), known as photonic bandgaps (PBGs) or photonic crystals at optical frequencies, are periodic structures able to inhibit wave propagation at certain frequencies due to the well known Bragg effect, derived from periodicity [Yablonovitch (1993); Joannopoulos, Meade, and Winn (1995)]. In planar technology, EBG-based structures have been proposed in applications such as microwave reflectors [Qian, Radisic and Itoh (1997); Erro, Laso, Lopetegi, Benito, Garde, and Sorolla (2000); Laso, Lopetegi, Erro, Benito, Garde and Sorolla (2000a); Falcone, Lopetegi, Irisarri, Laso, Erro, and Sorolla (1999); Laso, Lopetegi, Erro, Benito, Garde and Sorolla (2000b) ], high-Q resonators [Lopetegi, Falcone and Sorolla (1999); Yun and Chang (2001)], spurious suppression in filters [Lopetegi, Laso, Hernández, Bacaicoa, Benito, Garde, Sorolla and Guglielmi (2001); Lopetegi, Laso, Falcone, Martín, Bonache, Pérez-Cuevas and Sorolla (2004); Martín, Falcone, Bonache, Lopetegi, Laso and Sorolla (2002); Martín, Bonache, Gil, Falcone, Lopetegi, Laso and Sorolla (2004); Martín, Falcone, Bonache, Laso, Lopetegi and Sorolla (2003a)], and harmonic suppression in active circuits [Radisic, Qian, and Itoh (1998); Hang, Radisic, Qian, and Itoh (1999); Yang, Qian, and Itoh (1999); Xue, Shum, and Chan (2001); Lee, Lim, Park, Ahn, and Nam (2002)], among others. In the previous applications, the EBG structures typically consist of transmission lines with ground plane etching (e.g., holes at periodic position), or with modulation of the line width (non-uniform transmission lines). In both cases, stop bands appear at the Bragg frequency, given by

$$f = \frac{v_p}{2l} \tag{1}$$

and at its harmonics, where $v_p$ is the phase velocity and $l$ is the period of the EBG structure. According to the previous expression, the first stop band occurs at that frequency satisfying that the period is half the wavelength (the rejection level and stopband bandwidth depend on the magnitude of the perturbation and number of periods, and analytical expressions can be found in [Martín (2015)]).

Other periodic transmission lines are implemented by loading it with shunt capacitances. Such reactive elements increase the effective capacitance of the line, providing a slow-wave effect that decreases the phase velocity [Görür (1994); Görür, Karpuz and Alkan (1998); Sor, Qian, and Itoh (2001); Nesic (2002); Martín, Falcone, Bonache, Laso, Lopetegi and Sorolla (2003b); Martín, Bonache, Gil, Falcone, Lopetegi, Laso and Sorolla (2004); Kaddour, Issa, Franc, Corrao, Pistono, Podevin, Fournier, Duchamp, and Ferrari (2009); Franc, Kaddour, Issa, Pistono, Corrao, Fournier and Ferrari (2010); Abdel Aziz, Issa, Kaddour, Podevin, Safwat, Pistono, Duchamp, Vilcot, Fournier, and Ferrari (2012)]. Thus, capacitively loaded EBG-based lines behave as slow-wave transmission lines with stopbands related to periodicity. According to this, such artificial lines can be useful to simultaneously reduce device size in planar microwave circuits and to suppress spurious bands, inherent to distributed circuits. To avoid the presence of lumped elements (with the corresponding penalty in terms of cost

and fabrication complexity), capacitively loaded lines have been typically implemented by means of patch capacitances or with other planar geometries that effectively increase the line capacitance [Orellana, Selga, Sans, Rodríguez, Boria, and Martín (2015)]. In the field of microwave filters these slow-wave structures have been used to reduce size and improve the stopband response (by suppressing the spurious bands) [Martín, Bonache, Gil, Falcone, Lopetegi, Laso and Sorolla (2004); García-García, Bonache and Martín (2006)].

In the present paper, we deal with capacitively loaded EBG transmission lines, applied to the design of a class of bandpass filters able to provide wide pass bands but wide spurious bands as well. By replacing part of the distributed elements (transmission line sections) with patch loaded lines, the spurious bands can be substantially rejected, as will be shown later. Moreover, filter length is also reduced by the above-mentioned slow-wave effect. This idea was already proposed by some of the authors [García-García, Bonache and Martín (2006)]. Here, the main focus is to provide an automated and systematic synthesis procedure for such EBG-based filters relying on space mapping optimization [Bandler, Biernacki, Chen, Grobelny and Hemmers (1994)], and particularly using quasi-Newton type iteration (namely, implementing an iterative algorithm based on the so-called aggressive space mapping -ASM- [Bandler, Biernacki, Chen, Hemmers, and Madsen (1995)]).

The paper is organized as follows. In section 2, the topology and design of the classical (i.e., EBG-less) filters considered in this work are presented. Section 3 is focused on the considered slow-wave structures. In section 4, the general formulation of ASM is presented for coherence and completeness. In section 5, the ASM is applied to the synthesis of the slow-wave structures necessary to suppress the spurious bands of the filter and reduce device size. Section 6 presents the results, including measurements. Finally, the main conclusions are highlighted in section 7.

## 2. Wideband bandpass filters based on shunt stubs: topology and design

Let us first briefly review the topology and design of the wideband (EBG-less) filters in which the proposed EBG-based filters of this work are inspired. Such filters consist of a cascade of shunt stubs of equal length, alternating with transmission lines of twice the stub electrical length. The analysis of this type of filters was done by Levy [Levy (1970)]. By using $n$ stubs, an insertion function of degree $2n-1$ is implemented in these filters, which are useful to generate wide transmission bands. However, wideband spurious are also present in their frequency response. The schematic of the filter is depicted in Fig. 1. The network shown in Fig. 1 implements the transfer function described in expression (2a) as a function of the normalized frequency variable $\theta = \theta_c f/f_c$ [Hong and Lancaster (2001)]:

$$|S_{21}(\theta)|^2 = \frac{1}{1+\kappa^2 F_n^2(\theta)} \tag{2a}$$

with

$$F_n(\theta) = \frac{\left(1+\sqrt{1-x_c^2}\right)\cdot T_{2n-1}\left(\frac{x}{x_c}\right) - \left(1-\sqrt{1-x_c^2}\right)\cdot T_{2n-3}\left(\frac{x}{x_c}\right)}{2\cdot\cos\left(\frac{\pi}{2}-\theta\right)} \tag{2b}$$

$$x = \sin\left(\frac{\pi}{2}-\theta\right) \tag{2c}$$

$$x_c = \sin\left(\frac{\pi}{2}-\theta_c\right) \tag{2d}$$

where $T_n = \cos\left(n\cdot\cos^{-1}(x)\right)$ and $\kappa$ is the pass band ripple constant. The bandwidth of the filter is delimited by the frequencies $f_c$ and $(\pi/\theta_c - 1)f_c$; therefore, the bandwidth can be controlled by the value of the angle $\theta_c$. The impedance values of the short-circuit stubs and line elements can be chosen for optimum distributed highpass filters according to tabulated element values supplied e.g. in ref. [Hong and Lancaster (2001)].

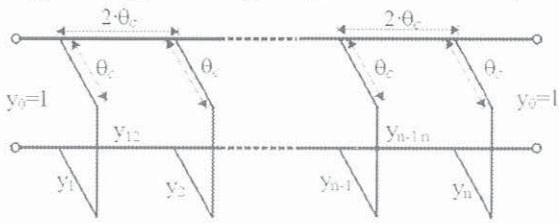


**Figure 1:** Schematic of the wideband bandpass filter where $y_i$ and $y_{jk}$ are the normalized characteristic admittances of the stubs and transmission lines, respectively.

## 3. Slow-wave structures based on capacitively-loaded lines

As mentioned before, the filters considered in the previous section exhibit wide spurious bands, and the first one is close to the band of interest. Such spurious can be eliminated by loading the line sections with patch capacitors [García-García, Bonache and Martín (2006)]. The effect of the capacitances in the line sections is twofold: (i) stop bands appear in the transmission spectrum of these line sections as consequence of periodicity; (ii) the phase velocity is reduced since the effective capacitance per unit length of the line increases. Thus, by loading the line sections with the patch capacitors, not only the filter spurious can be suppressed, but also the filter length can be reduced. Even though the main interest in this paper is to present an automated synthesis method for these capacitively-loaded filters, let us first briefly review the analysis of these capacitively-loaded lines.

In a transmission line periodically loaded with shunt connected capacitances (Fig. 2a), the dispersion relation is [Orellana, Selga, Sans, Rodríguez, Boria, and Martín (2015)]:

$$\cos\beta l = \cos kl - \frac{\omega C_{ls} Z_o}{2}\sin kl \tag{3}$$

where $k$ and $\beta$ are the phase constants of the unloaded and loaded line, respectively, $C_{ls}$ are the loading capacitances, $l$ is the distance between adjacent capacitances (period) and $Z_o$ is the characteristic impedance of the line sections between adjacent

capacitances. According to this dispersion relation, the structure exhibits a low pass filter type response with multiple spurious bands (or multiple stop bands). For design purposes, however, a lumped element circuit model of the capacitively loaded transmission line is convenient. This circuit model is depicted in Fig. 2(b), where $C$ and $L$ are the per-section capacitance and inductance of the line, respectively. This model is valid under the assumption that $C_{ls} >> C$. According to the lumped element equivalent circuit of the periodically loaded line, the first pass band of the structure is delimited by the following cut-off frequency [Martín (2015)]

$$f_B = \frac{1}{\pi\sqrt{L(C + C_{ls})}} \tag{4}$$

the characteristic (or Bloch) impedance of the loaded line at low frequencies is given by

$$Z_B = \sqrt{\frac{L}{C + C_{ls}}} \tag{5}$$

and the lower frequency of the first spurious band is

$$f_S = \frac{1}{2\sqrt{LC}} \tag{6}$$

The slow-wave factor, defined as the ratio between the phase velocity of the loaded and unloaded line is given by

$$swr = \frac{v_p}{v_{po}} = \frac{l/\sqrt{L(C + C_{ls})}}{l/\sqrt{LC}} = \frac{1}{\sqrt{1 + \frac{C_{ls}}{C}}} \tag{7}$$

and the electrical length of the unit cell (3) at low frequencies, i.e., far enough from the Bragg frequency, can be approximated by

$$\phi_{Cell} = \beta l = \omega\sqrt{L(C + C_{ls})} \tag{8}$$

Even though the previous equations are approximate, they are useful for design purposes.

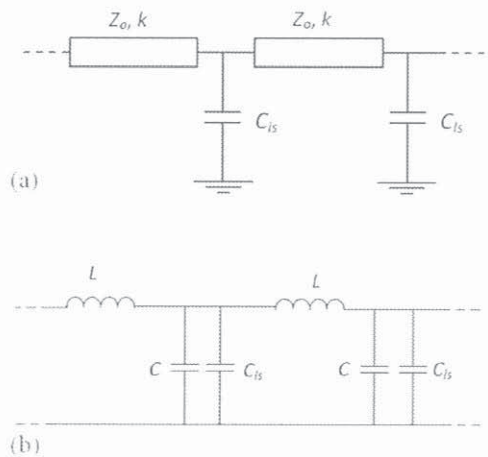


**Figure 2:** Schematic of the slow-wave structure based on a capacitively loaded line (a), and lumped element equivalent circuit model (b).

Note that the number of variables of the circuit model of Fig. 2(b) is three; hence three conditions are needed to determine these element values. The characteristic impedance (expression 5) is one of these conditions, directly dictated from filter specifications. The second one is given by (8), since we must set the phase shift per cell at a given frequency, for instance $f_c$. Inspection of (5) and (8) reveals that these two conditions determine univocally $L$ and $C + C_{ls}$. To infer $C$ and $C_{ls}$, the slow-wave factor (7) was used in [Martín (2015)] as an additional condition. Alternatively, (6) can be used if, rather than the reduction of the line length, the main interest is the control of the stopband bandwidth (note that expression 6 provides the upper limit of the stop band). An important aspect to be considered in the present application of these capacitively-loaded lines concerns the position of the first cutoff frequency, given by (4). This frequency must be forced to be between the first filter pass band (i.e., the band of interest) and the first spurious band; otherwise, either the first spurious is not efficiently suppressed, or the filter cutoff frequency is decreased. However, note that $f_B$ is determined from the phase of the unit cell at the considered frequency (expression 8). From (4) and (8), it follows:

$$\phi_{cell} = \frac{2f_c}{f_B} \tag{9}$$

Since the upper limit of the filter pass band and the lower limit of the first spurious bands are given by $(\pi/\theta_c-1)f_c$ and $(\pi/\theta_c+1)f_c$, it follows that the phase shift per cell is limited by the following values:

$$\frac{2\theta_c}{\pi+\theta_c} < \phi_{cell} < \frac{2\theta_c}{\pi-\theta_c} \tag{10}$$

Now, let us assume that the number of cells of each transmission line section is $N$. This means that $\phi_{cell} = 2\theta_c/N$ at $f_c$, or

$$\pi-\theta_c < N < \pi+\theta_c \tag{11}$$

Thus, according to this analysis, $N$ cannot be arbitrary, and the possible values are dictated by $\theta_c$.

## 4. General formulation of ASM

The expressions (5) and (8) are approximate and therefore, optimization of the patch loaded lines is necessary. Indeed, it is first necessary to find the schematic of such lines (Fig. 2a) providing exactly the required values of Bloch impedance and phase shift, and once this schematic is determined, the next step is the determination of the layout of such artificial lines. Following our previous work [Orellana, Selga, Sans, Rodríguez, Boria, and Martín (2015)], we have implemented two aggressive space mapping (ASM) algorithms; the first one provides the schematic; the second one generates automatically the layout. Our hypothesis is that, once the layouts of the capacitvely loaded transmission line sections are determined, the layout of the filter is simply constructed by cascading these artificial transmission line sections with the shunt stubs, also subjected to a simple ASM optimization algorithm.

For completeness, let us briefly review the general formulation of ASM. In ASM, two simulation spaces are considered [Bandler, Biernacki, Chen, Grobelny and Hemmers (1994); Bandler, Biernacki, Chen, Hemmers, and Madsen (1995)]: (i) the optimization space, $\mathbf{X_c}$, where the variables are linked to a coarse model, which is simple and computationally efficient, although not accurate, and (ii) the validation space, $\mathbf{X_f}$, where the variables are linked to a fine model, typically more complex and CPU intensive, but significantly more precise. In each space, a vector containing the different model parameters can be defined. Let us call such vectors $\mathbf{x_f}$ and $\mathbf{x_c}$ in the fine and coarse model spaces, respectively, and let us designate by $\mathbf{R_f}(\mathbf{x_f})$ and $\mathbf{R_c}(\mathbf{x_c})$ their corresponding responses. The goal in ASM is to minimize the error function in (12) following a quasi-Newton iterative process.

$$\mathbf{f}(\mathbf{x}_\mathbf{f}) = \mathbf{P}(\mathbf{x}_\mathbf{f}) - \mathbf{x}_\mathbf{c}^* \tag{12}$$

where $\mathbf{x_c}^*$ is the coarse model solution that gives the target response, $\mathbf{R_c}(\mathbf{x_c}^*)$, and $\mathbf{P}(\mathbf{x_f})$ is a parameter extraction function that gives the parameters of the coarse model from those of the fine model. Let us assume that $\mathbf{x_f}^{(j)}$ is the $j$-th approximation to the solution in the validation space, and $\mathbf{f}^{(j)}$ the error function corresponding to $\mathbf{f}(\mathbf{x_f}^{(j)})$. The next vector of the iterative process $\mathbf{x_f}^{(j+1)}$ is obtained according to

$$\mathbf{x}_\mathbf{f}^{(j+1)} = \mathbf{x}_\mathbf{f}^{(j)} + \mathbf{h}^{(j)} \tag{13}$$

where $\mathbf{h}^{(j)}$ is given by:

$$\mathbf{h}^{(j)} = -\left(\mathbf{B}^{(j)}\right)^{-1}\mathbf{f}^{(j)} \tag{14}$$

and $\mathbf{B}^{(j)}$ is an approximate to the Jacobian matrix which is also updated by a simplification of the classical Broyden formula [Bandler, Biernacki, Chen, Hemmers, and Madsen (1995); Broyden (1965)] at each iterative step.

$$\mathbf{B}^{(j+1)} = \mathbf{B}^{(j)} + \frac{\mathbf{f}^{(j+1)}\mathbf{h}^{(j)T}}{\mathbf{h}^{(j)T}\mathbf{h}^{(j)}} \tag{15}$$

In (15), $\mathbf{f}^{(j+1)}$ is obtained by evaluating (12) using a certain parameter extraction method providing the coarse model parameters from the fine model parameters, and the super-index $T$ stands for transpose. In the next section, the new proposed two-step ASM synthesis algorithm is explained in detail.

## 5. The ASM algorithm

The specific ASM algorithm for the synthesis of the capacitively-loaded transmission line sections was first presented in [Orellana, Selga, Sans, Rodríguez, Boria, and Martín (2015)]. It was divided in two steps: (i) the determination of the optimum schematic, providing the required specifications, and (ii) the generation of the layout. The first step is necessary since expressions (5) and (8) are approximate. The variables of the coarse space are the three specifications: Bloch impedance, $Z_B$, electrical length per unit cell,

$\beta l$, and slow-wave ratio, *swr*. The response of these variables in the coarse space is simply given by the electrical simulation of the circuit of Fig. 2(b) with the element values inferred from expressions (5), (7) and (8). The variables of the fine model are $Z_o$, $kl$ and $C_{ls}$, and the response of this model is given by the circuit simulation of the schematic of Fig. 2(a).

To initiate this first ASM, we must provide the values of the variables of the fine model according to some criterion. The most straightforward one is to identify $C_{ls}$ with the value of this variable inferred by isolation of (5), (7) and (8). The values of $C$ and $L$ also provide $Z_o$, i.e.,

$$Z_o = \sqrt{\frac{L}{C}} \tag{16}$$

and $kl$, given by:

$$kl = \omega\sqrt{LC} \tag{17}$$

Once the variables of the fine model are determined, the response is obtained by circuit simulation of the schematic (Fig. 2a). From this response (or from analytical expressions provided in [Orellana, Selga, Sans, Rodríguez, Boria, and Martín (2015)]), we extract the variables of the coarse model corresponding to the first iteration $\mathbf{x_c}^{(1)}$. Then, we compare such values with the target ($\mathbf{x_c}^*$) and this gives the first error function (12). After that, the matrix **B** must be calculated. To obtain the first approximation to this matrix, we slightly perturb each variable of the fine model from the first value inferred as indicated above. Then we obtain the circuit response, and from it we obtain the resulting variables of the coarse model corresponding to each perturbation. The relative changes can be expressed in a matrix form as follows:

$$\mathrm{B}^{(1)} = \begin{pmatrix} \dfrac{\delta Z_B}{\delta Z_o} & \dfrac{\delta Z_B}{\delta kl} & \dfrac{\delta Z_B}{\delta C_{ls}} \\ \dfrac{\delta \beta l}{\delta Z_o} & \dfrac{\delta \beta l}{\delta kl} & \dfrac{\delta \beta l}{\delta C_{ls}} \\ \dfrac{\delta swr}{\delta Z_o} & \dfrac{\delta swr}{\delta kl} & \dfrac{\delta swr}{\delta C_{ls}} \end{pmatrix} \tag{18}$$

which corresponds to the initial matrix **B**. Once the matrix $\mathbf{B}^{(1)}$ is known, the fine model parameters of the following iteration can be derived from (14), and the process is iterated until convergence is obtained.

Once the schematic is determined, layout synthesis is achieved by considering a specific ASM algorithm where the dimension of the (square) patch capacitor and the host line length are determined independently (the host line width is not considered an optimization variable since the analytical formulas are very accurate). The specific procedure, detailed in [Orellana, Selga, Sans, Rodríguez, Boria, and Martín (2015)], involves thus two independent sub-ASM processes.

Once the layouts of the capacitively-loaded line sections are determined, determination of the layout of the shunt stubs is required to complete the filter synthesis. However, this last step is simple since only optimization of the stub length is necessary.

## 6. Results

To demonstrate the potential of the proposed ASM scheme, let us consider as an example the synthesis of a filter with the following specifications: $f_c$ = 1 GHz, bandwidth $BW$ = 3 GHz, and 3 stubs (i.e., $n$ = 3). With these filter parameters, the electrical length of the stubs is found to be $\theta_c = 36^\circ$, and that of the transmission line sections is, hence, $2\theta_c = 72^\circ$. The characteristic impedances of the transmission line sections and stubs, as well as their lengths and widths, are indicated in Fig. 3(a), corresponding to the topology of the conventional implementation (the *Rogers RO4003C* substrate with thickness $h$ = 0.813 mm and dielectric constant $\varepsilon_r$ = 3.55 is considered). Fig. 3(b) depicts the simulated frequency response, where the presence of the spurious band, close to the band of interest, can be appreciated (the electromagnetic simulation has been carried out by means of *Keysight Momentum* and the response of the schematic by means of the circuit simulator of *Keysight ADS*).

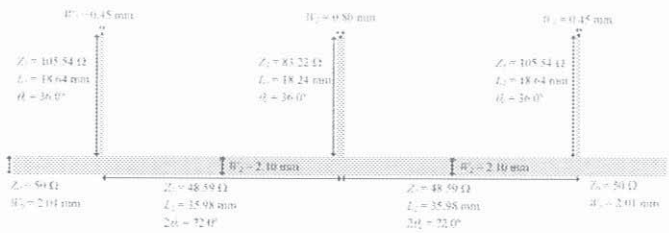

(a)

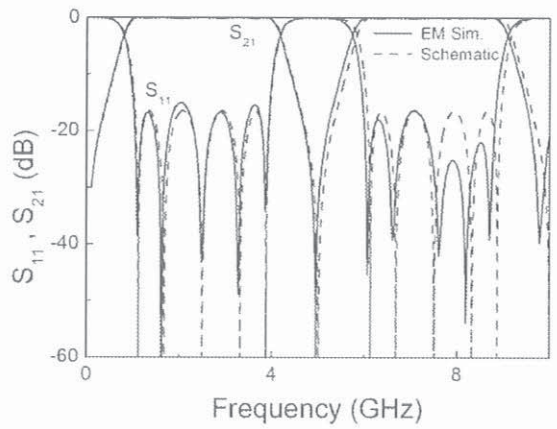


(b)

**Figure 3:** Layout of the conventional filter of the reported example (a) and simulated frequency response (b).

Let us now replace the transmission line sections of characteristic impedance 48.59 Ω with capacitively-loaded slow wave transmission lines. The considered slow wave factor is $swr = 0.5$. According to (11) and the value of $\theta_c$, the number of cells of the transmission lines must be set to $N = 3$. Therefore, $\phi_{cell} = \beta l = 24^{\circ}$. According to these values, inversion of expressions (5), (7) and (8) provides the following element values for the circuit of Fig. 2(b): $C = 0.34$ pF, $C_{ls} = 1.03$ pF and $L = 3.24$ nH. From equations (16)-(17), the values of the first iteration of the fine model, $\mathbf{x_f}^{(1)}$ are: $Z_o = 97.18$ Ω, $kl = 12.0^{\circ}$, and $C_{ls} = 1.03$ pF. Using the first ASM algorithm, we have determined the optimum schematic. Convergence, with a relative error of 0.09%, has been achieved after 2 iterations. The resulting values of the fine model are $Z_o = 98.28$ Ω, $kl = 12.0^{\circ}$, and $C_{ls} = 1.01$ pF. The electrical length and characteristic impedance of the schematic (unit cell) using the previous values of the fine model parameters is depicted in Fig. 4. The frequency response that results by cascading three cells is shown in Fig. 5. In view of these figures, at schematic level the resulting electrical length at $f_c$, Bloch impedance and slow-wave factor of the cell after convergence are found to be $Z_B = 48.62$ Ω, $\phi_{cell} = 23.99^{\circ}$ and $swr = 0.50$, respectively.

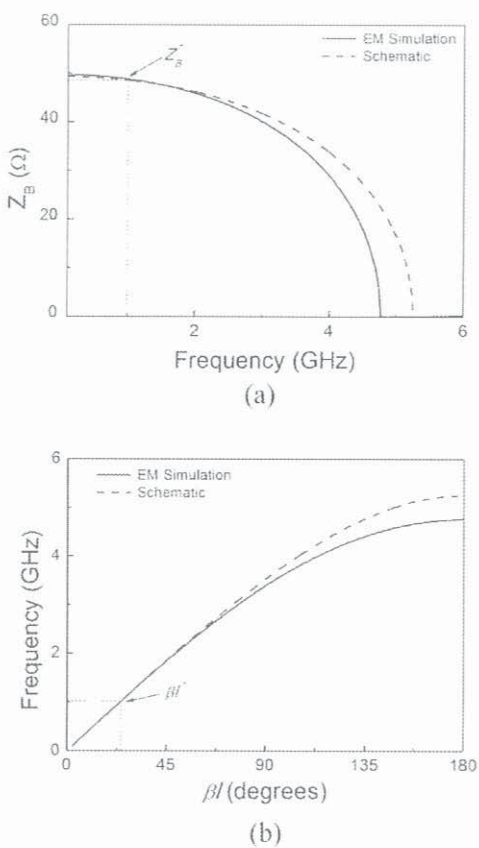


**Figure 4:** Characteristic impedance (a) and electrical length (b) of the synthesized unit cell.

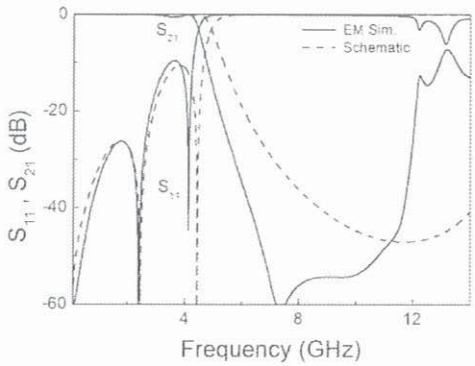


**Figure 5:** Frequency response of the synthesized artificial transmission line consisting of three cells.

Once the optimum schematic has been obtained, the application of the second ASM has led us to the layout (unit cell) depicted in Fig. 6. The response of this structure, considering three cells, inferred from electromagnetic simulation using the *Keysight Momentum* commercial simulator, is also depicted in Fig. 5, and reveals that the Bragg frequency lies between the upper cutoff frequency of the first pass band and the lower cutoff frequency of the spurious band. There is some discrepancy between the response of the schematic and the one inferred from electromagnetic simulation due to the fact that the model of the patch capacitors is valid at low frequencies (such discrepancies can be also appreciated in Fig. 4). Nevertheless, the Bragg frequency obtained from electromagnetic simulation has the correct value, and a huge stop band, useful for the suppression of the spurious band of the filter, results.

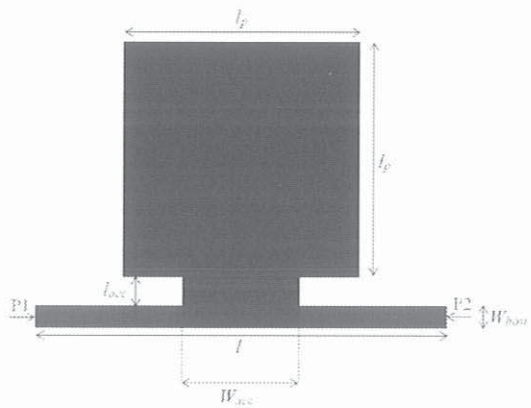


**Figure 6:** Layout of the unit cell. Dimensions are: $l = 6.767$ mm, $l_p = 4.282$ mm, $W_{acc} = 2.141$ mm ($0.5l_p$), $l_{acc} = 0.583$ mm, $W_{host} = 0.475$ mm

By cascading three unit cells, we have constructed the capacitively-loaded transmission line sections of the filter. The final layout of the filter is depicted in Fig. 7(b), where it is compared to the conventional one in Fig. 7(a). The responses (inferred from lossless electromagnetic simulation) are compared in Fig. 7(c). The filter has been fabricated by

means of a *LPKF-H100* drilling machine and has been characterized by means of the *Agilent E8364B* vector network analyzer. The photograph of the prototype is depicted in Fig. 8(a), whereas Fig. 8(b) depicts the measured frequency response compared to the one inferred from electromagnetic simulation (including losses). Thanks to the presence of the capacitively loaded lines, significant attenuation of the spurious band (better than 36 dB up to 10 GHz) is achieved.

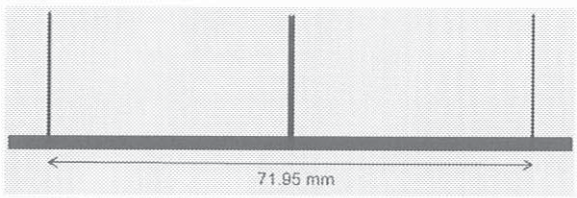


(a)

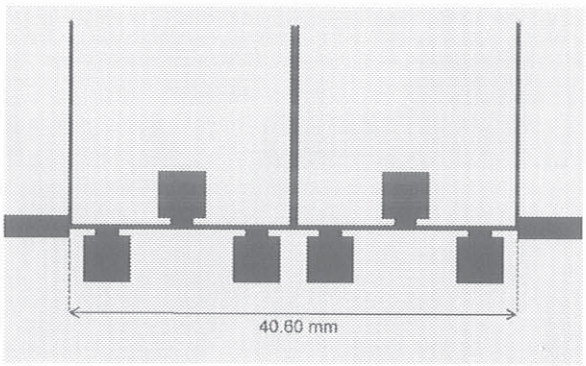


(b)

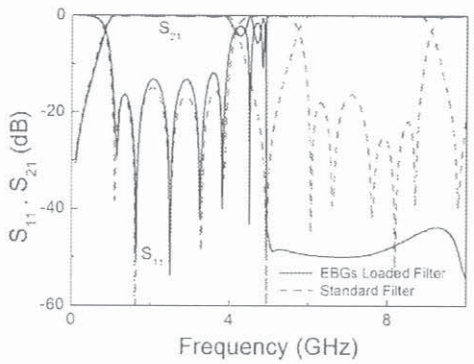


(c)

**Figure 7:** Layout of the conventional filter (a), layout of the synthesized EBG loaded filter (b), and simulated frequency response of both filters (c). Dimensions are indicated.

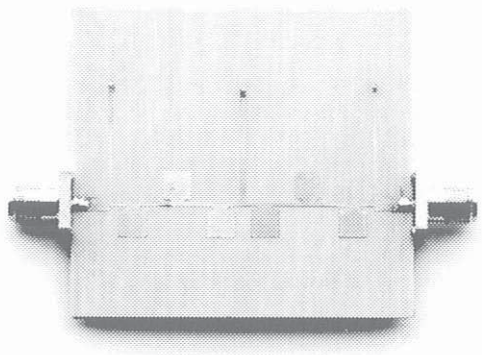

(a)

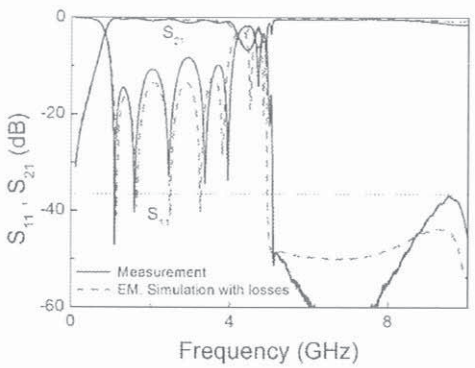


(b)

**Figure 8:** Photograph of the fabricated filter (a) and frequency response (b).

## 7. Conclusions

In summary, it has been demonstrated that aggressive space mapping (ASM) optimization can be applied to the synthesis of wideband bandpass filters based on capacitively-loaded electromagnetic bandgap (EBG) transmission lines. A systematic design approach, based on a two-step ASM iterative algorithm, where first the optimum circuit schematic is determined, and then the filter layout is generated, has been presented. Thanks to the slow wave effect of the capacitively loaded lines, significant compactness, as compared to the conventional filter implementation, has been achieved. Moreover, the designed filter is spurious free up to high frequencies due to the reflection properties of the EBG-based transmission lines.

## Acknowledgements

This work has been supported by MINECO (Spain) under projects TEC2013-40600-R and TEC2013-49221-EXP, by AGAUR-Generalitat de Catalunya under project 2014SGR-157, and by FEDER funds. Ferran Martín is in debt to Institució Catalana de Recerca i Estudis Avançats (ICREA) for supporting his work. Marco Orellana acknowledges the support of the *Universidad de Costa Rica*, MICITT and CONICIT to study at the *Univesitat Autònoma de Barcelona*.

## References

**Abdel Aziz, M.; Issa, H.; Kaddour, D.; Podevin, F.; Safwat, A.M.E.; Pistono, E.; Duchamp, J.-M.; Vilcot, A.; Fournier, J.-M.; Ferrari, P.** (2012): Slow-wave high-Q coplanar striplines in CMOS technology and their RLCG model, *Microw. Opt. Techn. Lett.*, vol. 54, pp. 650-654.

**Bandler, J.W.; Biernacki, R.M.; Chen, S.H.; Grobelny, P.A.; Hemmers, R.H.** (1994): Space mapping technique for electromagnetic optimization, *IEEE Trans. Microw. Theory Tech.*, vol. 42, pp. 2536-2544.

**Bandler, J.W.; Biernacki, R.M.; Chen, S.H.; Hemmers, R.H.; Madsen, K.** (1995): Electromagnetic optimization exploiting aggressive space mapping, *IEEE Trans. Microw. Theory Tech.*, vol. 43, pp. 2874-2882.

**Broyden, C. G.** (1965): A Class of Methods for Solving Nonlinear Simultaneous Equations, *Mathematics of Computation*, vol. 19, no. 92, pp. 577-593.

**Erro, M. J.; Laso, M. A. G.; Lopetegi, T.; Benito, D.; Garde, M. J.; Sorolla, M.** (2000): Optimization of tapered bragg reflectors in microstrip technology, *Int. J. Infrared Millimeter Waves*, vol. 21, pp. 231- 245.

**Falcone, F.; Lopetegi, T.; Irisarri, M.; Laso, M. A. G.; Erro, M. J.; Sorolla, M.** (1999): Compact photonic bandgap microstrip structures, *Microw. Opt. Techn. Lett.*, vol 23, pp. 233-236.

**Franc, A.-L.; Kaddour, D.; Issa, H.; Pistono, E.; Corrao, N.; Fournier, J.-M.; Ferrari, P.** (2010): Impact of technology dispersion on slow-wave high performance shielded CPW transmission lines characteristics, *Microw. Opt. Techn. Lett.*, vol. 52, pp. 2786, 2789.

**García-García, J.; Bonache, J.; Martín, F.** (2006): Application of electromagnetic bandgaps (EBGs) to the design of ultra wide band pass filters (UWBPFs) with good out-of-band performance, *IEEE Trans. Microw. Theory Tech.*, vol. 54, pp. 4136-4140.

**Görür, A.** (1994): A novel coplanar slow-wave structure, *IEEE Microw. Guided Wave Lett.*, vol. 4, pp. 86–88.

**Görür, A.; Karpuz, C.; Alkan, M.** (1998): Characteristics of periodically loaded CPW structures, *IEEE Microw. Guided Wave Lett.*, vol. 8, pp. 278-280.

**Hang, C. Y.; Radisic, V.; Qian, Y.; Itoh, T.** (1999): High efficiency power amplifier with novel PBG ground plane for harmonic tuning, *IEEE MTT-S Int. Microw. Symp. Dig.*, Anaheim, CA, June 1999, pp. 807-810.

**Hong, J.-S.; Lancaster, M.L.** (2001): *Microstrip Filters for RF/Microwave Applications*, New York, John Wiley.

**Joannopoulos, J. D.; Meade, R. D.; Winn, J. N.** (1995): *Photonic Crystals: Molding the Flow of Light*, Princeton, NJ, Princeton University Press.

**Kaddour, D.; Issa, H.; Franc, A.-L.; Corrao, N.; Pistono, E.; Podevin, F.; Fournier, J.-M.; Duchamp, J.-M.; Ferrari, P.** (2009): High-Q slow-wave coplanar transmission lines on 0.35-μm CMOS process, *IEEE Microw. Wireless Compon. Lett.*, vol. 19, pp. 542-544.

**Laso, M. A. G.; Lopetegi, T.; Erro, M. J.; Benito, D.; Garde, M. J.; Sorolla M.** (2000): Multiple-frequency-tuned photonic bandgap microstrip structures, *IEEE Microw. Guided Wave Lett.*, vol. 10, pp. 220-222.

**Laso, M. A. G.; Lopetegi, T.; Erro, M. J.; Benito, D.; Garde, M. J.;Sorolla, M.** (2000): Novel wideband photonic bandgap microstrip structures, *Microw. Opt. Techn. Lett.*, vol. 24, pp. 357-360.

**Lee, Y. T.; Lim, J. S.; Park, J. S.; Ahn, D.; Nam, S.** (2002): A novel phase noise reduction technique in oscillators using defected ground structure, *IEEE Microw. Wireless Compon. Lett.*, vol. 12, pp. 39-41.

**Levy, R.** (1970): A new class of distributed prototype filters with applications to mixed lumped/distributed component design, *IEEE Trans. Microw. Theory Tech.*, vol. 18, pp. 1064-1071.

**Lopetegi, T.; Falcone, F.; Sorolla, M.** (1999): Bragg reflectors and resonators in microstrip technology based on electromagnetic crystal structures, *Int. J. Infrared Millimeter Waves*, vol. 20, pp. 1091-1102.

**Lopetegi, T.; Laso, M.A.G.; Hernández, J.; Bacaicoa, M.; Benito, D.; Garde, M.J.; Sorolla, M.; Guglielmi, M.** (2001): New microstrip wiggly-line filters with spurious passband suppression, *IEEE Trans. Microw. Theory Tech.*, vol. 49, pp 1593-1598.

**Lopetegi, T.; Laso, M.A.G.; Falcone, F.; Martín, F.; Bonache, J.; Pérez-Cuevas, L.; Sorolla, M.** (2004): Microstrip wiggly line band pass filters with multispurious rejection, *IEEE Microw. Wireless Compon. Lett.*, vol. 14, pp.531-533.

**Martín, F.; Falcone, F.; Bonache, J.; Lopetegi, T.; Laso, M.A.G.; Sorolla, M.** (2002): New periodic-loaded electromagnetic bandgap coplanar waveguide with complete spurious passband suppression, *IEEE Microw. Wireless Compon. Lett.*, vol. 12, pp. 435-437.

**Martín, F.; Falcone, F.; Bonache, J.; Laso, M.A.G.; Lopetegi, T.; Sorolla, M.** (2003): Dual electromagnetic bandgap CPW structures for filter applications, *IEEE Microw. Wireless Compon. Lett.*, vol. 13, pp. 393-395.

**Martín, F.; Falcone, F.; Bonache, J.; Laso, M.A.G.; Lopetegi, T.; Sorolla, M.** (2003): New CPW low pass filter based on a slow wave structure, *Microw. Opt. Techn. Lett.*, vol. 38, pp. 190-193.

**Martín, F.; Bonache, J.; Gil, I.; Falcone, F.; Lopetegi, T.; Laso, M.A.G.; Sorolla, M.** (2004): Compact spurious free CPW band pass filters based on electromagnetic bandgap structures, *Microw. Opt. Techn. Lett*, vol. 40, pp. 146-148.

**Martín, F.** (2015): "*Artificial Transmission Lines for RF and Microwave Applications*", John Wiley, Hoboken, NJ.

**Nesic, D.** (2002): A new type of slow-wave 1-D PBG microstrip structure without etching in the ground plane for filter and other applications, *Microw. Opt. Techn. Lett.*, vol. 33, pp. 440-443.

**Orellana, M.; Selga, J.; Sans, M.; Rodríguez, A.; Boria, V.; Martín, F.** (2015): Synthesis of slow-wave structures based on capacitive-loaded lines through aggressive space mapping (ASM), *International Journal of RF and Microwave Computer-Aided Engineering*, vol. 25, pp. 629-638.

**Qian, Y.; Radisic, V.; Itoh, T.** (1997): Simulation and experiment of photonic band-gap structures for microstrip circuits, *Proc. Asia-Pacific Microwave Conf.*, Hong Kong, Dec. 1997, pp. 585-588.

**Radisic, V.; Qian, Y.; Itoh, T.** (1998): Broad-band power amplifier using dielectric photonic bandgap structure, *IEEE Microw. Guided Wave Lett.*, vol. 8, pp. 13-14.

**Sor, J.; Qian, Y.; Itoh, T.** (2001): Miniature low-loss CPW periodic structures for filter applications, *IEEE Trans. Microw. Theory Tech.*, vol. 49, pp. 2336-2341.

**Xue, Q.; Shum, K. M.; Chan, C. H.** (2001): Novel oscillator incorporating a compact microstrip resonant cell, *IEEE Microw. Wireless Compon. Lett.*, vol. 11, pp. 202-204.

**Yablonovitch, E.** (1993): Photonic band gap structures, *J. Opt. Soc. Amer. B* 10, pp. 283-295.

**Yang, F. R.; Qian, Y.; Itoh, T.** (1999): A novel uniplanar compact PBG structure for filter and mixer applications, *IEEE MTT-S Int. Microw. Symp. Dig.*, Anaheim, CA, June 1999, pp. 919-922.

**Yun, T-Y.; Chang, K.** (2001): Uniplanar one-dimensional photonic-bandgap structures and resonators, *IEEE Trans. Microw. Theory Tech.*, vol. 49, pp. 549-553.

# Artículos de la parte no Fundamental de la Tesis

# Design of Capacitively-Loaded Coupled Line Bandpass Filters with Compact Size and Spurious Suppression

Marco Orellana, Jordi Selga, *Member IEEE*, Paris Vélez, *Member IEEE*, Marc Sans, Ana Rodríguez, *Member IEEE*, Jordi Bonache, *Member IEEE*, Vicente E. Boria, *Senior Member IEEE*, and Ferran Martín, *Fellow IEEE*

***Abstract*— This paper is focused on the synthesis of capacitively-loaded coupled lines for the design of bandpass filters with compact size and spurious suppression. The filters consist of cascaded pairs of coupled lines periodically-loaded with patch capacitors. The loading capacitances provide a slow-wave effect to the coupled lines useful for filter miniaturization, whereas periodicity introduces band gaps that can be controlled in order to achieve spurious suppression. Filter design is achieved following an automated process based on aggressive space mapping (ASM) optimization. The two reported examples, a 3rd-order filter with central frequency $f_0$ = 1.0 GHz, 8 % fractional bandwidth and 0.1 dB ripple level, and a 5th-order filter with central frequency $f_0$ =1.8 GHz, 8 % fractional bandwidth and 0.1 dB ripple level, demonstrate the potential of the proposed ASM-based design approach, as well as the effectiveness of the loading capacitances to reduce filter size and reject the spurious bands. Significant size reduction in both filters is achieved, whereas the out-of-band rejection is better than 30 dB and 45 dB in the order-3 and order-5 filter, respectively, up to at least $4f_0$.**

***Index Terms*– Bandpass filters, slow-wave transmission lines, coupled lines, electromagnetic bandgap (EBG), circuit synthesis, microstrip technology, space mapping (SM).**

## I. INTRODUCTION

Size reduction and spurious suppression have been (and are still) two challenging issues in planar microwave filter design. There are many approaches to achieve compact size and/or spurious cancellation. Among them, periodic transmission lines, including non-uniform and reactively loaded lines, have been used as building blocks for the design of microwave filters, where the ordinary lines are replaced with these artificial lines (see [1] and references therein).

Periodicity gives rise to stop bands, due to the well known Bragg effect [2],[3]. Such periodicity can typically be achieved by modulating the transverse dimensions of the line [1],[4],[5] or by etching holes (or other patterns) in the ground plane [6]-[10]. The result is a periodic variation of the line impedance (and coupling coefficient [1],[11]-[13]), that causes the appearance of stop bands useful for spurious suppression. To this end, it is necessary to tune the period of the lines in order to set the Bragg frequency, where maximum attenuation occurs, within the spurious band [4]. Multiple tuned periodic transmission lines can also be designed in order to achieve signal rejection at various (desired) frequencies [10]. By using this strategy, efficient multi-spurious suppression in coupled line bandpass filters has been demonstrated [14].

By modulating the transverse dimensions of the line, significant rejection (and hence efficient spurious suppression) can be obtained. However, this strategy has not impact on filter size. For size reduction and simultaneous spurious rejection, transmission line sections with periodically-loaded capacitors become a solution [15]-[18]. Periodicity is responsible for spurious elimination, as discussed before, whereas the loading capacitors enhance the effective capacitance of the line, thus reducing the phase velocity. These periodic capacitively-loaded slow-wave transmission lines are therefore promising candidates for the purpose of this paper, i.e., the design of compact and spurious free bandpass filters based on coupled lines. Nevertheless, the application of these slow-wave structures to the design and implementation of other compact and spurious-suppressed filters has been demonstrated [19]-[22]. Capacitively-loaded lines have also been applied to the miniaturization of couplers [23], and other periodic slow-wave structures based on inductive [24] or combined inductive/capacitive [25]-[30] loading have been reported. The slow-wave concept based on capacitive or dielectric loading has also been used for size reduction in CMOS passive and active devices operating at millimeter wavelengths [31]-[35].

In this paper, slow-wave coupled lines based on patch capacitors [36]-[39] are applied to the implementation of compact bandpass filters with wide stop band (this paper is indeed an extended version of the paper [40]). Special emphasis is put on justifying the conditions to achieve efficient cancellation of the spurious bands (related to the number of patch capacitors per coupled line section), and we present an accurate design methodology for the capacitively-loaded coupled lines (CLCLs). The design approach is based on aggressive space mapping (ASM) optimization [41]-[47], where the layouts of the coupled lines are unattendedly generated from the design parameters (even/odd mode impedances and electrical length) provided by the specifications, and from the required slow-wave

This work was supported by MINECO-Spain (projects TEC2013-47037-C5-1-R, TEC2013-40600-R, TEC2013-49221-EXP), *Generalitat de Catalunya* (project 2014SGR-157), *Institució Catalana de Recerca i Estudis Avançats* (who awarded Ferran Martín), and by FEDER funds. Marco Orellana acknowledges the support of the Universidad de Costa Rica, MICITT and CONICIT.

M. Orellana, J. Selga, P. Vélez, M. Sans, J. Bonache and F. Martín are with GEMMA/CIMITEC, Departament d'Enginyeria Electrònica, Universitat Autònoma de Barcelona, 08193 Bellaterra, Spain. E-mail: Ferran.Martin@uab.es.

A. Rodríguez and V. E. Boria are with Departamento de Comunicaciones-iTEAM, Universitat Politècnica de València, 46022 Valencia, Spain. E-mail: vboria@dcom.upv.es.

factor (which determines the level of miniaturization of the final filter as compared to the conventional counterpart).

The paper is organized as follows. In Section II, the topology of the CLCLs, the circuit model of the unit cell, and the main design equations, are presented. From these equations, we are able to obtain the schematic of the coupled lines, which is the starting point for optimization using the developed ASM algorithm (presented in Section III). Two filter examples, where the synthesized coupled line sections are merely cascaded, are reported in Section IV. Finally, the main conclusions of this work are highlighted in Section V.

## II. TOPOLOGY OF THE CAPACITIVELY-LOADED COUPLED LINES, MODELING AND DESIGN

The topology and circuit schematic of the proposed CLCLs (unit cell) are depicted in Fig. 1(a) and (b), respectively. The square patches are described by the two capacitances $C_{ls}$ (note that the inductive effect of the wide and short strip connecting the patches to the coupled lines is neglected). The impedances $Z_{oe}$ and $Z_{oo}$ are the characteristic impedances of the even and odd modes, respectively, of the unloaded coupled lines, whereas $k_e$ and $k_o$ are the phase constants for such modes. Hence, the electrical lengths of the unloaded coupled lines are $\phi_e = k_e l$ (even mode) and $\phi_o = k_o l$ (odd mode), provided $l$ is the physical length of such lines. The equivalent circuits for the even and odd modes, inferred by removing one of the halves and considering the bi-section symmetry plane as a magnetic (even mode) and an electric (odd mode) wall, are depicted in Fig. 1(c) and (d). In this work, it is assumed that the coupling between the square patches is negligible.

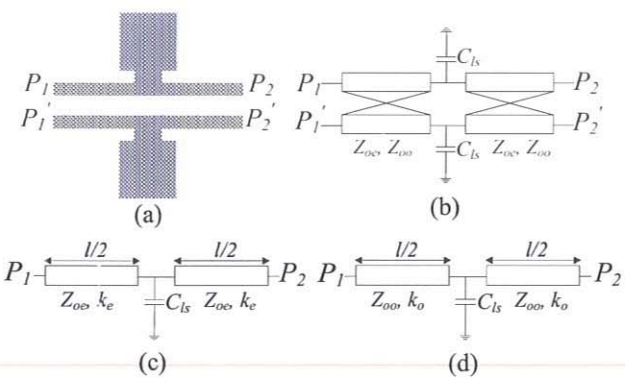


Fig. 1. Typical topology (unit cell) of the CLCLs (a), equivalent circuit schematic (b), and circuit model for the even (c) and odd (d) modes.

The dispersion relation for the even mode is given by [1]

$$\cos(\beta_e l) = \cos(k_e l) - \frac{\omega C_{ls} Z_{oe}}{2} \sin(k_e l) \tag{1}$$

whereas the characteristic (Bloch) impedance is

$$Z_{Be} = \frac{Z_{oe}\left\{\sin(k_e l) - Z_{oe}\omega C_{ls} \sin^2(k_e l/2)\right\}}{\sin(\beta_e l)} \tag{2}$$

where $\beta_e$ is the phase constant of the loaded coupled lines for the even mode (providing an electrical length of $\varphi_e = \beta_e l$ for that mode), and $\omega = 2\pi f$ is the angular frequency. Formally, identical expressions are obtained for the dispersion and Bloch impedance of the odd mode by simply changing the sub-indices, i.e.,

$$\cos(\beta_o l) = \cos(k_o l) - \frac{\omega C_{ls} Z_{oo}}{2} \sin(k_o l) \tag{3}$$

$$Z_{Bo} = \frac{Z_{oo}\left\{\sin(k_o l) - Z_{oo}\omega C_{ls} \sin^2(k_o l/2)\right\}}{\sin(\beta_o l)} \tag{4}$$

Note that, contrary to ordinary coupled lines, these CLCLs are intrinsically dispersive and exhibit pass bands and stop bands for both modes [1],[20]. In this work, the considered CLCL-based bandpass filters will be designed to operate in the first allowed band of their constitutive CLCLs, whereas the first rejected band of the CLCLs will be tailored in order to suppress the spurious bands, unavoidable in ordinary coupled line bandpass filters. The presence of the patch capacitors modifies the coupling level of the unloaded lines, but the impedances of the even and odd modes of the loaded coupled lines, as well as the electrical length at the frequency of interest, can be adjusted to the values required by design.

An important parameter in capacitively-loaded artificial lines is the slow-wave ratio, defined as the ratio between the phase velocities of the loaded and unloaded line, or equivalently, as the ratio between the phase constants of the unloaded and loaded lines. Since the phase velocities (or phase constants) for each mode (even and odd) in coupled lines are not (in general) identical (although very similar if the coupling level is small), the slow-wave ratio should be defined for each mode, i.e.,

$$swr_e = \frac{k_e l}{\beta_e l} \tag{5}$$

$$swr_o = \frac{k_o l}{\beta_o l} \tag{6}$$

### *A. Design of the CLCLs: determination of the circuit schematic*

Let us now use the previous equations for the determination of the circuit schematic of the CLCLs able to satisfy certain specifications. This means to provide the electrical parameters of the circuit of Fig. 1(b), i.e., $C_{ls}$, $Z_{oe}$, $Z_{oo}$, and either $k_e l$ or $k_o l$ (since $k_e l$ and $k_o l$ are mutually dependent through $Z_{oe}$, $Z_{oo}$). With regard to the specifications, since the purpose of this work is the design of coupled line bandpass filters, the even and odd mode impedances of the CLCLs ($Z_{Be}$ and $Z_{Bo}$) are dictated by filter specifications (order, fractional bandwidth and ripple level) according to well-known formulas [48]. Note however that, due to dispersion, the Bloch impedances are frequency dependent, and therefore the required values of $Z_{Be}$ and $Z_{Bo}$ are forced to be satisfied at the filter central frequency, $f_0$. Each CLCL section (composed at least of one unit cell) should exhibit an electrical length at $f_0$ of $\pi/2$ for each mode (as corresponds to conventional parallel coupled line bandpass filters). Since this is not possible in practice (at least in microstrip technology), an alternative condition depending on these two electrical lengths is necessary. For instance, we can force the average electrical length of the CLCL section corresponding to the two modes to satisfy this requirement, or

$$N\frac{\left(\varphi_e\big|_{f_0} + \varphi_o\big|_{f_0}\right)}{2} = \frac{\pi}{2} \tag{7}$$

where $N$ is the number of unit cells of the loaded coupled line (nevertheless, it has been found that there is a more appropriate condition, to be discussed later). Finally, a fundamental parameter that determines the level of miniaturization of the final filter is the slow-wave ratio. We will set the slow-wave ratio corresponding to the even mode, $swr_e$, to a predefined value. Note, however, that $swr_e$ is not related to filter performance, but only to filter size. The fact that the circuit schematic of the CLCLs [Fig. 1(b)] includes an additional parameter ($C_{ls}$), as compared to ordinary coupled lines, is the key factor in having certain control on filter size reduction.

Inspection of equations (1)-(7) reveals that there are eight unknowns in the model, that is, $C_{ls}$, $Z_{oe}$, $Z_{oo}$, $k_el$, $k_ol$, $swr_o$, $\beta_ol$ and $\beta_el$ ($Z_{Be}$, $Z_{Bo}$ and $swr_e$ are fixed according to the previous paragraph). However, as previously mentioned, $k_el$ and $k_ol$ are linked through $Z_{oe}$ and $Z_{oo}$, which means that all model parameters can be univocally determined. To this end, we have proceeded as follows. We provide a guess value for $\varphi_e = \beta_el$. From (1) and (5) evaluated at $\omega_0 = 2\pi f_0$ we obtain

$$C_{ls}Z_{oe} = \frac{2\{\cos(swr_e \cdot \beta_e l) - \cos(\beta_e l)\}}{\omega_o \sin(swr_e \cdot \beta_e l)} \tag{8}$$

where all the parameters in the right hand side are known. By introducing (8) in (2), we can express $Z_{oe}$ as a function of $Z_{Be}$, $swr_e$ and $\beta_el$, that is

$$Z_{oe} = \frac{Z_{Be} \cdot \sin(\beta_e l)}{\sin(swr_e \cdot \beta_e l) - C_{ls}Z_{oe}\omega_0 \sin^2(swr_e \cdot \beta_e l/2)} \tag{9}$$

provided $C_{ls}Z_{oe}$ in the denominator of (9) is given by (8). Once $Z_{oe}$ is known, $C_{ls}$ is calculated from (8). Note also that $k_el$ is known from (5). The determination of the four remaining parameters ($Z_{oo}$, $k_ol$, $swr_o$ and $\beta_ol$) is not simple since the relation between $k_el$ and $k_ol$ (through $Z_{oe}$ and $Z_{oo}$) depends on substrate parameters. Thus, we have proceed by providing a tentative value of $swr_o$, starting with $swr_o = swr_e$, and numerically solving equations (3), (4) and (6). With the resulting element values ($Z_{oo}$, $k_ol$ and $\beta_ol$) and substrate parameters, we check if $k_ol$ and $k_el$ are compatible. If this is not the case, we sweep $swr_o$ until the resulting values of $k_ol$ and $k_el$ are compatible with $Z_{oo}$, $Z_{oe}$, and the parameters of the substrate (which provide the transverse geometry of the unloaded coupled lines). We repeat this procedure until the condition (7), or another equivalent condition, to be specified later, is satisfied.

Let us consider as an example the design of a pair of capacitively-loaded coupled lines with $Z_{Be} = 72.12\ \Omega$ and $Z_{Bo} = 38.91\ \Omega$, $swr_e = 0.5$ and $(\varphi_e + \varphi_o)/2 = \pi/4$ at 2.4 GHz. The application of the previous procedure, considering the parameters of the *Rogers RO3010* substrate with dielectric constant $\varepsilon_r = 10.2$ and thickness $h = 1.27$ mm, gives $C_{ls} = 0.57$ pF, $Z_{oe} = 152.76\ \Omega$, $Z_{oo} = 58.65\ \Omega$, $k_el = 26.6^\circ$, $k_ol = 24.9^\circ$, $swr_o = 0.68$, $\beta_el = 53.2^\circ$, and $\beta_ol = 36.9^\circ$. From these values, we have obtained the four-port S-parameters of the schematic, and from these values and well known transformations [49], we have inferred the S-parameters for the even and odd modes. By transformation to *ABCD* parameters, we have then obtained the Bloch impedance and electrical length for each mode [1],[48]. The results, depicted in Fig. 2, demonstrate that the target values are satisfied to a good approximation.

Once the electrical parameters of the CLCL are found, the next step is to determine the layout (unit cell). To this end, an aggressive space mapping (ASM) optimization algorithm is developed (it will be discussed in the next section). The seeding layout, necessary to initiate such ASM algorithm, is obtained from the value of $C_{ls}$, which gives the dimensions of the patch capacitors according to the parallel plate capacitor formula, from $Z_{oo}$ and $Z_{oe}$, which provide the width and separation of the unloaded coupled lines, and from $k_ol$ and $k_el$, which provide their length. A commercial transmission line calculator (such as the one included in *Keysight* Momentum) can be used to determine the width, separation and length of the unloaded coupled lines. As can be seen in Fig. 2, the full-wave EM simulation of the layout (unit cell) agrees very well with the results of the designed circuit schematic.

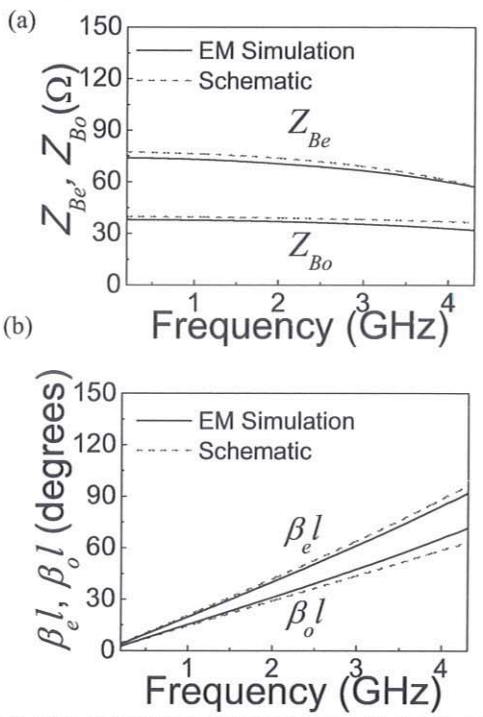


Fig. 2. Even and odd mode Bloch impedance (a) and electrical length (b) corresponding to the schematic of the designed CLCL unit cell reported in the example.

### *B. Optimizing spurious suppression*

In the preceding subsection, it has been assumed that the number of cells per coupled line section, $N$, is not a design parameter. However, $N$ determines the onset and bandwidth of the first stopband of the CLCL (as will be shown), and hence it should not be arbitrarily chosen. $N$ must be determined according to a systematic procedure, in order to guarantee that the first and a certain number of spurious bands of the bandpass filter under design are efficiently suppressed. Such procedure, based on the approximate lumped element equivalent circuit model of the unit cell, is presented and discussed in this subsection. Such model, depicted in Fig. 3, assumes that the interaction between both lines is dominated by electric coupling, and that the electrical length of the unit cell is small. These approximations are reasonable provided the intention is to estimate the effects of $N$ on spurious suppression, rather than to use this model for design purposes. $L$ and $C$ are the inductance and capacitance of the lines, $C_{ls}$ is the capacitance of the square patches (as mentioned before),

and $C_c$ is the coupling capacitance between the lines. The models for even and odd mode excitation are also included in Fig. 3.

The dispersion and Bloch impedances of the models of Figs. 1(c) and (d) and the corresponding models of Figs. 3 (b) and (c) converge at low frequencies (small electrical length) and tend to diverge as the frequency approaches the cutoff frequencies of the fundamental modes (even and odd modes). Such frequencies determine the onset of the stop band for each mode, caused by the periodicity. Nevertheless, if $C_{ls}/C >> 1$, the discrepancy between both models is very small up to the cutoff frequencies, as it has been demonstrated in reference to single-ended capacitively-loaded transmission lines [1]. The previous condition ($C_{ls}/C >> 1$) is roughly satisfied in this work, since one of the objectives is to achieve significant miniaturization, and this is intimately related to the ratio $C_{ls}/C$, as will be later shown.

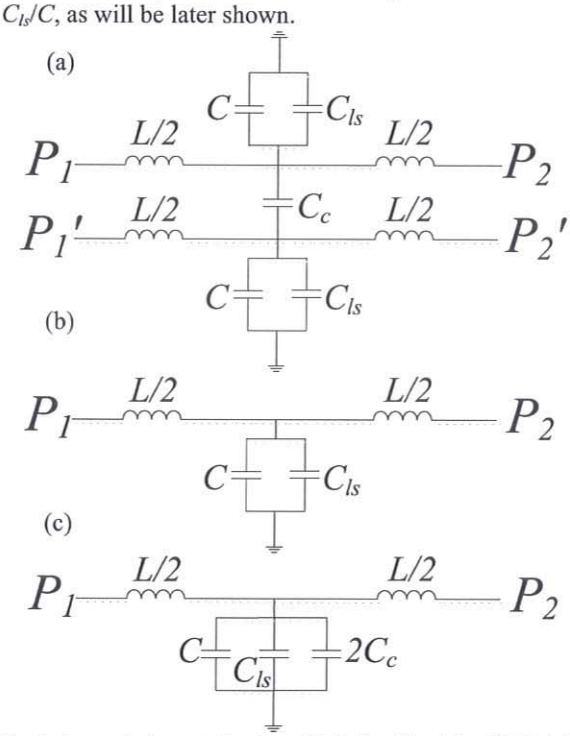


Fig. 3. Lumped element circuit model (unit cell) of the CLCL (a), and circuit model for even (b) and odd (c) mode excitation.

Even though CLCLs are dispersive (as mentioned before), under the long wavelength approximation (far enough from the cutoff frequencies), it can be assumed that the even and odd mode Bloch impedances are frequency independent and given by:

$$Z_{Be} = \sqrt{\frac{L}{C + C_{ls}}} \tag{10a}$$

$$Z_{Bo} = \sqrt{\frac{L}{C + C_{ls} + 2C_c}} \tag{10b}$$

as derived from the equivalent circuits for the even and odd modes, depicted in Fig. 3. Similarly, the electrical lengths (unit cell) for the even and odd modes can be expressed as linear functions of frequency, i.e.,

$$\varphi_{e,cell} = \beta_e l = \omega\sqrt{L(C + C_{ls})} \tag{11a}$$

$$\varphi_{o,cell} = \beta_o l = \omega\sqrt{L(C + C_{ls} + 2C_c)} \tag{11b}$$

In the framework of the lumped (even and odd) models, the slow-wave factors for each fundamental mode are given by

$$swr_e = \frac{k_e l}{\beta_e l} = \frac{\omega\sqrt{LC}}{\omega\sqrt{L(C + C_{ls})}} = \frac{1}{\sqrt{1 + \frac{C_{ls}}{C}}} \tag{12a}$$

$$swr_o = \frac{k_o l}{\beta_o l} = \frac{\omega\sqrt{L(C + 2C_c)}}{\omega\sqrt{L(C + C_{ls} + 2C_c)}} = \frac{1}{\sqrt{1 + \frac{C_{ls}}{C + 2C_c}}} \tag{12b}$$

Under low coupling level (satisfied if $C >> 2C_c$), the phase constants and slow-wave factors for both modes can be assumed to be roughly the same. Although it is not possible to achieve tightly couples lines in edge coupled configurations, depending on the required filter bandwidth the coupling level between the lines may be moderate, and therefore the above condition ($C >> 2C_c$) is not strictly valid necessarily. Nevertheless, for the purpose of this subsection, we will assume that the phase constants and slow-wave factors for both modes are identical. The reason is that we do not need accurate expressions to determine the number of cells, $N$, per coupled line section.

According to the previous paragraph, expression (7) can be rewritten as

$$\varphi\big|_{f_0} = \frac{\pi}{2N} \tag{13}$$

where $\varphi = \varphi_e = \varphi_o$, in coherence with the considered approximation. In order to determine $N$, the relative position of the cutoff frequency, $f_C$, of the CLCLs with regard to the filter central frequency, $f_0$, must be taken into account. Under the considered approximation ($C >> 2C_c$), the cutoff frequency for both modes is identical and given by [1],[18]

$$f_C = \frac{1}{\pi\sqrt{L(C + C_{ls})}} \tag{14}$$

By combining (14) and (11a), it follows

$$\varphi\big|_{f_0} = 2\pi f_0\sqrt{L(C + C_{ls})} = 2\frac{f_0}{f_C} \tag{15}$$

and by introducing (13) in (15), the ratio between the cutoff frequency and the filter central frequency can be expressed as:

$$\frac{f_C}{f_0} = \frac{4N}{\pi} \tag{16}$$

In coupled line bandpass filters, the first spurious band appears at $2f_0$. For the suppression of that band, it is thus necessary that $f_C < 2f_0$. Therefore, according to expression (16), it follows that the number of stages (unit cells) of the coupled lines, $N$, must satisfy:

$$N < \frac{\pi}{2} \tag{17}$$

giving a single stage ($N = 1$). If the number of unit cells is $N \geq 2$, then the first spurious band cannot be efficiently suppressed. However, it is not necessary that the number of unit cells of each coupled line section is the same. Expression (17) dictates that at least one of the coupled line sections must be designed with a single unit cell in order to reject the first spurious band of the filter. In practice, we have designed the filters reported in this work by combining

coupled line sections with one and two unit cells, as will be later shown.

In order to estimate the capability of the CLCL sections in rejecting multiple harmonic bands, the upper limit of the stop band must be determined. It is given by [1],[18]

$$f_S = \frac{1}{2\sqrt{LC}} \tag{18}$$

where, again, it has been assumed that $f_S$ is identical for the even and odd modes. Note that this expression is not inferred from the lumped element equivalent circuit model of Fig. 3(b) [or (c)], since this model does not predict the presence of a finite stop band above $f_C$, but an unlimited stop band. To obtain expression (18), the distributed model of Fig. 1(c) [or (d), under the considered low coupling level approximation] is necessary. Analysis of (1) reveals that the upper limit of the stop band occurs when $\beta_e l = k_e l = \pi$ (note that this is not in contradiction with a *swr* smaller than one, since the *swr* makes sense in the first pass band of the slow wave structure). Since

$$k_e l = 2\pi f\sqrt{LC} \tag{19}$$

expression (18) is obtained.

By dividing (18) and (14), the ratio between $f_S$ and $f_C$ is obtained

$$\frac{f_S}{f_C} = \frac{\pi}{2}\sqrt{1+\frac{C_{ls}}{C}} = \frac{\pi}{2}\frac{1}{swr} \tag{20}$$

with $swr = swr_e = swr_o$. By introducing (16) in (20),

$$\frac{f_S}{f_0} = \frac{2N}{swr} \tag{21}$$

That is, the number of spurious bands that can be rejected with $N$ =1 (a value necessary to reject the first harmonic band) is determined by the slow-wave factor. Let us consider, for instance, that $swr$ = 1/2, corresponding to 50% size reduction. With this value and expression (21), the stop band extends up to $f_S = 4f_0$, and hence the first ($2f_0$) and second ($3f_0$) spurious bands are expected to be efficiently suppressed.

Let us now consider that $N$ = 2. In this case, expressions (16) and (21) give $f_C = 2.55f_0$ and $f_S = 8f_0$, respectively. Hence, we expect that coupled line sections with two capacitive stages are able to reject from the second ($3f_0$) up to the sixth ($7f_0$) spurious band. Note that these results indicate that by combining CLCL sections with single and two capacitive unit cells in the considered filter, a very wide stop band (provided the slow-wave ratio is set to $swr_e$ = 1/2) should result. This is the considered situation in the examples reported in Section IV.

## III. THE ASM OPTIMIZATION TOOL

ASM is an optimization tool that has been applied in many different scenarios, in particular to the synthesis of planar microwave circuits that can be described by lumped element equivalent circuits, or by a combination of lumped and distributed (transmission line sections or stubs) elements [50]-[54]. In ASM optimization, two different simulation spaces are considered: (i) the optimization space, $\mathbf{X_c}$, where the variables are linked to a coarse model, which is simple and computationally efficient, although not accurate, and (ii) the validation space, $\mathbf{X_f}$, where the variables are linked to a fine model, typically more complex and CPU intensive, but substantially more precise. In each space, a vector containing the different model parameters is defined. Such vectors are denoted as $\mathbf{x_f}$ and $\mathbf{x_c}$ for the fine and coarse model spaces, respectively, and their corresponding responses are designated as $\mathbf{R_f}(\mathbf{x_f})$ and $\mathbf{R_c}(\mathbf{x_c})$.

In the optimization of planar circuits, the variables of the optimization space are typically a set of lumped elements (inductors and/or capacitors) [52], a set of electrical parameters (e.g., electrical length or characteristic impedance of a transmission line), or a combination of the previous elements/parameters [50],[53],[54]. In this space, the response is inferred from the electrical simulation of the lumped element circuit or circuit schematic. The variables of the validation space are a set of geometrical parameters that define the circuit layout, and the response in this space is obtained from the electromagnetic simulation of that layout. If the number of geometrical parameters necessary to completely define the geometry is too high, some of them are fixed to certain (reasonable) values [53],[54]. Moreover, substrate parameters are usually fixed and hence they are not optimization variables. In ASM it is very convenient to deal with the same number of parameters in both spaces since this eases the implementation of the ASM algorithm.

In ASM, the target solution is determined through an iterative quasi-Newton type algorithm, and a parameter transformation mapping the fine model parameter space to the coarse model parameter space is needed. In planar circuits, such parameter transformation is simply a parameter extractor, providing the elements of the coarse model from the response of the fine model (e.g., the element values of the circuit model, inferred from the electromagnetic simulation of the circuit layout by applying specific parameter extraction techniques). Thus, the goal in ASM is to minimize the following error function:

$$\mathbf{f}(\mathbf{x_f}) = \mathbf{P}(\mathbf{x_f}) - \mathbf{x_c}^* \tag{22}$$

where $\mathbf{x_c}^*$ is the coarse model solution that gives the target response, $\mathbf{R_c}(\mathbf{x_c}^*)$, and $\mathbf{P}(\mathbf{x_f})$ provides the coarse model parameters from the fine model parameters by means of a parameter extraction procedure, as mentioned above (examples of parameter extraction in transmission lines loaded with electrically small resonators can be found in [55],[56]).

Let us assume that $\mathbf{x_f}^{(j)}$ is the $j$-th approximation to the solution in the validation space, and $\mathbf{f}^{(j)}$ the error function corresponding to $\mathbf{f}(\mathbf{x_f}^{(j)})$. The next vector of the iterative process $\mathbf{x_f}^{(j+1)}$ is obtained by a quasi-Newton iteration according to

$$\mathbf{x_f}^{(j+1)} = \mathbf{x_f}^{(j)} + \mathbf{h}^{(j)} \tag{23}$$

where $\mathbf{h}^{(j)}$ is given by:

$$\mathbf{h}^{(j)} = -\left(\mathbf{B}^{(j)}\right)^{-1}\mathbf{f}^{(j)} \tag{24}$$

and $\mathbf{B}^{(j)}$ is an approach to the Jacobian matrix, which is updated according to the Broyden formula [42]:

$$\mathbf{B}^{(j+1)} = \mathbf{B}^{(j)} + \frac{\mathbf{f}^{(j+1)}\mathbf{h}^{(j)T}}{\mathbf{h}^{(j)T}\mathbf{h}^{(j)}} \tag{25}$$

In (25), $\mathbf{f}^{(j+1)}$ is obtained by evaluating (22), and the super-index $T$ stands for transpose.

In complex circuits, such as filters, dealing with all the variables of both spaces simultaneously may be too cumbersome. However, if the structure to be designed consists of several uncoupled stages or sections, it is possible to optimize each section separately, then cascade or group them, and post optimize if necessary. Moreover,

within each circuit section, if there is small correlation between certain elements of both spaces, it is potentially possible to divide the algorithm in different ASM sub-processes. This approach reduces complexity and computational time, and has been successfully applied, e.g. to the design of bandpass filters based on stepped impedance resonators [53],[54].

In this work, the considered filters are implemented by cascading CLCL sections, and we assume that inter-section coupling is negligible. Therefore, each coupled line section is synthesized independently. Additionally, the dimensions of the capacitive patches are optimized independently, using a one-variable (for each space) ASM sub-process developed before by the authors [50]. This means that we first determine patch dimensions, and such dimensions are not optimization variables in the ASM algorithm specifically developed to obtain the whole coupled line section layout. For convenience, let us designate the first one-variable ASM sub-algorithm as patch-ASM, and the second one, involving the whole capacitively-loaded coupled line section, as CLCL-ASM.

In brief (see further details in [50]), the variables of the fine and coarse models in the patch-ASM are the side length ($l_p$) of the capacitive patch and the capacitance $C_{ls}$, respectively. The geometry is depicted in Fig. 4, where a square shaped patch connected to the host line through a wide and short access strip (to avoid any inductive effect) is considered. The distance between the host line and the patch (length of the access strip, $l_{acc}$) is set to a fixed value (0.6 mm), whereas its width ($W_{acc}$) is set to a fraction of the patch dimension $l_p$ (specifically, it has been found that 50% of the patch dimension is a good choice). The first value of $l_p$ is inferred from the target value of $C_{ls}$ (derived from the procedure explained in Section II), through the parallel plate capacitor formula. Then the capacitance of this patch is inferred from the electromagnetic simulation by considering the ports indicated in Fig. 4, specifically by inferring the admittance of the shunt load. Once the capacitance is obtained, it is compared to the target value, and the iterative ASM process is started -using expression in eq. (23)-, unless the error is smaller than a certain predefined value.

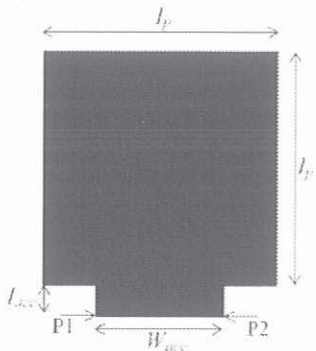


Fig. 4. Topology and relevant dimensions of the capacitive patch.

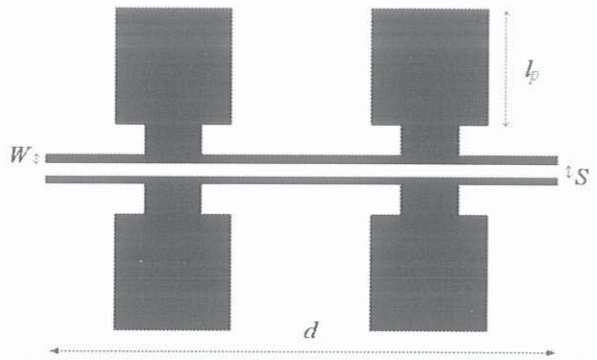


Fig. 5. Topology and relevant dimensions of the patch-loaded coupled line section, where two unit cells have been considered.

For the CLCL-ASM algorithm, the variables in the validation space are the width, $W$, separation, $S$, and length, $d$, of the unloaded coupled lines (Fig. 5). Note that the length $d$ must satisfy $d = N \cdot l$. In principle, the natural variables in the optimization space should be the even and odd mode Bloch impedances ($Z_{Be}$ and $Z_{Bo}$) of the CLCLs, and the average electrical length of the two modes at $f_0$, i.e., $\varphi_{av} = N(\varphi_e + \varphi_o)/2$ [see expression (7)]. The reason is that the target values of these impedances ($Z_{Be}^*$ and $Z_{Bo}^*$) for each coupled line section are directly dictated by filter specifications, and the average electrical length of the loaded coupled lines is usually forced to be $\varphi_{av}^* = \pi/2$. Nevertheless, we have actually considered different optimization variables, to be specified next.

We terminate in open circuits two crossed ports of the patch-loaded coupled lines, so that a two-port circuit results. Assuming that the electrical lengths of both modes are identical, i.e., $\varphi = N\varphi_e = N\varphi_o$, the image impedance of this circuit is related to $Z_{Be}$, $Z_{Bo}$ and $\varphi$ by [48]

$$Z_I = \frac{1}{2}\sqrt{(Z_{Be} - Z_{Bo})^2 \csc^2 \varphi - (Z_{Be} + Z_{Bo})^2 \cot^2 \varphi} \quad (26)$$

and it takes the maximum value when $\varphi = \pi/2$, i.e.,

$$Z_{I,\max} = \frac{Z_{Be} - Z_{Bo}}{2} \quad (27)$$

Moreover, the real part of the image impedance around $\varphi = \pi/2$ is delimited to a band with cutoffs, $\varphi_1$ and $\varphi_2$, given by

$$\cos\varphi_1 = -\cos\varphi_2 = \frac{Z_{Be} - Z_{Bo}}{Z_{Be} + Z_{Bo}} \quad (28)$$

Note that from the target values of $Z_{Be}^*$ and $Z_{Bo}^*$, we can define target values for the maximum image impedance, $Z_{I,max}^*$, and for the phase of the lower cutoff frequency, $\varphi_1^*$. The image impedance can be inferred from the simulated S-parameters of the constructed two-port structure by conversion to *ABCD* parameters, i.e.,

$$Z_I = \frac{B}{\sqrt{A^2 - 1}} \quad (29)$$

and from it, we can identify $Z_{I,max}$ and $\varphi_1$. Using (27) and (28), $Z_{Be}$ and $Z_{Bo}$ can be isolated and thus extracted. However, $Z_{I,max}$ and $\varphi_1$ (rather than $Z_{Be}$ and $Z_{Bo}$) are the considered optimization variables in the coarse space.

The phase $\varphi$ of the pair of patch-loaded coupled lines is related to the phase of the two-port structure, $\psi$, by [43]

$$\cos\psi = \frac{Z_{Be} + Z_{Bo}}{Z_{Be} - Z_{Bo}} \cos\varphi \quad (30)$$

Moreover,

$$\cos\psi = \frac{A+D}{2} = A \tag{31}$$

since $A = D$ in our case. Hence, from the S-parameters and transformation to *ABCD* parameters, the phase of the two port structure, $\psi$, can be inferred, and from it we can obtain $\varphi$ using (30). Note that, according to (30), $\psi = \pi/2$ gives $\varphi = \pi/2$ and vice versa. Hence we can directly use $\psi$ for optimization purposes, and consider the frequency where $\psi = \pi/2$, i.e., $f_{\pi/2}$, as the third variable of the coarse space. Obviously the target is $f_{\pi/2}^{*} = f_0$.

In the previous procedure, the involved formulation is strictly valid if the phases of the two modes are identical, which is not the case, as mentioned before. However, the values of $Z_{Be}$ and $Z_{Bo}$ that result by considering the CLCLs as a two-port [i.e., by isolation from expressions (27) and 28)] are in good approximation to those inferred from the procedure explained in Section II.A, and (30) represents a phase condition for the electrical length of the two modes as reasonable as (7). Note, however, that forcing $\psi = \pi/2$ does not mean that the average values of the electrical lengths is strictly $\pi/2$ (but roughly that value). Nevertheless, it has been found that with this procedure, the coupled line filter sections, once cascaded, provide a filter response very close to the target.

Once the three variables of the optimization and validation spaces have been determined, the CLCL-ASM algorithm is implemented. As mentioned before, the first layout is generated from the values of $Z_{oe}$, $Z_{oo}$ and $Nk_el$, $Nk_ol$ derived from the procedure indicated in Section II, and a transmission line calculator. Since the dimensions of the patch capacitors are inferred from an independent ASM sub-process (patch-ASM), such dimensions are those that are considered in the first and successive layouts of the whole CLCL section. From the seeding layout, the parameters of the coarse model ($Z_{I,max}$, $\varphi_I$, $f_{\pi/2}$) are extracted and subsequently compared to the target values in order to infer the first error function. Next, the new layout of the iterative process is inferred from (23), with **h** given by (24) and the initial Broyden matrix calculated as:

$$\mathbf{B} = \begin{pmatrix} \frac{\delta Z_{I,\max}}{\delta W} & \frac{\delta Z_{I,\max}}{\delta S} & \frac{\delta Z_{I,\max}}{\delta d} \\ \frac{\delta \varphi_1}{\delta W} & \frac{\delta \varphi_1}{\delta S} & \frac{\delta \varphi_1}{\delta d} \\ \frac{\delta f_{\pi/2}}{\delta W} & \frac{\delta f_{\pi/2}}{\delta S} & \frac{\delta f_{\pi/2}}{\delta d} \end{pmatrix} \tag{32}$$

The process is then iterated until convergence is obtained. In this work, the algorithm ends when the following norm

$$\left\| f_{norm} \right\| = \sqrt{\left(\frac{f_{\pi/2}}{f_{\pi/2}^{*}} - 1\right)^2 + \left(\frac{\phi_1}{\phi_1^{*}} - 1\right)^2 + \left(\frac{Z_{I,\max}}{Z_{I,\max}^{*}} - 1\right)^2} \tag{33}$$

is smaller than 0.5 %.

## IV. DESIGN EXAMPLES

### A. 3rd-order filter

Using the previously reported ASM algorithm, we have generated the layout of an order-3 filter consisting of four cascaded CLCL sections, as a first illustrative example. A Chebyshev response was considered with central frequency $f_0 = 1.0$ GHz, fractional bandwidth $FBW = 8\%$ and ripple level of $L_{Ar} = 0.1$ dB. With these specifications, the impedances of the coupled line sections were found to be $Z_{Be} = 73.54\ \Omega$ and $Z_{Bo} = 38.64\ \Omega$ for coupled line sections 1 and 4, and $Z_{Be} = 56.44\ \Omega$ and $Z_{Bo} = 44.89\ \Omega$ for coupled line sections 2 and 3. The layout of the conventional filter, inferred from a simplified version of the proposed ASM (provided the patch capacitors are not present) is depicted in Fig. 6(a). The considered substrate is the *Rogers RO3010*, with thickness $h = 1.27$ mm and dielectric constant $\varepsilon_r = 10.2$, and electromagnetic simulations were carried out by means of the *Keysight Momentum* commercial simulator. The frequency response is depicted in Fig. 7, where the presence of spurious bands, at $2f_0$ and at higher harmonic frequencies can be appreciated. Such filter has been designed for comparison purposes. Moreover, a very good agreement in terms of central frequency, bandwidth and the ripple level can be observed.

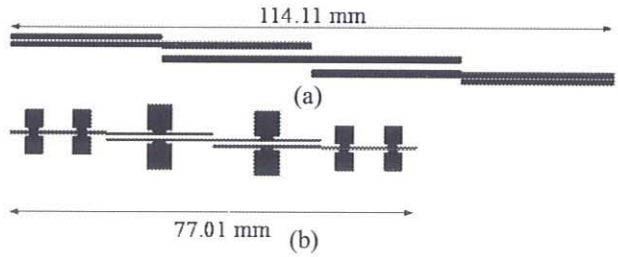


Fig. 6. Layouts of the designed coupled line bandpass filters. (a) conventional; (b) capacitively-loaded. Both layouts are drawn to the same scale.

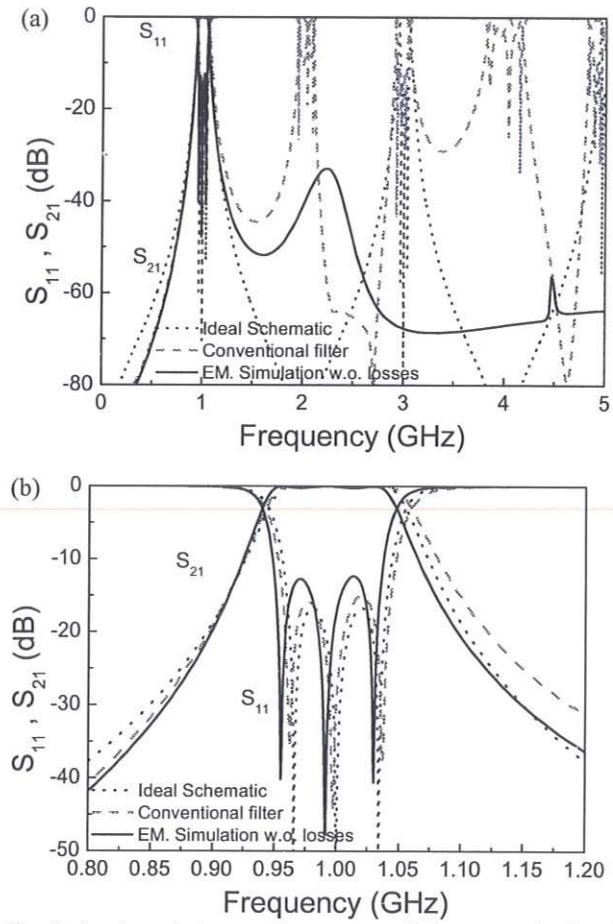


Fig. 7. Lossless electromagnetic response of the conventional and capacitively-loaded coupled line bandpass filters of Fig. 6. (a) Wideband response; (b) zoom view of the pass band.

For the design of the capacitively-loaded coupled line bandpass filter, a single unit cell for filter sections 2 and 3 has been considered, whereas for sections 1 and 4, the coupled lines are loaded with two pairs of patches. By this procedure, we ensure a wide stop band, as discussed in Section II. The slow wave ratio has been considered to be $swr_e = 0.5$. By using (1)-(9), the value of the patch capacitances and the electrical parameters of the coupled line sections can be found (see Table I).

TABLE I
ELEMENTS OF THE SCHEMATIC OF FIG. 1 USED TO DETERMINE THE SEEDING LAYOUT OF THE ASM

| *Stage* | $Z_{oe}$ (Ω) | $Z_{oo}$ (Ω) | $C_{ls}$ (pF) | $k_e l$ | $k_o l$ |
|---|---|---|---|---|---|
| 1,4 | 154.84 | 57.65 | 1.293 | 25.23° | 23.68° |
| 2,3 | 145.48 | 79.59 | 2.349 | 50.66° | 47.36° |

Moreover, the resulting slow wave ratio for the odd mode, and electrical lengths of the CLCL sections are $swr_o = 0.682$, $\beta_e l = 50.47^\circ$, and $\beta_o l = 34.72^\circ$, respectively, for sections 1 and 4, and for sections 2 and 3 are $swr_o = 0.625$, $\beta_e l = 101.32^\circ$, and $\beta_o l = 75.78^\circ$. With these values, the parameters of the fine model inferred from a transmission line calculator (except $l_p$, which has been obtained by means of the parallel plate capacitor formula) have been found to be the ones indicated in Table II. Note that the average value of $\beta_e l$ and $\beta_o l$ is not $\pi/4$ (sections 1 and 4) or $\pi/2$ (sections 2 and 3). The reason is that, rather than expression (7), we have actually forced $\psi = \pi/2$, since this provides a seeding layout closer to the final one for each filter stage. By forcing $\psi = \pi/2$, the average values of the electrical lengths of the coupled lines are not necessarily $\pi/2$, as mentioned before.

TABLE II
ELEMENTS OF THE FINE MODEL FOR THE INITIAL LAYOUT

| *Stage* | *W*(mm) | *S*(mm) | *d* (mm) | $l_p$ |
|---|---|---|---|---|
| 1,4 | 0.1220 | 0.1950 | 16.648 | 4.264 |
| 2,3 | 0.0980 | 0.4840 | 16.619 | 5.747 |

Once the seeding layout has been inferred, application of the patch-ASM has provided a side length of $l_p = 3.432$ mm for the capacitors of sections 1 and 4, and $l_p = 4.754$ mm for the capacitors of sections 2 and 3. Application of the CLCL-ASM has provided the final filter layout after 12 and 5 iterations for the synthesis of the coupled line sections with a single and two unit cells, respectively. The variables in each space after convergence are indicated in Tables III and IV.

TABLE III
ELEMENTS OF THE FINE MODEL AFTER CONVERGENCE

| *Stage* | *W*(mm) | *S*(mm) | *d* (mm) | $l_p$ |
|---|---|---|---|---|
| 1,4 | 0.1703 | 0.1950 | 18.193 | 3.432 |
| 2,3 | 0.3729 | 0.7866 | 20.312 | 4.754 |

TABLE IV
ELEMENTS OF THE COARSE MODEL AFTER CONVERGENCE

| *Stage* | $Z_{I,max}$(Ω) | $\varphi_I$ | $f_{\pi/2}$ (GHz) | $C_{ls}$ (pF) |
|---|---|---|---|---|
| 1,4 | 17.466 | 72.06° | 1.002 | 1.293 |
| 2,3 | 5.755 | 83.52° | 0.998 | 2.359 |

Fig. 8 shows the image impedance and the phase $\psi$ at several iterations for the coupled line sections with one and two unit cells, where it can be appreciated that the curves progressively evolve so that the variables of the coarse model tend to the target values, also indicated. The final layout of the filter, generated by simply cascading the different coupled line sections is depicted in Fig. 6(b). Substantial size reduction, as compared to the conventional filter is achieved by virtue of the considered slow wave factor. The electromagnetic simulation of this filter is depicted in Fig. 7. It can be seen that the response in the region of interest is very similar to the one of the ordinary filter. However, the spurious bands are efficiently suppressed up to very high frequencies. It is also important to mention that no further optimization has been required to achieve such response.

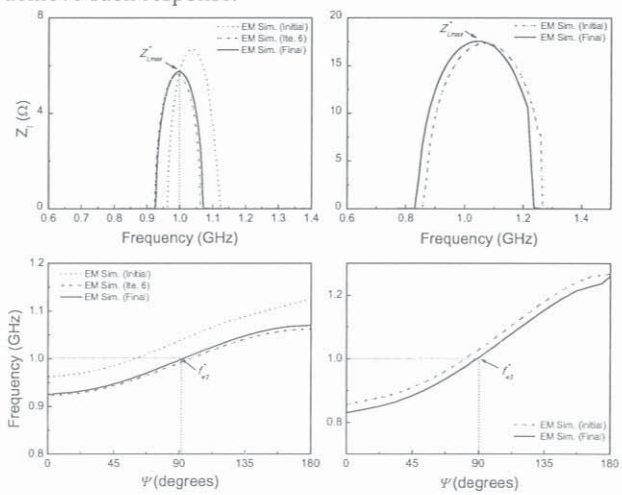


Fig. 8. Image impedance and phase $\psi$ of the coupled line sections at various iterations. (a) Single unit cell sections; (b) two unit cell sections.

The designed device has been fabricated by means of an *LPKF H-100* drilling machine. The fabricated device and the measured frequency response, inferred by means of the *Agilent PNA N5221A* vector network analyzer, are depicted in Fig. 9, where the electromagnetic simulation with losses is also included for comparison. A reasonable agreement between both responses can be observed, and spurious band rejection is better than 30 dB up to at least $5f_0$.

In order to further justify the potential of the proposed approach to reject spurious bands, and particularly the effects of the CLCL sections with $N = 2$ (two capacitive stages), we have considered the CLCL sections 1 and 4 of the filter of Fig. 6(b). Specifically, we have carried out the simulation of the schematic (i.e., with ideal capacitors and coupled lines) corresponding to the even mode, by means of *Keysight ADS*. Fig. 10 shows the dependence of the characteristic even mode impedance, $Z_{Be}$, of the CLCL section with frequency. It can be appreciated that the value at 1GHz (filter central frequency) is close to the design value indicated before ($Z_{Be} = 73.54\ \Omega$), but the important aspect in terms of spurious rejection is that a stop band between 2.54 GHz and 7.14 GHz appears. These values are in reasonable agreement with the predictions of Section II.B (see last paragraph).

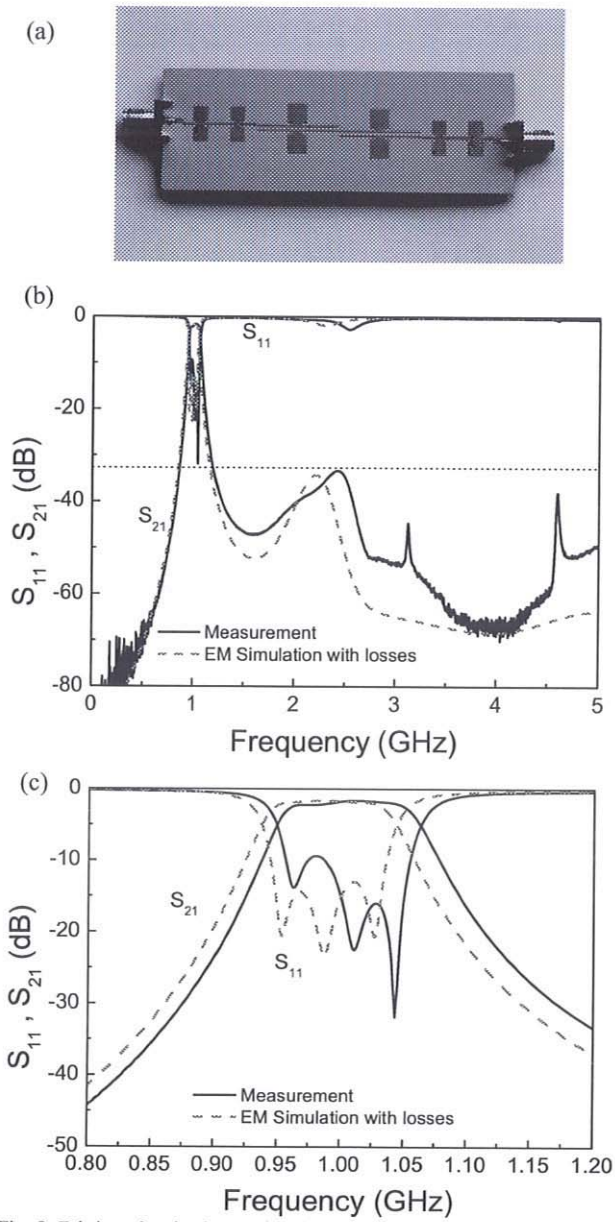


Fig. 9. Fabricated order-3 capacitively-loaded coupled line bandpass filter (a) and frequency response (b). The zoom view of the pass band is depicted in (c).

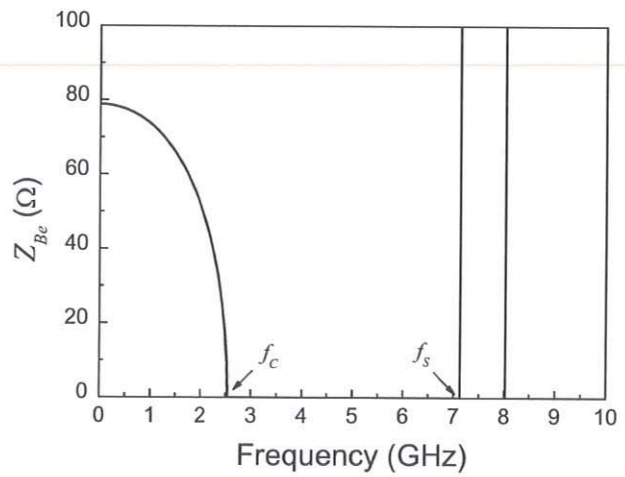


Fig. 10. Even mode characteristic impedance of the CLCL sections 1 and 4 of the filter of Fig. 6(b).

### B. $5^{th}$-order filter

To demonstrate the potential of the proposed approach based on ASM optimization, a second illustrative example was considered. Specifically, an order-5 Chebyshev bandpass filter consisting of six cascaded CLCL sections has been designed with the following specifications: $f_0 = 1.8$ GHz, $FBW = 8\%$ and ripple level of $L_{Ar} = 0.1$ dB. Accordingly, the impedances of the coupled line sections were found to be $Z_{Be} = 72.03\ \Omega$ and $Z_{Bo} = 38.93\ \Omega$ for coupled line sections 1 and 6, $Z_{Be} = 55.51\ \Omega$ and $Z_{Bo} = 45.49\ \Omega$ for coupled line sections 2 and 5, and $Z_{Be} = 54.11\ \Omega$ and $Z_{Bo} = 46.47\ \Omega$ for coupled line sections 3 and 4. Once the final layout is generated (by considering a *Rogers RO3010* substrate, with thickness $h = 1.27$ mm and dielectric constant $\varepsilon_r = 10.2$), the comparison between the lossless electromagnetic frequency response of the obtained capacitively-loaded coupled line filter and the conventional filter is shown in Fig. 11. It can be observed that there is a very good agreement between the responses in terms of central frequency, bandwidth and the ripple level, but the capability to suppress spurious band in the CLCL-based filter is apparent.

For the design of the order-5 CLCL bandpass filter, a single unit cell for filter sections 2, 3, 4, and 5 has been considered, whereas for sections 1 and 6, the coupled lines are loaded with two pairs of patches in order to suppress efficiently the spurious bands, as discussed in Section II. In this example the slow-wave ratio for the even mode of each coupled line section is also set to $swr_e = 0.5$. With this value, the patch capacitances and the electrical parameters of the unloaded coupled line sections are indicated in Table V.

TABLE V
ELEMENTS OF THE SCHEMATIC OF FIG. 2 USED TO DETERMINE THE SEEDING LAYOUT OF THE ASM

| *Stage* | $Z_{oe}$ (Ω) | $Z_{oo}$ (Ω) | $C_{ls}$ (pF) | $k_e l$ | $k_o l$ |
|---|---|---|---|---|---|
| 1,6 | 151.63 | 58.79 | 0.732 | 25.18° | 23.61° |
| 2,5 | 142.30 | 83.24 | 1.328 | 50.24° | 46.92° |
| 3,4 | 137.64 | 89.48 | 1.364 | 49.62° | 46.323° |

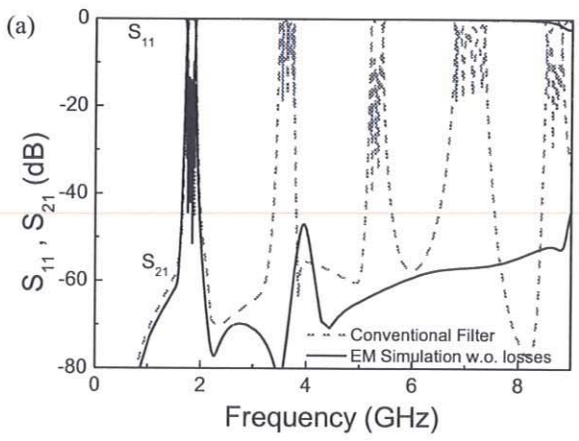

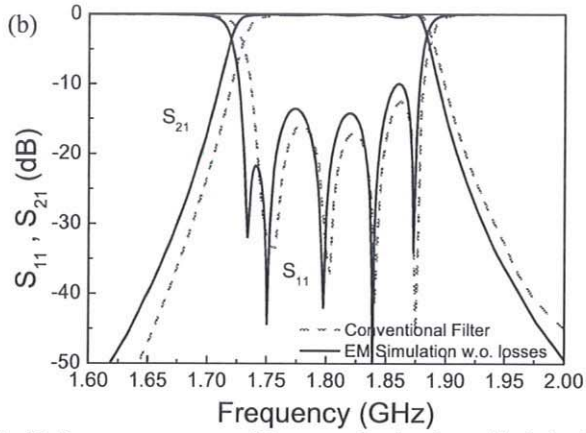


Fig. 11. Frequency responses of the conventional and capacitively-loaded coupled line order-5 bandpass filters. (a) Wideband response; (b) zoom view of the pass band.

Furthermore, the resulting slow wave ratio for the odd mode, $swr_o$, and electrical lengths of the CLCL sections ($\beta_e l$, $\beta_o l$) are as follows. For sections 1 and 6: $swr_o = 0.674$ $\beta_e l = 42.37^\circ$, $\beta_o l = 35.02^\circ$, for 2 and 5 sections: $swr_o = 0.610$, $\beta_e l = 100.47^\circ$, and $\beta_o l = 79.93^\circ$, and for 3 and 4 sections: $swr_o = 0.587$, $\beta_e l = 99.24^\circ$, and $\beta_o l = 78.92^\circ$. With these values, the parameters of the fine model have been found to be the ones indicated in Table VI.

TABLE VI
ELEMENTS OF THE FINE MODEL FOR THE INITIAL LAYOUT

| *Stage* | *W*(mm) | *S*(mm) | *d* (mm) | $l_p$ |
|---|---|---|---|---|
| 1,6 | 0.1270 | 0.2190 | 9.2180 | 3.208 |
| 2,5 | 0.0965 | 0.5723 | 9.1430 | 4.321 |
| 3,4 | 0.0930 | 0.7480 | 9.0140 | 4.380 |

(a)

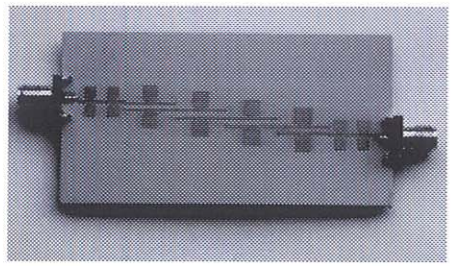

(b)

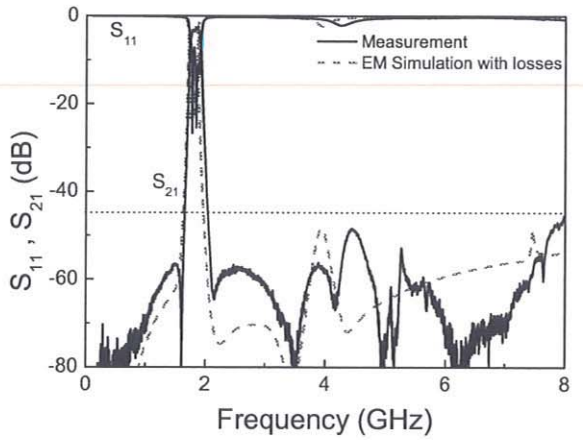


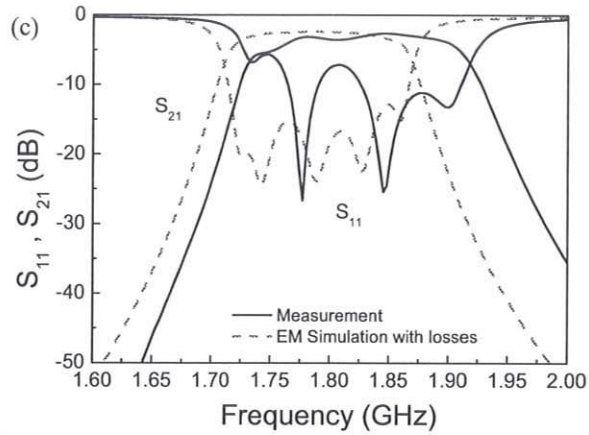


Fig. 12. Fabricated order-5 capacitively-loaded coupled line bandpass filter (a) and frequency response (b). The zoom view of the pass band is depicted in (c).

The variables in each space after convergence are indicated in Tables VII and VIII. A prototype has been fabricated -see Fig. 12(a)- and measured by using the aforementioned procedure. A reasonable agreement between the electromagnetic simulation (with losses) and measured frequency response of the proposed 5th order capacitively-loaded coupled line filter can be observed in Fig. 12 (b). Spurious band rejection is better than 45 dB up to at least $4f_0$. As an added value, the final device size has been reduced by a factor of 70 % as compared to the conventional counterpart.

TABLE VII
ELEMENTS OF THE FINE MODEL AFTER CONVERGENCE

| *Stage* | *W*(mm) | *S*(mm) | *d* (mm) | $l_p$ |
|---|---|---|---|---|
| 1,6 | 0.2053 | 0.2319 | 10.213 | 2.360 |
| 2,5 | 0.4010 | 1.0296 | 11.349 | 3.276 |
| 3,4 | 0.4270 | 1.3431 | 11.292 | 3.326 |

TABLE VIII
ELEMENTS OF THE COARSE MODEL AFTER CONVERGENCE

| *Stage* | $Z_{l,max}(\Omega)$ | $\varphi_l$ | $f_{\pi/2}$ (GHz) | $C_{ls}$ (pF) |
|---|---|---|---|---|
| 1,6 | 16.5187 | 72.97° | 1.8045 | 0.7321 |
| 2,5 | 4.9959 | 84.44° | 1.7955 | 1.3283 |
| 3,4 | 3.8043 | 85.52° | 1.800 | 1.3644 |

## V. COMPARISON TO OTHER APPROACHES

As mentioned in the introduction, coupled line bandpass filters with spurious suppression based on periodic [4] or quasi-periodic [14] structures with transverse width modulation were reported in 2001 and 2004, respectively. These filters provide very efficient spurious cancellation, specially the filter reported in [14], with 30 dB suppression up to the sixth spurious band, but dimensions are not reduced in such filters. In [57], a method to suppress only the first spurious band in coupled line bandpass filters was proposed. Such technique consists of etching a floating ground-plane conductor, which effectively equalizes the even and odd mode phase velocities of the microstrip coupled lines. However, this approach does not represent any advantage in terms size reduction (although it efficiently suppresses the first harmonic band with a measured rejection level of roughly 35 dB).

Other strategies to reduce size and achieve spurious cancellation in coupled line bandpass filters are based on reactive loading [58]-[62]. However, in these techniques, essentially the coupled lines (either open-ended or with

grounded cross ports) are either inductively or capacitively loaded in the terminations. Conversely, the strategy proposed in this paper is based on the theory of periodic structures, and coupled line sections with one or two capacitive stages are combined to achieve efficient spurious rejection, as has been justified previously. In the filter reported in [58], 25% size reduction and a rejection level of better than 47 dB until the second spurious band ($3f_0$) are achieved. In [61], a coupled line bandpass filter with 40 dB suppression until 6.6 $f_0$ is reported. Such filter is short, but at the expense of meandering the coupled lines. In [62], a filter with extremely small size (roughly 90% size reduction as compared to the conventional one) is reported, but a rejection level better than 40 dB is achieved only up to the second spurious band. Other filters reported in [62] exhibit a good balance between size and spurious suppression but these filters incorporate lumped elements in their designs.

In the filters reported in this paper a good balance between size reduction and spurious suppression is achieved, and filter design is simple since it is based on an automated approach. Particularly, the order-5 filter of Section IV.B exhibits a rejection level better than 45 dB up to at least $4f_0$. Additionally, lumped elements are not incorporated in the proposed design approach.

## VI. Conclusions

In conclusion, capacitively-loaded coupled line bandpass filters and a systematic design approach for such filters, based on aggressive space mapping (ASM) optimization, have been proposed for the first time in this paper. As compared to the conventional counterparts, the proposed filters are smaller and spurious free up to higher frequencies, due to the slow-wave effect and stopband functionality introduced by the loading capacitances (in practice implemented by means of square patches). A model of the capacitively-loaded coupled line sections, useful for design purposes, i.e., for the determination of the seeding layout necessary to iterate the ASM process, has been proposed. Specifically, from filter specifications and the required slow wave ratio (directly related to the miniaturization factor), the model provides the even and odd mode characteristic impedances of the host coupled lines, their electrical length, and the value of the loading capacitances, for each coupled line section. From these values, the first (seeding) layout of each capacitively-loaded coupled line can be inferred using analytical formulas or a transmission line calculator. Importantly, it has been demonstrated that the number of capacitive unit cells (or pair of patches) of the coupled line sections cannot be arbitrary. Indeed, to efficiently suppress the first spurious band, it is necessary that at least one coupled line sections is implemented by a single unit cell, and spurious suppression up to very high frequencies can be achieved by combining coupled line sections with different number of unit cells (single and two unit cells in the reported example).

In order to simplify the optimization process of the coupled line sections, the ASM has been divided in two ASM sub-processes. One of them devoted to determine the dimensions (side length) of the patch capacitances; the second one (using these patch dimensions), focused on the automated determination of the layout of each patch-loaded coupled line section. The two illustrative synthesis examples, an order-3 and an order-5 bandpass filter, reported in this paper, have demonstrated the effectiveness of the proposed ASM algorithm to unattendedly determine the layouts of the different coupled lines. By cascading such designed coupled line sections, it has been found that the filter response satisfies the specifications to a good approximation. Moreover, filter size has been reduced to 67 % and 70 %, for the order-3 and order-5 filters, respectively, as compared to the conventional counterparts, and the first spurious bands (at least up to the fourth one and to the third one for the order-3 and order-5 filters, respectively) are efficiently rejected.

## References


[1] F. Martín, *Artificial Transmission Lines for RF and Microwave Applications*, John Wiley, Hoboken, NJ, 2015.

[2] E. Yablonovitch, "Photonic band gap structures", *J. Opt. Soc. Amer.* B 10, pp. 283-295, 1993.

[3] J. D. Joannopoulos, R. D. Meade, and J. N. Winn, *Photonic Crystals: Molding the Flow of Light*, Princeton University Press, Princeton, NJ, 1995.

[4] T. Lopetegi, M.A.G. Laso, J. Hernández, M. Bacaicoa, D. Benito, M.J. Garde, M. Sorolla and M. Guglielmi, "New microstrip wiggly-line filters with spurious passband suppression", *IEEE Trans. Microw. Theory Tech.*, vol. 49, pp 1593-1598, 2001.

[5] I. Arnedo, M. Chudzik, J. Schwartz, I. Arregui, A. Lujambio, F. Teberio, D. Benito, M.A.G. Laso, D. Plant, J. Azaña, and T. Lopetegi, "Analytical solution for the design of planar EBG structures with spurious-free frequency response", *Microw. Opt. Techn. Lett.*, vol. 54, pp. 956-960, 2012.

[6] V. Radisic, Y. Qian, R. Coccioli, T. Itoh, "Novel 2-D photonic bandgap structure for microstrip lines", *IEEE Microw. Guided Wave Lett.*, vol. 8, pp. 69-71, 1998.

[7] F. Falcone, T. Lopetegi, and M. Sorolla, "1-D and 2-D photonic bandgap microstrip structures", *Microw. Opt. Techn. Lett.*, vol. 22, pp. 411- 412, 1999.

[8] M. A. G. Laso, T. Lopetegi, M. J. Erro, D. Benito, M. J. Garde and Mario Sorolla, "Novel wideband photonic bandgap microstrip structures", *Microw. Opt. Techn. Lett.*, vol. 24, pp. 357-360, 2000.

[9] F. Falcone, T. Lopetegi, M. Irisarri, M. A. G. Laso, M. J. Erro, and M. Sorolla, "Compact photonic bandgap microstrip structures", *Microw. Opt. Techn. Lett.*, vol 23, pp. 233-236, 1999.

[10] M. A. G. Laso, T. Lopetegi, M. J. Erro, D. Benito, M. J. Garde, and M. Sorolla, "Multiple-frequency-tuned photonic bandgap microstrip structures", *IEEE Microw. Guided Wave Lett.*, vol. 10, pp. 220-222, 2000.

[11] V. V. Shevchenko, *Continuous Transitions in Open Waveguides*, Golem, Boulder, CO, 1971.

[12] B. Z. Katsenelenbaum, L. Mercader, M. Pereyaslavets, M. Sorolla, and M. Thumm, *Theory of Nonuniform Waveguides – the Cross-section Method*, IEE Electromagnetic Waves Series, 44, London, UK, 1998.

[13] T. Lopetegi, *Photonic Band Gap Structures in Microstrip Technology: Study Using the Coupled Mode Formalism and Applications*, PhD Thesis Dissertation, Pamplona, Spain, 2002.

[14] T. Lopetegi, M. A. G. Laso, F. Falcone, F. Martín, J. Bonache, L. Pérez-Cuevas, M. Sorolla, "Microstrip wiggly line band pass filters with multispurious rejection", *IEEE Microw. Wireless Compon. Lett.*, vol. 14, pp.531-533, 2004.

[15] A. Görür, "A novel coplanar slow-wave structure," *IEEE Microw. Guided Wave Lett.*, vol. 4, pp. 86–88, 1994.

[16] A. Görür, C. Karpuz and M. Alkan, "Characteristics of periodically loaded CPW structures", *IEEE Microw. Guided Wave Lett.*, vol. 8, pp. 278-280, 1998.

[17] F. Martín, J. Bonache, I. Gil, F. Falcone, T. Lopetegi, M. A. G,. Laso and M. Sorolla, "Compact spurious free CPW band pass filters based on electromagnetic bandgap structures", *Microw. Opt. Techn. Lett*, vol. 40, pp. 146-148, 2004.

[18] J. García-García J. Bonache and F. Martín, "Application of electromagnetic bandgaps (EBGs) to the design of ultra wide band pass filters (UWBPFs) with good out-of-band performance", *IEEE Trans. Microw. Theory Tech.*, vol. 54, pp. 4136-4140, 2006.

[19] F. Martín, F. Falcone, J. Bonache, T. Lopetegi, M.A.G. Laso, M. Sorolla, "New periodic-loaded electromagnetic bandgap coplanar waveguide with complete spurious passband suppression", *IEEE Microw. Wireless Compon. Lett.*, vol. 12, pp. 435-437, 2002.

[20] F. Martín, F. Falcone, J. Bonache, T. Lopetegi, M. A. G. Laso, M. Sorolla, "Analysis of the reflection properties in electromagnetic

bandgap coplanar waveguides loaded with reactive elements", *Prog. Electromag. Research, PIER*, vol. 42, pp. 27-48, 2003.

[21] F. Martín, F. Falcone, J. Bonache, M.A.G. Laso, T. Lopetegi, M. Sorolla, "New CPW low pass filter based on a slow wave structure", *Microw. Opt. Techn. Lett.*, vol. 38, pp. 190-193, 2003.

[22] F. Martín, F. Falcone, J. Bonache, M. A. G. Laso, T. Lopetegi, M. Sorolla, "Dual electromagnetic bandgap CPW structures for filter applications", *IEEE Microw. Wireless Compon. Lett.*, vol. 13, pp. 393-395, 2003.

[23] K. W. Eccleston and S.H.M. Ong, "Compact planar microstripline branch-line and rat-race couplers", *IEEE Trans. Microw. Theory Tech.*, vol. 51, pp 2119-2125, 2003.

[24] L. Zhu, "Guided-wave characteristics of periodic microstrip lines with inductive loading: slow-wave and bandstop behaviors", *Microw. Opt. Techn. Lett.*, vol. 41, pp. 77-79, 2004.

[25] F.-R. Yang, K-P. Ma, Y. Qian, and T. Itoh, "A uniplanar compact photonic-bandgap (UC-PBG) structure and its applications for microwave circuits", *IEEE Trans. Microw. Theory Tech.*, vol. 47, pp. 1509-1514, 1999.

[26] J. Sor, Y. Qian, and T. Itoh, "Miniature low-loss CPW periodic structures for filter applications", *IEEE Trans. Microw. Theory Tech.*, vol. 49, pp. 2336-2341, 2001.

[27] D. Nesic, "A new type of slow-wave 1-D PBG microstrip structure without etching in the ground plane for filter and other applications", *Microw. Opt. Techn. Lett.*, vol. 33, pp. 440-443, 2002.

[28] S-G. Mao, M-Y. Chen, "A novel periodic electromagnetic bandgap structure for finite-width conductor-backed coplanar waveguides", *IEEE Microw. Wireless Compon. Lett.*, vol. 11, pp. 261-263, 2001.

[29] S-G. Mao, C-M. Chen, and D-C. Chang, "Modeling of slow-wave EBG structure for printed-bowtie antenna array", *IEEE Ant. Wireless Propag. Lett.*, vol. 1, pp. 124-127, 2002.

[30] C. Zhou, and H. Y. David Yang, "Design considerations of miniaturized least dispersive periodic slow-wave structures", *IEEE Trans. Microw. Theory Tech.*, vol. 56, pp. 467-474, 2008.

[31] D. Kaddour, H. Issa, A.-L. Franc, N. Corrao, E. Pistono, F. Podevin, J.-M. Fournier, J.-M. Duchamp, and P. Ferrari, "High-Q slow-wave coplanar transmission lines on 0.35-µm CMOS process", *IEEE Microw. Wireless Compon. Lett.*, vol. 19, pp. 542-544, 2009.

[32] T. LaRocca, J. Y.-C. Liu, and M.-C. F. Chang, "60 GHz CMOS amplifiers using transformer-coupling and artificial dielectric differential transmission lines for compact design", *IEEE J. Solid-State Circuits*, vol. 44, pp. 1425–1435, 2009.

[33] J. J. Lee and C. S. Park, "A slow-wave microstrip line with a high-Q and a high dielectric constant for millimeter-wave CMOS applications", *IEEE Microw. Wireless Compon. Lett.*, vol. 20, pp. 381–383, 2010.

[34] A.-L. Franc, D. Kaddour, H. Issa, E. Pistono, N. Corrao, J.-M. Fournier and P. Ferrari, "Impact of technology dispersion on slow-wave high performance shielded CPW transmission lines characteristics", *Microw. Opt. Techn. Lett.*, vol. 52, pp. 2786-2789, 2010.

[35] M. Abdel Aziz, H. Issa, D. Kaddour, F. Podevin, A. M. E. Safwat, E. Pistono, J.-M. Duchamp, A. Vilcot, J.-M. Fournier, and P. Ferrari, "Slow-wave high-Q coplanar striplines in CMOS technology and their RLCG model", *Microw. Opt. Techn. Lett.*, vol. 54, pp. 650-654, 2012.

[36] J. G. Lee, W. S. Lee, J. J. Ryu, Y. K. Moon, J. H. Jang, H. C. Kim, and H. C. Choi, "Compact semilumped bandstop resonators using the capacitively loaded parallel coupled microstrip line", *Microw. Opt. Techn. Lett.*, vol. 49, pp. 367-369, Feb. 2007.

[37] L. Li, F. Xu, K. Wu, S. Delprat, J. Ho, and M. Chaker, "Slow-wave line coupler with interdigital capacitor loading", *IEEE Trans. Microw. Theory Techn.*, vol. 55, no. 11, pp. 2427-2433, Nov. 2007.

[38] C. I. Shie, J. C. Cheng, S. C. Chou, and Y. C. Chiang, "Transdirectional coupled-line couplers implemented by periodical shunt capacitors", IEEE Trans. Microw. Theory Techn., vol. 57, no 12, pp. 2981-2988, Dec. 2009.

[39] H. M. Liu, S. J. Fang, Z. B. Wang, and Y. Zhou, "Miniaturization of trans-directional coupled line couplers using series inductors", *Prog. Electromagn. Res. C*, vol. 46, pp. 171-177, 2014.

[40] J. Selga, P. Vélez, M. Orellana, A. Rodríguez, V. Boria, F. Martín, "Size reduction and spurious suppression in microstrip coupled line bandpass filters by means of capacitive electromagnetic bandgaps", *IEEE MTT-S Int. Microw. Symp.* (IMS'16), San Francisco, May 2016.

[41] J. W. Bandler, R. M. Biernacki, S. H. Chen, P. A. Grobelny and R.H. Hemmers, "Space mapping technique for electromagnetic optimization", *IEEE Trans. Microw. Theory Techn.*, vol. 42, pp. 2536-2544, Dec. 1994.

[42] J. W. Bandler, R. M. Biernacki, S. H. Chen, R. H. Hemmers, and K. Madsen, "Electromagnetic optimization exploiting aggressive space mapping", *IEEE Trans. Microw. Theory Techn.*, vol. 43, pp. 2874-2882, Dec. 1995.

[43] M. H. Bakr, J. W. Bandler, K. Madsen, J. E. Rayas-Sánchez, and J. Søndergaard, "Space-mapping optimization of microwave circuits exploiting surrogate models," *IEEE Trans. Microw. Theory Techn.*, vol. 43, no. 12, pp. 2297–2306, Dec. 2000.

[44] J. W. Bandler, Q. S. Cheng, D. M. Hailu, and N. K. Nikolova,"A space mapping design framework," *IEEE Trans. Microw. Theory Techn.*, vol. 53, no. 11, pp. 2601–2610, Nov. 2004.

[45] J. V. Morro, P. Soto, H. Esteban, V. E. Boria, C. Bachiller, M. Taroncher, S. Cogollos, and B. Gimeno, "Fast automated design of waveguide filters using aggressive space mapping with a new segmentation strategy and a hybrid optimization algorithm," *IEEE Trans. Microw. Theory Techn.*, vol. 53, no. 4, pp. 1130–1142, Apr. 2005.

[46] S. Koziel, Q. S. Cheng, and J. W. Bandler, "Space mapping", *IEEE Microwave Magazine*, vol. 9, pp. 105-122, Dec. 2008.

[47] Q. S. Cheng, J. C. Rautio, J. W. Bandler, and S. Koziel, "Progress in simulator-based tuning-the art of tuning space mapping," *IEEE Microw. Mag.*, vol. 11, no. 4, pp. 96–110, Jun. 2010.

[48] D. M. Pozar, *Microwave Engineering*, Addison Wesley, 1990.

[49] W.R. Eisenstadt, *Microwave Differential Circuit Design Using Mixed-Mode S-parameters*, Artech House, Norwood, MA, 2006.

[50] M. Orellana, J. Selga, M. Sans, A. Rodríguez, V. Boria, F. Martín, "Synthesis of slow-wave structures based on capacitive-loaded lines through Aggressive Space Mapping (ASM)", *Int. J. RF Microw. Comput. Aided Eng.*, vol. 25, pp. 629-638, Sep. 2015.

[51] J. Selga, A. Rodríguez, M. Gil, J. Carbonell, V.E. Boria, and F. Martín, "Synthesis of Planar Microwave Circuits through Aggressive Space Mapping using commercially available software packages", *Int. J. RF Microw. Computer-Aided Engineering*, vol. 20 (5), pp. 527-534, Sep. 2010.

[52] J. Selga, A. Rodríguez, V. E. Boria, and F. Martín, "Synthesis of Split Rings based Artificial Transmission Lines through a New Two-Step, Fast Converging, and Robust Aggressive Space Mapping (ASM) Algorithm", *IEEE Trans. Microw. Theory Techn.*, vol. 61(6), pp. 2295-2308, Jun. 2013.

[53] M. Sans, J. Selga, A. Rodríguez, J. Bonache, V.E. Boria, and F. Martín, "Design of planar wideband bandpass filters from specifications using a two-step aggressive space mapping (ASM) optimization algorithm", *IEEE Trans. Microw. Theory Techn.*, vol. 62, pp. 3341-3350, Dec. 2014.

[54] M. Sans, J. Selga, P. Vélez, A. Rodríguez, J. Bonache, V.E. Boria and F. Martín, "Automated design of common-mode suppressed balanced wideband bandpass filters by means of agressive space mapping (ASM)", *IEEE Trans. Microw. Theory Techn.*, vol. 63, no. 12, pp. 3896-3908, Dec. 2015.

[55] J. Bonache, M. Gil, I. Gil, J. Garcia-García and F. Martín, "On the electrical characteristics of complementary metamaterial resonators", *IEEE Microw. Wireless Compon. Lett.*, vol. 16, pp. 543.545, Oct. 2006.

[56] F. Aznar, M. Gil, J. Bonache, J.D. Baena, L. Jelinek and R. Marqués and F. Martín, "Characterization of miniaturized metamaterial resonators coupled to planar transmission lines" *J. Appl. Phys.*, vol. 104, paper 114501-1-8, Dec. 2008.

[57] M.C. Velázquez-Ahumada, J. Martel, and F. Medina, "Parallel coupled microstrip filters with floating ground-plane conductor for spurious-band suppression", *IEEE Trans. Microw. Theory Techn.*, vol. 53, no. 5, pp. 1823-1828, May 2005.

[58] P. Cheong, S.-W. Fok, and K.-W. Tam, "Miniaturized parallel coupled-line bandpass filter with spurious-response suppression," *IEEE Trans. Microw. Theory Techn.*, vol. 53, no. 5, pp. 1810 - 1816, May 2005.

[59] S.-S. Myoung, and J.-G. Yook, "Miniaturisation and harmonic suppression method of parallel coupled line filters using lumped capacitors and grounding", *Electron. Lett.*, vol. 41, pp. 849-851, Jul. 2005.

[60] S.-S. Myoung, Y. Lee and J.-G. Yook, "Bnadwidth compensation method for miniaturized coupled-line filters", *IEEE Trans. Microw. Theory Techn.*, vol. 55, no. 7, pp. 1531 - 1538, Jul 2007.

[61] S. Lee and Y. Lee, "Generalized miniaturization method for coupled-line bandpass filters by reactive loading", *IEEE Trans. Microw. Theory Techn.*, vol. 58, no.9, pp. 2383-2391, Sep. 2010.

[62] J.-H. Park, S. Lee, and Y. Lee, "Extremely miniaturized bandpass filters based on asymmetric coupled lines with equal reactance", IEEE Trans. Microw. Theory Techn., vol. 60, no. 2, pp. 261 – 269, Feb. 2012.

**Marco Orellana** was born in San José, Costa Rica, in 1985. He earned a Licentiate degree in Electrical Engineering from the Universidad de Costa Rica (UCR) in 2009. In 2011 obtained the Master degree in Micro and Nanoelectronics Engineering at the Universitat Autònoma de Barcelona with the support of the Erasmus Mundus Programme and the UCR. He has been instructor at the School of Electrical Engineering at UCR. He is currently working on his Doctoral Thesis at the Universitat Autònoma de Barcelona focused on the automation of metamaterial-based structures design.

**Jordi Selga** (S'11-M'14) was born in Barcelona, Spain, in 1982. He received the B.S. Degree in Telecommunications Engineering - Electronic Systems in 2006, the M.S. Degree in Electronics Engineering in 2008 and the PhD degree in Electronics Engineering in 2013 from the Universitat Autònoma de Barcelona (UAB), Barcelona, Spain. Since 2008 is member of CIMITEC-UAB, a research centre on Metamaterials supported by TECNIO (Catalan Government). He was holder of a national research fellowship from the *Formación de Profesorado Universitario* Program of the Education and Science Ministry (Reference AP2008-4707). He is currently working in subjects related to metamaterials, CAD design of microwave devices, EM optimization methods and automated synthesis of planar microwave components at the UAB.

**Paris Vélez** (S'10-M'14) was born in Barcelona (Spain) in 1982. He received the degree in Telecommunications Engineering, specializing in Electronics in 2008 and the Electronics Engineering degree in 2010 from the Universitat Autònoma de Barcelona. In 2014 he received his PhD in Electrical Engineering from the UAB with a thesis entitled "Common mode suppression differential microwave circuits based on Metamaterial concepts and semilumped resonators". During the PhD he was awarded with a predoctoral teaching and research fellowship by the Spanish Government from 2011 to 2014. Dr. Vélez is a reviewer of the IEEE T-MTT and of other journals. Actually, his scientific activity is focused on the miniaturization of passive circuits RF / microwave based Metamaterials.

**Marc Sans** was born in Terrassa (Barcelona), Spain, in 1982. He received the B.S. Degree in Telecommunications Engineering - Electronic Systems in 2006, the M.S. Degree in Telecommunications Engineering in 2008 and the M.S. Degree in Electronics Engineering in 2013 from the Universitat Autònoma de Barcelona (UAB). In 2008 he started his professional career as a RF Engineer at Sony-FTVE developing the RF stage of TV receivers. In 2010 he moved to Mier Comunicaciones S.A. to carry out the design of passive and active devices for VHF-UHF broadcasting units. Since 2014 he is working towards the PhD Degree at CIMITEC-UAB in the synthesis of microwave devices based on EM optimization techniques.

**Ana Rodriguez** (S'10) was born in Lugo, Spain. She received the Telecommunications Engineering degree from the Universidade de Vigo (UV), Spain, in 2008. As a student, she participated in the Erasmus exchange program, developing the Master Thesis at the University of Oulu, Finland. Since the end of 2008, she has joined the Institute of Telecommunications and Multimedia Applications (iTEAM), which is part of the scientific park at the Universitat Politècnica de València (UPV), Spain. She obtained "Master en Tecnología, Sistemas y Redes de Comunicaciones" in 2010 from UPV, and the PhD degree in 2014. Her main research interests include CAD design of microwave devices, EM optimization methods and metamaterials.

**Jordi Bonache** (S'05-M'07) was born in 1976 in Barcelona (Spain). He received the Physics and Electronics Engineering Degrees from the Universitat Autònoma de Barcelona in 1999 and 2001, respectively and the PhD degree in Electronics Engineering from the same university in 2007. In 2000, he joined the "High Energy Physics Institute" of Barcelona (IFAE), where he was involved in the design and implementation of the control and monitoring system of the MAGIC telescope. In 2001, he joined the Department of Electronics Engineering of the Universitat Autònoma de Barcelona where he is currently Associate Professor. From 2006 to 2009 worked as executive manager of CIMITEC. Currently is leading the research in RFID and antennas in CIMITEC. His research interests include active and passive microwave devices, metamaterials, antennas and RFID.

**Vicente E. Boria** (S'91-A'99-SM'02) was born in Valencia, Spain, on May 18, 1970. He received his "Ingeniero de Telecomunicación" degree (with first-class honors) and the "Doctor Ingeniero de Telecomunicación" degree from the Universidad Politécnica de Valencia, Valencia, Spain, in 1993 and 1997, respectively. In 1993 he joined the "Departamento de Comunicaciones", Universidad Politécnica de Valencia, where he has been Full Professor since 2003. In 1995 and 1996, he was holding a Spanish Trainee position with the European Space Research and Technology Centre, European Space Agency (ESTEC-ESA), Noordwijk, The Netherlands, where he was involved in the area of EM analysis and design of passive waveguide devices. He has authored or co-authored 10 chapters in technical textbooks, 135 papers in refereed international technical journals, and over 180 papers in international conference proceedings. His current research interests are focused on the analysis and automated design of passive components, left-handed and periodic structures, as well as on the simulation and measurement of power effects in passive waveguide systems.

Dr. Boria has been a member of the IEEE Microwave Theory and Techniques Society (IEEE MTT-S) and the IEEE Antennas and Propagation Society (IEEE AP-S) since 1992. He is reviewer of the IEEE Transactions on Microwave Theory and Techniques, and Proceeding of the IET (Microwaves, Antennas and Propagation). Presently, he serves as Associate Editor of IEEE Microwave and Wireless Components Letters and IET Electronics Letters. He is also a member of the Technical Committees of the IEEE-MTT International Microwave Symposium and of the European Microwave Conference.

**Ferran Martín** (M'04-SM'08-F'12) was born in Barakaldo (Vizcaya), Spain in 1965. He received the B.S. Degree in Physics from the Universitat Autònoma de Barcelona (UAB) in 1988 and the PhD degree in 1992. From 1994 up to 2006 he was Associate Professor in Electronics at the Departament d'Enginyeria Electrònica (Universitat Autònoma de Barcelona), and since 2007 he is Full Professor of Electronics. In recent years, he has been involved in different research activities including modelling and simulation of electron devices for high frequency applications, millimeter wave and THz generation systems, and the application of electromagnetic bandgaps to microwave and millimeter wave circuits. He is now very active in the field of metamaterials and their application to the miniaturization and optimization of microwave circuits and antennas. He is the head of the Microwave Engineering, Metamaterials and Antennas Group (GEMMA Group) at UAB, and director of CIMITEC, a research Center on Metamaterials supported by TECNIO (Generalitat de Catalunya). He has organized several international events related to metamaterials, including Workshops at the IEEE International Microwave Symposium (years 2005 and 2007) and European Microwave Conference (2009), and the Fifth International Congress on Advanced Electromagnetic Materials in Microwaves and Optics (Metamaterials 2011), where he has acted as chair of the Local Organizing Committee. He has acted as Guest Editor for three Special Issues on Metamaterials in three International Journals. He has authored and co-authored over 500 technical conference, letter, journal papers and book chapters, he is co-author of the book on Metamaterials entitled *Metamaterials with Negative Parameters: Theory, Design and Microwave Applications* (John Wiley & Sons Inc. 2008), author of the book *Artificial Transmission Lines for RF and Microwave Applications* (John Wiley & Sons Inc. 2015), and he has generated 15 PhDs. Ferran Martín has filed several patents on metamaterials and has headed several Development Contracts.

Prof. Martín is a member of the IEEE Microwave Theory and Techniques Society (IEEE MTT-S). He is reviewer of the IEEE Transactions on Microwave Theory and Techniques and IEEE Microwave and Wireless Components Letters, among many other journals, and he serves as member of the Editorial Board of IET Microwaves, Antennas and Propagation and International Journal of RF and Microwave Computer-Aided Engineering. He is also a member of the Technical Committees of the European Microwave Conference (EuMC) and International Congress on Advanced

Electromagnetic Materials in Microwaves and Optics (Metamaterials). Among his distinctions, Ferran Martín has received the 2006 Duran Farell Prize for Technological Research, he holds the *Parc de Recerca UAB – Santander* Technology Transfer Chair, and he has been the recipient of two ICREA ACADEMIA Awards (calls 2008 and 2013). He is Fellow of the IEEE since 2012 and Fellow of the IET since 2016.

# Application of Aggressive Space Mapping (ASM) Optimization to the Design of Electromagnetic Bandgap (EBG) based Wideband Microwave Bandpass Filters

Marco Orellana[1], Jordi Selga[1], Paris Vélez[1], Marc Sans[1], Ana Rodríguez[2], Vicente Boria[2] and Ferran Martín[1]

[1]*CIMITEC, Departament d'Enginyeria Electrònica, Universitat Autònoma de Barcelona, 08193 Bellaterra, Spain*
*E-mail: Ferran.Martin@uab.cat*
[2]*Departamento de Comunicaciones-iTEAM, Universitat Politècnica de València, 46022 Valencia, Spain*

***Abstract***

*In this paper, it is demonstrated that capacitively-loaded periodic (EBG) transmission line slow-wave structures with required electrical length and Bloch impedance can be automatically synthesized by means of Aggressive Space Mapping (ASM) optimization. These artificial transmission lines are then used to replace the ordinary line sections in a class of wideband bandpass filters consisting of a combination of such line sections and shunt-connected grounded stubs placed at equidistant positions. Size reduction, due to the slow-wave effect of the capacitively loaded lines, and spurious suppression, due to the stop band functionality of the EBG line sections, are the benefits of this approach, but the main aspect of this paper is the fact that the design procedure of the filter (layout generation) is automated and unattended.*

## 1. Introduction

Aggressive space mapping (ASM) is a technique useful for the automated design of planar microwave circuits based on quasi-Newton type iteration [1]. Two spaces are defined: (i) a coarse space, typically related to an equivalent circuit model (or schematic) of the considered structures, which is computationally efficient but not accurate; and (ii) a fine model, where the response is typically inferred from electromagnetic simulation of the layout of the structure (hence accurate but time consuming). Optimization is based on an iterative process where, departing from an initial set of parameters of the fine model (providing the layout), the target response is obtained by up-dating a Jacobian matrix, whose elements are inferred from the effects that a variation in the variables of one space cause in the variables of the other space. Using this approach, we have implemented an ASM-based algorithm, able to provide the layout of transmission lines periodically-loaded with patch capacitances, where the target is the required line impedance, the electrical length at a certain frequency, and the slow-wave factor, which has direct implication in miniaturization [2]. Then we have used the ASM algorithm to synthesize artificial lines, which are useful to reduce the size of a class of wideband bandpass filters, and simultaneously suppress the harmonic spurious bands [3].

## 2. Designed structure and results

The specifications of the bandpass filter are: order-3, central frequency $f_0$ = 2.95 GHz, bandwidth 4.8 GHz. The layout of the conventional filter is depicted in Fig. 1, together with the frequency response. The impedance of the lines and stubs, as well as the electrical lengths at the lower cutoff frequency ($f_c$ = 1.4 GHz), are indicated. Then the transmission line sections are replaced with optimized patch loaded EBG-based artificial lines, with a slow-wave factor of 0.5. The lines have been also designed to reject the spurious bands. Fig. 2 shows the layout

the synthesized filter, compared to the ordinary one, as well as the comparison of the electromagnetic response, also compared to the one of the conventional counterpart. As can be appreciated, significant size reduction is achieved, and the spurious are efficiently rejected. Moreover the layout of the filter has been obtained by first synthesizing the artificial line sections with the developed ASM algorithm, and by cascading the different stages afterwards. No further optimization has been required.

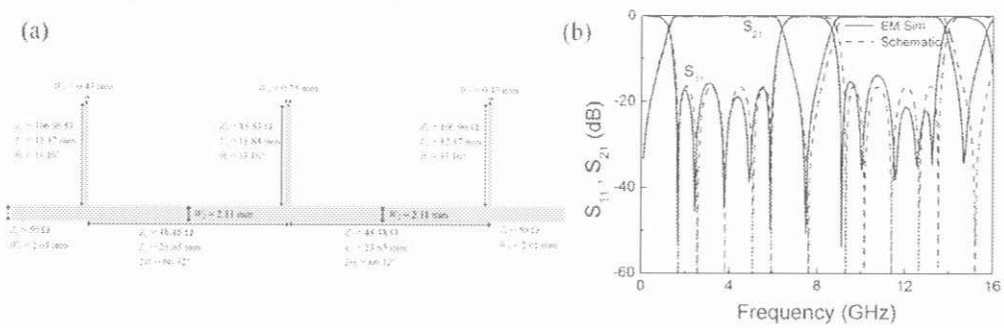


**Fig. 1**. Layout (a) and frequency response (b) of the conventional bandpass filter with indicated dimensions. The parameters of the substrate are dielectric constant $\varepsilon_r = 3.55$ and thickness $h = 0.813$ mm.

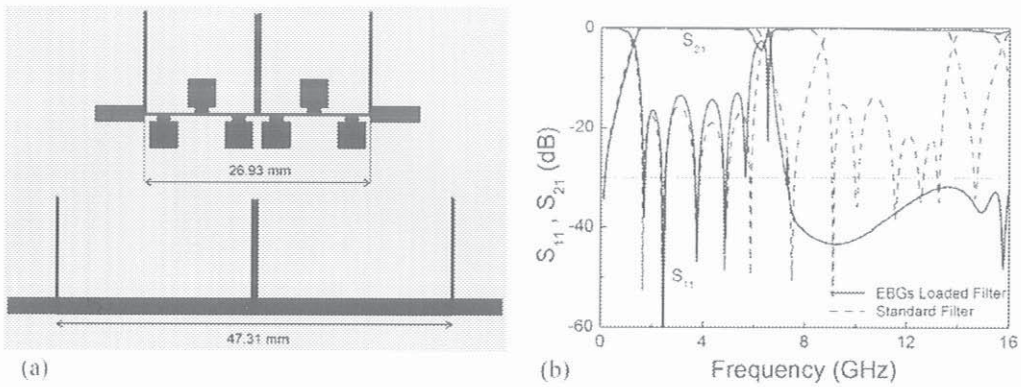


**Fig. 2**. Layout of the EBG-based filter compared to the ordinary one (a) and frequency response (b).

## 3. Conclusion

It has been demonstrated that ASM-based optimization is useful for the design of capacitively-loaded slow-wave transmission lines, and for their application to the miniaturization and spurious suppression in band pass filters.

## Acknowledgement

This work has been supported by MINECO projects TEC2013-40600-R, TEC2013-47037-C5-1-R and TEC2013-49221-EXP, by Universidad de Costa Rica, MICITT and CONICIT.

## References

[1] J.W. Bandler, R.M. Biernacki, S.H. Chen, R.H. Hemmers, and K. Madsen, "Electromagnetic optimization exploiting aggressive space mapping", *IEEE Trans. Microw. Theory Tech.*, vol. 43, pp. 2874-2882, 1995.

[2] M. Orellana, J. Selga, M. Sans, A. Rodríguez, V. Boria, F.Martín, "Synthesis of slow-wave structures based on capacitive-loaded lines through aggressive space mapping (ASM)", *International Journal of RF and Microwave Computer-Aided Engineering*, vol. 25, pp. 629-638, September 2015.

[3] J. García-García J. Bonache and F. Martín, "Application of electromagnetic bandgaps (EBGs) to the design of ultra wide band pass filters (UWBPFs) with good out-of-band performance", *IEEE Trans. Microw. Theory Tech.*, vol. 54, pp. 4136-4140, 2006.

# Size Reduction and Spurious Suppression in Microstrip Coupled Line Bandpass Filters by means of Capacitive Electromagnetic Bandgaps

Jordi Selga[1], Paris Vélez[1], Marco Orellana[1], Marc Sans[1], Ana Rodriguez[2], Vicente E. Boria[2], and Ferran Martín[1]

[1]GEMMA/CIMITEC, Departament d'Enginyeria Electrònica, Universitat Autònoma de Barcelona, Bellaterra, 08193, Spain.

[2] Departamento de Comunicaciones-iTEAM, Universidad. Politécnica de Valencia, 46022, Spain.

e-mail: Jordi.Selga@uab.cat

**Abstract — This paper is focused on the application of electromagnetic bandgaps based on capacitive loading to the implementation of microstrip coupled line bandpass filters with reduced size and spurious suppression. Size reduction is due to the slow-wave effect caused by the loading capacitances of the different coupled lines, whereas spurious suppression is related to periodicity. By properly designing the capacitively-loaded coupled line sections of the filter, implemented by means of square patches in practice, it is possible to significantly reduce filter size and simultaneously achieve spurious cancellation. As an example, an order-3 Chebyshev bandpass filter with 30% length reduction (as compared to the conventional counterpart) and spurious rejection up to the third harmonic is reported.**

**Index Terms — Bandpass filters, transmission lines, electromagnetic metamaterials, periodic structures.**

## I. Introduction

Electromagnetic bandgaps (EBGs) are periodic structures able to inhibit wave propagation at certain frequencies as consequence of the well-known Bragg effect, derived from periodicity [1]. In planar technology, EBG-based structures have been applied in many different scenarios, including passive and active circuits. In the later case, efficiency improvement in devices such as power amplifiers, mixers, oscillators or active antennas has been demonstrated by reducing the harmonic content [2]. In passive circuits, many efforts have been devoted to spurious cancellation, especially in planar filters. In most cases, spurious suppression has been achieved by periodically modulating the transverse dimensions of the transmission line sections [3], [4]. By these means, efficient rejection of spurious bands has been demonstrated, particularly in structures with multiple tuned EBGs [4]. However, this approach has not any effect on size reduction.

To simultaneously achieve spurious suppression and filter miniaturization, one solution is to periodically load the constitutive transmission line sections with shunt capacitors. These reactive elements effectively increase the line capacitance, thus reducing the phase velocity (slow-wave effect) and hence the size of the structure [5]. This approach has been successfully applied in different type of filters, such as wideband bandpass filters based on grounded stubs separated by transmission line sections loaded with patch capacitors [6].

In this paper, capacitively-loaded coupled line sections [7], consisting on coupled line pairs loaded with square patches, are applied to the design of bandpass filters with small size and spurious suppression. The reported example, i.e. an order-3 Chebyshev bandpass filter with central frequency 2.4 GHz, 8% fractional bandwidth and 0.15 dB ripple level, demonstrates the potentiality of the approach, with 30% length reduction as compared to the conventional coupled line bandpass filter, and more than 30 dB suppression up to the 3rd harmonic band.

## II. Topology and Even/Odd Mode Analysis of the Capacitively-Loaded Coupled Lines

The topology and circuit schematic of the capacitively-loaded coupled line unit cell are depicted in Fig. 1, where $C_{ls}$ is the capacitance of the square patches and $Z_{oe}$ and $Z_{oo}$ are the characteristic impedances for the even and odd modes, respectively. The equivalent circuits for these modes, inferred by removing one of the halves and considering the axial symmetry plane as a magnetic (even mode) or an electric (odd mode) wall, are depicted in Fig. 2. Parameters $k_e$ and $k_o$ are the phase constants of the unloaded coupled lines for the even and odd modes, respectively, and $l$ is the physical length of such lines. Hence the electrical lengths are $\phi_e = k_e l$ (even mode) and $\phi_o = k_o l$ (odd mode). In this work, it is assumed that the coupling between the square patches is negligible.

The dispersion relation for the even mode is given by the following expression [8]:

$$\cos(\beta_e l) = \cos(k_e l) - \frac{\omega C_{ls} Z_{oe}}{2}\sin(k_e l) \tag{1}$$

whereas the characteristic (Bloch) impedance is given by:

$$Z_{Be} = \frac{Z_{oe}\left\{\sin(k_e l) - Z_{oe}\omega C_{ls}\sin^2(k_e l/2)\right\}}{\sin(\beta_e l)} \tag{2}$$

In (1) and (2), $\beta_e$ is the phase constant of the loaded coupled lines for the even mode (providing an electrical length of $\varphi_e = \beta_e l$ for that mode), and $\omega = 2\pi f$ is the angular frequency.

978-1-5090-0698-4/16/$31.00 ©2016 IEEE

Formally, identical expressions are obtained for the dispersion and Bloch impedance of the odd mode by simply changing the sub-indices:

$$\cos(\beta_o l) = \cos(k_o l) - \frac{\omega C_{ls} Z_{oo}}{2}\sin(k_o l) \tag{3}$$

$$Z_{Bo} = \frac{Z_{oo}\left\{\sin(k_o l) - Z_{oo}\omega C_{ls}\sin^2(k_o l/2)\right\}}{\sin(\beta_o l)} \tag{4}$$

An important parameter in capacitively-loaded artificial lines is the slow-wave ratio, defined as the ratio between the phase velocities of the loaded and unloaded line, or equivalently, as the ratio between the phase constants of the unloaded and loaded lines. Since the phase velocities (or phase constants) for each mode (even and odd) in coupled lines are not (in general) identical (although very similar), the slow-wave ratio should be defined for each mode, i.e.,

$$swr_e = \frac{k_e l}{\beta_e l} \tag{5}$$

$$swr_o = \frac{k_o l}{\beta_o l} \tag{6}$$

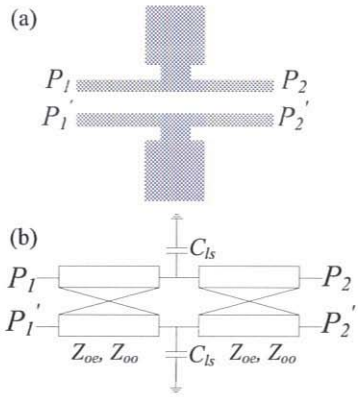


Fig. 1. Unit cell topology (a) and circuit schematic (b) of the proposed capacitively-loaded coupled lines.

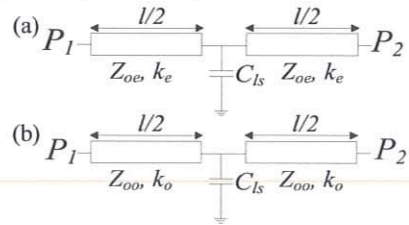


Fig. 2. Equivalent circuits of the capacitively-loaded coupled lines for the even (a) and odd (b) modes.

## III. Design of the Capacitively-Loaded Coupled Lines

For the design of the capacitively-loaded coupled lines, it is necessary to provide the electrical parameters of the circuit of Fig. 2, i.e., $C_{ls}$, $Z_{oe}$, $Z_{oo}$, and either $k_e l$ or $k_o l$ (since $k_e l$ and $k_o l$ are mutually dependent through $Z_{oe}$, $Z_{oo}$). For the purpose of this work, the design of bandpass filters, the even and odd mode impedances of the capacitively-loaded coupled lines ($Z_{Be}$ and $Z_{Bo}$) are dictated by filter specifications according to well-known formulas [9]. Note that capacitively-loaded coupled lines are intrinsically dispersive and exhibit frequency dependent Bloch impedances. Therefore, the required values of $Z_{Be}$ and $Z_{Bo}$ are forced to be satisfied at the filter central frequency, $f_0$. Each coupled line section (composed at least of one unit cell) should exhibit an electrical length at $f_0$ of $\pi/2$ for each mode. Since this is not possible in practice (at least in microstrip technology), the usual procedure is to force the average electrical length of the capacitively-loaded coupled line section corresponding to the two modes to satisfy this requirement, or $N(\varphi_e + \varphi_o)/2 = \pi/2$, where $N$ is the number of unit cells of the loaded coupled line. A fundamental parameter that determines the level of miniaturization of the final filter is the slow-wave ratio. We will set the slow-wave ratio corresponding to the even mode, $swr_e$, to a predefined value.

According to the previous paragraph, there are eight unknowns in the model ($C_{ls}$, $Z_{oe}$, $Z_{oo}$, $k_e l$, $k_o l$, $swr_o$, $\beta_o l$ and $\beta_e l$), whereas there are seven equations. However, as previously mentioned, $k_e l$ and $k_o l$ are linked through $Z_{oe}$ and $Z_{oo}$, which means that all the parameters can be univocally determined. The procedure is as follows. We provide a guess value for $\beta_e l$. From (1) and (5) evaluated at $\omega_0 = 2\pi f_0$ it follows

$$C_{ls} Z_{oe} = \frac{2\left\{\cos(swr_e \cdot \beta_e l) - \cos(\beta_e l)\right\}}{\omega_o \sin(swr_e \cdot \beta_e l)} \tag{7}$$

where all the parameters in the right hand side are known. By introducing (7) in (2), we can express $Z_{oe}$ as a function of $Z_{Be}$, $swr_e$ and $\beta_e l$, that is

$$Z_{oe} = \frac{Z_{Be} \cdot \sin(\beta_e l)}{\sin(swr_e \cdot \beta_e l) - Z_{oe} C_{ls} \omega_0 \sin^2(swr_e \cdot \beta_e l/2)} \tag{8}$$

provided $C_{ls} Z_{oe}$ in the denominator of (8) is given by (7). Once $Z_{oe}$ is known, $C_{ls}$ is calculated from (7). Note also that $k_e l$ is known from (5). The determination of the four remaining parameters ($Z_{oo}$, $k_o l$, $swr_o$ and $\beta_o l$) is not simple since the relation between $k_e l$ and $k_o l$ (through $Z_{oe}$ and $Z_{oo}$) depends on the substrate parameters. Thus, we have proceed by providing a tentative value of $swr_o$, starting with $swr_o = swr_e$, and numerically solving equations (3), (4) and (6). With the resulting element values ($Z_{oo}$, $k_o l$ and $\beta_o l$) and substrate parameters, we check if $k_o l$ and $k_e l$ are compatible. If this is not the case, we sweep $swr_o$ until the resulting values of $k_o l$ and $k_e l$ are compatible with $Z_{oo}$, $Z_{oe}$, and the parameters of the substrate (which provide the transverse geometry of the unloaded coupled lines). We repeat this procedure until the condition $N(\varphi_e + \varphi_o)/2 = \pi/2$ (or another condition involving these phases) is satisfied. Once the electrical parameters of the capacitvely-loaded coupled lines have been found, the dimensions of the patch capacitors are calculated by means of the parallel plate capacitor formula. For the width, separation and length of the unloaded coupled lines, the transmission line calculator included in *Keysight* Momentum is used.

978-1-5090-0698-4/16/$31.00 ©2016 IEEE

Let us consider as an example the design of a pair of capacitively-loaded coupled lines with $Z_{Be} = 72.12\ \Omega$ and $Z_{Bo} = 38.91\ \Omega$, $swr_e = 0.5$ and $(\varphi_e + \varphi_o)/2 = \pi/4$ at 2.4 GHz. The application of the previous procedure, considering the parameters of the *Rogers RO3010* substrate with dielectric constant $\varepsilon_r = 10.2$ and thickness $h = 1.27$ mm, gives $C_{ls} = 0.57$ pF, $Z_{oe} = 152.76\ \Omega$, $Z_{oo} = 58.65\ \Omega$, $k_e l = 26.6^\circ$, $k_o l = 24.9^\circ$, $swr_o = 0.68$, $\beta_e l = 53.2^\circ$, and $\beta_o l = 36.9^\circ$. From these values, we have obtained the four-port S-parameters of the schematic, and from these values and well known transformations, we have inferred the S-parameters for the even and odd modes. By transformation to *ABCD* parameters, we have then obtained the Bloch impedance and electrical length for each mode. The results, depicted in Fig. 3, demonstrate that the target values are satisfied to a good approximation. After optimization, using aggressive space mapping (ASM), the final layout, also depicted in Fig. 3, has been inferred, and the electromagnetic simulation reveals that the agreement with the results of the circuit schematic is good.

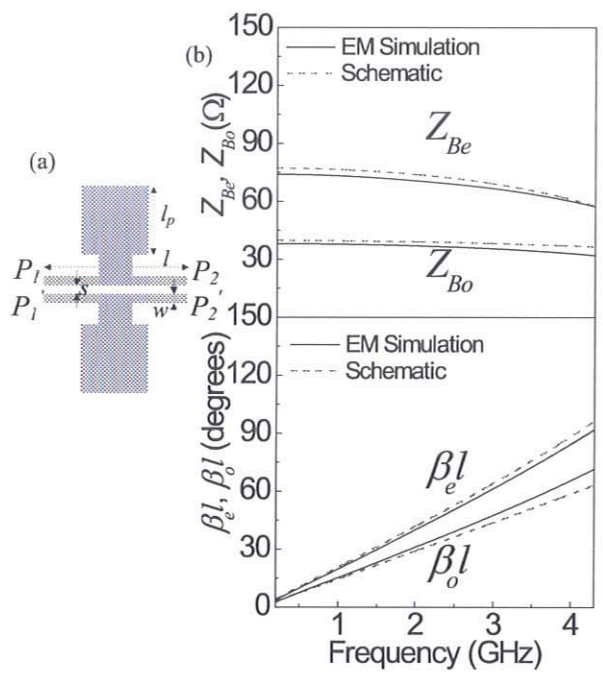


Fig. 3. Layout (a) and even and odd mode Bloch impedance and electrical length (b) corresponding to the designed capacitively-loaded coupled line unit cell. Dimensions are: $l$ = 3.962 mm, $l_p$ = 1.885 mm, $w$ = 0.252 mm, and $s$ = 0.238 mm.

## IV. Filter Design

The designed filter is an order-3 Chebyshev bandpass filter with central frequency $f_0 = 2.4$ GHz, 8% fractional bandwidth and 0.15 dB ripple level. With these specifications, the impedances of the first and fourth coupled line stages are $Z_{Be} = 72.12\ \Omega$ and $Z_{Bo} = 38.91\ \Omega$, whereas the values for the intermediate stages (second and third) are found to be $Z_{Be} = 56.08\ \Omega$ and $Z_{Bo} = 45.12\ \Omega$. The slow-wave factor (common mode) is set to $swr_e = 0.5$, and the number of unit cells is set to $N = 2$ for the first and fourth stages (hence $(\varphi_e + \varphi_o)/2 = \pi/4$), and $N = 1$ for the second and third (giving $(\varphi_e + \varphi_o)/2 = \pi/2$). With this number of stages, spurious rejection over a wide band is achieved.

Using the design method reported in the previous section, the parameters of the loaded coupled line unit cells are $C_{ls} = 0.55$ pF, $Z_{oe} = 151.79\ \Omega$, $Z_{oo} = 58.73\ \Omega$, $k_e l = 25.2^\circ$, $k_o l = 23.6^\circ$, $swr_o = 0.67$, $\beta_o l = 35.0^\circ$ and $\beta_e l = 50.3^\circ$ for the first and fourth stages, and $C_{ls} = 0.99$ pF, $Z_{oe} = 143.99\ \Omega$, $Z_{oo} = 81.14\ \Omega$, $k_e l = 50.4^\circ$, $k_o l = 47.1^\circ$, $swr_o = 0.62$, $\beta_o l = 76.2^\circ$ and $\beta_e l = 100.7^\circ$ for the second and third sections. Note that for the first and fourth stages the values are slightly different than those indicated in the example of Section III. The reason is that for filter design, we have found that the best phase condition is to force the electrical length of the resulting two-port of each coupled line section (related to $\varphi_e$ and $\varphi_o$, [9]) to $\pi/2$. Through ASM optimization, the layouts of each coupled line section have been inferred, and then such sections have been cascaded, resulting in the topology of Fig. 4 (a). No further optimization has been carried out.

Fig. 4(b) shows the lossless electromagnetic simulation, compared to the responses of the schematic and conventional filter. The lossy electromagnetic simulation and measured data, inferred from the *Agilent PNA N5221A* network analyzer, are shown in Fig. 5. According to these last figures, the capability to suppress the spurious bands is significant.

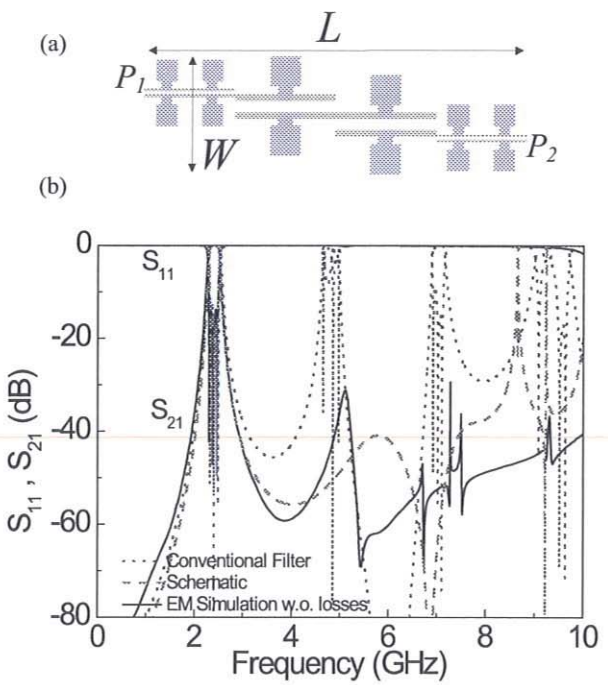


Fig. 4. Layout (a) and lossless frequency response (b) of the designed filter. Dimensions are: $L$ = 33.1 mm and $W$ = 9.8 mm.

978-1-5090-0698-4/16/$31.00 ©2016 IEEE

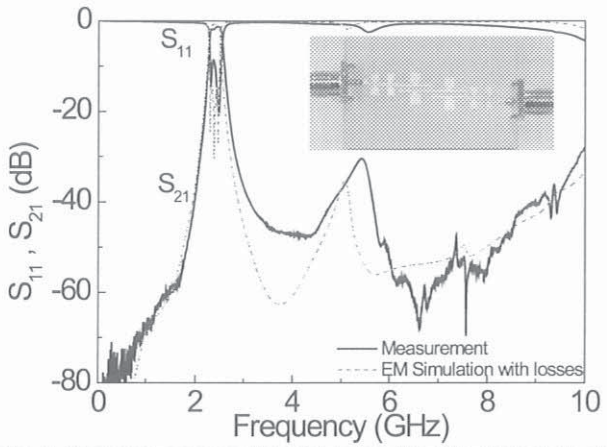


Fig. 5. Frequency response of the fabricated filter (the photograph of the fabricated prototype is shown in the inset).

## V. Conclusion

Coupled line sections loaded with patch capacitors are useful to reduce size and suppress spurious bands in coupled line bandpass filters. A design methodology, based on the even/odd mode analysis of these structures, has been reported and applied to the design of a compact and spurious suppressed order-3 bandpass filter. A 30% length reduction, as compared to the ordinary coupled line filter, and out of band rejection better than 30 dB up to at least $4f_0$ GHz (9.6 GHz), has been achieved. These results point out the potential of these capacitively-loaded coupled lines for filter design.

## Acknowledgement

This work has been supported by MINECO (Spain) under project TEC2013-40600-R and FEDER Funds. Thanks are also given to AGAUR-Generalitat de Catalunya for partially funding this research activity through the project 2014SGR-157. Ferran Martín is in debt to ICREA for supporting his work.

## References

[1] E. Yablonovitch, "Photonic band gap structures", *J. Opt. Soc. Amer.* B 10, pp. 283-295, 1993.

[2] V. Radisic, Y. Qian, T. Itoh, "Broad-band power amplifier using dielectric photonic bandgap structure", *IEEE Microwave and Guided Wave Letters*, vol. 8, pp. 13-14, Jan. 1998.

[3] T. Lopetegi, M. A. G. Laso, J. Hernández, M. Bacaicoa, D. Benito, M.J. Garde, M. Sorolla and M. Guglielmi, "New microstrip wiggly-line filters with spurious passband suppression", *IEEE Trans. Microw. Theory Tech.*, vol. 49, pp 1593-1598, 2001.

[4] T. Lopetegi, M. A. G. Laso, F. Falcone, F. Martín, J. Bonache, L. Pérez-Cuevas, M. Sorolla, "Microstrip wiggly line band pass filters with multispurious rejection", *IEEE Microw. Wireless Compon. Lett.*, vol. 14, pp.531-533, 2004.

[5] A. Görür, "A novel coplanar slow-wave structure," *IEEE Microw. Guided Wave Lett.*, vol. 4, pp. 86–88, 1994.

[6] J. García-García J. Bonache and F. Martín, "Application of electromagnetic bandgaps (EBGs) to the design of ultra wide band pass filters (UWBPFs) with good out-of-band performance", *IEEE Trans. Microw. Theory Tech.*, vol. 54, pp. 4136-4140, 2006.

[7] C. I. Shie, J. C. Cheng, S. C. Chou, and Y. C. Chiang, "Transdirectional coupled-line couplers implemented by periodical shunt capacitors", *IEEE Trans. Microw. Theory Techn.*, vol. 57, no 12, pp. 2981-2988, Dec. 2009.

[8] F. Martín, *Artificial Transmission Lines for RF and Microwave Applications*, John Wiley, Hoboken, NJ, 2015.

[9] D. M. Pozar, *Microwave Engineering*, Addison-Wesley, Reading, MA, 1990.

978-1-5090-0698-4/16/$31.00 ©2016 IEEE